12-2013

Magnetic Anisotropy and Exchange in (001) Textured FePt-based Nanostructures

Tom George
University of Nebraska-Lincoln, tageorge@huskers.unl.edu

MAGNETIC ANISOTROPY AND EXCHANGE IN (001) TEXTURED FePt-BASED NANOSTRUCTURES

by

Tom Ainsley George

A DISSERTATION

Presented to the Faculty of
The Graduate College at the University of Nebraska
In Partial Fulfillment of Requirements
For the Degree of Doctor of Philosophy

Major: Physics and Astronomy

Under the Supervision of Professor David J. Sellmyer

Lincoln, Nebraska

December, 2013

MAGNETIC ANISOTROPY AND EXCHANGE IN (001) TEXTURED FePt-BASED NANOSTRUCTURES

Tom Ainsley George, Ph.D.

University of Nebraska, 2013

Adviser: David J. Sellmyer

Hard-magnetic $L1_0$ phase FePt has been demonstrated as a promising candidate for future nanomagnetic applications, especially magnetic recording at areal densities approaching 10 Tb/in^2. Realization of FePt's potential in recording media requires control of grain size and intergranular exchange interactions in films with high degrees of $L1_0$ order and (001) crystalline texture, including high perpendicular magnetic anisotropy. Furthermore, a write-assist mechanism must be employed to overcome the high coercivity of $L1_0$ FePt nanograins. The research described in this dissertation examines potential solutions to the aforementioned problems. Specifically, a nonepitaxial method of fabricating highly (001) textured thin films is investigated by careful tuning of the as-deposited structure. Such highly textured films could be useful as a template for bit-patterned media. Secondly, control of grain size and intergranular magnetic interactions is demonstrated using non-magnetic additions of Al_2O_3, C, and Au. Finally, large reductions in the coercivity of high anisotropy, epitaxially grown $L1_0$ FePt islands are achieved in an exchange-coupled composite system by adding an exchange coupled layer of FePt:SiO_2 with moderate anisotropy. The results show promise for the implementation of $L1_0$ FePt in future magnetic recording media and other nanomagnetic applications.

DEDICATION

To my late father, Professor Thomas Adrian George, whose quiet inspiration, modesty, and commitment to excellence have provided me with the model of the man I forever strive to be.

To my wonderful wife, Annie, without whose encouragement I would not have succeeded. I sincerely thank her for her patience and understanding through some very difficult times.

ACKNOWLEDGMENTS

I am indebted to many people who have helped me along this venture. In the following I will include as many as I can, but this will be by no means exhaustive.

First and foremost, I want to sincerely thank my adviser, Professor David Sellmyer, for his unwavering support and guidance. His patient tutelage has allowed me to become the scientist I am today. I have learned so much from not only his scientific expertise but his affable yet professional character. It has been an honor to be a part of his research group and I will forever value his advice.

I would also like to sincerely thank my supervisory committee of Professors Roger Kirby, Ralph Skomski, and Jeff Shield, for their challenging questions, useful guidance, and patience in helping me complete my Ph.D. work. In particular, I would like to thank Professor Skomski for providing complementary theoretical models with which to interpret my experimental data and for including me in his related projects.

As a member of Professor Sellmyer's group I have had the opportunity to work with many excellent scientists. I want to thank Dr. Jian Zhou, Dr. Minglang Yan, Dr. Yingfan Xu, Dr. Korey Sorge, Dr. Maria Daniil, Dr. Parashu Kharel, and Dr. Bala Balasubramanian for their mentoring at various stages of my development. I would like to thank Professor Sy-Hwang Liou, Professor Sitaram Jaswal, and Dr. Yi Liu for numerous useful discussions regarding experimental and theoretical aspects of my work and physics in general. In addition, I have profited greatly from interactions with visiting scholars Dr. Emmanuel Kockrick, Dr. Johan Engelen, Professor Mircea Chipara, and Dr. Damien LeRoy, to all of whom I extend my sincerest gratitude. I was fortunate enough to experience a mutually beneficial mentorship of several undergraduates and I would be remiss not to thank Steven Ray, Craig Meeks, Adam Attig, Anatol Hoemke, and Justin Baize for their hard work in the lab and the friendships that resulted.

I would like to thank Professor Alexei Gruverman and Dr. Haidong Lu for their collaboration on the electric modulation of magnetization in BTO/LSMO interfaces.

A Ph.D. program is a difficult journey and I am thankful for the companionship of my classmates and close colleagues. I would like to thank fellow group members Dr. Zhen Li, Dr. Xiaohui Wei, Dr. Yao Zhao, Dr. Rui Zhang, Dr. Yongsheng Yu, Xiaolu Yin, and Baskhar Das for sharing their journeys with me and becoming part of mine. Thanks also goes to the many other friends made within the department through shared classes or just enjoying their company; thank you Professor Christian Binek, Dr. Shawn Hilbert, Shawn Langan, Verona Skomski, Dr. Andrew Baruth, Dr. J.D. Burton, Dr. Srinivas Polisetty, Steven Rosenboom, Dr. Toney Kelly, Chad Peterson, Dr. Dale Johsnton, Kayle DeVaughn, Dr. Marcus Natta, Dr. Xi He, Dr. Yi Wang, Dr. Abhijit Mardana, and Dr. Tathagata Mukherjee. My PhD experience was thoroughly enriched by the friendships forged along the way.

I would like to thank present and former members of the wonderful support staff in the Physics Department and the Nebraska Center for Materials and Nanomagnetism at UNL: Shelli Krupicka, Theresa Sis, Kay Haley, Jenny Becic, Therese Janovec, Cindia Carlson-Tsuda, Patty Fleek, Joyce McNeil, Marge Wolfe, Jen Barnason, Cyndy Petersen, Les Marquart, Mike Jensen, Keith Placek, Pat Pribil, Bob Rhynalds, Brian Farleigh, and Dr. John Kelty.

Scientific research is not possible without funding. I would like to acknowledge support from the following agencies: NSF-MRSEC (NSF-DMR-0820521), DOE-BES (DE-FG02-04ER46152), INSIC, and NCMN.

Last but not least I would like to thank my family: my mom, Denise, and sister, Katie Rasmussen, for providing consistent and unconditional support; my wife, Annie, and two wonderful children, Aran and Bella, for providing necessary and welcomed distractions from the rigors of work; and my in-laws, Pat and Mary Rowan.

CONTENTS

List of Figures

List of Tables

CHAPTER 1 INTRODUCTION

Advanced magnetic materials form the foundation on which nearly all twenty-first century technologies stand. From the computers, smart-phones, and modern cars integral to daily life to achieving a future of energy sustainability, complex magnets are ubiquitous with modern technology. Their unheralded yet pivotal role goes mostly unnoticed and unappreciated due to their small size and level of integration in devices. A highly competitive market for consumer electronics has fueled the incredible down-scaling of devices epitomized by Moore's law and developments in magnetic materials have followed in parallel [1.1-1.3]. Figure 1.1 depicts advances in magnetic materials from the 1980's to the early 2000's as quantified by two benchmarks of magnetic technologies: the energy product of permanent magnets and the areal density of magnetic recording media. This rate can only be sustained through the continued development of new magnetic materials. Multibillion-dollar industries can drive the implementation and incremental tuning of new materials in devices at an incredible pace; however, the seeds for true progress lay in the fundamental research performed at universities around the world. In that spirit, this dissertation reports a series of experimental investigations on magnetic thin films based on $L1_0$-phase FePt focusing on a number of magnetic and structural aspects relevant for future magnetic recording media.

Connections between a material's magnetic behavior and its microstructure have been known for well over a century. Developments in magnetic theory in the early 20^{th} century demonstrated a general underperformance of magnets when compared to predictions based on their intrinsic properties [1.1]. Advances in solid-state theory and computer-aided modeling in the middle-to-late twentieth century began to reveal the critical interplay between intrinsic and extrinsic properties in magnetic systems [1.4-1.6]. Among other approaches, this new-found

knowledge led to the development of composite magnets consisting of two or more regions with vastly different magnetic properties. By controlling the micro/nanoscale geometries at which the phases are intermixed, a hybrid system can potentially outperform a single-phase magnet. In a previously unintuitive fashion, enhancements also have included non-magnetic dopants to great effect. For example, the hardening of Co-Cr alloys by adding Pt, of Ni by Al, or of Fe by C or N.[1] Each successful improvement revealed new insights which in turn gave direction for further research. Early empirical approaches for boosting magnet performance have mostly given way to deliberate material manipulations at the very length scales on which the intricacies of magnetism operate; magnet optimization now occurs at the nano- and atomic scale [1.7].

Two key properties of magnetic materials are the exchange interaction and magnetocrystalline anisotropy (MCA). Exchange stems from the quantum-mechanical overlap of electron wave functions either within an atom or between neighboring atoms. The overlap creates competition between electrostatic and kinetic energies and the relative spin alignment, parallel or antiparallel, is enforced by the Pauli Exclusion Principle. The exchange interaction is generally a very short-range effect, but it can also dictate interactions between magnetic grains in close proximity. The magnitude and type of coupling present at various length scales significantly contributes to the overall behavior of a magnet. Magnetic anisotropy in general provides a magnet's hardness by defining an energy dependence of its magnetization orientation with respect to particular crystalline or macroscopic axes. Magnetic anisotropy determines the ground state for a magnet's moment and the directions away from which the moment is difficult to rotate, i.e. the easy and hard magnetization axes. MCA is the strongest type of magnetic anisotropy and results from spin-orbit coupling involving unquenched orbitals

[1] Magnetic hardening of Fe by C or N has long been known, yet the exact mechanism remained a mystery until the latter half of the 20th century.

where the latter is due to anisotropic local crystalline environments. It is in order to manipulate exchange interactions and MCA that the fabrication and study of magnetic materials must be approached on nano and atomic length scales.

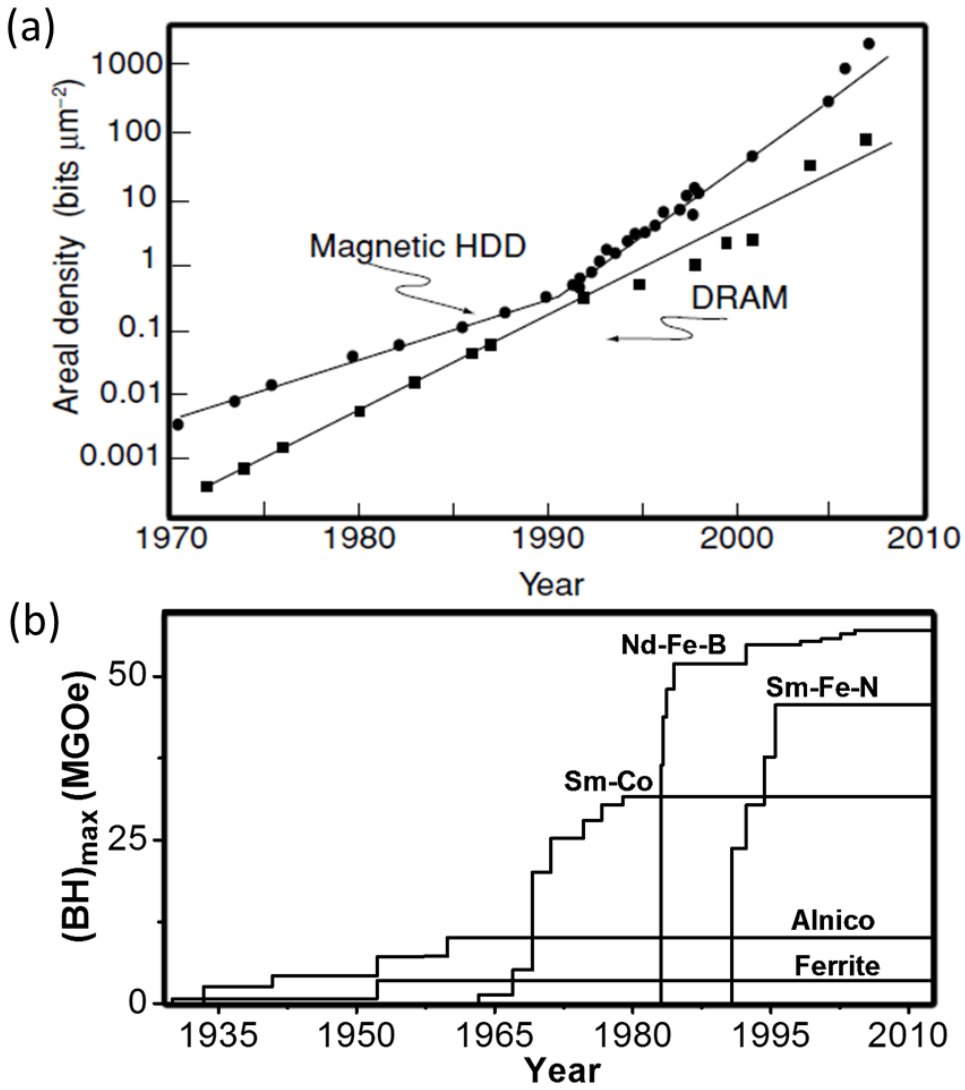

FIG. 1.1. Tracking the progress of magnetic material technologies: a) shows the improvements in areal density of magnetic recording (1 bit μ/m^2 = 0.645 $Gbit/in^2$) along with parallel progress in solid-state memory (DRAM); b) shows advancements in the strength of permanent magnets by the common metric of energy product, $(BH)_{max}$ (100 kJ/m^3 = 12.57 MGOe). Part (a) after Ref. 1.1.

A particularly recognizable application of advanced magnetic materials, and the primary motivation for this dissertation, is in magnetic hard disk drives (HDD). The information storage

industry has always been a primary mover and beneficiary of advances in magnetic materials. The industry sprang from innovations by IBM in designing the first magnetic HDD in the 1950's as a storage solution for implementing a Von Neumann computer. Researchers at IBM's San Jose Research Laboratory were searching for a method of storing calculations and machine-instructions in a permanent yet readily and rapidly accessible fashion; the idea of a "secondary storage" level was thus conceived. Designed to work alongside fast yet volatile core memory technologies (now known as random access memory, or RAM), a second tier of data storage was needed to save computation results and system commands for retrieval and immediate use by the system. Such strict requirements demanded a solution that was faster than the ponderous and bulky nonvolatile storage schemes of the day and yet more stable than vacuum tubes. In developing a thin-film magnetic media for the Random Access Method of Accounting and Control (RAMAC) 305 system, IBM designed a new non-volatile storage technology that was balanced in cost, speed, and storage density.

The process of magnetic recording follows three relatively straightforward operations: (1) a localized magnetic field polarizes a specific magnetic element or region of a magnetic material (writing a bit); (2) a magnetic sensor detects the transitions defining the magnetic topography of the media (reading a bit); and (3) the recorded magnetization state must remain stable for a desired retention period, typically on the order of ten years (storing the bit). The bit manipulation and sensing operations are performed by a read head and a write head, respectively, which have been combined into a single component: the read/write head. The collective unit is mounted on an actuator arm which can sweep an arc across the recording disk as it spins, allowing access to the entire recordable area. A small magnetic flux loop generated via electromagnetic induction and focused by specially designed soft-magnetic poles on the write head accomplishes the write operation. The magnitude of this write-field is determined by

the pole geometry and material properties. The read head is essentially a magnetic sensor designed to detect stray fields from the magnetic transitions defining individual bits of recorded data. Over the years the underlying sensing mechanism has evolved from electromagnetic induction, to magneto-resistance, to the currently used quantum-tunneling based devices [1.8-1.10], with each iteration improving the sensitivity tremendously. The design of the HDD recording media itself consists of a hard, or semi-hard, magnetic coating on a rigid disk of specialized glass. The long-term storage requirement of magnetic recording is ensured by the appropriate choice of material. The implementation of a modern magnetic HDD system actually utilizes four types of advanced magnets: macroscopic hard magnets for the actuator motors; microscopic soft magnets to focus the write-fields; nanometer-thick magnetic films within complex spintronic stacks for the read heads; and submicron-to-nanoscale semi-hard granular magnetic thin films for the media itself.

The ever-increasing amount of digital information being produced constantly pushes magnetic HDDs to higher recording densities. As shown in figure one, early hard drives were capable of storing only a few thousand bits/in^2; the recording density of IBM's RAMAC 305 was 2.5 kbits/in^2. This increased to the order of mega- to gigabits/in^2 through the 1990's and then up to 250 Gbits/in^2 in 2009 [1.8].[2] The tolerable specifications of the key components within a magnetic HHD (e.g. write-field magnitude, read-head sensitivity, or bit size) are interconnected as epitomized by the so-called "trilemma" of magnetic recording [1.11]. The trilemma states the three criteria which must be simultaneously satisfied in a magnetic recording system: long-term stability, writability, and readability. Therefore, improvements in storage density over the years have required coincident progresses in many of the other aspects of the system. Scaling component sizes to smaller dimensions was, at times, effective. However, inevitably,

[2] As of the writing of this dissertation Seagate has demonstrated media beyond the 1 TBit/in^2 mark.

technological and/or physical bottlenecks to further advances within a single facet of the technology have slowed overall development. Fortunately, through tremendous effort and forethought, the research community has provided the necessary material science breakthroughs or paradigm shifts in recording methodology to avoid completely halting the surging HDD market. As this ongoing process is maintained, the restrictions imposed by the trilemma direct and constrain the research of potential media materials. Details of the trilemma are elaborated in the following.

The product of a magnet's volume and magnetic anisotropy energy density defines a metric for the stability of a material's ferromagnetic moment to thermal fluctuations over time.[3] When this stability factor is comparable in magnitude to the product of the operating temperature, in Kelvin, and Boltzmann's constant (k_B), the magnet will undergo stochastic reversal on a time scales shorter than typical measurement times. Such a magnet is said to be superparamagnetic and is useless for data storage; in fact, the ratio of the stability metric to thermal energy must be significantly greater than one in a viable storage medium. Consequently, the magnet's anisotropy must be increased in order to maintain thermal stability as its volume shrinks. Magnetic anisotropy arises from both extrinsic and intrinsic properties as exemplified by shape and MCA, respectively. The magnetostatic configuration determined by a magnet's geometry defines its shape anisotropy while MCA, as discussed earlier, results from the system's electronic and crystal structure. The relatively small magnitude of shape anisotropy (~0.1 MJ/m^3) versus typical magnetocrystalline anisotropies (>1 MJ/m^3) meant that once areal densities reached a critical value in the 1980's further improvements required looking beyond elongated, soft magnetic iron oxide particles to materials with significant magnetocrystalline anisotropy [1.3].

[3] The volume referred to here is not the bulk volume of the magnet but the elementary volume associated with reversal, as will be described in chapter two.

Fortunately, nature provides a number of materials with high magnetocrystalline anisotropy as candidates for magnetic recording media, as listed in Table 1.1. However, the use of an arbitrarily hard material to attain extreme thermal stability factors is prohibited by the need to be able to write to the recording media. Writing, i.e. magnetizing, a magnetic bit essentially requires the write field to be strong enough to overcome the effective anisotropy energy of that bit. Since write fields are finite, the second criterion of the trilemma places strict limitations on the usable magnetic material based on the available write head technology. Write heads have come a long way since the middle of the 20th century in how the applied field is directed or focused onto the media. However, the theoretical limit for a write field is limited by the saturation magnetization of the pole material (25 kOe for Fe-Co [1.8,1.12]), placing a hard limit on the capabilities of pure field-writing schemes.

The third criterion of the magnetic recording trilemma, readability, considers the minimum detectable stray fields from bit transitions as well as requiring the signal contain minimal error or noise to be interpretable by the signal processing routine. The signal-to-noise ratio (SNR) denotes the ratio of the magnetic signal to the magnitude of the media and read-head noise. SNR is statistical in nature, to account for the random flipping of grains due to thermal activation or nearby write activity and SNR roughly scales with the number of grains per bit. High SNR is thus achieved in media by incorporating many magnetically isolated grains per data bit. The tolerable SNR of the signal processor, the design of the reading scheme, and minimum stable grain volume dictates the minimum number of necessary grains per bit, thereby limiting the achievable recording density.

Magnetic HDD recording density has progressed at a greater than 30% compound growth rate since its invention, reaching rates as high as 100% during periods of limited bottlenecks. Early evolution followed from scaling down the media-to-head spacing and

improving the write field homogeneity. Grains sizes during this time were reduced incrementally using improving fabrication techniques with little concern for the superparamagnetic limit. The discovery of giant magnetoresistance (GMR) and, subsequently, tunneling magnetoresistance (TMR) and their implementation in HDDs in the late 1990's and the current century has greatly increased read-head sensitivities. These enhancements have allowed for tremendous reductions in grain size through the use of materials with increasingly higher anisotropies. Co-Cr thin films replaced ferrite particle-based recording media in the 1980's. The subsequent discovery and understanding of a magnetically induced phase separation (MIPS) phenomenon in Co-Cr alloys has provided a wealth of tenable media candidates. The MIPS process yields highly desirable microstructures of partially decoupled high anisotropies grains [1.3]. Ternary and quaternary alloys of Co-Cr with Pt, Ta, and/or B showed incremental improvements in MCA and were implemented in various media incarnations throughout the late 20th and early 21st centuries. Up until 2006, commercial recording media followed a longitudinal recording mode where the magnetic moments lay in the film plane.[4] It had been known since the early days of MHDDs that higher write fields could be applied and detrimental intergranular interactions could be reduced by orienting the moments of the media out of the plane with high perpendicular magnetic anisotropy (PMA) [1.13]. Material candidates for future PMA recording media drew considerable attention from the research community beginning in the early 1990's and in 2006, the first commercial hard drive using CoCrPt in the perpendicular mode was marketed by Toshiba.

The high sensitivity of GMR/TMR based read heads opened the door for the large decreases in media grain size highlighted by the recording density improvements through the 1990's and early 2000's. With the superparamagnetic limit of current media in sight, and scaling

[4] IBM's RAMAC 305 used the longitudinal mode, but its first successor, the ADF 1301, was designed in the perpendicular mode. However, after a failure to cut down on bit-errors, IBM switched back to longitudinal recording in the early 1960's.

of conventional media technologies seemingly capped at around 1 Tb/in^2, a new material must be developed for future MHDD media to reach 10 Tb/in^2 and beyond [1.8]. The $L1_0$ phase of FePt has long been known for its high anisotropy and corrosion resistance [1.14] and therefore has been widely accepted as sitting atop a short list of contenders for future magnetic recording media, as seen in Table 1.1. The hard phase magnetocrystalline anisotropy of nearly 70 Merg/cm^3 (7 MJ/m^3) is second only to the highly chemically reactive $SmCo_5$. In order to satisfy the trilemma of magnetic recording in the perpendicular mode and provide a significant improvement to current media, multiple roadblocks must be addressed: the magnetic grains must be well aligned and possess significant PMA; the grain sizes must be ~4 nm and homogeneous in size and property distribution; and the switching field must be reduced to values attainable by write head. The advent of heat-assisted magnetic recording (HAMR) lessens the concern of needing enormous write fields and puts the ideal implementation of $L1_0$ FePt in sight.

Table 1.1. A list of material parameters of common hard magnetic materials, where K_u is the anisotropy energy density, M_s is the saturation magnetization, H_K is the anisotropy field, and T_c is the material's Curie temperature. Table after Ref. 1.15.

Material	Structure	K_u (10^7 erg/cm^3)	M_s (emu/cm^3)	H_K (kOe)	T_c (K)
Co_3Pt	···	2	1100	36.4	1200
$CoCr_8Pt_{22}$	hcp	0.7	500	28.0	1000
Co_3/Pt_{10}	multilayers	1.2	450	53.3	700
Co_3/Pd_{10}	multilayers	0.6	360	33.3	700
FePt	$L1_0$	7	1140	122.8	750
CoPt	$L1_0$	4.9	800	122.5	840
$SmCo_5$	hcp	20	910	439.6	1000
$Nd_2Fe_{14}B$	···	4.6	1270	72.4	585

This dissertation reports a multi-pronged investigation of magnetron sputtered hard magnetic $L1_0$ phase FePt thin films through bottom-up fabrication techniques. Control of the crystallographic texture and degree of chemical order are of great interest while varying the

nanostructure and reducing the switching field through both epitaxial and nonepitaxial growth techniques. The studies focus on manipulating the magnetic properties of FePt-based systems by varying the deposition and processing parameters or via the addition of a ternary material. The effects on $L1_0$ phase formation, sample morphology, and degree of crystalline texture are examined in each case. The remaining chapters of this dissertation are organized in the following way: Chapter 2 introduces key concepts in the magnetism and fabrication of nanostructured thin films and provides background on the $L1_0$ phase of FePt. Chapter 3 summarizes the experimental procedures used in this work. Chapter 4 reports the effects of varying deposition and processing parameters on the non-epitaxial formation of highly (001) textured $L1_0$ FePt thin films. Chapter 5 extends the work in Chap. 4 while investigating the effects of adding an elemental or oxide dopant to FePt thin films to enhance their nanostructure and magnetic properties. Chapter 6 reports two studies of an exchange-coupled system of magnetically hard and soft FePt aimed at reducing coercivity while maintaining thermal stability. Chapter 7 presents a summary of the work and reiterates the pertinent conclusions of the dissertation.

References

1.1 J. M. D. Coey, *Magnetism and Magnetic Materials*. (Cambridge University Press, Dublin, 2009).

1.2 B. D. Terris and T. Thomson, Journal of Physics D: Applied Physics **38** (12), R199 (2005).

1.3 G. W. Qin, Y. P. Ren, N. Xiao, B. Yang, L. Zuo and K. Oikawa, International Materials Reviews **54**, 157-179 (2009).

1.4 A. Aharoni, Reviews of Modern Physics **34** (2), 227-238 (1962).

1.5 F. B. Hagedorn, Journal of Applied Physics **41** (6), 2491-2502 (1970).

1.6 H. Kronmüller, K. D. Durst and M. Sagawa, Journal of Magnetism and Magnetic Materials **74** (3), 291-302 (1988).

1.7 B. Balasubramanian, B. Das, W. Y. Zhang and D. J. Sellmyer, Advanced Materials **25** (42), 6090-6093 (2013).

1.8 R. Wood, Journal of Magnetism and Magnetic Materials **321** (6), 555-561 (2009).

1.9 S. Parkin, MRS Bulletin **31** (05), 389-394 (2006).

1.10 S. Khizroev and D. Litvinov, Journal of Applied Physics **95** (9) (2004).

1.11 H. J. Richter, Journal of Physics D: Applied Physics **40**, R149-R177 (2007).

1.12 H. J. Richter, Journal of Applied Physics **111** (3), 033909 (2012).

1.13 S. Iwasaki and Y. Nakamura, IEEE Transactions on Magnetics **13** (5), 1272-1277 (1977).

1.14 L. Graf and A. Kussmann, Z. Phys. **36** (1935).

1.15 D. Weller, O. Mosendz, G. Parker, S. Pisana and T. S. Santos, physica status solidi (a) **210** (7), 1245-1260 (2013).

CHAPTER 2 BACKGROUND AND THEORY

This chapter introduces concepts relevant to understanding fabrication and structural and magnetic characterization of FePt-based nanostructured thin films. Section 2.1 describes key aspects of magnetic behavior relevant to high-anisotropy magnetic thin films and nanogranular systems. Magnetization reversal mechanisms, magnetic viscosity, and energy barriers are introduced and the thermal-stability metric is derived. General properties of interacting and non-interacting magnetic grains and composite systems with heterogeneous magnetic properties are described. Section 2.2 covers the basic concept of the thin-film fabrication techniques used in this dissertation, namely film-structure formation and evolution during magnetron sputtering and thermal processing. The chapter concludes with a general introduction to $L1_0$ FePt in Section 2.3, including some background, basic structural and magnetic properties, and general details regarding FePt-sample fabrication as well those specifically relevant to this research.

2.1 Magnetism in Nanostructured Thin Films

The magnetic response of any system depends on a combination of intrinsic properties of the constituent materials and extrinsic properties determined by the system's structure. Relevant intrinsic properties include saturation magnetization (M_s), Curie temperature (T_c), exchange (J), and magnetocrystalline anisotropy (MCA). Intrinsic properties typically depend on a material's electronic structure and therefore are linked to the magnet's atomic composition and variations in the local atomic environment. Extrinsic properties include coercivity (H_c), susceptibility (χ), and remanent magnetization (M_r), and are greatly affected by a magnet's nano- and microstructure. The nanostructuring of magnetic materials seeks to take advantage of the intrinsic properties of a material within a structure that has optimal extrinsic properties. This section addresses some concepts key to understanding the magnetic behavior of thin films and

heterogeneous nanomagnetic systems in general. A few simple models are introduced to illustrate the dependence of the measured behavior on both nanostructure and intrinsic properties of a magnetic material.

2.1.1 General Concepts

The quantum mechanical property of exchange enforces relative alignment between interacting spins via competing electrostatic potential and electron kinetic energies while simultaneously obeying the Pauli Exclusion Principle. Intra-atomic exchange between electrons within an atom stabilizes atomic magnetic moments and interatomic exchange between neighboring atoms leads to magnetic order in ferro- and anti-ferromagnets. Positive (negative) exchange stabilizes ferromagnetic (antiferromagnetic) spin alignments against thermal energy. The Curie (Néel) temperature, T_c (T_N), is the temperature above which thermal fluctuations overcome exchange energy and atomic spins randomize. In the mean-field approximation for *z* nearest interacting neighbors, a simplified expression for T_c is [2.1],

$$T_c \propto \frac{z\langle J \rangle}{k_B}, \tag{2.1}$$

thereby the interatomic exchange determines the maximum useful operating temperature of a magnet.

Magnetic anisotropy (***K***) describes the energy-dependence of a spin-orientation with respect to the magnet's structure. The lowest-energy spin configuration defines an easy anisotropy axis, parallel-to-which the magnetic moments align in their ground state, and the highest energy configuration defines a hard-axis. The magnitude of *K* represents the energy required to rotate the spins from the easy to hard axis, *i.e*. the energy difference between those two configurations. MCA, the strongest type of magnetic anisotropy, stems from the quantum-mechanical interaction between spin and orbital moments which are strongly influenced by the

surrounding crystal-field. MCA links the energy of a spin state to the local crystal-structure and its strength results from the rigidity of orbital moments within that environment.

A key feature of ferromagnets is their hysteretic response to an applied magnetic field, $\boldsymbol{M}(\boldsymbol{H})$. Understanding the underlying causes of magnetic hysteresis in complex magnets is a critical step to further improve magnetic materials in general. Analytical descriptions of magnetic hysteresis work well for ideal systems, yet they fail to accurately describe processes in highly heterogeneous, i.e. real or technical, magnets. A common starting place is to examine the minima of a magnet's free energy. Expressions for magnetic free energy, as defined by intrinsic and extrinsic properties, create a landscape on which the position and movement of magnetic moments define the magnetization processes. Typical free energy functions include the applied magnetic field, temperature, and parameterizations of other relevant properties. For example, for a magnet whose anisotropy is symmetric about a single axis [2.1],

$$E = \int \left[A \left\{ \nabla \left(\frac{\boldsymbol{M}}{\boldsymbol{M_s}} \right) \right\}^2 - K_1 \frac{(\boldsymbol{n} \cdot \boldsymbol{M})^2}{M_s^2} - \mu_o \boldsymbol{M} \cdot \boldsymbol{H} - \frac{\mu_0}{2} \boldsymbol{M} \cdot \boldsymbol{H_d}(\boldsymbol{M}) \right] \mathrm{d}V \,, \tag{2.2}$$

where K_1 is the second-order uniaxial magnetic anisotropy along the direction defined by $\boldsymbol{n}$, and, the exchange stiffness A accounts for interatomic exchange, as $A \sim J$. From the general expression for uniaxial anisotropy density, E_a,

$$\frac{E_a}{V} = K_1 \sin^2\theta + K_2 \sin^4\theta + K_3 \sin^6\theta \,, \tag{2.3}$$

only K_1 is used in Eq. (2.2) since fourth and sixth order anisotropy terms, K_2 and K_3, are typically orders of magnitude smaller and can be neglected. The parameter K_u is sometimes used to denote a non-specific uniaxial magnetic anisotropy. The effect of exchange is based on the relative directions of neighboring moments, whereas anisotropy increases the system's energy when moments point away from the anisotropy axis without concern for parallel or anti parallel spin configuration.

The last two terms in Eq. (2.2) are the Zeeman energy and magnetostatic self-energy terms, respectively. Zeeman energy is the energy required to rotate a magnetic moment $\pi/2$ away from a parallel alignment with the applied field. The magnetostatic self-energy is similar in nature, but results from the interaction between internal dipole moments and the magnet's demagnetizing field, $\boldsymbol{H}_D$, resulting from a its magnetization state. This internal field consists of the sum of all dipole moment fields throughout a magnet's volume. The phenomenon can be treated as a magnetic field generated by magnetic surface "charges" created at any surface emanating magnetic flux, *i.e.* $\boldsymbol{n}_{surface} \cdot \boldsymbol{M}$, in an analogous way to surface electrons producing an electric field. The self-energy can be expressed by,

$$E_{self} = \frac{-\mu_0}{2} \int \boldsymbol{M} \cdot \boldsymbol{H}_D dV \, . \tag{2.4}$$

In the general case of a homogeneously magnetized ellipsoid of revolution, the demagnetizing field reduces to $\boldsymbol{H}_D = -D\boldsymbol{M}$, such that it points antiparallel and with a magnitude in proportion to the magnetization. The demagnetization factor, *D,* depends on the geometry and axes of the magnet being considered. For example, $D=1/3$ isotropically for a sphere, whereas $D=1$ for moments perpendicular to an infinite sheet and zero within its plane. Since this field always opposes the magnetization, the demagnetizing field has the effect of destabilizing the magnet. The reorientation of a magnet's internal moments to minimize this self-energy results in shape anisotropy. The direction along which this the energy is minimized denotes the easy-axis of magnetization, in an analogous yet generally weaker fashion to MCA.

A magnet's equilibrium magnetization state is defined by the global minimum of its free energy landscape. By applying a magnetic field or changing the temperature, the landscape's curvature is altered and the magnetization changes as the spin states follow their lowest energy configuration. New global energy minima can manifest non-locally to the current state, thereby trapping the magnetization in a local minimum. The energy required to jump to the new global

minimum represents the energy barrier (E_b) to reversal. In switching a magnet, applying a reverse-magnetic field eventually creates new global minima and increasing the field's magnitude lowers the energy barrier separating the old and new equilibrium states. Magnetization reversal occurs when the initial state becomes unstable to the energy landscape's local curvature and the spins move into the reversed state. Thermal energy of the order $k_B T$ constantly pushes the moment against local barriers, causing reversal over barriers smaller than this value and a temperature dependence of the reversal field.

In addition to the contributions of various intrinsic properties, a magnet's switching field, H_c, and other extrinsic properties also depend on real-structure details. Structural inhomogeneities of varying scales can lead to vastly different equilibrium states and switching behavior. Even when neglecting the complications of thermal effects, understanding the causes of magnetic hysteresis becomes incredibly thorny for complex magnetic heterostructures. However, simplified magnetic models provide a useful starting place to connect observed magnetic behavior with intrinsic properties.

2.1.2 Field Dependent Behavior

A typical magnetic measurement examines a magnet's response in the same direction as a varying applied field. The hysteretic nature of a ferromagnet leads to a magnetization curve which depends on all prior fields to which the magnets has been exposed. $M(H)$ curves measured from specific initial states can reveal information about the magnetization process. Tracking the moment of a demagnetized magnet from zero applied field until saturation traces an initial magnetization curve. A measurement looping from positive to negative saturation and back forms a full hysteresis loop for the magnet. A hysteresis loop that does not saturate the magnet is a minor loop. Measuring the moment starting from any point of an initial curve or full loop as the field is relaxed back to zero then to saturation in the opposite direction records a

recoil curve. Pairing the remanent moment at the end of a recoil curve with the initial recoil field defines a point on a remanence curve. Examples of a major hysteresis loop and two standard remanence curves are described below.

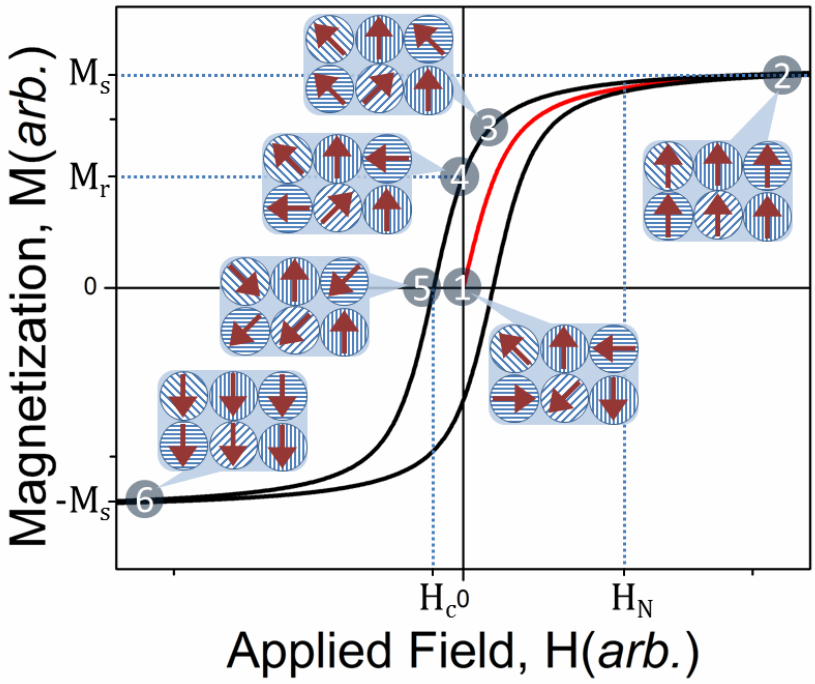

FIG. 2.1. Example of *M*(*H*) hysteresis loop, including diagrams of a six-grain proxy magnetic system for six different magnetization states along the hysteresis loop. See text for details.

An example of a typical major hysteresis loop is shown in Fig. 2.1. A schematic of six exemplary grains constituting a magnet are shown with their plausible spin states at six positions along the loop. Each magnetically isolated grain has an easy axis making a 0°, 45°, or 90° angle to the applied field direction, as illustrated by the parallel sets of blue lines within each grain. The direction of the spin state is given by the red arrows. At zero applied field, a magnet in its virgin or demagnetized state has randomized moments which yield zero magnetization (point 1 in Fig. 2.1). An increasing positive applied field begins to align the moments along that direction following the initial magnetization curve (in red). The magnetization mechanism of the magnet determines the shape of this curve; typically, concave-up curvature indicates a pinning mechanism and concave-down indicates nucleation or rotation (the isolated spherical grains

shown in Fig. 2.1 follow rotation). The magnet becomes saturated, $M = M_s$, at the saturation field, $H = H_s$, signifying that all moments are aligned with the applied field (point 2). Gradually reducing the applied magnetic field decreases the magnetization as the individual magnetic moments relax toward their anisotropy axes (point 3); the nucleation field (H_N) denotes the point at which the magnetization deviates from M_s. The non-linear change in magnetization with field gives the magnetic susceptibility, $\chi = \mathrm{d}M/\mathrm{d}H$. The magnitude of magnetization retained along the measured direction upon removal of the applied field after saturation (point 4) is termed the remanent magnetization (M_r). Applying a negative field rotates the moments into the reverse direction and at the coercive field H_c, the averaged moments yield zero magnetization (point 5). Further increasing the negative applied field eventually saturates the magnet in the fully reversed state. Reversing the process from negative back to positive saturation follows a symmetric curve and completes the hysteresis loop.[5] Cycling a magnet through one full loop costs energy essentially equal to the area enclosed by the *M*(*H*) loop and that energy is typically dissipated as heat.

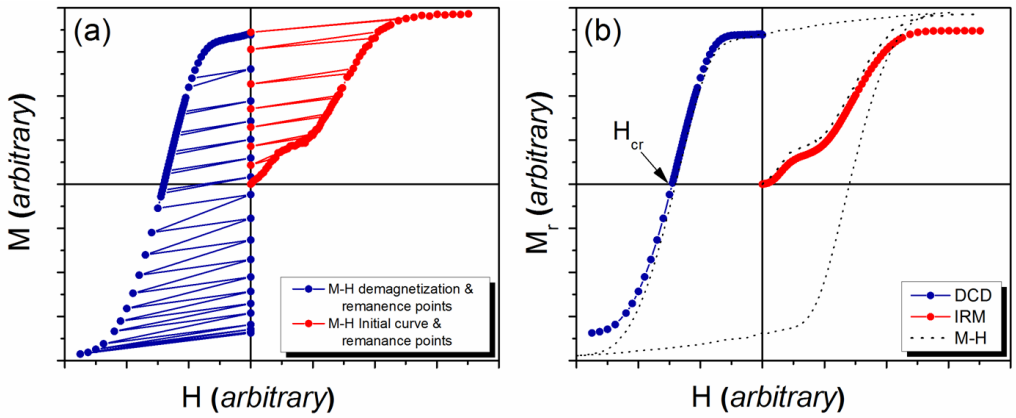

FIG. 2.2. (a) Measurement procedure for acquiring remanent moments from *M*(*H*) demagnetization (blue) and virgin curves (red) for M_{DCD} and M_{IRM} remanence curves, respectively. (b) The resulting remanence M_{DCD} (blue) and M_{IRM} (red) curves plotted with corresponding *M*(*H*) loop (dotted line).

[5] Non-symmetric hysteresis loops caused by exchange bias effects are not considered in this work.

Two standard remanence curves are the isothermal remanent magnetization (M_{IRM}) and the direct-current demagnetization (M_{DCD}) curves, depicted by the solid red and blue curves in Fig. 2.2(b), respectively. The corresponding full and initial loops are included as dashed curves for comparison. An M_{IRM} curve is created by consecutively measuring the remanent moment during an initial magnetization curve. After reaching a set point on that curve, H_{set}^{A}, the field is reduced to zero and the remanence is measured, M_r^A. The field is then increased to a larger set value, $H_{set}^{B} > H_{set}^{A}$, and once again removed to measure a new remanence, M_r^B. This process is continued to build the curve $M_{IRM}(H_{set})$ until the set field is greater than the saturation field, at which point the remanence has reached a maximum. A M_{DCD} curve is acquired in a similar fashion, but instead starts from the saturated state and uses set-fields changing progressively between +/-H_s, following a demagnetization branch of the major hysteresis loop.

The phenomenon of magnetic hysteresis arises from the irreversibility of ferromagnetic moments. Paramagnetic and diamagnetic moments follow the applied field along the same path irrespective of direction or history of a changing applied field. On the other hand, ferromagnetic moments become trapped in local energy minima at particular values of the applied field, causing the magnetization to remain fixed even when the field is removed. This is the nature of the irreversible moments measured by a remanence sequence. The application of progressively larger set-fields accesses consecutively larger energy barriers and thereby a larger fraction of irreversible moments. A direct $M(H)$ scan includes contributions from both the irreversible and reversible moments of a magnet. Reversible moments result from para- and diamagnetic phases as well as magnetically soft regions exchange-coupled to un-reversed hard grains. The field at which a M_{DCD} curve reaches zero magnetization is the remanent coercivity, H_{cr}. The field-derivative of an M_{IRM} and M_{DCD} scan yield irreversible susceptibilities, χ_{irr}^{IRM} and χ_{irr}^{DCD}, respectively. The different initial states of M_{IRM} and M_{DCD} curves emphasize different

magnetization reversal mechanisms. Comparing pairs of M_{DCD} and M_{IRM} curves can reveal the nature of the dominant magnetization process and magnetic interactions within a system and will be discussed further in Section 3.3.4.

2.1.3 Stoner-Wohlfarth and General Multi-domain Magnets

A starting point for understanding the magnetic behavior of a system is to consider a single idealized particle which can be fully described analytically. The Stoner-Wohlfarth (S-W) model accurately describes the magnetization processes of an isolated ellipsoid of revolution with essentially infinite exchange and uniaxial magnetic anisotropy (see Fig. 2.3). The condition for infinite exchange simplifies the problem to the coherent rotation of a single macrospin against an energy barrier defined by the particle's effective anisotropy (K_{eff}), the combination of shape anisotropy and K_u. The expression for the energy of a S-W particle of volume V is [2.1],

$$\frac{E_{S-W}}{V} = K_u sin^2\theta + (1-3D)M_s^2 sin^2\theta - \mu_o M_s \cos(\theta - \varphi). \quad (2.5)$$

The terms on the right-hand-side of Eq. (2.5) represent the uniaxial anisotropy, shape-anisotropy, and Zeeman energy densities, respectively. A field applied at an angle of φ to the anisotropy axis rotates the particle's moment to an angle θ, as shown in Fig. 2.3. Minimizing Eq. (2.5) for a varying applied field at a constant φ fully simulates an $M(H)$ hysteresis loop of a S-W magnet. A spherical S-W particle (D = 1/3), such as each grain in Fig. 2.1, reverses at its anisotropy field when $\varphi = -\pi$,

$$H_A = \frac{2K_{eff}}{\mu_0 M_s}. \quad (2.6)$$

The concept of an anisotropy field enables the estimation of K_1 in uniaxial magnets. Judicious use of the S-W model provides a useful starting point for describing the magnetic behavior of complex granular magnets.

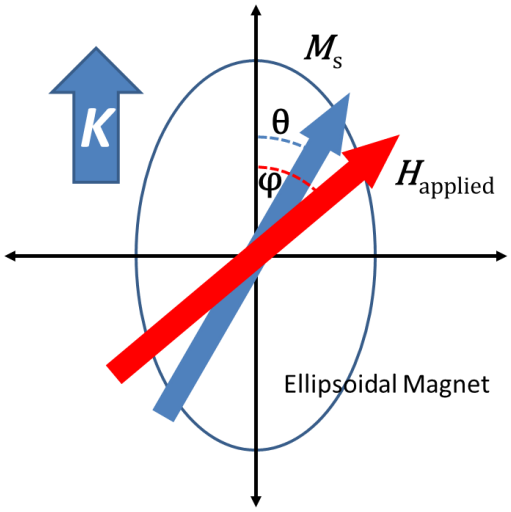

FIG. 2.3. Schematic of an ellipsoidal magnetic particle with a vertical uniaxial anisotropy easy-axis and magnetic moment, M_s, rotated to an angle of ϑ under a field, $H_{applied}$, applied at an angle of φ.

The applicability of the S-W model is limited by a magnet's dimensions and finite exchange. Ferromagnetic exchange interactions strongly align neighboring spins but are effective only over short distances. Longer-ranged, magnetostatic interactions seek to close magnetic flux lines, resulting in non-collinear or antiparallel spin configurations. In particular, magnetostatic interactions in asymmetrically shaped magnets can yield a strong shape anisotropy. As a result, a magnet's dimensions and exchange strength greatly determines its behavior. Ellipsoidal S-W particles reverse coherently by rotation, yet as a particle's size increases or its interatomic exchange weakens, the macrospin model fails as magnetostatic energy begins to dominate exchange and reversal becomes incoherent.

Departure from S-W behavior occurs due to competing magnetostatic and exchange energies. As such, dimensional analysis of the relevant terms in Eq. (2.2) yields the exchange length (l_{ex}),

$$l_{\mathrm{ex}} = \sqrt{\frac{A}{\mu_0 M_s^2}}. \tag{2.7}$$

The critical dimension at which reversal becomes incoherent, R_{coh}, is proportional to $l_{ex}/(1-D)^{1/2}$. The inclusion of *D* exemplifies the effect of a sample's geometry on the reversal mechanism. Specifically, for oblate ellipsoids with $R_x = R_y = R$, $2R_z = t$, and $t << R$ (thin film limit),

$$R_{\mathrm{coh}} = \frac{2q(D)}{\sqrt{1-D}} l_{ex}. \tag{2.8}$$

The factor $q(D)$ is the root of an equation involving spheroidal Bessel functions and for thin films approaches the value of 2.115 [2.2]. For an infinite thin film, typically quoted with D_z=1, the coherence radius would approach infinity, but in reality, for non-zero thickness, $D_z = 1 - \pi t/4R$, and [2.3],

$$R_{coh} = 22.78 \frac{A}{\mu_0 M_s^2 t}. \tag{2.9}$$

The flux closure favored by magnetostatic self-interactions in particles slightly larger than R_{coh} leads to a non-collinear rotation, or curling, of internal moments during reversal. This effectively prohibits moments from pointing directly at the surfaces to form flux emitting magnetic poles. As a reversal mechanism, curling only slightly decreases a magnet's nucleation field from that of the coherent mode.

As a magnet's dimensions increase beyond l_{ex}, energy gains from flux closure win-out over anisotropy and exchange leading to the formation of subdivisions of coherent magnetization called magnetic domains. Magnets whose ground state supports one domain are called single-domain (SD) particles, whereas larger particles whose size or heterogeneous nature necessitates multiple domains are called multi-domain (MD) magnets. In the ground state, collinear spins within each domain follow the local anisotropy axis and the moments of neighboring domains align to maximize flux closure. Spins within the region separating neighboring domains, the domain wall (DW), incrementally rotate between the states at the wall boundaries in the most efficient manner. Exchange punishes non-collinearities while

anisotropy preserves alignment in a specific direction. The creation of a DW within a magnetic particle, and therefore the transition from a SD to a MD state, costs energy (ϒ),

$$\gamma = 4\sqrt{AK_1}\,. \tag{2.10}$$

The width of a DW, commonly referred to as the Bloch-wall width (δ_B) is given by,

$$\delta_B = \pi\sqrt{\frac{A}{K_1}}, \tag{2.11}$$

reflecting the opposing effects of exchange and anisotropy. Spherical magnetic particles with dimensions less than R_{sd} remain in a SD ground state, where,

$$R_{\mathrm{sd}} \approx \frac{36\sqrt{AK_1}}{\mu_0 M_s^2}\,. \tag{2.12}$$

A stable SD state reflects the equilibrium configuration only and domain walls can form during a magnetization process. Note that S-W particles are inherently SD, yet the converse is not necessarily true.

Magnetization processes in MD magnets of arbitrary morphologies become localized and depend on the interplay between Zeeman, magnetostatic, and exchange energy terms acting over various length scales. Real-structure features such as crystal defects and grain boundaries play significant roles in determining the details of reversal and therefore the switching field. Modern analysis techniques such as atomistic and micromagnetic modeling incorporate localized features to simulate magnetization processes. *Ab-initio* atomistic modeling assigns parameters per-spin; however, computational limitations restrict such simulations to relatively small systems. In micromagnetic modeling, site-resolved parameters are approximated on a continuum basis to examine the effect on the free-energy landscape [such as Eq. (2.2)] of features on the order of a few nanometers. Real-structure features are characterized by localized parameter variations and comparison of simulation results with

experimental data can reveal insight into their qualitative effects on magnetization reversal processes. In particular, local extrema in the free energy expression representing defects can act as either nucleation sites for initiating reversal or locations which inhibit or pin domain wall motion.

When reducing the field applied after saturating a MD magnet, the uniform spin state destabilizes at H_N and a reverse domain is formed. Essentially, the energy gained by closing some of the magnetic flux is greater than that required to flip a region of spins and form the domain wall surrounding it. The average unit volume of magnetic moments which switch together during a nucleation event is called the activation volume (V^*), or nucleation volume [2.4-2.6]. Without barriers to domain-wall motion, a reverse domain will expand rapidly. In real magnets, inhomogeneities tend to pin domain walls and impede further reversal. Subsequent wall propagation requires additional energy to overcome the immobilized state, either from thermal fluctuations or an increase of the reverse field to a point greater than the pinning (or depinning) field (H_{DP}). Increasing the magnitude of the field expands the reverse domain past pinning sites and can also simultaneously causes further nucleation events to generate additional reverse domains. Complete magnetization reversal occurs once the reverse domains cover the entire magnet. A schematic of the size-dependence of the switching field is shown in Fig. 2.4: coercivity peaks in the upper limits of coherent rotation and decreases along with particle size due to thermal energy and with increasing size due to a higher probability of nucleation-inducing defects and the onset of a MD state.

A magnet's reversal mechanism is generally classified as pinning or nucleation depending on which process most controls achieving the reversed state. Facile domain-wall motion permits rapid reversal after nucleation in a nucleation controlled magnet. In a pinning-type magnet, readily nucleated domains become trapped by inhomogeneities. Therefore, a

magnet's switching field can be approximated by H_N or H_P. Generally, both reversal mechanisms are present in real magnets but to differing degrees. Respective pinning and nucleation energy barrier distributions are accessible from the susceptibilities of M_{IRM} and M_{DCD} remanence curves [2.5].

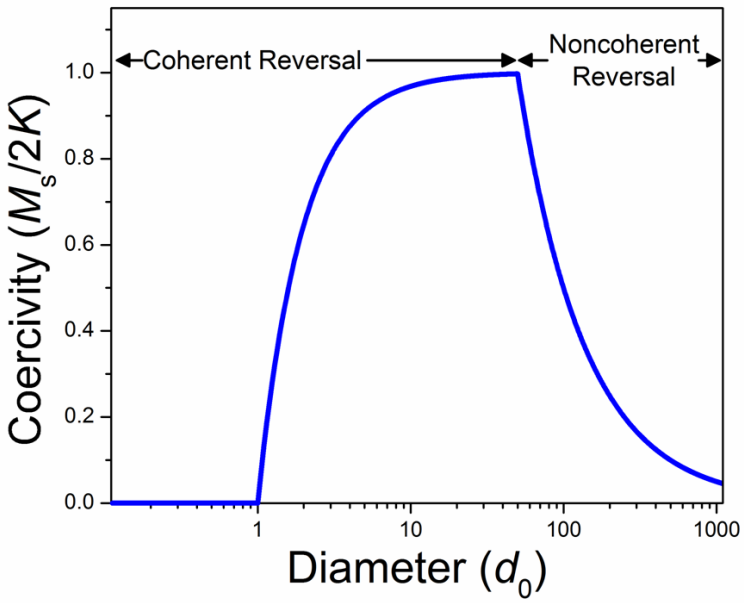

FIG. 2.4. Schematic of coercivity dependence on particle size. Plotted using expressions from Ref. 2.6. Real systems exhibit a less drastic drop in coercivity for increasing particle size across the transition between reversal types.

2.1.4 Granular Magnets

The complex behavior of heterogeneous granular magnets can be approximated as a system of interacting magnetic particles.[6] The resulting magnetization process depends on the relative strengths of the intergranular interactions and the distribution of magnetic properties within the system. Phenomenological approaches and model approximations such as mean-field modeling offer ways to simplify the otherwise complex analysis. However, a tradeoff exists when using such a procedure in that the underlying physics causing the behavior is sometimes not explicitly revealed or even included. Magnetic interactions must be treated carefully due to

[6] A distinction can be made between granular and particulate systems, but in the context of magnetic behavior the difference is moot as both coexist on the continuum of reversal processes with idealized multidomain magnets on one end and perfectly non-interacting entities on the other.

their varied interaction strengths and ranges and the constraints of a phenomenological model must be respected. For example, a significant limitation to micromagnetic mean-field modeling is the disproportionate strength of the exchange interaction with respect to magnetostatic energies; appropriate use of mean-field models typically assumes weak exchange. The consequences of intergranular interactions and property distributions on the magnetic behavior of granular magnets are considered in the following.

In the limit of completely non-interacting particles the reversal process of the collective reduces to the sum of individual particle reversals. Phenomenologically, the switching behavior can be described by the integration of a normalized distribution function $P(H_c)$ representing the range of switching fields of the particles. For such a collection of irreversible spins, the magnetization state at an applied field (H), after increasing from negative saturation, is given by [2.2],

$$M(H) = -M_s + 2M_s \int_{-\infty}^{H} P(h)dh\,. \tag{2.13}$$

As the field variable (*h)* sweeps from negative saturation (*negative infinity*) to H, a particle whose switching field is less than H will switch, and their moment will contribute to a positive magnetization. From Eq. (2.13), the susceptibility is $\chi = 2M_s P(H_c)$.

The necessity of a switching field distribution (SFD) function becomes clear when studying technical granular magnets due to inherent variance in intrinsic and extrinsic magnetic properties between grains. Each grain possesses a unique size, shape, anisotropy $\boldsymbol{K}$, etc., which collectively define its switching field. A SFD function in Eq. (2.13) reasonably parameterizes the combined effect of these variations. The intrinsic switching field distribution $\Delta^{i}_{\mathrm{SFD}}$ quantifies the dispersion of the switching field function, usually as the standard deviation *σ* of the function's peak divided by the average switching field. Experimentally, χ_{irr}^{DCD} approximates the system's

switching field distribution, therefore the switching field distribution Δ_{SFD} is estimated from the standard deviation of χ_{irr}^{DCD}, $\sigma(\chi_{irr}^{DCD})$, as

$$\Delta_{\mathrm{SFD}} = \frac{\sigma(\chi_{irr}^{DCD})}{H_{\mathrm{cr}}}. \tag{2.14}$$

However, interparticle interactions skew the shape of a intrinsic switching field distribution function as derived from a measured *M*(*H*) or remanence curves. Interactions must be accounted for in order to access the $\Delta_{\mathrm{SFD}}^{i}$of the particles; only for collections of non-interacting magnetic particles does $\Delta_{\mathrm{SFD}} = \Delta_{\mathrm{SFD}}^{i}$. Two methods of experimentally estimating $\Delta_{\mathrm{SFD}}^{i}$ are described in Section 2.1.5.

Intergranular interactions vary with the nature and dimensions of interceding grain boundaries. Grains in close contact or with small separations by ferro- or paramagnetic regions tend to be exchange coupled with mutually parallel spin configurations.[7] Strongly exchange coupled grains form cooperative units for magnetization reversal called interaction domains. Their behavior is analogous to the previously discussed standard magnetic domains of MD particles. Nucleation of a reverse interaction-domain typically occurs in a grain or grain-boundary where the magnetic properties are at a global minimum. Reversal proceeds by pinning as grain boundaries and interfaces act as extensive inhomogeneities. In general, exchange-coupled neighbors reverse at fields intermediate to their individual switching fields. Section 2.1.5 discusses this idea further in considering coupled magnetically hard and soft layers or grains, with a focus on the switching mechanism and critical fields of the composite system.

On the other hand, large separations or non-magnetic grain-boundaries yield dominant magnetostatic interactions favoring antiparallel alignment. Magnetostatic interactions encourage antiferromagnetically aligned neighbors and a ground state of alternating

[7] Antiferromagnetic coupling can occur due to the Ruderman-Kittel-Kasuya-Yoshida (RKKY) mechanism or an indirect exchange interaction. RKKY interactions are not considered in this work.

magnetization directions in a striped domain structure. The long-range nature of the dipolar interaction leads to the necessity of a somewhat complicated effective demagnetizing field for particulate magnets. In addition to an individual grain's self-demagnetizing field, the summation over dipolar interactions between it and all other particles forms a global demagnetizing field [2.8]. During localized, incoherent reversal, the macroscopic demag field no longer resembles that of a homogeneous magnet and an accurate analytical treatment becomes prohibitive. Once reversal commences the antiparallel orientation between the nucleated particle or reverse-domain and its un-switched neighborhood accomplishes some degree of flux closure. Effectively, the inhomogeneous state formed during reversal is favorable with respect to magnetostatic energy and can hinder complete saturation in creating vestigial domains.

In micromagnetic mean-field approximations, interactions between a test element and the remainder of the system are averaged and mapped onto the applied field. In this way, the upper bound of the integral in Eq. (2.13) for independent switching events is modified by the addition of a term proportional to the current magnetization state, λM. The parameter λ characterizes the averaged interactions. A positive (negative) value denotes ferromagnetic (antiparallel) coupling of the element with its environment. Following this concept, a linear expression for M can be written

$$M(H) = \chi_0(H + \lambda M), \tag{2.15}$$

where χ_0 is the susceptibility of an analogous system without interactions. The micromagnetic susceptibility of the interacting system under mean field approximations becomes,

$$\chi = \frac{\chi_0}{1 - \chi_0\lambda}. \tag{2.16}$$

Of particular interest in recording media studies is the value of χ at coercivity, as denoted by the parameter α. This loop-slope parameter reflects the degree of exchange coupling in a granular media and has been shown to be closely related to media noise [2.9]. The concept of α and its

relationship to intergranular exchange coupling is used in Chapter Five in examining the varying interaction strength within two series of granular hard magnetic films.

2.1.5 Exchange-Coupled Magnets

Tailoring composite magnetic materials at length scales comparable to domain-wall widths lies at the heart of nanomagnetic engineering. Combining magnetically hard and soft phases offers a route for designing magnets with properties far outclassing those of a single-phase. Exchange-coupled (EC) magnets have been proposed for high-performance permanent magnets [2.10-2.12], magnetic micro-actuators and systems [2.13, 2.14], and extremely high density magnetic recording media (>1 Tb in^{-2}) [2.15-2.18]. Permanent magnets see improved energy-products due to enhanced magnetization provided by the soft-phase. On the other hand, switching-fields of high-anisotropy recording media are reduced to manageable levels by the exchange-coupled soft-phase while thermal stability is guaranteed by the hard-phase. The latter application is the focus of Chapter 6 and the following provides some background and general aspects of EC magnetic systems with an emphasis on their use in magnetic recording.

Early studies of exchange-coupled systems in the 1960's were motivated by the need to theoretically describe the behavior of practical magnetic materials with high anisotropy, in particular to solve Brown's paradox [2.19] regarding the inexplicably low switching-fields measured in those types of magnets [2.20-2.23]. Continuum micromagnetics and numerical analysis determined that reduced coercive fields could be reasonably modeled by treating structural imperfections as inhomogeneities in intrinsic magnetic properties. Examining the role of the exchange mechanism between regions of different properties, i.e. magnetic phases, opened the door for envisioning high-performance nano-engineered multi-phase magnets.

One of the earliest studied and simplest models of an exchange-coupled magnet consists of two stacked layers of infinite lateral extent. Relevant parameters K, A, M, and

thickness (t) can be varied for each layer, where the relative Kvalues distinguishes the phases as magnetically hard or soft. Initial work considered only in-plane anisotropies until interest in EC magnets for PMR applications grew circa 2004. The renewed interest spurred new efforts in modeling more relevant geometries with perpendicular uniaxial anisotropy, for example vertically-coupled columnar grains [2.17,2.18] and "capped" particle structures [2.24,2.25]. The term exchange-coupled composite (ECC) media [2.26] was coined to describe a morphology of laterally decoupled composite grains, with each grain consisting of coupled hard and soft subgrains. The name domain-wall assisted magnetic recording (DWAMR) media [2.27] was also devised to describe the involvement of domain-wall formation and propagation in the reversal process. Various degrees of interphase exchange-coupling [2.18,2.28,2.29], layer geometries [2.30] and spatial variations of the soft-phase anisotropy [2.31,2.32] have been investigated in subsequent years. In particular, the so-called graded media design employs an anisotropy profile through the soft-phase, parallel to the easy-axis direction. Beside the enhanced writability, studies modeling EC systems for PMR have paid attention to the resulting thermal stability, switching times, and potential noise characteristics [2.29,2.33-2.35]. The work done on ECC systems in this dissertation focuses on reductions of the switching field and the remainder of this section focuses on that aspect.

The switching behavior of EC systems has been demonstrated by numerical modeling and micromagnetic simulations. Two switching modes, nucleation and depinning, can be identified for different soft-phase thickness with respect to the critical length scale (l_{cr}) [2.36],

$$l_{\mathrm{cr}} = \sqrt{\frac{2A_{\mathrm{hard}}}{K_{\mathrm{hard}}}}. \tag{2.17}$$

When the soft phase dimension (t_{soft}) is smaller than l_{cr} the system rotates coherently by nucleation at the field H_{N}. Conversely, if $t_{\mathrm{soft}} \geq l_{\mathrm{cr}}$, an incoherent processes occurs beginning

with nucleation in the soft phase furthest from the interface. For sufficiently thick t_{soft}, typically greater than δ_{B} of the hard phase (see below), a full domain wall forms in the soft phase. As an applied field is increased in the reverse direction the wall becomes pinned at the phase interface and reversibly compressed for further increases in the field. The reversibility of the soft-phase magnetization near the interface has led to the term "exchange-spring." Eventually the wall depins and penetrates through the hard phase causing irreversible switching of the magnet. Ground state spin configurations of EC magnets with perpendicular anisotropy also depend on the thickness of the soft phase, but with respect to different critical length scale (l_{cr}^{*}) [2.36],

$$l_{\mathrm{cr}}^{*} \approx \sqrt{\frac{2A_{\mathrm{soft}}}{\mu_0 M_{\mathrm{soft}}^2 - 2K_{\mathrm{soft}}}}. \tag{2.18}$$

Moments in soft layers thinner than l_{cr}^{*} maintain parallel orientation with the hard-phase, whereas spins begin to cant toward an axis defined by the effective anisotropy of the soft phase in thicker layers.

Explicit switching field reductions can be determined only for limiting cases such as infinite layer thickness, zero soft phase anisotropy, or infinite hard phase anisotropy. When both phases are smaller than l_{cr}, sometimes called the limit of extreme nanostructuration [2.37], the system behaves essentially as a single-phase magnet with properties equal to the volume average of the constituent phases. In this case, the coercive field is given by [2.23,2.38],

$$H_{\mathrm{c}} = 2\,\frac{t_{\mathrm{hard}}K_{\mathrm{hard}} + t_{\mathrm{soft}}K_{\mathrm{soft}}}{t_{\mathrm{hard}}M_{\mathrm{hard}} + t_{\mathrm{soft}}M_{\mathrm{soft}}}. \tag{2.19}$$

In the limit of infinite layer thicknesses of both the hard and soft phases, the depinning field can be estimated by [2.39],

$$H_{\mathrm{dp}} = \frac{2K_{\mathrm{hard}}}{\mu_0 M_{\mathrm{hard}}}\frac{1-\varepsilon_{\mathrm{K}}\varepsilon_{\mathrm{A}}}{(1+\sqrt{\varepsilon_{\mathrm{A}}\varepsilon_{\mathrm{M}}})^2} - M_{\mathrm{hard}}\frac{1-\varepsilon_{\mathrm{A}}\varepsilon_{\mathrm{M}}^2}{(1+\sqrt{\varepsilon_{\mathrm{A}}\varepsilon_{\mathrm{M}}})^2}, \tag{2.20}$$

where,

$$\varepsilon_K = \frac{K_{\mathrm{soft}}}{K_{\mathrm{hard}}}\,, \qquad \varepsilon_A = \frac{A_{\mathrm{soft}}}{A_{\mathrm{hard}}}\,, \qquad \varepsilon_M = \frac{M_{\mathrm{soft}}}{M_{\mathrm{hard}}}\,. \tag{2.21}$$

The second term in Eq. (2.20) stems from the stray fields energy inherent in the Neel walls of EC magnets with PMA and a vertical stacking geometry and does not apply when considering EC magnets with in-plane anisotropy. Nucleation of a reverse domain in the soft phase occurs at the field [2.39],

$$H_{\mathrm{N}} = \frac{2K_{\mathrm{soft}}}{\mu_0 M_{\mathrm{soft}}} - D_{\mathrm{soft}} M_{\mathrm{soft}} + M_{\mathrm{soft}} \frac{\pi^2 \sqrt{2} l_{\mathrm{ex}}^2}{4 t_{\mathrm{soft}}^2}\,, \tag{2.22}$$

where l_{ex} is given by Eq. (2.17) and D_{soft} is the demagnetization factor due to the soft phase geometry. Equation (2.20) reveals approximated switching-field reductions versus a comparable SW particle for a few assumed material parameters. When $A_{\mathrm{hard}} = A_{\mathrm{soft}} = A$, $M_{\mathrm{hard}} = M_{\mathrm{soft}} = M_{\mathrm{s}}$ and $K_{\mathrm{soft}} = 0$, the switching field becomes $H_{\mathrm{dp}} = K_{\mathrm{hard}}/2\mu_0 M_{\mathrm{s}}$, or one-quarter of the anisotropy field of a SW particle. A ¼ reduction represents the maximum possible for these parameters, as was determined by early analytical investigations [2.20]. Interestingly, a greater reduction by a factor of five is possible for an infinite two-layer EC magnet with homogeneous anisotropies if $K_{\mathrm{hard}} = 5K_{\mathrm{soft}}$ [2.23]

As an inherent interface phenomenon, the depinning reversal mechanism is independent of the layer thicknesses of an EC magnet. However, micromagnetic simulations and finite element analysis have determined that the infinite layer approximation is only applicable when a full domain wall can be accommodated in the soft layer. In general, the width of a domain wall (δ_{DW}) under an applied field H_{app} can be approximated by [2.27],

$$\delta_{\mathrm{DW}} \approx \sqrt{\frac{A\theta_0^2}{H_{\mathrm{app}}\mu_0 M_{\mathrm{s}}(1-\cos\theta_0) + K_1 \sin^2\theta_0}}\,. \tag{2.23}$$

The angle θ_0 is the alignment of the spins at the interface relative to the easy-axis at the point of switching, and is given by,

$$\theta_0 = \cos^{-1}\left[\frac{\sqrt{\lambda}-1}{\sqrt{\lambda}+1}\right], \tag{2.24}$$

where,

$$\lambda = \frac{A_{\mathrm{soft}} M_{\mathrm{soft}}}{A_{\mathrm{hard}} M_{\mathrm{hard}}}. \tag{2.25}$$

For the situation considered above ($A_{\mathrm{hard}} = A_{\mathrm{soft}} = A, M_{\mathrm{hard}} = M_{\mathrm{soft}} = M_{\mathrm{s}}$) with $K_{\mathrm{soft}} = 0$, equation (2.23) reduces to,

$$\delta_{\mathrm{DW}} = \frac{\pi}{2}\sqrt{\frac{A}{H_{\mathrm{app}}\mu_0 M_{\mathrm{s}}}}. \tag{2.26}$$

Plugging in the reduced switching field yields,

$$\delta_{\mathrm{DW}} = \pi\sqrt{\frac{A}{2K_{\mathrm{hard}}}}. \tag{2.27}$$

Therefore, infinite-layer approximations for reduced switching fields are applicable when the soft phase dimensions exceed $\sim\delta_{\mathrm{B}}$ of the hard phase. For soft phase thicknesses decreasing below this value the switching field increases as the reversal mode transitions from noncoherent to coherent at $\sim\delta_{\mathrm{cr}}$ and continues to increase up to that of the hard-phase in the limit $t_{\mathrm{soft}} \to 0$. Certain graded-anisotropy designs have been predicted to result in switching field reduction greater than one-fifth. A quadratic anisotropy variation was determined to be optimal, with a nearly four-fold gain in thermal stability over a comparable S-W grain, and yields a coercivity reduction inversely proportional to the length of the graded region [2.31,2.32]. This implies the ability to circumvent any hard-phase switching field by using tall columns for PMR. However, domain walls typically become pinned in the middle of a graded grain and the localized write field would need to reach that point with sufficient strength to affect reversal. The disturbance on neighboring grains by an unfocused field with such range has a negative impact on the practical areal density [2.40]. Thermal stability is guaranteed by the hard phase volume of the

magnet and is optimized for a thickness of $4\sqrt{A_{\mathrm{hard}}/K_{\mathrm{hard}}}$. EC magnet design for PMR requires maximizing the thermal stability of the hard phase while optimizing the intrinsic and extrinsic parameters of the soft phase.

2.1.6 Thermal Effects

A ferromagnetic moment at non-zero temperature is in constant competition with thermal energy. In general, both intrinsic properties MCA and M_s exhibit temperature dependence. Additionally, thermal energy excites spins by an average energy ~$k_B T$ that continuously threatens to push a magnet configuration over accessible energy barriers, thereby changing a system's magnetization. These thermal fluctuations lead to a time dependence of magnetization,

$$M(t) = M_s e^{\frac{-t}{\tau}}. \tag{2.28}$$

where τ is the relaxation time for a moment to jump to a new energy minimum. The relaxation time follows an Arrhenius-like behavior,

$$\tau = \tau_0 e^{\frac{\Delta E}{k_B T}}, \tag{2.29}$$

where τ_0 is the inverse of the attempt frequency, $f_0 \approx 10^9 - 10^{12}$ s^{-1} and ΔE is the energy barrier associated with reversal.

The temperature dependence of magnetization leads to the important concept of thermal stability of magnetic moments. A ferromagnetic moment can only be measured if the spins are stable long enough for the measurement to be completed. This statistical argument leads to a blocking temperature (T_B) below which the spins are thermally randomized and the magnet adopts superparamagnetic behavior. For a typical laboratory measurement (t = 100 s), the blocking temperature can be defined as,

$$T_B = \frac{\Delta E}{25 k_B}. \tag{2.30}$$

Magnetic recording requires a significantly higher degree of thermal stability. Typically, media are designed for a retention time of ~10 years. Approximating each magnetic bit as a single S-W particle of volume V with $\Delta E = K_u V$, Eq. (2.29) estimates,

$$\xi \equiv \frac{K_u V}{k_B T} \approx 40\,. \tag{2.31}$$

The ratio on the left-hand side of the equation, known as the thermal stability factor (ξ), relates grain volume, anisotropy, and operating temperature. Only magnetic materials which satisfy or exceed the relation in Eq. (2.31) have potential as a recording media.

Experimentally, ξ is accessible by analyzing the measurement time or temperature dependence of a magnet's coercivity [2.41]. At coercivity, an equal number of spins in a magnet point in either direction along the measurement axes. Therefore, Eq. (2.28) can be written as $^1/_2 = \mathrm{e}^{-t/\tau}$. Plugging Eq. (2.29) in for τ and solving for the energy barrier yields,

$$\Delta E = k_B T \ln\left(\frac{t f_0}{\tau_0 \ln 2}\right), \tag{2.32}$$

where the time constant τ_0 has been changed to f_0=1/τ_0. The stability factor ξ depends on thermal reversal occurring at zero applied-field. During a hysteresis measurement, the energy barrier to reversal changes with applied field and the zero-field barrier must be extrapolated. A typical field-dependent form of ΔE is,

$$\Delta E = \Delta E_0 \left(1 - \frac{H}{H_0}\right)^n, \tag{2.33}$$

where ΔE_0 and H_0 are the zero-field energy barrier and static coercivity, respectively. The exponent n varies depending on the applied field angle and the underlying symmetry of the energy landscape [2.42]. For example, n = 2 for S-W particles with an applied field parallel to the easy-axis whereas misaligned S-W particles obey a barrier expression with n = 3/2. Experimental values for n range from 1 to 2. A field-dependent value between 1.62 and 1.85 has been determined for misalignments of ~1° between the applied field and easy axis of a single-domain

particle [2.43], and a value of 1 has been determined for columns with quadratically graded anisotropy [2.44]. Plugging equation (2.33) in to (2.32) with the corresponding field value H_c yields the Sharrock equation,

$$H_c = H_0\left\{1 - \left[\frac{k_B T}{\Delta E_0}\ln\left(\frac{t f_0}{\ln 2}\right)\right]^{1/n}\right\}. \quad (2.34)$$

Thermal stability factors and energy barriers can be estimated using Eq. (2.34) by fitting switching field versus measurement temperature or switching time versus applied field data sets.

2.2 Fabricating Thin-Film Nanostructures

Physical vapor deposition onto a heated substrate or utilizing post-deposition annealing offers a bottom-up route for the fabrication of nanostructured thin films. The variety of available deposition techniques and the effects of each systems' parameters allows for a multitude of means of controlling a resulting film's structure. Thin-film growth techniques also offer the ability to control crystalline texture through epitaxial relationships with the substrate or a seed layer. Common deposition methods include molecular beam epitaxy (MBE), electron-beam (E-beam) evaporation, pulse-laser deposition (PLD), and plasma sputtering; each method has its particular strengths and drawbacks. Sputter deposition is perhaps the simplest method and lends itself well to scaling a laboratory process to industrial levels. Sputtering rates are highly variable, ranging from slower than 1 Å/s to as fast as ~1 μm/min, and the technique can be used with materials with a wide range of melting temperatures.

The magnetic thin films examined for this dissertation were deposited by magnetron sputtering onto amorphous SiO_2 substrates at ambient temperatures or single-crystal MgO substrates at elevated temperatures. Films deposited at ambient temperatures were subsequently processed by a rapid-thermal-annealing oven (rapid thermal annealer, RTA). The

following subsections introduce some concepts of magnetron sputtering and nanostructured thin-film formation, using both *in-situ* and post-deposition annealing techniques.

2.2.1 Thin-Film Deposition by Magnetron Sputtering

Magnetron sputtering is a widely used vacuum deposition technique for fabricating metal and insulator coatings, or thin films, ranging from nano- to micrometers in thickness. In cathode sputtering, the target, a two-inch disk of the material to be deposited, is placed directly onto the cathode, or sputtering gun. After introducing an inert working-gas, such as Ar, into the previously evacuated deposition chamber, a voltage applied to the gun generates an electric field between the cathode and the grounded chamber. At the break-down voltage of the working-gas, a plasma ignites above the target. The deposition process proceeds as positively charged gas ions from the plasma accelerate in the cathode's electric field and bombard the target, releasing surface atoms by elastic collisions. Ejected material travels isotropically from the target surface to be adsorbed onto a substrate and construct the thin film. Newly deposited atoms are typically referred to as adatoms.

In direct current (DC) sputtering the negative polarity of the gun is fixed while radio frequency (RF) sputtering oscillates the polarity to maintain a plasma. The former works well for conducting targets whereas the latter enables the sputtering of insulating targets where surface-charge buildup impedes the process. Magnetron sputtering differs from standard cathode sputtering in its use of magnetic fields to enhance the plasma density. Permanent magnets placed under the surface of the gun generate magnetic field lines above the target. Plasma ions are forced to travel in a helical path through the field, creating additional ions through collisions with neutral gas atoms. Magnetron sputtering allows for operation at relatively low working-gas pressures due to the enhanced ionization process.

The sputtering process, and thereby the structure of the fabricated film, can be controlled by a number of experimental parameters during deposition. The voltage applied to the cathode, commonly termed the “sputtering power”, affects the ionizing potential as well as the kinetic energy of the ions. Ions with higher energy can increase the plasma density by generating secondary collisions and are also more effective in overcoming binding energies of target material to release atoms. A higher sputtering power leads to a greater rate of ejected atoms. If the applied power is too low, the plasma will not ignite. Conversely, if the applied power is too high, arcing could occur between the target cathode and the grounded chamber.

The working-gas flow-pressure determines the density of ionizing gas available for ignition and, therefore, the resulting plasma density. Higher plasma densities typically lead to a greater number of ion-target collisions and a higher flux of ejected atoms. The sputtering rate, or yield, which is the actual amount of material accumulated on the substrate, is enhanced by an increased material flux. However, at a critical gas density the mean-free-path of the atoms travelling to the substrate is significantly reduced to the point of preventing their deposition. Therefore, too high of a working-gas pressure will impede deposition while a pressure too low precludes plasma ignition. Additionally, a high rate of collisions between sputtered atoms and the working gas atoms at high pressures can result in strong variations in the angle of adatom flux.

In addition to sputtering power and working-gas pressure, various geometric factors of the deposition system can affect the process. The target-to-substrate distance determines the substrate’s angle of coverage in the plume of sputtered material. Additionally, large distances invite collisions with the working gas atoms which can decrease the deposition rate or even change the average angle of approach of adatoms. A large deposition angle or excessively high substrate temperatures can cause the impending atoms to reflect or “bounce” off the surface

instead of physisorbing. A high angle of adatom flux can also cause shadowing on portions of the growing film, leading to three-dimensional growth and an increased vacancy density.

2.2.2 Thin-Film Growth

Initial film growth during physical-vapor deposition begins as sputtered atoms adsorb onto the substrate surface. If an adatom remains stable after contacting the substrate it can form a nucleation site for further growth. Initial nucleation sites start as a pair of similar atoms and are typically spaced ~10 nm apart [2.45]. As deposition continues, these sites grow into island-like regions as subsequent adatoms attach directly or diffuse across the bare substrate to the island edges. Given the correct conditions these islands will eventually coalesce and form a continuous coating, or film, on the substrate.

The morphology of a sputtered thin film strongly depends on deposition parameters, substrate type and temperature, and the properties of the involved materials. A key consideration is adatom mobility, as determined by the residual kinetic energy after physisorption and the substrate temperature. High sputtering pressures or large substrate-target distances increase the number of thermalizing collisions experienced by sputtered atoms en route to the substrate, causing significant loss of kinetic energy. Elevated substrate temperatures impart energy to adatoms and can enable surface diffusion. The substrate temperature is typically parameterized by a reduced or homologous temperature, defined as the ratio of the substrate temperature to the melting point of the film. Surface diffusion is normally active for homologous temperatures greater than 0.3. High adatom mobility and active surface diffusion allow a growing film to rearrange into energy minimizing configurations and achieve near-equilibrium structures. However, the ability to reconfigure is lost for fast deposition rates, such that evolving layers become buried before achieving their final

arrangement. The film growth is said to be quenched if atomic mobility is too low or the deposition rate too high.

Material properties relevant to film development include the surface energies, Υ, of the deposited material and the substrate. A system will strive to minimize total surface energy, and large differences in Υ can lead to a film dewetting the substrate and prohibiting continuous coverage. The relative miscibilities of a film's constituent elements dictate the formation of homogeneous solid solutions or phase-separated composites.

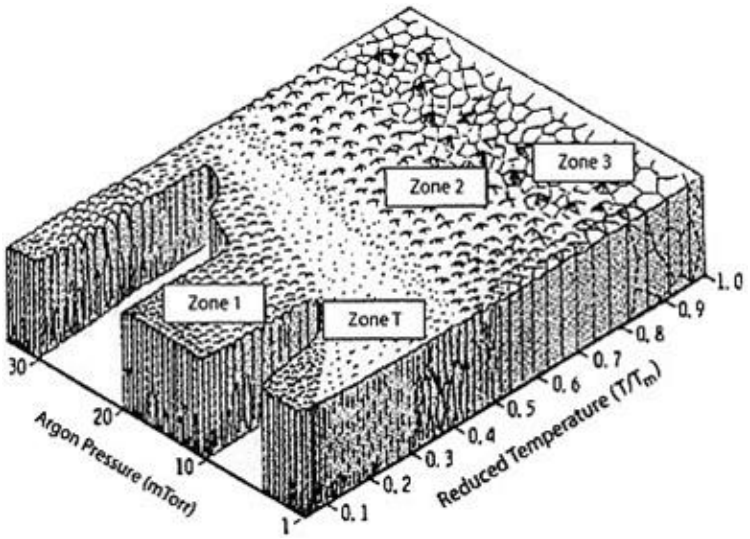

FIG. 2.5. Diagram of thin film zone structures. After Ref. 2.41.

Three different growth modes have been classified for high adatom mobility or small dimer spacings [2.45]: two-dimensional Frank-Van der Merwe growth; three-dimensional Volmer-Webber growth; and Stranski-Krastanov growth. The third mode begins like Frank-Van der Merwe growth for the first few monolayers then transitions to the Volmer-Webber mode for continued growth. A film's growth mode is determined by the combined effect of the various deposition parameters and the resulting film structure depends on the dominant growth mode. Four standard film structures, or zones, have been identified and are shown in Fig. 2.5 [2.45]. Films with Zone 1 or Zone T structures generally result from quenched growth, whereas films of

Zones 2 or 3 make use of thermally activated atomic rearrangement along the surface or within the bulk of a developing film.

The structure and morphology of a film can change significantly during growth depending on the available kinetic energy and the current state of the film. Surface atoms will diffuse to minimize grain boundary, surface, and strain energies. A compressive strain state can develop as the smaller lattice parameters of early grains transition to the larger bulk values. Grain growth during deposition occurs to eliminate grain boundaries, defects, and vacancies. Grain growth, coalescence, and defect elimination can induce in-plane tensile strain, relaxing any compressive strain and in some cases leading to a residual tensile strain state. Preferential, or abnormal, grain growth occurs when there exists a larger driving force for the growth of one particular grain configuration of over any other. Such preferred configurations originate from large surface energy anisotropies or variable strain states of the growing crystallites. A close epitaxial relationship between the film and substrate or preceding layer can alter the strain in the growing film. Mismatched lattices lead to large strains as the film continues to grow. Both preferential and epitaxial growth can yield crystallographic texture.

Volume diffusion can occur during deposition for homologous temperatures greater than 0.5 and can lead to the nucleation of new phases within the film bulk out of a previously metastable as-deposited structure. Recrystallization of the equilibrium phase may also be triggered by a high strain-energy density built-up during film growth. A heterogeneous, nanocomposite morphology develops if an immiscible minority phase has sufficient energy to segregate to the boundaries of the host phase. A widely used nanostructuring technique is to optimize the ratio of two immiscible phases and the deposition conditions to achieve a nanocomposite structure with homogeneously dispersed nanoparticles of one material distributed within a matrix of the other.

Morphological changes minimizing surface energy of the film and substrate can have a drastic effect on the resulting topology. High substrate temperatures can lead to dewetting and the formation of a discontinuous film or an island-like morphology. A simplified expression for continuous growth involving interface energies is

$$\Delta\gamma = \gamma_{sub} + \gamma_{sub/film} - \gamma_{film} > 0\,, \tag{2.35}$$

where γ_{sub}, $\gamma_{sub/film}$ and γ_{film} are the energies of the substrate-free, substrate-film, and film-free interfaces, respectively. An island-like film would be expected for $\Delta\gamma < 0$.

2.2.3 Post-Deposition Processing

Quenched growth modes or low substrate temperatures can kinetically inhibit energy-minimizing processes, yielding highly non-equilibrium as-deposited structures. Metastable states, poor crystallinity, crystalline defects, intergranular vacancies, and residual strain states are common in such thin films. Due to the non-equilibrium nature of magnetron sputtering it is often necessary to employ post-deposition processing to achieve a desired phase or microstructure. Annealing activates diffusion, promotes grain growth and recrystallization, and accelerates equilibration. The mutually beneficial, simultaneous occurrence of multiple aforementioned solid state reactions are known as combined reactions [2.47,2.48]. Combined reactions tend to augment the equilibration of a film's structure through enhanced kinetics. The result of post-deposition annealing a polycrystalline thin film is a function of temperature, dwell time, and heating/cooling rates. Successful transformation of a disordered, metastable film into the ordered phase by annealing hinges on the ordering process as well as the kinetic limitations imposed by the as-deposited structure.

The thermodynamic driving force per unit volume for a disorder-order transformation can be estimated by the change in Gibbs free energy,

$$\Delta G_{\mathrm{V}} \cong \frac{\Delta H_{\mathrm{V}} \Delta T}{T_{\mathrm{cr}}}, \tag{2.36}$$

where ΔH is the enthalpy of formation, T_{cr}, the equilibrium ordering temperature, and ΔT is the degree of undercooling below that temperature [2.49]. The motivation to order is proportional to ΔT. The total driving force, ΔG, for a first-order ordering transformation, in which the ordered phase nucleates and grows within a matrix of the disordered phase, can be estimated by,

$$\Delta G = -V\Delta G_{\mathrm{V}} + A\gamma + V\Delta G_{\mathrm{S}}. \tag{2.37}$$

Nucleation by a first-order process is affected by the associated changes in free energy density, ΔG_{V}, interfacial energy, Υ, and strain energy, ΔG_{S}, for with a volume *V* with area *A*.

A homogeneous as-deposited film can order readily via a polymorphic transformation which may proceed readily without the need for long-range atomic diffusion. However, the process can be delayed by the necessity for diffusion in order to achieve the correct stoichiometry or precursor crystal structure. Atomic diffusion in a heterogeneous structure is driven by mixing entropy, and the diffusion rate depends on available paths. For example, surface diffusion occurs more readily than bulk diffusion, and changes lattice distortions caused by the shifting atoms, which affects strain energy either positively or negatively. In general, the time necessary to nucleate the ordered phase, t_{s}, can be given by,

$$t_s = t_0 e^{\left(\frac{\Delta G^* + Q_{\mathrm{D}}}{k_{\mathrm{B}} T}\right)}, \tag{2.38}$$

representing the effect of an increased nucleation time due to energy barriers for phase formation, ΔG^*, and for diffusion, Q_{D} [2.47]. The associated nucleation energy barrier can be expressed by,

$$\Delta G^* = \frac{16\pi\gamma^3}{3(\Delta G_{\mathrm{V}} - \Delta G_{\mathrm{S}})^2}, \tag{2.39}$$

such that the height is proportional to the cube of the interface energy, Υ, between the ordered and disordered phases, and inversely so to the square of the difference between the changes in

free energy density, ΔG_V, and the strain energy, ΔG_S, due to the creation of the new phase [2.50]. The temperature dependencies of the diffusion and ordering energy barriers give rise to the characteristic "C" shape of temperature-time-transformation (TTT) plots, as shown in Fig. 2.6. At low temperatures, ΔG^* is relatively small due to the large undercooling temperature while diffusion is sluggish; conversely, ΔG^* increases at higher temperatures while diffusion is greatly enhanced.

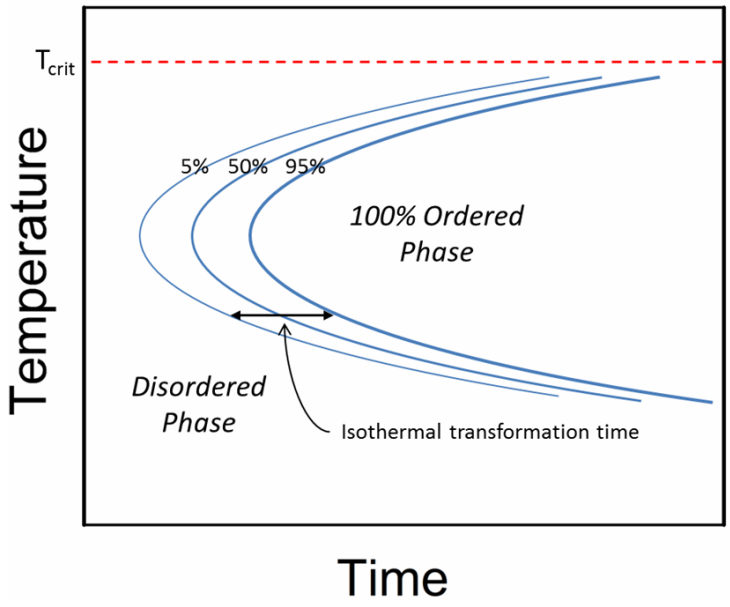

FIG. 2.6. Example TTT diagram. Percentages indicate degree of ordering achievable along those particular curves.

Given sufficient energy crystalline grains will grow in such a way as to minimize grain boundary energy. An expression for the velocity, v, of a growing grain,

$$v \propto \left[\gamma_{\mathrm{gb}}\left(\frac{1}{\bar{r}}-\frac{1}{r}\right)+\frac{\Delta\gamma_{\mathrm{s}}+\Delta\gamma_{\mathrm{i}}}{h}+\Delta W_{\varepsilon}\right], \tag{2.40}$$

includes terms for the surface energies, γ, strain energy, W_ε, and both the radius of the average grain in the film, $\bar{r}$, and that of the grain in question, r. The first term represents the drive for growth from average grain boundary energy and the difference in curvature between the grain in question and an average grain in the film. The second term describes the motivation for

growth due to differences in interface energies between the grain in question and the average grain, both for film-to-free-surface, $\Delta\gamma_s$, and film-to-substrate, $\Delta\gamma_i$. The factor of h, the grain height, emphasizes the strength of the top and bottom interface effects in thinner films. The third term, ΔW_ε, describes the effect of the difference in strain energy between the growing grain and an average grain. Similarly to *in-situ* grain growth, a subpopulation of grains with a larger driving force or smaller energy barrier for growth will grow more rapidly than the average grain. Such growth can result in crystalline texture.

The concepts presented above will be expounded upon in Sec. 2.4 as they pertain to FePt sample preparation and in subsequent chapters within this dissertation. Chapter Four discusses the effects of strain-induced selected grain growth and ordering in non-epitaxial FePt thin films. Chapter Five examines chemical ordering, grain growth, and non-epitaxial texturing in FePt thin films doped with a ternary element. The samples used for Chapter Six utilized the Volmer-Webber growth mode to fabricate ordered and highly textured isolated magnetic islands on MgO substrates.

2.3 $L1_0$-Phase FePt

$L1_0$-phase FePt possesses a magnetocrystalline anisotropy of $K_1 \approx 7$ MJ/m^3 (70 Merg/cm^3), second only to $SmCo_5$. The excellent magnetic hardness and chemical inertness of FePt has drawn interest in its use for permanent magnet [2.51-2.57], medical, and advanced magnetic recording media applications [2.58]. The atomic layering of Pt of the $L1_0$ structure also has potential in catalytic applications. By comparison, the two other ordered Fe-Pt phases have attracted little interest. The two $L1_2$ cubic structures are magnetically soft and antiferromagnetic, i.e., Fe_3Pt and $FePt_3$, respectively. Fe_3Pt has shown utility in heterogeneous nanostructures combined with the hard $L1_0$ phase for exchange-enhanced permanent magnets. Antiferromagnetic $FePt_3$ has been investigated as a pinning layer for spintronic applications. Of

all the potential applications for Fe-Pt alloys, the use of the $L1_0$ phase in advanced magnetic recording media has dominated the interest of the scientific community since the middle of the 1990's.

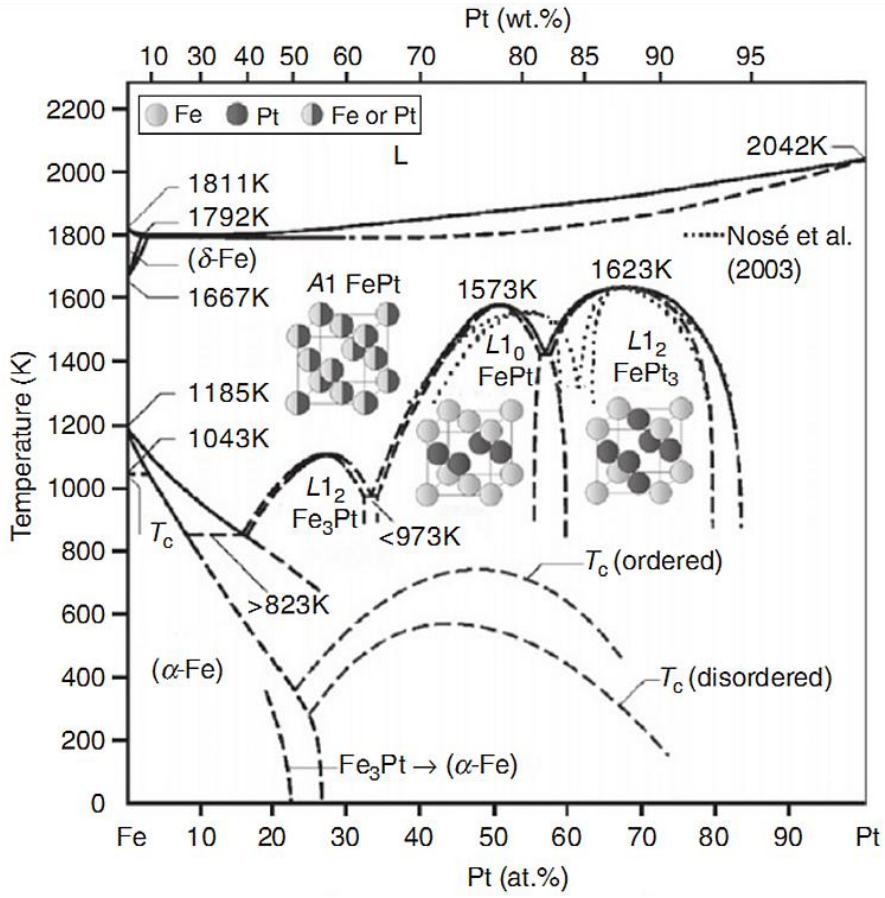

FIG. 2.7. Phase diagram of Fe-Pt alloy, from Ref. 2.59.

The earliest research on hard magnetic alloys of Fe and Pt in the 1930's reported a peak Curie temperature of around ~480 °C for a chemically ordered phase with equiatomic stoichiometry [2.60]. Further studies revealed a phase diagram comprising of the three ordered phases for Fe:Pt stoichiometries of approximately 1:3, 1:1, and 3:1. As depicted in Fig. 2.711, within the equiatomic region, FePt forms the ordered $L1_0$ phase below 1300 °C. Similarly, ordered $L1_2$ compounds form in the vicinity of Fe_3Pt and $FePt_3$ stoichiometries below their respective ordering temperatures. Above the order-disorder temperature at any alloy composition, Fe-Pt forms a magnetically soft *face-centered-cubic* (fcc) solid solution. The

compositional breadths of the ordered phases permit the coexistence of neighboring Fe-Pt phases at equilibrium.

Experimental investigations of FePt have taken many forms over the years. Work in the 1970's focused on bulk samples fabricated by arc-melting or melt-spinning with the motivation for permanent magnet applications [2.51-2.53]. Interest in FePt thin films began in the 1980's as a cost-effective way to study the system's magnetic and microstructural properties [2.61-2.63]. A rising interest in high-anisotropy thin films for magnetic-recording media and specialized permanent-magnet applications spurred increased research activity in the 1990's [2.64,2.65]. New fabrication techniques and new potential applications for magnetic nanoparticles arose early in the 21st century. In particular, chemical and gas-phase cluster aggregation methods were developed for fabricating FePt nanoparticles with controlled particle size, size-distributions and magnetic properties [2.66-2.76]. The possibility of fabricating stand-alone FePt nanoparticles or loading them into porous matrices excited interest in catalytic applications and self-organized magnetic assemblies [2.66,2.77,2.78]. The ability to create core-shell nanostructures added functionality to magnetic particles, drawing interest for medical applications [2.79,2.80].

As magnetic recording became the dominant motivation for FePt research, thin films became the experimental system of choice. FePt films have been fabricated by MBE, PLD, E-beam evaporation, and sputtering techniques and grown on single crystal substrates, amorphous substrates, and specially designed seed-layers. Studies have investigated the effects of deposition pressure, substrate temperature, film thickness, deposited-layer configurations, Fe-Pt stoichiometry, and post-deposition processing conditions for both epitaxial and non-epitaxial film growth. Chapter 4 of this dissertation examines variations in the as-deposited structure in post-deposition annealed films grown non-epitaxially on SiO_2 substrates. Chapter 5 extends Chapter 4 by adding a dopant material. Chapter 6 looks at FePt nanostructures grown

epitaxially on single-crystal MgO substrates at different deposition temperatures. The following subsections discuss the crystal structure, ordered-phase formation, and magnetic properties of FePt samples.

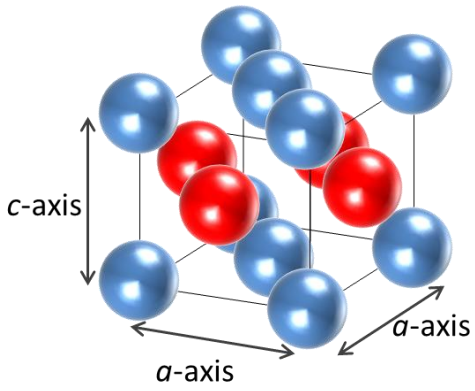

FIG. 2.8. Atomic positions of Fe (red) and Pt (blue) in tetragonally distorted $L1_0$ structure.

2.3.1 Crystal Structure

The $L1_0$ crystal structure follows the AuCu prototype, space group P4/mmm, with a tetragonally distorted fcc (or face-centered-tetragonal, fct) unit cell[8]. The commonly used name, $L1_0$, originates from the *Strukturbericht* designation for intermetallics of this type. A schematic of the $L1_0$ structure is shown in Fig. 2.8. Each element contributes two atoms to the unit cell, forming alternating atomic layers along the *c*-axis of the crystal. The layering of smaller Fe atoms with larger Pt atoms creates the tetragonal distortion along that axis. Bulk $L1_0$ FePt has unit cell dimensions of 3.842 Å (*a*-axis) by 3.702 Å (*c*-axis) [2.81]. The ratio of the unequal lattice parameters, *c*/*a*, defines a system's tetragonality and is frequently used to experimentally fingerprint the presence of the $L1_0$ phase in samples.

Elevated temperatures activate atomic hopping which creates antisites in the ordered structure and destroys the layered arrangement. At temperatures approaching 1300 °C the ordered structure transforms via a thermodynamically second order transformation into the

[8] The $L1_0$ ordered phase of FePt can also be described as a body-centered-cubic structure with the same symmetries, but convention is to use the face-centered-tetragonal designation.

disordered fcc A1 phase via nucleation and growth of disordered domains [2.47,2.82]. Fe and Pt atoms in the disordered fcc phase occupy lattice sites in proportion to the sample's stoichiometry. A lattice parameter of 3.807 Å has been determined for bulk equiatomic fcc FePt [2.83]. Away from even stoichiometry the lattice parameter varies according to Vegard's law [2.84].

The precise positioning of Fe and Pt atoms within the $L1_0$ lattice defines the ordered structure and the degree to which that order holds over many unit cells describes a sample's long-range chemical order. A quantification of the chemical order S examines the average site occupancy of a sample in the relation,

$$S = \frac{(r_{Fe} - x_{Fe})}{y_{Pt}} = \frac{(r_{Pt} - x_{Pt})}{y_{Fe}}, \tag{2.41}$$

where the terms *r*, *y*, and *x* represent the fractions of correctly positioned atoms, available designated lattice sites, and atomic ratios for Fe and Pt, respectively [2.85]. The order parameter is linear in (r_{Fe} + r_{Pt}) and ranges from 0 for completely disordered structure with random site occupancy, to 1 for a fully ordered crystal. The above expression for S accounts for the broad stoichiometric range allowable to form the $L1_0$ phase. Perfect order, with S = 1, is only possible for a 1:1 atomic ratio; a deviation in composition of Δx limits the maximum attainable value for the order parameter to $S_{max} = 1 - 2\Delta x$. The order parameter S is experimentally accessible by examining ratios of XRD intensities and is demonstrated in Chapter 3.

2.3.2 Fabrication of $L1_0$-Phase FePt

Experimental realization of $L1_0$ phase FePt bulk or thin-film samples requires either fabrication at elevated temperatures or the use of thermal annealing following a low-temperature fabrication route. Direct formation of ordered FePt thin-films is feasible using deposition temperatures > 300 °C [2.86-2.92]. Key considerations for this method include deposition temperature, rate, and scheme, Fe:Pt stoichiometry and substrate or seed-layer

type. Post-fabrication processing becomes necessary due to the propensity of Fe-Pt to form in metastable states with multiple nonequilibrium phases when alloyed at relatively low temperatures. The necessary processing time and temperature to achieve the $L1_0$ phase depends on the as-fabricated morphology, residual-strain and defect densities, and Fe:Pt stoichiometry. The following sections elucidate the important aspects of each method.

2.3.2.1 Post-fabrication Ordering

Many fabrication techniques, such as Ar-ion sputtering, yield metastable samples due to their non-equilibrium nature. For example, rapidly quenched ribbons, ball-milled elemental powders [2.93], thin films [2.82,2.87,2.94-2.96], and nanoparticles [2.66,2.70] fashioned at temperatures less than 300 °C result in morphologies of fcc FePt grains, isolated regions of elemental Fe and Pt, or a combination thereof. These undesirable states are "frozen in" due to kinetic limitations to achieving the ordered phase. The thermodynamic driving force for ordering is large in samples with near-equiatomic average stoichiometry due to the high order-disorder temperature [2.93,2.97]. Ideally, the polymorphic fcc-to-fct transformation involves only local atomic shuffling or short-range diffusion. However, spontaneous ordering is hindered by kinetic barriers to atomic diffusion over significant distances, and, along with strain considerations, post-fabrication annealing at elevated temperatures is required. The temperature at which those barriers are overcome and a disordered sample exhibits signs of the ordered phase is the known as the kinetic ordering temperature.[9]

The fcc-$L1_0$ ordering transformation occurs by nucleation and growth of the ordered phase within a matrix of disordered grains [2.47,2.82,2.98-2.100]. In polycrystalline samples, ordered grains have been identified nucleating heterogeneously at A1 grain boundaries [2.98,2.101,2.102] and from precursor grains. The exact nature of a precursor grain depends on

[9] The term kinetic ordering temperature is used to avoid confusion with the thermodynamic ordering temperature relevant to cooling from the fcc phase.

the local stoichiometry and processing history. FePt nanoparticles synthesized by organometallic chemical synthesis nucleate at pure Pt or Pt-rich clusters [2.103]. Typical precursors in thin-film and bulk samples are fcc-phase FePt grains possessing some degree of short-range order (SRO) [2.47,2.82,2.104-2.107]. Such modified fcc-grains seemingly develop randomly throughout the bulk of a sample, appearing at lattice distortions [2.104] or where the local stoichiometry approaches a one-to-one ratio. At processing temperatures below 300 °C, localized atomic rearrangements in disordered fcc crystallites have been identified as an early-stage-ordering process which leads to the development of SRO and precursor grains[2.106,2.108]. On the other hand, $L1_2$ ordered Fe_3Pt and $FePt_3$ grains serve as precursor phases at interdiffusing Fe/Pt interfaces between elemental regions [2.109-2.111]. Since the $L1_0$ phase is more thermodynamically stable than either $L1_2$ phase, subsequent transformation is expected after further diffusion has favorably altered the local stoichiometry.

The temperature used in a post-fabrication annealing process dictates the nucleation site-density and growth velocity of ordered grains through the thermal activation of atomic diffusion. At relatively low temperatures where volume diffusion is limited, the available sites for nucleating ordered grains are limited by the as-fabricated structure. Studies indicate a constant density of nucleation sites in thin FePt films grown at temperatures below 370 °C [2.82]. and in isolated FePt nanoparticles [2.112]. Similarly, a study modeling ordering kinetics finds agreement between low temperature experimental data and a model assuming an athermal nucleation-site density [2.113]. Once nucleated, ordered domains located within a homogeneous region of fcc grains tend to form coherent boundaries with the surrounding matrix. The resulting low-energy boundaries are relatively immobile, leading to sluggish growth and expansion of the ordered phase. Reflecting this tendency, the energy barrier for ordered-grain growth was determined to be larger than that for nucleating new ordered domains in thin

films [2.101]. Consequently, the availability of nucleation sites tends to limit the degree of order in FePt samples annealed at temperatures below ~400 °C [2.82,2.101,2.107,2.112,2.114].

Atomic diffusion begins to play a significant role in the ordering process for annealing temperatures ≳400 °C. *In-situ* TEM of Fe and Pt multilayers at elevated temperatures suggest that interdiffusion occurs for temperatures greater than 400 °C [2.110]. In relation to the ordering process, an examination of the high-temperature ordering kinetics of FePt nanoparticles indicates that Pt diffusion likely poses the largest barrier to fcc – $L1_0$ ordering [2.115]. In general, diffusion homogenizes the Fe:Pt stoichiometry and enhances ordered-phase grain growth. The former process effectively enables the formation of new nucleation sites. The motion of grain boundaries during the latter further boosts diffusion since atomic mobility is significantly faster along grain boundaries than within a grain. At elevated temperatures all preexisting nuclei transform and ordering proceeds rapidly by grain growth.

The enhancement in ordering kinetics at elevated temperatures is countered by the inverse temperature dependence of the thermodynamic driving force, seen in Eq. (2.36). Combining these low- and high-temperature trends leads to an ordering process described by a "nose-shaped," or C-curve, TTT diagram [2.116]. A schematic of this behavior is shown in Fig. 2.69. The curves trace isotransformation lines, i.e., regions of constant ordered-fraction. The shortest isothermal annealing time occurs across the point of the curves and incomplete ordering typically results in a mixture of ordered and disordered phases. The exact shape of a transition curve inevitably depends on the types of kinetic barriers imparted during fabrication.

Additionally, ordering kinetics can be enhanced as a result of combined reactions occurring during annealing of deformed FePt samples or thin films with high defect densities. Ordered nuclei formed as a result of combined reactions tend to have incoherent boundaries with the surrounding material [2.47,2.117] and those highly mobile boundaries improve

subsequent diffusion and grain growth. The wide variety of kinetic ordering temperatures and resulting degrees of chemical order reported for FePt in the literature are partly due to the effects of seemingly subtle differences in fabrication details on the ordering process.

2.3.2.2 Stoichiometry Considerations

Despite the ordered crystal structure containing exactly two of each atom, FePt samples have demonstrated optimal properties at numerous different compositions in both thin film and bulk forms. Sample variability is related to the development of different microstructures and phase-mixtures due to the different available kinetic routes afforded by the as-fabricated morphology, as discussed above, and stoichiometry. In particular, a wide range of kinetic ordering temperatures and resulting degrees of chemical order have been found in FePt thin films near even-stoichiometry. Differential scanning calorimeter (DSC) and *in-situ* diffraction experiments have quantified composition-dependent kinetic and thermodynamic parameters involved in the ordering process to illuminate this phenomenon.

The phase diagram (see Fig.2.7) shows that the $L1_0$ phase exists in a fairly broad compositional range around 1:1 with significant overlap with the two neighboring $L1_2$ ordered phases of Fe_3Pt and $FePt_3$. This overlap indicates the possibility for multiple ordered phases to coexist in equilibrium. Mixtures of $L1_0$ and $L1_2$ phases have been identified experimentally in annealed ML thin-films, partially milled powders, and cold-rolled elemental foils [2.111,2.118,2.119]. Therefore, in non-equilibrium samples prepared by a particular thermal annealing process, sample variability in range of 45 – 60 at.% Fe stems from effects of composition on the ordering kinetics and not the equilibrium properties of the Fe-Pt alloys.

Milled Fe-Pt powders with a compositional range of 45 – 60 at.% Fe develop chemical order just above 300 °C and exhibit essentially the same change in enthalpy during the ordering process. However, the process proceeds at a considerably slower rate for stoichiometries away

from 50:50, where the energy barrier to ordering is a minimum [2.109]. More pronounced compositional dependencies are found in thin films. Micron thick, co-deposited single-layer films indicate a shallow peak in absolute enthalpy change for slightly Fe-rich compositions. The kinetic ordering temperature and energy barrier exhibit similar minima over the same composition range, with variations of ~100 °C and 0.8 eV, respectively [2.113]. Comparable trends exist for ordering in Fe-rich single-layer 50 nm [2.108,2.120] and 150 nm films [2.121].

Unfortunately, contradictory results have been obtained in films fabricated by different means. In 1 μm ML films, instead of decreasing with Fe content, the heat of formation remains relatively constant over the range of 44 – 50 at.% Fe (Fe-rich films were not investigated in that study) [2.110]. Thinner, 60 nm ML films exhibit higher coercivities in the range of 40 – 50 at.% Fe after annealing anywhere between 300 and 600 °C, with a broad maximum for *S* occurring in that range after annealing at 600 °C [2.122]. By employing a modified sputtering gun featuring multi-pole magnetic plasma confinement to alter the as-deposited film morphology, ordering at 300 °C was only achieved at 47 at.% Fe in a 150 nm film and no other composition [2.121]. Similarly, epitaxial films grown at 300 °C only display $L1_0$ order at the Pt-rich composition of 38 at.% Fe [2.123].

The effects of stoichiometry on ordering kinetics have been presumed to relate to the relative atomic sizes of Fe and Pt, with radii of about 1.24 and 1.40 Å, respectively [2.124]. Arguments regarding the benefits of using an excess of either species have been made. Some researchers contend that by expanding the crystal lattice additional Pt atoms enhance atomic diffusion [2.122] or strain to drive the ordering process [2.123]. Others claim that the larger Pt atoms would only slow down ordering kinetics [2.113]. Ordered-nuclei densities and grain-boundary velocities extracted from modeled DSC data from micron thick films indicate a higher nuclei density and a slower grain-boundary velocity in Pt-rich films [2.50]. That study estimates

that, in general, Pt-rich films order 300 times slower than comparable Fe-rich films, yet the opposite may be true in thinner films. The latter has yet to be verified experimentally. A simple calculation using the diffusion parameters given in Table 1 suggests that Pt atoms diffuse slower than Fe in equiatomic FePt below 472 °C, above-which the converse becomes true. Such a crossover in relative atomic mobility adds a complicated temperature-dependence to understanding the possible benefits to ordering in off-stoichiometric FePt samples.

Table 2.1. Diffusion constants for Fe and Pt in FePt.

Diffusant	D_0 (m^2/s)	$E_{barrier}$ (eV)	Reference
Fe	3.45×10^{-13}	1.65	[2.125]
Pt	1×10^{-4}	2.9	[2.126]

2.3.2.3 Effects of As-fabricated Morphology

As indicated previously when comparing stoichiometry effects in single- and multi-layer films, changes in as-fabricated morphology can greatly alter a subsequent ordering process. In particular, an initially homogeneous morphology of A1 FePt tends to follow a different route to equilibrium than one consisting of multiple phases [2.94,2.119]. For example, DSC studies of 1 μm single-layer films measured enthalpy changes of around 8 kJ/g-atom [2.108], whereas similarly fabricated ML films released ~25 kJ/g-atom [2.111]. The large increase in released heat indicates the occurrence of additional kinetic processes such as diffusion and grain growth. Another study demonstrated that the kinetic ordering temperature can be lowered to 300 °C by depositing multilayers of Fe/Pt in 25 nm thin-films [2.94], as compared with 400 °C in codeposited films [2.98,2.127]. The examples given compare results from different, somewhat unrelated studies[10] in the literature and unspecified factors of each study's sample fabrication could play significant roles in determining the observed variations.

[10] Although the two DSC studies were performed at the same institution, neither one explicitly addresses the difference in results.

One particular study did explicitly investigate variations in the ordering process with phase and morphology homogeneity in three different partially milled $Fe_{50}Pt_{50}$ powders [2.109]. By using milling times of 2, 4 or 7 hours, the powders consisted of 20 – 200 nm thick α-Fe and Pt lamella with a ~5 nm thick fcc FePt interfacial layers, thinner α-Fe and Pt lamella with a thicker (tens of nm) interfacial fcc FePt layer, or homogenous fcc FePt, respectively. Grains sizes for α-Fe, Pt, and fcc-FePt phases evolved from 17, 23, and ~5 nm to 7, 9, and 15 nm for 2 and 4 hour millings, respectively. After 7 hours, only 15 nm grains of fcc FePt were present. The study determined a trend of decreasing absolute evolved enthalpy and increasing energy barrier for longer milling time. Variations in measured behavior were attributed to morphological differences between the three samples and their subsequent transformation routes. All powders developed the $L1_0$ phase at ~300 °C, yet the initial rate of low-temperature ordering was proportional to powder's milling time and, consequently, fcc phase fraction. Despite its accelerated process, the ordered fraction in 7-hour milled powder saturated at 400 °C with 90 wt.% $L1_0$ phase (S = 0.96). In contrast, the 2-hour milled sample required annealing at 660 °C to achieve the same ordered fraction (S = 0.99).[11] The 4-hour milled sample transformed at an intermediate pace to the other powders with respect to annealing time and temperature. Its ordered-phase fraction surpassed 90 wt.% (S = 0.99) after 19 hours at 450 °C, and reached ~99 wt.% at 570 °C (after 12 hours of non-isothermal annealing). The transformation process and related kinetics were described in the following way: Initially, $L1_0$ phase grains nucleate within or at the interfaces of the available fcc regions at the same temperature for all powders. The 7-hr milled powders transformed rapidly, concurrent with defect healing. Ordering by short-range diffusion plateaued at 400 °C, resulting in a mostly-ordered state. During annealing of the ML-like powders, interfacial $L1_2$ $FePt_3$ and Fe_3Pt grains formed due to interlayer diffusion, similar to

[11] Unfortunately, 660 °C was the highest temperature investigated in that study and the still-increasing ordered fraction could likely have improved further.

what is seen via *in-situ* TEM in epitaxially grown Fe/Pt multilayers [2.110]. Longer annealing times and/or higher temperatures were required to homogenize the stoichiometry to allow transformation into the $L1_0$ phase. However, the composition-gradients provided a continuous driving force for long-range diffusion, resulting in a higher degree of order. Such a force did not exist in the 7-hour annealed powder and the ordering process decelerated and became stagnant.

The study described above demonstrates that an optimal preprocessed morphology for achieving fully ordered FePt powders consists of a heterogeneous microstructure structure of Fe, Pt, and fcc-FePt lamella. The admixture of fcc phase provides nucleation sites to initiate ordering at lower temperatures and the compositional-inhomogeneities essentially sustain a driving force for continued ordering at high temperatures. ML films exhibiting a low-kinetic ordering temperature of ~300 °C consisted of both repeated (Fe 20.2 Å/Pt 17.3 Å) as-deposited bilayers and interfacial fcc-FePt grains, and a ML structure remained in the partially ordered film after processing [2.94]. Thin films deposited on fused quartz with the structure (Fe 25 Å/Pt 25 Å)$_{10}$ indicate that significant interdiffusion only occurs above 300 °C and a stacked structure remains intact for temperatures below 400 °C [2.128,2.129]. The proportions of the different phases present in an as-deposited film dictate diffusion rates and necessary diffusion lengths to complete ordering. Scale reduction by accumulated cold rolling of Fe and Pt foils shows an inverse dependence of the kinetic ordering temperature on internal layer thickness in the range from 10 μm to 10 nm [2.119]. Interlayer diffusion commences at ~350 °C to form both $L1_0$ and $L1_2$ ordered phases. Conversely, the onset temperature for interdiffusion remains constant at ~310 °C for ML thin-films with individual layer thicknesses in the range of a few nanometers [2.130]. Interestingly, the negative gradient-energy term calculated for those films predicts an increased Fe-Pt interdiffusion coefficient for larger individual layer thicknesses, and this trend

was observed in ML thin-films with periods ranging from 1 – 18 nm [2.102]. Therefore, there are trade-offs between diffusivity and diffusion length in optimizing the Fe/Pt dimensions, and ordering speed and the resulting degree of ordering in tailoring the fraction of as-fabricated fcc phase.

Another consideration of the ordering transformation in polycrystalline FePt concerns the volume difference between disordered and ordered crystallites and the related lattice strains incurred by such a change. In converting to the ordered state, fcc grains undergo an expansion of the *a*-lattice by ~1.6% and a shrinking of the *c*-lattice by ~2.3%, for a total volume increase of ~1%. The strain-energy associated with this volume change can decrease the drive for ordering [2.131]. Bulk or coarse grained FePt samples typically accommodate this ordering strain by forming transformation twins with mutually perpendicular c-axes conjugated along the {101} plane [2.47]. Prior to the appearance of the ordered phase, changes associated with grain growth and defect elimination have been identified in the disordered fcc grains of FePt nanocrystalline thin films annealed between 275 and 375 °C, in-line with the development of precursor grains [2.106,2.108]. Concurrently, in-plane compressive strain caused by the different thermal expansion coefficients of the substrate and film relaxes. The strain-state then shifts to in-plane tensile as the ordered phase forms [2.106]. In FePt thin-films processed at high temperatures, the generated strain-energy can induce preferential grain growth and recrystallization, both of which have consequences on the non-epitaxial formation of (001) texture. The mechanism behind non-epitaxial texturing of FePt thin films is discussed further in the next subsection.

2.3.2.4 In-situ Ordering

As an alternative to post-fabrication processing, the ordered $L1_0$ phase can be formed *in-situ* in a single step at elevated temperatures. In particular, ordered FePt thin films can be

successfully fabricated by MBE and sputtering deposition onto amorphous and single crystal substrates, with or without seed layers, at temperatures ≳300 °C. The temperature required to achieve a high degree of order depends on deposition rate, working gas pressure, substrate/seed layer type, and the deposition recipe. In general, the necessary temperature for achieving an ordered film *in-situ* is less than that needed for post-deposition fabrication due to the ease of surface diffusion relative to volume diffusion. Additional reduction in ordering temperature can be achieved by controlling the manner in which the Fe and Pt atoms are deposited. For example, depositing alternating near-monatomic layers of Fe and Pt at rates ~0.1 Å/s in ultra-high vacuum reduces the necessary substrate temperature to achieving an ordered film to less than 230 °C [2.132]. In contrast to post-deposition ordering, *in-situ* ordering of FePt was initially considered to be a continuous process [2.86,2.133]. However, subsequent studies determined that the *in-situ* ordering process may actually be of first-order; the formation of a precursor fcc phase gives the appearance of a continuous reaction [2.89,2.104,2.134].

High-temperature deposition also enables epitaxial growth to simultaneously define the crystalline texture while forming the $L1_0$ ordered phase [2.87,2.88]. Studies have examined *c*-axis textured FePt by depositing onto various single crystal substrates as well as a number of different seed layers, specially designed with epitaxial relationships to the $L1_0$ basal plane. Single-crystal substrates of (001) MgO, $SrTiO_3$ and (0001) Al_2O_3 have lattice parameters closely matching the $L1_0$ *a*-axis, and buffer layers of Pt, Au, or PtAu have been employed to improve the match [2.90,2.135-2.137]. Highly textured seed layers of (001) Cr, CrPt, and MgO deposited on amorphous substrates or Ta adhesion layers at carefully tuned parameters can also induce epitaxial growth in a subsequent FePt film [2.92,2.138,2.139]. Other seed layers for (001) FePt growth have included: Ag [2.140,2.141], CrRu [2.142], NiTa [2.143], RuAl [2.144], TiN [2.145], MnPt [2.146], and CrV [2.147].

2.3.2.5 Thin-Film Morphology

The resulting morphology of an ordered FePt film is partially determined by the deposition or processing temperature and the type of substrate or seed/buffer layers being employed. Depositing metallic FePt onto material with a lower free-interface surface energy can lead to dewetting behavior during high temperature deposition or processing. The condition for this to occur is given by the relationship in Eq. (2.35). Typically, discontinuous and island-like morphologies of FePt thin films are seen after deposition onto oxide substrates at a temperature exceeding 450 °C [2.89,2.133]. During post-deposition annealing, an initially continuous as-deposited film can develop deep grooving at its grain boundaries which can expose the substrate underneath. If given sufficient energy and time, a nucleated void will grow to minimize surface energy and yield a highly discontinuous film [2.148-2.151]. As will be discussed in Section 2.4.4, a film's magnetic properties depend strongly on its morphology. Therefore, careful tuning of deposition and processing parameters can help to control the resulting magnetic properties of an $L1_0$-ordered FePt thin film.

FePt films fabricated for this dissertation utilize multilayering of Fe and Pt to achieve a compositional gradient. The effects on non-epitaxial growth of ordered and (001) textured grains for varying Fe:Pt compositions and ML structures are addressed in Chapters 4.

2.3.3 Non-Epitaxial Texturing of FePt Thin Films

In order to realize $L1_0$ FePt as a perpendicular recording medium, the films must be fabricated with a high degree of c-axis, or (001), crystalline texture. Non-epitaxial texturing methods provide an alternative to the high-temperature deposition of epitaxial growth. As discussed in the previous section, FePt films deposited on amorphous substrates at ambient or relatively low temperatures grow in the fcc phase and require post-deposition processing to achieve the $L1_0$ phase. Typical of most fcc metallic crystals, surface-energy driven grain growth

leads to (111) fiber texture in un-processed FePt films and conventional thermal treatments do little to change that orientation. The non-epitaxial of FePt was discovered at the turn of the century by rapidly annealing an as-deposited ML structure of repeated FePt and SiO_2 or B_2O_3 layers [2.152,2.153]. It was soon realized that the same result could be achieved in pure Fe/Pt ML films [2.154]. The resulting texture was found to depend on multiple sample fabrication parameters: individual layer thickness and their configurations within the ML structure [2.155-158], Fe-Pt stoichiometry [2.159], total film thickness [2.151,2.154,2.157,2.160-2.164], processing time [2.150,2.155], temperature and ramp-rate [2.159,2.161,2.165,2.166], initial stress/strain state [2.166], and, where applicable, the oxide content [2.153,2.159]. Other non-epitaxial methods of fabricating (001) textured FePt films have subsequently been realized in, for example, extremely thin post-deposition annealed single layer films [2.150,2.157], ML structures with MgO [2.163], films with high residual tensile strain [2.165,1.67], and a 30 nm film deposited at 620 °C [2.168]; in some cases only partial texture was achieved [2.167,2.169]. Nonepitaxial texturing is also possible with ternaries of C [2.170], Ag [2.171,172], Au [2.173], Ni [2.174], and Cu [2.173,2.175,2.176] using ML deposition plus RTA treatment. The above works can be divided into four categories based on the understood texturing mechanism: a ordering-strain induced micromechanical rotation of $L1_0$ grains during cooling in molten B_2O_3 [2.177]; hetero-epitaxial growth with (100)-MgO multilayers [2.163]; strain energy driven selective grain growth (SEDSGG) [2.166,2.78]; and other, i.e. the mechanism for *in-situ* texture formation on an amorphous substrate is unclear [2.168]. The SEDSGG mechanism is believed to drive the non-epitaxial growth of (001) textured film in Chapters 4 and 5 of this dissertation. The remainder of this subsection will describe the principles of SEDSGG.

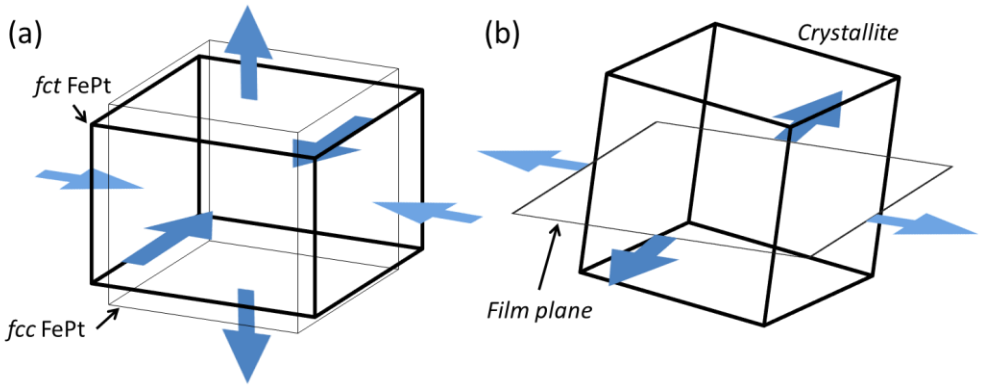

FIG. 2.9. Schematic of (a) ordering strain and (b) biaxial in-plane strain.

Atomistic calculations of strain energy have demonstrated the preference of (001) crystallites in post-deposition annealed FePt thin films when accounting for an anisotropic ordering transformation strain and a biaxial in-plane tensile strain [2.178,2.179]. Figure 13 illustrates the ordering and in-plane strains on a cubic/tetragonal crystal. Essentially, a preferred texture results when the anisotropic ordering strain caused by the expansion of the disordered crystallite's basal plane is accommodated by a biaxial tensile strain. Therefore, (001)-textured $L1_0$ grains are energetically favorable when the plane of this biaxial strain is parallel to the film plane. At the same time, a biaxial in-plane compressive strain stabilizes (100)-textured grains. Additionally, grains satisfying the Vook-Witt grain-interaction condition can stabilize (001)-texture even under zero or compressive biaxial strain [2.160]. The Vook-Witt condition is an anisotropic grain interaction model with equal interactions in the film plane and zero out of the plane, leading to equal biaxial in-plane strains and zero out-of-plane stress. The relative ease of thin films to satisfy the Vook-Witt condition[12] explains the inverse-thickness dependence of (001) texture exhibited by non-epitaxially grown FePt films.

[12] Grains in thinner films typically have fewer interactions in the vertical, out-of-plane direction and a greater chance of spanning the film thickness.

Tensile strain occurs in thin films due to volume shrinkage from defect elimination and grain growth, and this strain can become anisotropic during two-dimensional grain growth, once vertical growth has become stagnant. Experimental evidence of strain-states in post-deposition RTA processed FePt thin films correlates an in-plane tensile strain-state with (001) texture, supporting of the above model. Measurements of residual strain after annealing cycles ranging from 3-300 seconds indicate that a 25 nm film retains a tensile in-plane strain state after annealing for durations of up to ~20 seconds at 550 °C, after which a compressive strain state is found [2.178]. In another study, residual in-plane tensile stresses greater than 2.5 GPa corresponded to relatively high degrees of (001) orientation in 40 nm post-deposition annealed FePt films [2.166]. Both studies confirmed the presence of the ordered phase and indicated a sensitivity of the texturing mechanism to the details of the annealing process, namely the heat-rate. A transition from tensile to compressive strain during annealing suggests that there is a limited time frame for (001) texture to develop; ordering and growth must occur rapidly during this beneficial tensile strain-state. Once (001) texture has been established in stable, large grains, two-dimensional growth of those textured grains proceeds by SEDSGG. The latter study demonstrates a relationship between the magnitude of the residual stress and the heating rate; texture resulted when the annealing heating-rate was greater than 10 K/s, with the best texture found using ~40 K/s. Interestingly, poorer (001) texture was found when using higher rates. By limiting a film's exposure to lower temperatures, fast heating rates can avoid the recovery-type, dynamical stress relaxation processes observed below 300 °C, before the onset of ordering [2.108,2.166]. Such processes relax the ordering strain beneficial to drive SEDSGG. It should be mentioned that only two studies of non-epitaxially textured FePt films did not use a high RTA

ramp rate: a study on *in-situ* texturing [2.168] and one of a ~6nm FePt film deposited at extremely slow rates [2.157].[13]

The high temperatures used for successful non-epitaxial texturing facilitates rapid growth of $L1_0$ ordered grains via thermally activated atomic diffusion. Precursor grains of the as-deposited film readily nucleate the ordered phase and the small nuclei grow quickly to span the thickness of the film. Subsequent two-dimensional grain growth and satisfaction of the Vook-Witt condition trigger recrystallization and further growth of (001)-textured grains. Reducing the kinetic ordering temperature of FePt thin films by modifying the as-deposited structure can enhance the resulting degree of texture. Both multilayering and doping with low-surface energy materials have proven successful in achieving non-epitaxial (001)-texture FePt thin films and are the topics of Chapters 4 and 5, respectively.

2.3.4 Magnetic Properties of $L1_0$-Phase FePt

Reported magnetic properties of $L1_0$ FePt samples have been nearly as varied as the fabrication methods used due to the intimate connection between magnetic behavior and structural details. Reported coercivities have ranged from less than 2 kOe [2.51-2.53,2.136,2.180] in powders samples to nearly 90 kOe [2.181] in isolated single-crystal islands. Such disparate results spawned multiple, and at times contrasting, theories regarding the underlying reversal mechanism and even the precise values of the intrinsic parameters. The disappointingly small coercivities in early powders were attributed to poor defect and stoichiometry control. Investigations of thin films in the 1990's produced mixed conclusions regarding the roles of microstructure, crystalline defects, and intrinsic MCA; even the source of the MCA and the role of Pt were largely unclear. Subsequent theoretical and experimental

[13] The 6 nm film consisted of a stack of 3nm Fe and Pt layers. The slow deposition rates appear to allow for *in-situ* texture formation within each layer. Subsequent high-temperature annealing enables fast interdiffusion and ordering while maintaining the nascent texture.

studies have since mostly illuminated these uncertainties. As in any magnetic system, the measured behavior of a FePt sample is governed by the combination of the intrinsic properties of constituent atoms and alloys and the structure in which they occur. The following section introduces key intrinsic and extrinsic magnetic properties of $L1_0$ FePt.

The current understanding of the intrinsic magnetic properties of $L1_0$ FePt developed from somewhat contradicting experimental and theoretical results. It has been determined that the excellent intrinsic magnetic properties of $L1_0$ phase FePt result from the properties of atomic Fe and Pt and their interaction within the anisotropic layered crystal structure. Delocalized 3d Fe and 5d Pt electron orbitals hybridize between the atomic layers and the sizable Fe magnetic moment induces a moment on neighboring Pt atoms. Strong spin-orbit coupling stabilizes a 5d orbital moment on the Pt, and the interaction of this with the tetragonal crystal field produces the uniaxial MCA of 7 MJ/m^3 (70 $Merg/c^3$). The measured saturation magnetization of 1140 kA/m (1140 emu/cc) results from contributions of ~2.8 μ_B from Fe and ~0.3 μ_B from polarized Pt atoms [2.182-2.184].

Early first-principles calculations examining stable spin configurations in $L1_0$ FePt predicted a large MCA when accounting for spin-polarized Pt [2.185-2.187]. The exact magnitude of polarization was predicted to vary with structural details and chemical order, particularly the local environment of Fe atoms. Atomic coordination beyond nearest neighbors and intra- and interlayer atomic distances affect the strength and sign of Fe-Fe exchange coupling. Structural or chemical disorder can lead to frustrated and non-collinear spin states [2.188]. In a perfectly ordered equiatomic system, intralayer exchange between Fe atoms remains strongly ferromagnetic for all anticipated structural parameters [2.187,2.189]. On the other hand, Fe-Fe interlayer exchange coupling depends intensely on the atomic layer separation and the presence of intervening Pt atoms [2.186-2.188,2.190,2.191] The resulting

interlayer exchange determines the degree of spin polarization of the Pt atoms and thereby the MCA [2.186,2.188,2.191-2.193]. Experiments in the 1980's and 1990's using magneto-optical Kerr rotation indicated the presence of an appreciable Pt magnetic moment in $L1_0$ FePt as well as in the similarly ordered 3d-5d alloy of CoPt [2.62,2.194]. Neutron diffraction and x-ray magnetic circular dichroism experiments later confirmed the polarization of Pt [2.183,2.184].

Early first-principle calculations predicted an AFM ground state for the interlayer Fe-Fe exchange in perfectly ordered $L1_0$ FePt [2.182,2.187-2.190,2.192]. Opposing Fe spins cancel at the Pt sites, resulting in zero spin-polarized moment and a reduced or vanishing MCA. That AFM order in $L1_0$ FePt has not been observed experimentally could be due to innate imperfections in laboratory-fabricated samples. Perfect order or homogeneous 1:1 stoichiometry is difficult to achieve in practice and any Pt antisites would serve as a bridge for the ferromagnetic interlayer coupling necessary for the high MCA [2.188,2.192]. In contrast, recent first-principle calculations determined that a larger degree of spin-polarization on the interceding Pt atoms exists that would stabilize FM interlayer exchange even for perfectly ordered crystals [2.187,2.195].

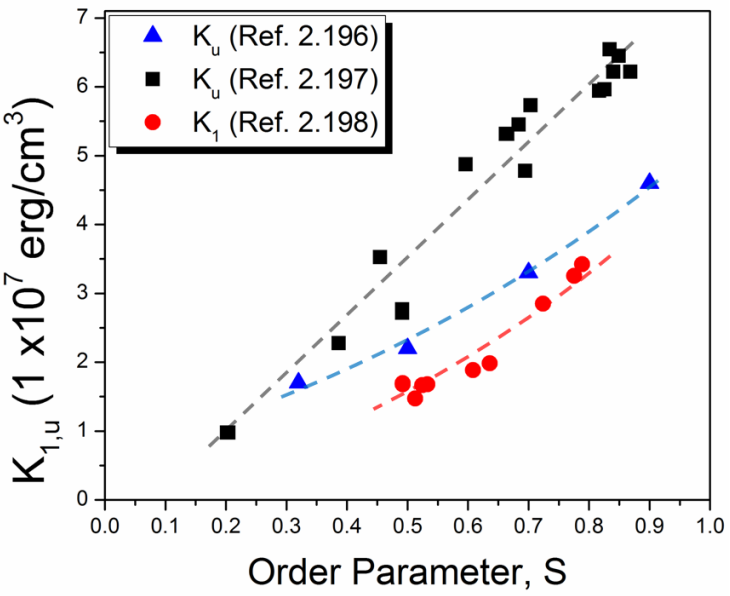

FIG. 2.10. Measured relationship between anisotropy and chemical order in $L1_0$ phase FePt thin films. Dashed lines added to guide the eye. Data digitized from Refs. listed.

Experimentally, the sensitivity of the MCA on atomic coordination and spacing strongly couples the measured magnetic behavior of an FePt sample to its chemical order, strain-state, and measurement temperature [2.186,2.188,2.191-2.193,2.195,2.196]. A direct correlation has been found between the degree of chemical order, *S*, and the magnitude of MCA [2.196-2.199], as shown in Fig. 2.10. A change in interatomic distance, particularly along the *c*-axis, alters the magnitude and possibly the sign of the interlayer exchange. Therefore, strain and defects causing global or local variations in the tetragonality ratio, respectively, can have profound effects on magnetic behavior. For example, the proportionality of T_c and *J* in the expression for the Curie temperature [Eq. (2.1)] indicates that disturbing the magnitude of the average exchange will alter the magnetic ordering temperature. As such, a suppressed T_c has been found experimentally for decreased interlayer exchange in strained FePt nanoparticles with enhanced tetragonality [2.187].

A number of structural features common to FePt samples are known to greatly affect a sample's extrinsic magnetic properties. Real-structure features such as grain size, grain size distribution, defect density, sample homogeneity and overall morphology play crucial roles in determining whether magnet's reversal process will be dominated by a nucleation or pinning mechanism [2.96,2.127,2.136,2.200,2.201]. The highest coercivities measured of any $L1_0$ FePt-based sample were from the nucleation dominated reversal of highly-textured, single-crystal, isolated single-domain islands epitaxially grown on MgO substrates [2.181]. Films similar to this were fabricated for the work presented in Chap. 6. As particle size or defect density increases, nucleation occurs more readily and pinning becomes the dominant reversal mechanism

The first order nature of FePt ordering can yield a multiphase microstructure of ordered and disordered grains after inadequate processing. Poor stoichiometry can also lead to a mixture of phases, in this case a combination of the three ordered Fe-Pt phases, even after long

annealing processes. Relatively large soft regions nucleate at small fields and poor interphase exchange coupling leads to two-step switching behavior. Well-coupled, finely interspersed phases result in volume-averaged magnetic properties [2.65]. Boundaries between hard and soft phases serve as effective pinning sites to domain wall motion [2.96]. Consequently, the degree of chemical order of a FePt magnet is strongly reflected in its magnetic hardness either through intrinsic MCA dependence or as an indication of a mixture of the ordered and disordered phases [2.96,2.120,2.196-2.199].

Additional pinning sites to magnetic reversal arise from the polytwin nature of FePt samples processed post-fabrication. Effective pinning sites in polycrystalline samples include interfaces between neighboring *c*-domains (twin boundaries) and anti-phase boundaries (APBs). The relative strengths of twin, anti-phase, order-disorder, and interphase boundaries as pinning-sites in FePt samples have been debated. Individual twin boundaries and ABPs are typically too small to be effective, i.e. having dimensions smaller than δ_B. Clusters of *c*-domains tend to act cooperatively to form macroscopic interaction domains and it has been demonstrated that pinning occurs strongly at regions of high twin-boundary density [2.202,2.203]. Aside from epitaxial thin films, the magnetically hardest FePt samples consist of highly ordered, ~10 nm diameter grains [2.59].

2.4 References

2.1 R. Skomski, *Simple Models of Magnetism*. (University Press, Oxford, 2008).

2.2 A. Aharoni, *Introduction to the Theory of Ferromagnetism*. (Oxford University Press, Oxford, 1996).

2.3 R. Skomski, H. P. Oepen and J. Kirschner, Physical Review B **58** (6), 3223-3227 (1998).

2.4 D. J. Sellmyer, M. Yu and R. D. Kirby, Nanostructured Materials **12**, 1021-1026 (1999).

2.5 T. Thomson and K. O. Grady, Journal of Physics D: Applied Physics **30** (11), 1566 (1997).

2.6 J. Vogel, J. Moritz and O. Fruchart, Comptes Rendus Physique **7**, 977-987 (2006).

2.7 E. F. Kneller and F. E. Luborsky, Journal of Applied Physics **34** (3), 656-658 (1963).

2.8 R. Skomski, G. C. Hadjipanayis and D. J. Sellmyer, IEEE Transactions on Magnetics **43** (6), 2956-2958 (2007).

2.9 N. Honda, T. Kiya, J. Ariake, K. Ouchi and S. Iwasaki, IEEE Transactions on Magnetics **38** (5), 2030-2032 (2002).

2.10 E. Kneller and R. Hawig, IEEE Transactions on Magnetics **27** (4) (1991).

2.11 R. Skomski, Journal of Applied Physics **76** (10), 7059-7064 (1994).

2.12 E. E. Fullerton, J. S. Jiang, M. Grimsditch, C. H. Sowers and S. D. Bader, Physical Review B **58** (18), 12193 (1998).

2.13 O. Cugat, J. Delamare and G. Reyne, IEEE Transactions on Magnetics **39** (6), 3607-3612 (2003).

2.14 C. T. Pan and S. C. Shen, Journal of Magnetism and Magnetic Materials **285** (3), 422-432 (2005).

2.15 J.-U. Thiele, S. Maat and E. E. Fullerton, Applied Physics Letters **82** (17), 2859-2861 (2003).

2.16 R. H. Victora and S. Xiao, IEEE Transactions on Magnetics **41** (2), 537-542 (2005).

2.17 D. Suess, T. Schrefl, S. Fahler, M. Kirschner, G. Hrkac, F. Dorfbauer and J. Fidler, Applied Physics Letters **87** (1), 012504-012503 (2005).

2.18 J. P. Wang, S. Weikang and J. Bai, IEEE Transactions on Magnetics **41** (10), 3181-3186 (2005).

2.19 W. F. Brown, Rev. Mod. Phys. **17** (1945).

2.20 A. Aharoni, Physical Review **119** (1), 127-131 (1960).

2.21 C. Abraham and A. Aharoni, Physical Review **120** (5), 1576-1579 (1960).

2.22 E. Goto, N. Hayashi, T. Miyashita and K. Nakagawa, Journal of Applied Physics **36** (9), 2951-2958 (1965).

2.23 F. B. Hagedorn, Journal of Applied Physics **41** (6), 2491-2502 (1970).

2.24 S. Li, B. Livshitz, H. N. Bertram, A. Inomata, E. E. Fullerton and V. Lomakin, Journal of Applied Physics **105**, 07C121 (2009).

2.25 H. Nemoto, I. Takekuma, H. Nakagawa, T. Ichihara, R. Araki and Y. Hosoe, Journal of Magnetism and Magnetic Materials **320** (22), 3144-3150 (2008).

2.26 R. H. Victora and X. Shen, Magnetic Recording Conference Digest A1 (2004).

2.27 A. Y. Dobin and H. J. Richter, Applied Physics Letters **89** (6), 062512-062513 (2006).

2.28 G. Asti, M. Ghidini, R. Pellicelli, C. Pernechele, M. Solzi, F. Albertini, F. Casoli, S. Fabbrici and L. Pareti, Physical Review B (Condensed Matter and Materials Physics) **73** (9), 094406-094416 (2006).

2.29 H. J. Richter, G. Choe and B. D. Terris, IEEE Transactions on Magnetics **47** (12), 4769-4774 (2011).

2.30 Y. Sonobe, D. Weller, Y. Ikeda, K. Takano, M. E. Schabes, G. Zeltzer, H. Do, B. K. Yen and M. E. Best, Journal of Magnetism and Magnetic Materials **235**, 424-428 (2001).

2.31 D. Suess, Applied Physics Letters **89** (11), 113105-113103 (2006).
2.32 Z. Lu, P. B. Visscher and W. H. Butler, IEEE Transactions on Magnetics **43** (6), 2941-2943 (2007).
2.33 R. H. Victora and S. Xiao, Proceedings of the IEEE **96** (11), 1799-1809 (2008).
2.34 D. Suess, J. Lee, J. Fidler and T. Schrefl, Journal of Magnetism and Magnetic Materials **321** (6), 545-554 (2009).
2.35 H. Sohn and R. H. Victora, IEEE Transactions on Magnetics **47** (10), 4073-4076 (2011).
2.36 H. Kronmüller and D. Goll, physica status solidi (b) **248** (10), 2361-2367 (2011).
2.37 G. Asti, M. Solzi, M. Ghidini and F. M. Neri, Physical Review B **69** (17), 174401 (2004).
2.38 R. Skomski and J. M. D. Coey, IEEE Transactions on Magnetics **29** (6), 2860-2862 (1993).
2.39 D. Goll and H. Kronmüller, Physica B: Condensed Matter **403**, 1854-1859 (2008).
2.40 R. Skomski, T. A. George and D. J. Sellmyer, Journal of Applied Physics **103**, 07F531-533 (2008).
2.41 J. P. Sharrock, Journal of Applied Physics **76** (10) (1994).
2.42 R. Skomski, J. Zhou, R. D. Kirby and D. J. Sellmyer, Journal of Applied Physics **99** (8), 08B906-903 (2006).
2.43 J. W. Harrell, IEEE Transactions on Magnetics **37** (1), 533-537 (2001).
2.44 D. Suess, J. Fidler, G. Zimanyi, T. Schrefl and P. Visscher, Applied Physics Letters **92** (17), 173111-173113 (2008).
2.45 D. Smith, *Thin-Film Deposition: Principles and Practice*. (McGraw-Hill, Boston, 1995).
2.46 J. A. Thornton, Journal of Vacuum Science and Technology **11** (4), 666-670 (1974).
2.47 T. J. Klemmer, C. Liu, N. Shukla, X. W. Wu, D. Weller, M. Tanase, D. E. Laughlin and W. A. Soffa, Journal of Magnetism and Magnetic Materials **266** (1-2), 79-87 (2003).
2.48 E. Hornbogen, Matallurgical and Materials Transactions A **947** (1979).
2.49 D. Potter and K. Easterling, *Phase Transformations in Metals and Alloys*. (Nelson Thornes Ltd, Cheltenham, 2001)
2.50 D. C. Berry and K. Barmak, Journal of Applied Physics **101** (1), 014905-014914 (2007).
2.51 Franklin, PR (1954).
2.52 K. Watanabe and H. Masumoto, Transactions of the Japanese Institute of Metals **24**, 627 (1983).
2.53 K. Watanabe and H. Masumoto, Journal of the Japanese Institute of Metals and Materials **48**, 930 (1984).
2.54 J. Zhou, R. Skomski, L. Xingzhong, T. Wei, G. C. Hadjipanayis and D. J. Sellmyer, IEEE Transactions on Magnetics **38** (5), 2802-2804 (2002).
2.55 X. Rui, J. E. Shield, Z. Sun, L. Yue, Y. Xu, D. J. Sellmyer, Z. Liu and D. J. Miller, Journal of Magnetism and Magnetic Materials **305** (1), 76-82 (2006).
2.56 P. Sharma, J. Waki, N. Kaushik, D. V. Louzguine-Luzgin, H. Kimura and A. Inoue, Acta Materialia **55** (12), 4203-4212 (2007).
2.57 Y. Liu, T. A. George, R. Skomski and D. J. Sellmyer, Journal of Applied Physics **111** (7), 07B537 (2012).
2.58 D. Weller, A. Moser, L. Folks, M. E. Best, L. Wen, M. F. Toney, M. Schwickert, J. U. Thiele and M. F. Doerner, IEEE Transactions on Magnetics **36** (1), 10-15 (2000).
2.59 J. Lyubina, in *Handbook of Magnetic Materials*, edited by Buschow (Elsevier, 2011), Vol. 19, pp. 291-395.
2.60 L. Graf and A. Kussmann, Z. Phys. **36** (1935).
2.61 L. V. Kirenskii, physica status solidi (a) **63** K27 (1981).
2.62 J. Aboaf, T. McGuire, S. Herd and E. Klokholm, IEEE Transactions on Magnetics **20** (5), 1642-1644 (1984).

2.63 T. Sugimoto, T. Katayama, Y. Suzuki, T. Koide, T. Sidara, M. Yuri, A. Itoh and K. Kawanishi, Physical Review B **48** (22), 16432-16439 (1993).
2.64 K. R. Coffey, M. A. Parker and J. K. Howard, IEEE Transactions on Magnetics **31** (6), 2737-2739 (1995).
2.65 J. P. Liu, C. P. Luo, Y. Liu and D. J. Sellmyer, Applied Physics Letters **72** (4), 483-485 (1998).
2.66 S. Sun, C. B. Murray, D. Weller, L. Folks and A. Moser, Science **287** (5460), 1989-1992 (2000).
2.67 D. J. Sellmyer, Nature **420** (6914), 374-375 (2002).
2.68 H. Zeng, S. Sun, T. S. Vedantam, J. P. Liu, Z. R. Dai and Z. L. Wang, Applied Physics Letters **80** (14), 2583-2585 (2002).
2.69 Y. C. Sui, Y. Zhao, M. Daniil, X. Z. Li and D. J. Sellmyer, Journal of Applied Physics **99**, 08G704-703 (2006).
2.70 K. E. Elkins, T. S. Vedantam, J. P. Liu, H. Zeng, S. Sun, Y. Ding and Z. L. Wang, Nano Letters **3** (12), 1647-1649 (2003).
2.71 C.-b. Rong, N. Poudyal, G. S. Chaubey, V. Nandwana, R. Skomski, Y. Q. Wu, M. J. Kramer and J. P. Liu, Journal of Applied Physics **102** (4), 043913-043914 (2007).
2.72 J. W. Harrell, D. E. Nikles, S. S. Kang, X. C. Sun, Z. Jia, S. Shi, J. Lawson, G. B. Thompson, C. Srivastava and N. V. Seetala, Scripta Materialia **53** (4), 411-416 (2005).
2.73 D. J. Sellmyer, C. P. Luo, Y. Qiang and J. P. Liu, in *Handbook of Thin Film Materials*, edited by H. S. Nalwa (Academic Press, 2002), Vol. 5, pp. 337-373.
2.74 B. Rellinghaus, S. Stappert, M. Acet and E. F. Wassermann, Journal of Magnetism and Magnetic Materials **266** (1-2), 142-154 (2003).
2.75 Y. Xu, Z. G. Sun, Y. Qiang and D. J. Sellmyer, Journal of Applied Physics **93** (10), 8289-8291 (2003).
2.76 S. Stoyanov, Y. Huang, Y. Zhang, V. Skumryev and G. Hadjipanayis, Journal of Applied Physics **93** (10) (2003).
2.77 C. Kim, T. Loedding, S. Jang, H. Zeng, Z. Li, Y. Sui and D. J. Sellmyer, Applied Physics Letters **91** (17), 172508-172503 (2007).
2.78 E. Kockrick, F. Schmidt, K. Gedrich, M. Rose, T. A. George, T. Freudenberg, R. Kraehnert, R. Skomski, D. J. Sellmyer and S. Kaskel, Chemistry of Materials **22** (2010).
2.79 R. M. Taylor, D. L. Huber, T. C. Monson, V. Esch and L. O. Sillerud, Journal of Vacuum Science & Technology B: Microelectronics and Nanometer Structures **30** (2), 02C101-106 (2012).
2.80 D. K. Kim, D. Kan, T. Veres, F. Normadin, J. K. Liao, H. H. Kim, S.-H. Lee, M. Zahn and M. Muhammed, Journal of Applied Physics **97** (10), 10Q918-913 (2005).
2.81 A. Menshikov, T. Tarnóczi and E. Krén, physica status solidi (a) **28** (1), K85-K87 (1975).
2.82 M. F. Toney, W.-Y. Lee, J. A. Hedstrom and A. Kellock, Journal of Applied Physics **93** (12), 9902-9907 (2003).
2.83 A. Y. Yermakov and V. V. Maykov, Fiz. Met. Metalloved **60** (1985).
2.84 T. J. Klemmer, N. Shukla, C. Liu, X. W. Wu, E. B. Svedberg, O. Mryasov, R. W. Chantrell, D. Weller, M. Tanase and D. E. Laughlin, Applied Physics Letters **81** (12), 2220-2222 (2002).
2.85 B. E. Warren, *X-ray Diffraction*. (Dover, New York, 1990).
2.86 R. F. C. Farrow, D. Weller, R. F. Marks, M. F. Toney, S. Hom, G. R. Harp and A. Cebollada, Applied Physics Letters **69** (8), 1166-1168 (1996).
2.87 M. R. Visokay and R. Sinclair, Applied Physics Letters **66** (13), 1692-1694 (1995).
2.88 A. Cebollada, D. Weller, J. Sticht, G. R. Harp, R. F. C. Farrow, R. F. Marks, R. Savoy and J. C. Scott, Physical Review B **50** (5), 3419 (1994).

2.89 Y. K. Takahashi, K. Hono, T. Shima and K. Takanashi, Journal of Magnetism and Magnetic Materials **267** (2), 248-255 (2003).
2.90 T. Shima, K. Takanashi, Y. K. Takahashi and K. Hono, Applied Physics Letters **81** (6), 1050-1052 (2002).
2.91 Watannabe, Japanese Journal of Applied Physics (1996).
2.92 Suzuki, Journal of the Magnetics Society of Japan (1999).
2.93 J. Lyubina, O. Gutfleisch, K. H. Muller, L. Schultz and N. M. Dempsey, Journal of Applied Physics **95** (11), 7474-7476 (2004).
2.94 C. P. Luo and D. J. Sellmyer, IEEE Transactions on Magnetics **31** (6), 2764-2766 (1995).
2.95 J. P. Liu, Y. Liu, C. P. Luo, Z. S. Shan and D. J. Sellmyer, Journal of Applied Physics **81** (8), 5644-5646 (1997).
2.96 R. A. Ristau, K. Barmak, L. H. Lewis, K. R. Coffey and J. K. Howard, Journal of Applied Physics **86** (8), 4527-4533 (1999).
2.97 K. Barmak, J. Kim, S. Shell, E. B. Svedberg and J. K. Howard, Applied Physics Letters **80** (22), 4268-4270 (2002).
2.98 R. A. Ristau, K. Barmak, K. R. Coffey and J. K. Howard, Journal of Materials Research **14** (8) (1999).
2.99 J. G. Na, Journal of Materials Science Letters **19** (13), 1171-1173 (2000).
2.100 F. Casoli, L. Nasi, F. Albertini, S. Fabbrici, C. Bocchi, F. Germini, P. Luches, A. Rota and S. Valeri, Journal of Applied Physics **103** (4), 043912-043918 (2008).
2.101 X. H. Li, B. T. Liu, W. Li, H. Y. Sun, D. Q. Wu and X. Y. Zhang, Journal of Applied Physics **101** (9), 093911-093915 (2007).
2.102 B. Yao and K. R. Coffey, Journal of Applied Physics **103**, 07E107-103 (2008).
2.103 H. Wang, J. Zhang, F. Yang, Y. Xu and Q. Li, Nanoscale Research Letters **5** (3), 489-493 (2010).
2.104 F. E. Spada, F. T. Parker, C. L. Platt and J. K. Howard, Journal of Applied Physics **94** (8), 5123-5134 (2003).
2.105 V. R. Reddy, S. Kavita and A. Gupta, Journal of Applied Physics **99** (11), 113906-113904 (2006).
2.106 S. N. Hsiao, S. K. Chen, T. S. Chin, Y. W. Hsu, H. W. Huang, F. T. Yuan, H. Y. Lee and W. M. Liao, Journal of Magnetism and Magnetic Materials **321** (16), 2459-2466 (2009).
2.107 J. Lyubina, O. Gutfleisch, R. Skomski, K. H. Muller and L. Schultz, Scripta Materialia **53** (4), 469-474 (2005).
2.108 K. W. Wierman, C. L. Platt, J. K. Howard and F. E. Spada, Journal of Applied Physics **93** (10), 7160-7162 (2003).
2.109 J. Lyubina, O. Isnard, O. Gutfleisch, K.-H. Muller and L. Schultz, Journal of Applied Physics **100** (9), 094308-094309 (2006).
2.110 T. Kaiser, W. Sigle, D. Goll, N. H. Goo, V. Srot, P. A. van Aken, E. Detemple and W. Jager, Journal of Applied Physics **103** (6), 063913-063916 (2008).
2.111 B. Wang, D. C. Berry, Y. Chiari and K. Barmak, Journal of Applied Physics **110** (1), 013903-013908 (2011).
2.112 Y. Ding and S. A. Majetich, IEEE Transactions on Magnetics **43** (6), 3100-3102 (2007).
2.113 D. C. Berry and K. Barmak, Journal of Applied Physics **102** (2), 024912-024919 (2007).
2.11 F. Q. Wang, X. H. Li, J. X. Guo, D. F. Guo, L. Xu, J. W. Zhao, B. T. Liu and X. Y. Zhang, Journal of Alloys and Compounds **508** (2), 512-515 (2010).
2.115 B. Rellinghaus, E. Mohn, L. Schultz, T. Gemming, M. Acet, A. Kowalik and B. Kock, IEEE Transactions on Magnetics **42** (10) (2006).

2.116 T. Klemmer, Y. Peng, X. Wu and G. Ju, IEEE Transactions on Magnetics **45** (2), 845-849 (2009).
2.117 Y. K. Takahashi and K. Hono, Scripta Materialia **53** (4), 403-409 (2005).
2.118 J. Lyubina, O. Ingo, M. Karl-Hartmut, G. Oliver, R. Manuel, W. Manfred and S. Ludwig, Journal of Physics: Condensed Matter **17** (26), 4157 (2005).
2.119 M. Verdier, M. Veron, F. Bley, F. Ingwiller, N. M. Dempsey and D. Givord, Philosophical Magazine **85** (26-27), 3157-3172 (2005).
2.120 B.-H. Li, F. Chun, Y. Tao, T. Jiao, Z. Zhong-Hai, Y. Guang-Hua and Z. Feng-Wu, Journal of Physics D: Applied Physics **39** (6), 1018 (2006).
2.121 K. Kawai, S. Honda, R. Sugiki, M. Komatsu and K. Kawabata, Journal of Magnetism and Magnetic Materials **287** (0), 214-218 (2005).
2.122 Y. L. Li, T. F. Feng, Q. Chen, A. P. Huang and Z. Y. Chen, Materials Letters **65** (17â€“18), 2589-2591 (2011).
2.123 T. Seki, T. Shima, K. Takanashi, Y. Takahashi, E. Matsubara and K. Hono, Applied Physics Letters **82** (15), 2461-2463 (2003).
2.124 L. E. Sutton, (Chemical Society, London, 1965).
2.125 M. Rennhofer, B. Sepiol, M. Sladecek, D. Kmiec, S. Stankov, G. Vogl, M. Kozlowski, R. Kozubski, A. Vantomme, J. Meersschaut, R. Rüffer and A. Gupta, Physical Review B **74** (10), 104301 (2006).
2.126 J. Kucera and B. Million, physica status solidi (a) **31** (1), 275-282 (1975).
2.127 S. W. Yung, Y. H. Chang, T. J. Lin and M. P. Hung, Journal of Magnetism and Magnetic Materials **116** (3), 411-418 (1992).
2.128 Y. Endo, N. Kikuchi, O. Kitakami and Y. Shimada, Journal of Applied Physics **89**, 7065-7067 (2001).
2.129 Y. Endo, K. Oikawa, T. Miyazaki, O. Kitakami and Y. Shimada, Journal of Applied Physics **94** (11), 7222-7226 (2003).
2.130 N. Zotov, J. Feydt, A. Savan and A. Ludwig, Journal of Applied Physics **100** (7), 073517-073511 (2006).
2.131 V. Tsurin, A. Ermakov, G. Lebedev, B. Filippov, physica status solidi (a) **33**, 325-332 (1976).
2.132 T. Shima, T. Moriguchi, S. Mitani and K. Takanashi, Applied Physics Letters **80** (2), 288-290 (2002).
2.133 M.-G. Kim and S.-C. Shin, Journal of Applied Physics **90** (5), 2211-2215 (2001).
2.134 Y. K. Takahashi, M. Ohnuma and K. Hono, Journal of Applied Physics **93** (10), 7580-7582 (2003).
2.135 M. Weisheit, L. Schultz and S. Fahler, Journal of Applied Physics **95** (11), 7489-7491 (2004).
2.136 M. H. Hong, K. Hono and M. Watanabe, Journal of Applied Physics **84** (8) (1998).
2.137 D. H. Wei, T. S. Chin, K. L. You, C. C. Yu, Y. Liou and Y. D. Yao, Journal of Magnetism and Magnetic Materials **303** (2), e265-e269 (2006).
2.138 A.-C. Sun, J.-H. Hsu, P. C. Kuo, H. L. Huang, H. C. Lu and S. F. Wang, Journal of Magnetism and Magnetic Materials **310** (2, Part 3), 2650-2652 (2007).
2.139 K. Kang, Z. G. Zhang, C. Papusoi and T. Suzuki, Applied Physics Letters **84** (3), 404-406 (2004).
2.140 Y.-N. Hsu, S. Jeong, D. E. Laughlin and D. N. Lambeth, 2001 (unpublished).
2.141 K. Kang, Z. G. Zhang, C. Papusoi and T. Suzuki, Applied Physics Letters **82** (19), 3284-3286 (2003).
2.142 J. S. Chen, B. C. Lim and J. P. Wang, Applied Physics Letters **81** (10), 1848-1850 (2002).

2.143 T. Maeda, IEEE Transactions on Magnetics **41** (10), 3331-3333 (2005).
2.144 W. K. Shen, J. H. Judy and J.-P. Wang, presented at the 49th Annual Conference on Magnetism and Magnetic Materials, Jacksonville, Florida (USA), 2005 (unpublished).
2.145 G. R. Trichy, J. Narayan and H. Zhou, Applied Physics Letters **89** (13), 132502-132503 (2006).
2.146. C.-C. Chiang, W.-C. Tsai, L.-W. Wang, H.-C. Hou, J.-W. Liao, H.-J. Lin, F.-H. Chang, B. J. Kirby and C.-H. Lai, Applied Physics Letters **99** (21), 212504-212503 (2011).
2.147 C. DongWon, K. SungMan, K. GyeungHo and J. WonYoung, IEEE Transactions on Magnetics **46** (6), 1856-1858 (2010).
2.148 S. H. Liou, Y. Liu, S. S. Malhotra, M. Yu and D. J. Sellmyer, Journal of Applied Physics **79**, 5060-5062 (1996).
2.149 Y.-C. Wu, L.-W. Wang, M. T. Rahman and C.-H. Lai, Journal of Applied Physics **103** (7), 07E126-126 (2008).
2.150 C. Brombacher, C. Schubert, K. Neupert, M. Kehr, J. Donges and M. Albrecht, Journal of Physics D: Applied Physics **44** (35), 355001 (2011).
2.151 Y. S. Yu, T. A. George, W. L. Li, L. P. Yue, W. D. Fei, H. Li, M. Liu and D. J. Sellmyer, Journal of Applied Physics **108** (7), 073906-073904 (2010).
2.152 C. P. Luo and D. J. Sellmyer, Applied Physics Letters **75** (20), 3162-3164 (1999).
2.153 C. P. Luo, S. H. Liou, L. Gao, Y. Liu and D. J. Sellmyer, Applied Physics Letters **77** (14), 2225-2227 (2000).
2.154 H. Zeng, M. L. Yan, N. Powers and D. J. Sellmyer, Applied Physics Letters **80** (13), 2350-2352 (2002).
2.155 M. L. Yan, N. Powers and D. J. Sellmyer, Journal of Applied Physics **93** (10), 8292-8294 (2003).
2.156 Y. Itoh, M. Takeuchi, A. Tsukamoto, K. Nakagawa, A. Itoh and T. Katayama, Japanese Journal of Applied Physics **41** (Part 2, No. 10A), L1066 (2002).
2.157 S. Nakagawa and T. Kamiki, Journal of Magnetism and Magnetic Materials **287**, 204-208 (2005).
2.158 Y. Ogata, Y. Imai and S. Nakagawa, Journal of Applied Physics **107** (9), 09A715-713 (2010).
2.159 M. L. Yan, H. Zeng, N. Powers and D. J. Sellmyer, Journal of Applied Physics **91** (10), 8471-8473 (2002).
2.160 J.-S. Kim and Y.-M. Koo, Thin Solid Films **516** (6), 1147-1154 (2008).
2.161 Y. H. Fang, P. C. Kuo, S. C. Chen, S. L. Hsu and G. P. Lin, Thin Solid Films **517** (17), 5185-5188 (2009).
2.162 J. K. Mei, F. T. Yuan, W. M. Liao, A. C. Sun, Y. D. Yao, H. M. Lin, J. H. Hsu and H. Y. Lee, IEEE Transactions on Magnetics **47** (10), 3633-3636 (2011).
2.163 H. J. Kim and S.-R. Lee, Journal of Applied Physics **97** (10), 10H304-303 (2005).
2.164 T. Narisawa, T. Hasegawa, S. Ishio and H. Yamane, Journal of Applied Physics **109** (3), 033918-033917 (2011).
2.165 J. K. Mei, F. T. Yuan, W. M. Liao, Y. D. Yao, H. M. Lin, H. Y. Lee and J. H. Hsu, Journal of Applied Physics **109** (7), 07A737-733 (2011).
2.166 S. N. Hsiao, S. H. Liu, S. K. Chen, T. S. Chin and H. Y. Lee, Applied Physics Letters **100** (26), 261909-261904 (2012).
2.167 P. Rasmussen, X. Rui and J. E. Shield, Applied Physics Letters **86** (19), 191915-191913 (2005).
2.168 S. C. Chen, T. H. Sun, C. L. Chang, C. L. Shen, P. C. Kuo and J. R. Chen, Thin Solid Films **519** (20), 6964-6968 (2011).

2.169 T. H. Sun, S. C. Chen, W. H. Su, C. L. Shen, P. C. Kuo and J. R. Chen, Thin Solid Films **520** (2), 774-777 (2011).
2.170 M. L. Yan, R. F. Sabirianov, Y. F. Xu, X. Z. Li and D. J. Sellmyer, IEEE Transactions on Magnetism **40** (4), 2470-2472 (2004).
2.171 M. L. Yan, R. Skomski, A. Kashyap, L. Gao, S. H. Liou and D. J. Sellmyer, IEEE Transactions on Magnetism **40** (4), 2495-2497 (2004).
2.172 Y. S. Yu, T. A. George, W. L. Li, L. P. Yue, W. D. Fei, L. Haibo and D. J. Sellmyer, IEEE Transactions on Magnetics **46** (6), 1817-1820 (2010).
2.173 Y. Ogata, Y. Imai and S. Nakagawa, Physics Procedia **16** (0), 36-41 (2011).
2.174 M. L. Yan, Y. F. Xu, X. Z. Li and D. J. Sellmyer, Journal of Applied Physics **97**, 10H309-303 (2005).
2.175 M. L. Yan, Y. F. Xu and D. J. Sellmyer, Journal of Applied Physics **99** (8), 08G903-903 (2006).
2.176 C. L. Platt and K. W. Wierman, Journal of Magnetism and Magnetic Materials **295** (3), 241-245 (2005).
2.177 T. Ichitsubo, S. Tojo, T. Uchihara, E. Matsubara, A. Fujita, K. Takahashi and K. Watanabe, Physical Review B **77** (9), 094114 (2008).
2.178 J.-S. Kim, Y.-M. Koo and N. Shin, Journal of Applied Physics **100** (9), 093909-093906 (2006).
2.179 J.-S. Kim, Y.-M. Koo, B.-J. Lee and S.-R. Lee, Journal of Applied Physics **99** (5), 053906-053906 (2006).
2.180 H. Lipson, D. Shoenberg and G. V. Stupart, Journal of the Institute of Metals **67** (1941).
2.181 T. Shima, K. Takanashi, Y. K. Takahashi and K. Hono, Applied Physics Letters **85** (13), 2571-2573 (2004).
2.182 A. Menshikov, A. Yu, Y. A. Dorofeyev, V. A. Kazantsev and S. K. Sidorov, Fizika Metallov I Metallovedenie **38**, 505-518 (1974).
2.183 J. Lyubina, I. Opahle, M. Richter, O. Gutfleisch, K.-H. Muller, L. Schultz and O. Isnard, Applied Physics Letters **89** (3), 032506-032503 (2006).
2.184 J. Honolka, T. Y. Lee, K. Kuhnke, A. Enders, R. Skomski, S. Bornemann, S. Mankovsky, J. Minar, J. Staunton, H. Ebert, M. Hessler, K. Fauth, G. Schütz, A. Buchsbaum, M. Schmid, P. Varga and K. Kern, Physical Review Letters **102** (6), 067207 (2009).
2.185 G. H. O. Daalderop, P. J. Kelly and M. F. H. Schuurmans, Physical Review B **44** (21), 12054-12057 (1991).
2.186 A. Sakuma, Journal of the Physical Society of Japan **63** (8) (1994).
2.187 H. Zeng, R. Sabirianov, O. Mryasov, M. L. Yan, K. Cho and D. J. Sellmyer, Physical Review B **66** (18), 184425 (2002).
2.188 R. Skomski, A. Kashyap and J. Zhou, Scripta Materialia **53** (4), 389-394 (2005).
2.189 M. E. Gruner, Journal of Physics D: Applied Physics **41** (13), 134015 (2008).
2.190 Z. Lu, R. V. Chepulskii and W. H. Butler, Physical Review B **81** (9), 094437 (2010).
2.191 P. V. Lukashev, N. Horrell and R. F. Sabirianov, Journal of Applied Physics **111** (7), 07A318-313 (2012).
2.192 G. Brown, B. Kraczek, A. Janotti, T. C. Schulthess, G. M. Stocks and D. D. Johnson, Physical Review B **68** (5), 052405 (2003).
2.193 S. D. Willoughby, Journal of Applied Physics **95** (11), 6586-6588 (2004).
2.194 T. Sugimoto, T. Katayama, Y. Suzuki and Y. Nishihara, Japanese Journal of Applied Physics **28** (12) (1989).
2.195 O. N. Mryasov, U. Nowak, K. Y. Guslienko and R. W. Chantrell, EPL (Europhysics Letters) **69** (5), 805 (2005).

2.196 S. Okamoto, N. Kikuchi, O. Kitakami, T. Miyazaki, Y. Shimada and K. Fukamichi, Physical Review B **66** (2), 024413 (2002).
2.197 H. Kanazawa, G. Lauhoff and T. Suzuki, Journal of Applied Physics **87** (9), 6143-6145 (2000).
2.198 Z. Lu, M. J. Walock, P. LeClair, W. H. Butler and G. J. Mankey, Journal of Vacuum Science & Technology A: Vacuum, Surfaces, and Films **27**, 1067-1070 (2009).
2.199 J. B. Staunton, S. Ostanin, S. S. A. Razee, B. Gyorffy, L. Szunyogh, B. Ginatempo and B. Ezio, Journal of Physics: Condensed Matter **16** (48), S5623 (2004).
2.200 H. Kronmüller and M. Bachmann, Physica B: Condensed Matter **306** (1-4), 96-101 (2001).
2.201 A. Berger, Physica B: Condensed Matter **407** (9), 1322-1329 (2012).
2.202 L. G. Onoprienko, G. S. Kandaurova and N. I. Vlasova, Fiz. Met. Metalloved **64** (54) (1987).
2.203 N. I. Vlasova, G. S. Kandaurova and N. N. Shchegoleva, Journal of Magnetism and Magnetic Materials **222**, 138-158 (2000).

CHAPTER 3 SAMPLE FABRICATION AND CHARACTERIZATION METHODS

This chapter describes sample fabrication, measurement procedures, data reduction and analysis methods used in this research. The first section describes the two magnetron sputtering systems used for sample fabrication, the 3M and the AJA, and the method for rate calibration. The following section describes the use of x-ray diffraction (XRD) for this work; specifically, the systems, measurements, and data reduction and analysis methods. The third section describes the magnetometers and magnetometry measurements used. The fourth section describes the use of atomic force microscopy (AFM) and magnetic force microscopy (MFM), and the final section describes electron microscopy.

3.1 Sputter Deposition

All samples investigated in this research were fabricated by magnetron sputtering by one of two deposition systems, named the AJA and the 3M. Low base pressures ranging between 1×10^{-7} and 1×10^{-8} Torr were achieved before deposition and a controlled flow of 5 mTorr Ar served as the working gas. Most films were deposited as repeated Fe/Pt bilayers using 50.8 mm elemental Fe and Pt targets. However, a pseudo-composite target was used for one sample in Chap. 4 and for a series of FePt:Au samples in Chap. 5. The composite target consisted of a Pt target with about 23 flat cylindrical Fe chips placed on its surface, each two mm diameter, 0.8 mm thick chip was held in place by the sputtering gun's magnets. A composition of $Fe_{51}Pt_{49}$[14] was empirically achieved in the composite-target-deposited films by varying the number and positions of the Fe chips as well as the power applied to the DC sputtering gun. Experiments presented in Chapters 5 and 6 employed additional targets of pure elemental (C, Au) or pure oxide (Al_2O_3, SiO_2) materials. All target surfaces were cleaned after exposure to

[14] Film compositions were determined by energy dispersive x-ray spectroscopy (see Sec. 3.5).

atmosphere by sputtering for 15-25 minutes at powers nearly three times rates used during an experiment. Materials were purchased from Kurt J. Lesker Company with purities of 4N or greater, except for Fe targets which were 3N.

Three different types of substrates were used in this work, depending on the desired nature of the film. Thermally oxidized single crystal <100> or <111> Si substrates were used in the studies described in Chap. 4 and Chap. 5. The 1000 Å thick amorphous SiO_2 layer permitted non-epitaxial growth. All films using Si substrates were deposited on 25.4 mm by 25.4 mm squares cut from ~100 mm diameter circular wafers. The research described in Chap. 6 utilized single-crystal (002)-MgO substrates for epitaxial growth of $L1_0$ FePt. The MgO substrates were squares of 100 mm^2. All substrates were cleaned via sonication in an alcohol reagent for ~40 minutes prior to deposition. All substrates were purchased backside-etched.

3.1.1 The 3M sputtering system

The 3M is home-built sputtering system equipped with three sputtering guns. The system uses a cryopump connected to the deposition chamber through a series of two valves: a pneumatically controlled gate valve and a manually controlled butterfly valve. A roughing pump connected in parallel assists initial evacuation of the chamber. The system can achieve a base pressure nearing 1×10^{-7} Torr after ~12 hours of pumping. The Ar working gas flows into the main chamber through a valve separate from the sputtering guns and flow-pressure was determined by the position of the butterfly valve. Since the 3M system has only one chamber, vacuum must be breached between sputtering runs to remove and load samples and to change targets.

The three sputtering guns in the 3M are powered by to two direct-current (DC) and one radio-frequency (RF) power supplies. The guns are aligned vertically to deposit up onto substrates mounted up-side-down about 76.2 mm away on a removable flat aluminum sample-

ring. Throughput is limited by the twelve assigned sample positions on the 356 mm ring. The sample-ring attaches to the underside of a water-cooled turntable that is rotated by a computer-controlled stepper motor. A 381 mm aluminum disc intercedes between the samples and the guns, about 12.7 mm below the substrate-ring. The disc rotates with the substrate ring and permits plasma exposure through a 63 mm by 63 mm square cut-out onto only one sample position. A user-defined recipe written in a QUICKBASIC program determines the sequence and duration of each exposure. Plasmas must be manually sparked prior to deposition and sputtering powers and Ar pressure are manually controlled.

3.1.2 The AJA sputtering system

The second system used in this research was purchased from AJA International and is equipped with four sputtering guns connected to two DC and two RF sources. The sputtering guns point confocally upwards at the substrate at an angle that can be adjusted *in-situ* if necessary. The system consists of a main deposition chamber and a sample load-lock to protect the main chamber from frequent exposure to atmosphere. A magnetically levitated transfer arm moves the four-inch circular sample holders between the two chambers. Turbo pumps backed by roughing pumps evacuate the chambers and the main chamber can achieve better than 5×10^{-8} Torr within an hour.[15] Ar flow-pressure is set and maintained by a computer-controlled gate valve preceding the main chamber's turbo pump.

Substrate holders affix to a "propeller" at an adjustable height along the central axis of the deposition chamber with the substrate surface facing downward. The propeller rotates at about 45 Hz to ensure homogeneous deposition. Two tungsten-halogen bulbs sitting above the propeller can heat the substrate up to about 900 °C. The temperature is measured by a properly

[15] This will take longer if the main chamber was recently opened or the load-lock was not allowed to reach a minimum vacuum of about 1×10^{-7} Torr.

calibrated[16] K-type thermocouple touching a quartz window behind the lamps and the temperature controller can be tuned to achieve efficient heat ramping.

Deposition in the AJA is nearly fully automated with computer control over working gas flow-pressure, gun power, substrate temperature, and the position of pneumatic shutters situated over each gun. Typical parameters for substrate height and gun tilt were 30 mm and 2.5 inches, respectively, as read by dials on the system.

3.1.3 Deposition Rates

Relatively low sputtering rates of a few tenths of an angstrom per second were used for film deposition in this research. Sputtering rates were tuned by varying the sputtering power with fixed 5 mTorr Ar flow pressure. Larger powers were required in the AJA system versus the 3M to achieve similar rates due to the different target-to-substrate distances. Typical deposition powers and corresponding rates are shown in Table 3.1 for the different sputtered materials in the relevant system and with the applicable power supply. In either system, deposition rates were calibrated after any significant change in deposition scheme, e.g. sputtering height, gun angle, target, power supply, etc.

Rate calibration involved characterizing specially deposited single-layer and multilayer films by x-ray reflectivity (XRR). Rates were estimated using the measured film thicknesses determined by XRR (see Sec. 3.2.2.1) and the set deposition times. The details of each calibration film depended on the material being calibrated and were designed to maximize the reflectivity signal. Pt calibration films consisting of single layers in the range of 10 – 20 nm produced high quality total-thicknesses oscillations, or Kiessig fringes, from the smooth interfaces, allowing for rate determination with ~1% precision. Little variation in Pt sputtering rates was found between sputtering sessions for similar deposition parameters. On the other

[16] The offset between the substrate temperature and the temperature read by the thermocouple was determined and accounted for by AJA International within the system settings.

hand, calibrating Fe deposition rates with XRR required multilayer films of repeated Fe/Pt bilayers in order to circumvent the high roughness typically found in sputtered Fe layers. Interceding Pt layers provide smoother interfaces for reflections and the repeated bilayer structure generates low-angle Bragg-like peaks with intensities significantly larger than typical Kiessig patterns. For a given deposition condition a pair of multilayer Fe/Pt films were fabricated to isolate Fe thickness, assuming consistent Pt deposition. Attributing any difference in thickness between a film-pair to changes in Fe thickness alone allowed for straight-forward calculation of the Fe rate. A typical recipe for a pair of Fe calibration films is (Fe 2 nm/Pt 3 nm)$_5$ and (Fe 5 nm/Pt 3 nm)$_5$, where thicknesses are estimated based on previous results. Similar multilayer calibration films using Pt were used to determine deposition rates for the other materials used in this work.

Table 3.1 Typical gun powers and deposition rates for different sputtered materials per system used and power supply type. Sputtering pressure was 5 mTorr.

Target	System	Power Supply	Gun Power (W)	Typical Rate (Å/s)
Fe	3M	DC	8	0.30
Fe	AJA	DC	30	0.35
Pt	3M	RF	19	0.21
Pt	3M	DC	4	0.62
Pt	AJA	RF	113	0.33
Pt	AJA	DC	15	0.37
Al_2O_3	3M	RF	75	0.24
Au	3M	DC	5	0.97
C	3M	DC	70	0.20
SiO_2	AJA	RF	300	0.17

Figure 3.1 shows three typical XRR spectra of single and multilayer calibration films. Total-thickness Kiessig fringes from a single ~20 nm Pt layer are visible beyond 8 ° 2-θ in part (a) of that figure. Both Kiessig and Bragg-like bilayer peaks from Fe/Pt bilayer films of different Fe thicknesses are visible in (b). The fitting software Leptos was used to extract layer thicknesses

from raw reflectivity data. A simulated curve generated by user-input parameters is fitted to the data using a genetic algorithm. The resulting simulation curves are included in the figure.

An error of ~10% remained in the calibrated sputtering rate for Fe, despite the intense super-structure peaks generated by the repeated Fe/Pt bilayers. The large error likely stemmed from a difference in peak periodicity between low and high angle XRR data. Such a discrepancy could be a result of a bilayer-thickness gradient due to poor film formation in the early layers. Interlayer diffusion occurring during deposition could create additional error as a smeared density transitions at the interfaces or the existence of intermetallic phases would obscure an accurate spectra fitting. Run-to-run uncertainties in the as-deposited film structure could arise from the mechanical motions innate to multilayer sputtering in the 3M and AJA systems. Variations in turntable speed in the 3M system and shutter speed in the AJA inevitably change the plasma exposure time in undeterminable ways. For example, the 3M begins counting exposure time only after the turntable has come to a halt. Variations in rotation speed will increases or decreases the exposure time before the table comes to a complete stop. In the AJA, pneumatically controlled shutter speeds vary with the input pressure. Changes in that pressure will be reflected in the exposure time of the plasma.

3.1.4 Post-deposition Processing

A post-deposition thermal process was required after deposition at ambient temperatures in order to achieve the desired phase and film properties. A RTP-600 rapid thermal annealer (RTA) from Modular Process Technology Corp. was utilized for this research. Samples to be annealed were cut in approximately 4.5 mm by 4.5 mm coupons, appropriate for magnetic measurements. Samples were placed on a 100 mm diameter Si wafer which served as the sample holder within the oven. The holder was suspended on three quartz pins pointing radially inward from a 125 mm diameter circular hole cut in a quartz tray. A K-type

thermocouple placed in close contact with the surface of the sample holder monitored the processing temperature. The tray loaded into a short quartz box inside the oven with 27 tungsten-halogen lamps providing the heat source. The system is capable of ramp speeds up to 200 °C/s to temperatures of 800 °C. A gas flow controller allows a forming gas to be used during annealing.

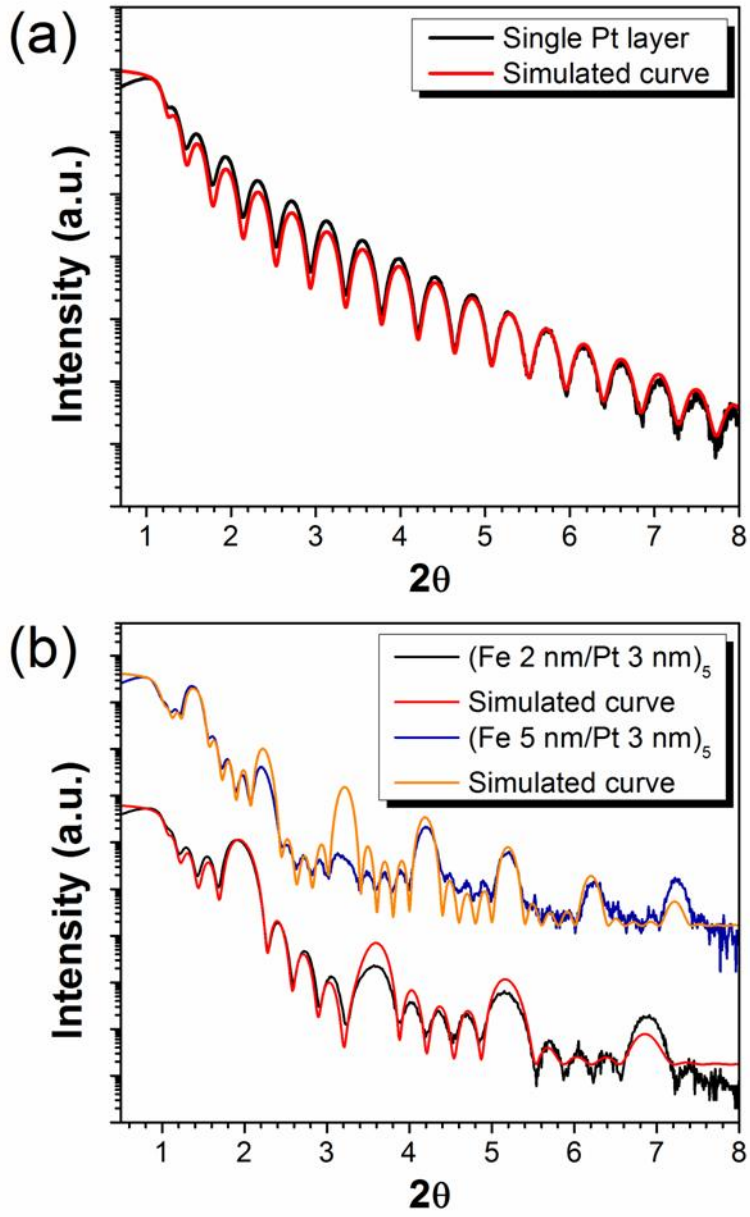

FIG. 3.1. Typical XRR spectra of a single Pt layer (a) and a pair of Fe/Pt bilayers (b).

3.2 X-ray Diffraction

The diffraction of x-rays from materials provides an invaluable method to characterize crystalline thin films. Careful analysis of an x-ray diffraction (XRD) spectrum can reveal information regarding chemical order, phase fraction, crystallographic texture, grain size, and strain in a thin film sample. Total and internal layer thicknesses and roughnesses can be examined by employing a low angle of incidence in x-ray reflectivity (XRR). In general, peak positions characterize lattice spacings and relative peak intensities reflect the atomic species occupying the lattice. Macro- and microstrains alter peak position and breadth, respectively.

Bragg's law of diffraction, $\lambda = 2d \sin\theta$, defines the angle θ at which a structure with repeated scattering sites spaced by *d* produce constructive interference when illuminated by a coherent beam of radiation of wavelength λ. The generated maxima correspond to diffraction peaks measured at the angle 2θ, as shown in Fig. 3.2. Using x-rays with wavelengths ~1.5 Å is therefore useful for characterizing crystalline thin films. Depending on the investigated material and the geometry of the XRD experiment, multiple diffraction peaks are typically produced within a measureable range of θ. Proper instrumental corrections and careful structural modeling can translate peak positions into characteristic lattice parameters with a precision of better than 0.001%.

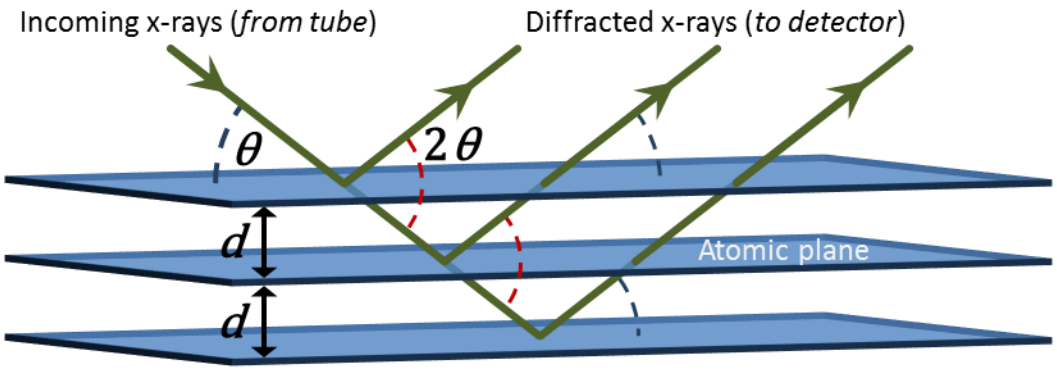

FIG. 3.2. Schematic of Bragg's law of diffraction. X-rays of wavelength λ impinge at an angle θ and diffract at 2-θ from crystal lattices with vertical spacing d.

The location of scattering sites in a unit cell determines diffracted peak positions through Bragg's law, whereas peak intensities are determined by each site's electron density and structural symmetry. Finite crystallite size or small distributions in the lattice spacing broaden observed peaks shapes from ideal delta-function spikes. A symmetric arrangement of identical atoms in a unit cell can lead to the extinction of certain diffraction peaks. These features complicate XRD spectrum analysis while at the same time providing useful information about a well modeled system. Of experimental interest are the integrated intensities, as expressed by [3.1],

$$I = K|Fe^{-M}|^2 p[LP]. \tag{3.1}$$

The structure factor F depends on the combined effect of each diffraction site within the crystal and is explained below. K contains various angular independent factors. The Debye-Waller factor, M, varies with the type of atom responsible for scattering at each site. Also known as the temperature factor, M corrects for thermal lattice vibrations on the diffraction peak intensities. The multiplicity factor, p, accounts for contributions from multiple lattice planes representing the same *d*-spacing due to symmetry. The final term, the Lorentz-Polarization (LP), denotes the geometric and instrumental contributions to integrated diffracted intensities which, among other things, depends on the orientations of the grains within a sample. Accurate quantification of a measured spectrum must account for these factors. Typical XRD analysis examines integrated intensity ratios such that the constant term K cancels, leaving the angular-dependent terms F, M, LP and p.

The structure-factor dependence of the diffracted intensity reflects contributions from all scattering sites within a unit cell and is a consequence of the wave-like nature of x-rays. The general expression for its contribution to the (*hkl*) diffraction line,

$$F_{hkl} = \sum f_n e^{2\pi i(hu_n + kv_n + lw_n)}, \tag{3.2}$$

is a summation over the all atomic scattering factors, f_n within the unit cell. Each f_n describes the amplitude and phase of the diffracted x-rays due to interactions with the n^{th} localized electron cloud located at the fractional coordinates (*u*, *v*, *w*) within the cell. Atomic scattering factors,

$$f = [f_0(\sin\theta/\lambda) + \Delta f' + \Delta f'']e^{-M}, \tag{3.3}$$

contain the uncorrected atomic scattering factor f_0 and the real and imaginary parts of anomalous dispersion *Δf'* and *Δf''*, respectively. For convenience, the element-specific Debye temperature factor *M* is included within *f*.

As the sum of all the atomic factors, the structure factor depends on the type and location of the different atoms within a crystal. The resulting chemical sensitivity of x-ray intensities enables the determination of relative atomic arrangements within a multi-element crystal. Complete destructive interference of diffracted x-rays in a direction otherwise satisfying Bragg's law occurs for certain crystal symmetries with homogeneous atomic compositions (real or statistical). Extinction of a diffraction line from a set of lattice planes occurs when an interceding plane exists at exactly one-half of the lattice spacing and consists of scattering sites with identical atomic scatting factors. This phenomenon relates to a system's Bravais lattice structure. Polymorphic systems, where transformations occur by small shifts in neighboring atomic assignments within the unit cell, can lead to a change in Bravais-lattice type. Previously extinct peaks which become visible due to such a transformation are designated superstructure peaks while those shared by both phases are called fundamental peaks [3.2]. Analysis of superstructure-to-fundamental peak intensity ratios reveals information regarding atomic site occupancy and thereby the degree of chemical order present within a crystalline specimen.

This subsection outlines the diffractometers, measurement procedures, and data analysis methods utilized in this dissertation.

3.2.1 Diffractometers

The two x-ray diffractometers used for structural characterization in this dissertation are described in the following. Each system is named after their manufacturer, Rigaku and Bruker.

3.2.1.1 The Rigaku Diffractometer

A Rigaku D/Max-B (Rigaku) is one of two diffractometers used for in this dissertation. The Rigaku uses Cu-Kα radiation (λ=1.542 Å) at 40 kV and 30 A, a 185 mm diffraction radius, 1 mm scattering and detector slits, and a curved graphite crystal monochrometer aligned at 13.27 degrees θ located on the detector arm. The angular divergence of the beam is about 0.0174 radians. Samples are affixed with silicon grease onto a quartz glass window inset in a rectangular aluminum plate. The bottom half of the plate is held firmly by metal clips at the center of the diffractometer circle. The quartz glass behind and around the sample gives only a small amorphous background signal.

The Rigaku scans in the Bragg-Brentano geometry and allows for coupled θ-2θ and decoupled ω-2θ scans. Locked-coupled scans sweep the detector through an angle of 2θ as the sample moves by θ. The angular relationship is fixed by alignment of the optics and is confirmed before every measurement. In decoupled ω-2θ rocking curves, the detector is fixed at the 2θ angle for the peak of interest and ω, the angle of the sample, is varied around the θ value of that peak.

3.2.1.2 The Bruker Diffractometer

The second diffractometer used for XRD measurements is a Bruker-AXS D8 Discover (Bruker). The Bruker also uses Cu-Kα radiation but operates at 40 kV and 40 A. The diffraction radius and slit configuration can be varied for different experimental setups. XRR scans use a radius of 185 mm whereas for high-angle measurements that is extended to 250 mm. The Bruker employs a Göbel mirror to direct a beam of parallel x-rays from the tube to the exit slit

with a divergence of only 0.03 degrees. Samples mount onto a vacuum chuck in the center of a 1/4-Circle Eulerian cradle which allows six degrees of freedom for moving the sample.

The Bruker operates in the parallel beam geometry and can perform the same types of scans as the Rigaku. The cradle permits better sample alignment than the Rigaku, for example alignment of the sample surface (*z* direction). The Bruker offers additional options, such as a snout and knife-edge attachments reduced the beam spot size and spread in the scattering direction, respectively. The two options mentioned were only employed for samples larger than about 10 mm.

3.2.2 X-ray Measurements

Three types of XRD measurements were utilized throughout this work: low-angle XRR, rocking curve, and high-angle XRD. The following subsections describe each type and how they are analyzed.

3.2.2.1 X-Ray Reflectivity Measurements

Probing a thin-film sample with specular x-rays in a small range just above the critical angle for total external reflection reveals the perpendicular distances between diffracting interfaces within the film. Interference between reflections from the film-free and the film-substrate interfaces generates intensity variations known as Kiessig fringes. The position, θ_m, of the m^{th} order peak of the Kiessig fringes relates to a film's critical angle, $\langle\theta_c\rangle$ and total thickness, T, by,

$$2T\sqrt{\sin^2\theta_m - \sin^2\langle\theta_c\rangle} = m\lambda\,. \tag{3.4}$$

A film consisting of repeated internal interfaces with equal spacing such as those between repeating bilayers of materials with different electron densities also produce a series of low-angle, Bragg-like peaks. These occur with much higher intensity but shorter frequency than

Kiessig fringes. The bilayer thickness, $B = T/N$, for a film with N bilayers can be determined from,

$$2\left(\frac{T}{N}\right)\sqrt{\sin^2\theta_m - \sin^2\langle\theta_c\rangle} = m\lambda\,. \tag{3.5}$$

Subtracting either of these two equations for neighboring peaks (i.e. m and $m+1$) removes the dependence on m. Using either of these two diffraction phenomenon can reveal useful information regarding thin film and bilayer thicknesses. A gradient in bilayer thickness or a material's electron density can create deviations from perfect periodicity of the peaks. Surface and interface roughnesses dampen the intensities. A comparison of diffuse and coherent scattering along with careful modeling of the system can quantify the roughness of a film's interfaces.

XRR measurements were used to calibrate deposition rates by analyzing the period of oscillations of either Kiessig fringes or low-angle Bragg peaks to determine layer thicknesses of specially designed calibration films (see Sec. 3.1.3). Figure 3.1 shows three examples of typical XRR spectra. Standard XRR measurements ran from 1-8 degrees 2-θ. Low-angle specular rocking curves were performed before each measurement to align the beam with the film surface and necessary offsets were applied to theta. No further sample alignment was possible with the Rigaku system. The Eulerian cradle of the Bruker system allowed for further alignment, in particular for *z* and χ.

3.2.2.2 Rocking Curves

Rocking curves measure the dispersion of a particular lattice direction from the film normal, i.e. the quality of a crystalline texture present in the film. Measurements of a rocking curve use a ω-2θ scan with the detector aligned to the Bragg angle of the peak in question, $2\theta_{\text{peak}}$, while the angle of the sample stage, ω, scans from (θ_{peak} - 6°) to ($\theta_{\text{peak}} + 6°$). The resulting curve is then fit with a Gaussian profile. The full-width at half-maximum, $\Delta\omega_{\text{FWHM}}$,

describes the angular dispersion of that particular crystalline axis within the grains of the sample.

3.2.2.3 High-angle XRD Measurements

Wide-angle XRD scans used in this work typically cover 20-54 degrees 2-θ to characterize phase and crystalline texture in the FePt thin films and nanostructures. Table 3.2 lists the characteristic peaks of interest for Fe-Pt alloys within this range. Correct peak identification reveals the phases present and peak shape contains information on the grain structure. Examining integrated intensity ratios between different diffraction peaks can quantify the degree of (001) texture via the Lotgering orientation factor (LOF) [3.3] and $L1_0$ order (S). High-angle diffraction spectra were fit using a series of Pseudo-Voigt peak functions to discern accurate peak positions, peak widths, and integrated intensities. The next subsection describes the procedures used to reduce XRD data and calculate grain sizes, LOF and S throughout this dissertation.

Table 3.2 XRD peaks for pertinent phases of Fe-Pt alloy and substrates used in this work.

Material (phase)	Peak Designations					Reference
	(001)	(110)	(111)	(200)	(002)	
FePt ($L1_0$)	24.039	32.9708	41.2177	47.3204	49.2262	[3.4]
FePt (fcc)	⋯	⋯	40.92	47.61	⋯	[3.5]
$FePt_3$ ($L1_2$)	22.9977	32.7497	40.3979	46.9933	⋯	[3.6]
Fe_3Pt ($L1_2$)	23.63	33.6637	41.543	48.3476	⋯	[3.7]
Substrate type	(111)		(200)	(004)		Reference
Si	28.4431		⋯	69.2365		[3.8]
MgO	⋯		42.9081	⋯		[3.9]

3.2.3 XRD Spectrum Fitting

Typical peak profiles in an XRD spectrum can be well modeled by Pseudo-Voigt (PV) functions [3.10]. A PV function of the form,

$$I = A\left[\mu\frac{2w}{\pi(4(\theta-\theta_c)^2+w^2)} + (1-\mu)\frac{\sqrt{4\ln 2}}{w\sqrt{\pi}}e^{-\frac{4\ln 2}{w^2}(\theta-\theta_c)^2}\right], \quad (3.6)$$

is used in this dissertation for fitting experimental data. The terms in Eq. (3.6), A, w, μ, and θ_c, correspond to the area, width, shape weighting factor, and position of the peak, respectively. The shape weighting factor μ balances the peak profile between that of a Lorentzian and a Gaussian shape.

Reduced spectra were fitted with pseudo-voigt peak functions of the form in Eq. (3.6) near five position of 2-theta applicable to $L1_0$ FePt: (001) – 23.8°, (110) – 32.5°, (111) – 40.5°, (200) – 47.5°, and (002) – 48.5°. Integrated intensity, peak position, and peak width along with the respective errors were extracted from the fitting results. A background signal proportional to $1/\theta^4$ corrected for air-scatter and incoherent diffraction, and both single-crystal and an amorphous substrate peaks were included as necessary. The non-linear fitting was performed with the Origin software using the Levenberg-Marquardt fitting routine. Appropriate limits were placed on the parameters to ensure convergence with $R^2 > 0.85$ in the worst cases, but typically > 0.95.

3.2.3.1 XRD Data Reduction

Raw x-ray data underwent system-specific corrections for absorption, sample-size and Lorentz-polarization before performing a fitting routine. In films thicker than ~1000 nm (depending on absorption factors), the angular dependence of the absorption reduces to a constant. This behavior is due to the ratio of sample surface exposure area to penetration depth; large exposure areas and small penetration depths at low angles balance with smaller exposure areas yet deeper penetration at high angles. When the film thickness can no longer be treated as infinite, this balance no longer occurs and an angular dependent absorption of the form,

$$A = (1 - e^{-2\mu t/\sin\theta})^{-1}\,, \tag{3.7}$$

multiplies the measured intensities. In Eq. (3.7), t is the sample thickness and μ is the equal to the product of density and mass absorption for a sample material. Additionally, if the sample length intersecting the diffraction plane (l) is smaller than the length of the X-spot (l'), then the additional scaling factor

$$A' = \frac{R\alpha}{l \sin\theta}, \tag{3.8}$$

must be included, where R is the radius of the diffractometer and α is the divergence slit angle. Aside from a few samples used for thickness calibration, all films characterized by XRD in this study are less than ~50 nm thick; typical nominal thicknesses are around 10 nm. Therefore, the data from each sample was corrected for x-ray absorption by multiplying the raw data by Eq. (3.7). The values for μ vary based on estimated Fe:Pt stoichiometry (Fe at.% of x) given by,

$$\mu = x(MAC_{Fe} * \rho_{Fe}) + (1 - x)(MAC_{Pt} * \rho_{Pt}). \tag{3.9}$$

For simplification, the value for *x* was chosen to be 0.5. Estimated corrections to the absorption factor could be applied after fitting, when necessary. Densities and MACs were taken from Ref. 3.1: $\rho_{\mathrm{Fe}} = 7.87$ g cm^{-3}; $\rho_{\mathrm{Pt}} = 21.4$ g cm^{-3}; $MAC_{\mathrm{Fe}} = 324$ cm g^{-1}; $MAC_{\mathrm{Pt}} = 205$ cm g^{-1}.

All samples were approximately 5 mm by 5 mm or slightly smaller. Considering the diffraction slit on the Rigaku system, α = 0.0174 radians, samples measured on that system were completely encompassed by the beam at all measured angles and the sample-size correction given by Eq. (3.8) was applied to all Rigaku data. The Bruker's optics made for a different situation. Due to the highly collimated x-rays from the Göbel mirror, the MES width (1 mm) and angle of incidence define the illuminated sample length on the Bruker as,

$$l' = \frac{w_{MES}}{\sin\theta}, \tag{3.10}$$

which is less than 5 mm for angles greater than 23 degrees 2θ. Therefore, no correction for sample size was necessary for data taken on the Bruker.

As the name suggests, the Lorentz-polarization factor contains two terms. The polarization portion (*P*) corrects for the interaction of unpolarized incident x-ray beam with the planar distribution of electrons at the scattering sites. The angular dependence of the term comes from Thomson's equation for such events,

$$P = 1 + cos^2(2\theta_{\mathrm{M}})\cos^2(2\theta)\,, \tag{3.11}$$

where θ_{M} is the characteristic angle of the monochrometer, if used. A derivation for this term can be found in Ref. [3.1].

The Lorentz term corrects for the trigonometric relationships between the diffraction angle and the spatial extent of the x-ray beam, crystallite orientation, and time spent satisfying the diffraction condition, $\theta = \theta_{\mathrm{B}}$. Due to its dependence on the diffraction crystal's orientations, the Lorentz factor presents a source of inaccuracy for samples with unknown degrees of crystalline texture. The general Lorentz factor (L) has the form,

$$L = \frac{1}{\sin 2\theta}\Psi(\theta)\,. \tag{3.12}$$

The $\sin^{-1}(2\theta)$ term accounts for the scanning-angle dependence of the diffracting volume and the Ψterm accounts for variations in crystallite orientations. In determining Ψ, one of two extreme cases is typically assumed: a powder sample with complete random orientation or a single-crystal sample with perfect alignment. In the case of the former,

$$\Psi = \frac{\cos\theta}{\sin 2\theta}\,. \tag{3.13}$$

For the latter, Ψ becomes constant. Since intensity ratios are used for the calculating the parameters of interest in this dissertation, the value of Ψ for the single-crystal case can be dropped. The true Lorentz correction for a thin film consisting of grains with various degrees of texture lies between the two extreme corrections [3.11]. Using an incorrect texture dependent factor to analyze sample trends where texture varies will inevitably lead to improper results. A

reasonable solution implemented in this work to mitigate the above problem is described at the end of Section 3.2.3.4.

All raw XRD spectra (I_{raw}) were subject to corrections for absorption, sample size and LP before fitting, i.e. $I_{corrected} = I_{raw}A(A')/LP$. A' was included only when necessary, as described above, and initially the single-crystal version of L was used. The fitting routine was performed on the corrected spectrum, $I_{corrected}$.

3.2.3.2 Determining Grain Size

Diffraction peak width (w) relates to the average vertical dimension[17] t of the crystallite responsible for that peak through the Scherrer equation [3.1],

$$t = \frac{0.9\lambda}{w\sqrt{\ln 4}\cos\theta_B}. \tag{3.14}$$

Care must be taken when applying Eq. (3.14) to thin films where microstrains can broaden peak widths. Nevertheless, the Scherrer equation provides a useful estimate of grain size from an XRD spectrum.

Extended lateral coherence of a diffraction plane in a crystalline thin film can lead to the appearance of satellite peaks surrounding that plane's main peak. These Kiessig-fringe-like oscillations occur for thin films consisting of smooth, flat, single-crystal grains of equal height with a high degree of mutual texture [3.12]. Fitting the intensity profile with a Laue function allows for extraction of the coherent domain thickness, or grain height, t. An alternative and simpler method examines the separation between the satellite peaks, $\Delta\theta$, to determine the number of diffracting planes, n. Together with the lattice parameter of the corresponding Bragg peak, d_{hkl}, as the thickness the stacking units, the expression,

$$\Delta\theta \approx \frac{\lambda}{2nd_{hkl}}, \tag{3.15}$$

[17] The vertical direction is parallel to the scattering vector and perpendicular to the lattice plane.

yields a total vertical dimension of the coherently diffracting grains of $t = N^{*}d_{hkl}$.

3.2.3.3 Determining Texture

The orientation and degree of c-axis texture of $L1_0$ phase FePt relates directly to the direction and degree of magnetic easy-axis alignment for a particular sample. Crystal texture can be quantified with x-ray diffraction by a number of different techniques. Collecting spectra with a two-dimensional detector allows for the creation of pole figures, from which a sample's texture coefficients can be determined. Such a technique, however, is tedious and requires significant effort to quantify even a single sample. A ω-2θ rocking curve of a particular diffraction peak determines the dispersion of the represented crystal-axis' texture with respect to the scattering vector (as described in Section 3.2.2.2). Alternatively, a semi-quantitative measure of texture, the Lotgering orientation factor (LOF), can be calculated from the same symmetric Bragg-Brentano geometry used in wide-angle θ-2θ scans. For simplicity and comparisons within sample sets, this study utilizes the latter two techniques.

The semi-quantitative Lotgering orientation factor is ascertained by comparing an experimental diffraction pattern with that of a powder sample [3.3]. An x-ray diffractometer equipped with a point detector in the symmetric Bragg-Brentano or Parallel Beam geometry probes lattice spacings perpendicular to the scattering vector. Any deviation in the measured relative peak intensities with respect to those of an isotropic powder pattern indicates the presence of preferential crystalline texture either along or away from the film normal. The ratio of summed integrated intensities from peaks representing the desired alignment to the sum of all peaks present within a given 2θ range, σ, is compared with the same for a randomly oriented powder sample, σ_0. The orientation factor is given by,

$$LOF = \frac{\sigma - \sigma_0}{1 - \sigma_0}, \tag{3.16}$$

and ranges from any negative number to positive one. A value of one represents perfect orientation of the investigated texture, zero represents no preferential, i.e. random orientation, and a negative value indicates preferential orientation other than the investigated direction.

This dissertation focuses on FePt thin films and nanostructures with texture of the [001]-axis perpendicular to the film plane. The wide-angle XRD measurement range of 20-56 2θ used in this study covers the (001), (110), (111), (200) and (002) diffraction peaks of $L1_0$ FePt. Therefore, the integrated intensity ratio for (00*l*) texture, σ_{00l}, becomes,

$$\sigma_{00l} = \frac{\sum I_{00l}}{\sum I_{hkl}} = \frac{I_{001} + I_{002}}{I_{001} + I_{110} + I_{111} + I_{200} + I_{002}}. \tag{3.17}$$

Using the integrated intensities for fully ordered $L1_0$-phase FePt powder from Ref. 3.4, σ_0 becomes ~0.227. This value for σ_0 represents a 1:1, fully ordered sample. A more accurate characterization by LOF would include the effect of variations in stoichiometry and order on integrated intensities.

The relationship between LOF and $\Delta\omega_{FWHM}$ for a particular crystal texture is nonlinear and the dispersion of the textured-axis becomes quite small once LOF is greater than ~0.9.

3.2.3.4 Determining Chemical Order of $L1_0$ FePt

In the chemically disordered phase of FePt, Fe and Pt atoms occupy each site on the fcc lattice with equal probability. The fcc Bravais lattice forbids reflections from the {001} and {110} planes. In the ordered $L1_0$ phase, Fe and Pt atoms sit in specific locations to form a monatomic layered structure (see Fig. 2.8). The chemically anisotropic structure has a tetragonal Bravais lattice which allows one third of the previously forbidden diffraction planes to participate in the resulting XRD pattern. Table 3.1 lists characteristic peaks for the disordered and ordered FePt phases. Due to the significant tetragonal distortion of the *c*-axis, the fcc (200) peak splits into

two separate (002) and (200) peaks upon ordering. For the same reason, the fcc (111) peak shifts to a slightly higher angle. Even though the peak splitting and shifting are due to the ordering process, the (111), (200) and (002) peaks are still considered fundamental peaks. Within the standard experimental range used for this work (20 – 54° 2θ), the appearance of the (001) and (110) peaks along with the splitting of the (200)/(002) peak serve to fingerprint samples in the chemically ordered $L1_0$ phase.

Experimental determination of S by diffraction techniques follows one of two methods. The first method examines the tetragonal distortion of the crystal lattice, c/a. Fully ordered FePt with alternating atomic planes of Fe and Pt has a characteristic c/a ratio (~0.964). Partial disorder leads to antisite occupancy and results in distortions different than that of a perfectly ordered structure [3.13]. An expression for S(c/a) is,

$$S(c/a) = \sqrt{\frac{1 - {}^{c}/_{a}}{1 - ({}^{c}/_{a})_{\mathrm{F}}}} \tag{3.18}$$

where $(c/a)_{\mathrm{F}}$ represents the lattice ratio for a fully ordered sample. Despite the high accuracy in determining lattice parameters, the tetragonality ratio method tends to exaggerate error due to the involvement of small number ratios. Values for S determined by this method actually have no direct relation to Eq. (2.41) since the c/a ratio only infers relative atomic locations. Additionally, macrostrains (and defects) common in thin films tend to skew lattice spacings [3.14]. On the other hand, peak positions are generally easier to extract from diffraction data.

The second method for calculating the degree of chemical order involves the ratio of superstructure (s) and fundamental (f) peak intensities. For binary intermetallics such as FePt, the structure factors for superstructure and fundamental peaks are defined differently [3.1,3.2],

$$\begin{aligned} F_{\mathrm{f}} &= 4(x_{\mathrm{Fe}} f_{\mathrm{Fe}} + x_{\mathrm{Pt}} f_{\mathrm{Pt}}), \\ F_{\mathrm{s}} &= 2S(f_{\mathrm{Pt}} - f_{\mathrm{Fe}}). \end{aligned} \tag{3.19}$$

Both structure factors depend on the individual atomic scattering factors, $f_{Fe/Pt}$. Fundamental peak intensities depend on the atomic composition, $x_{Fe/Pt}$, while F_S explicitly contains the order parameter, S. Solving the intensity ratios using Eq. (3.1) and (3.19) for S, with $x_{Fe/Pt}$ = 0.5, gives,

$$S(I_r) = \sqrt{\frac{I_s|f_{Fe} + f_{Pt}|^2 p_f}{I_f|f_{Pt} - f_{Fe}|^2 p_s}} \quad . \tag{3.20}$$

Values for $I_{s/f}$ were extracted from the PV peak fits of the (001) superstructure and (002) fundamental peaks (after data reduction described above). The values used for calculating $F_{f/s}$ [see Eq. (3.3)] and $p_{f/s}$ are given in Table 3.3.

Table 3.3 Multiplicity and atomic scattering factors for XRD fitting [3.15].

			Fe				Pt			
	2θ	p	f_0	$\Delta f'$	$\Delta f''$	M	f_0	$\Delta f'$	$\Delta f''$	M
(001)	24.039	2	22.4	-1.1	3.2	0.0062	71.5	-4.6	6.9	0.0061
(002)	49.226	2	17.39	-1.1	3.2	0.025	60.8	-4.6	6.9	0.024

Achieving a high degree of accuracy in S using integrated intensities requires a proper fitting routine with instrumental corrections. Strain-related effects tend to be less significant for integrated intensities than for lattice parameters. The parameter S(I_r) is employed throughout this dissertation to avoid such complications. Additionally, the lack of non-(00*l*) peaks in the θ-2θ scans of highly textured samples precludes the determination of the *a*-lattice parameter. Peaks representing *a*-lattice planes are used when possible to determine S(*a*/*c*). However, the diminutive size and breadth of those peaks can result in significant error.

As mentioned in Section 3.2.3.1, ascertaining an accurate value for S requires the use of the appropriate Lorentz factor based on a sample's texture. A common treatment for highly textured thin films is to use the single-crystal form of the Lorentz factor [3.16-3.18]. This procedure was followed for the work in this dissertation to ascertain an initial value for chemical order, S', and the LOF for (001) texture. From the determined LOF, a scaling factor (C) is

calculated and applied S' to compute a more accurate value for chemical order, S. The scaling factor simply extrapolates linearly between the two extreme cases based on the LOF of that sample,

$$C = \frac{S_{\mathrm{p}} - LOF\left(S_{\mathrm{p}} - S_{\mathrm{sc}}\right)}{S_{\mathrm{sc}}}. \tag{3.21}$$

The terms S_{sc} and S_p are the square-roots of the ratios of Lorentz corrections at 2θ of 24° and 49.1° for the single-crystal and powder forms, respectively. Therefore, $C = (0.481 + 0.2LOF)/0.681$. The ratios, for both the Rigaku and the Bruker systems, vary by only a few percent within +/- 1° of the listed 2θ values. Investigation to determine a more accurate Lorentz correction with a sound physical basis could be an interesting future project.

3.3 Magnetometry

This research utilized two Quantum Design magnetic property measurement system super-conducting quantum interference device (MPMS SQUID) magnetometers and a Micromag Model 2900 alternating gradient force magnetometer (AGFM) from Princeton Measurements Corporation. One SQUID is an XL model whereas the other is an earlier, upgraded model; however, both systems share many of the same features and produce data of equal quality for the purposes of the work presented here.[18] The AGFM was used predominately for samples with low coercivities or when the SQUID magnetometers were unavailable. Details of these systems' operation and a few measurement techniques used in this work are outlined in the following.

3.3.1 Alternating Gradient Force Magnetometer

An AGFM offers a relatively quick and reasonably sensitive means for measuring the magnetic response of a sample to an applied field. The system is essentially comprised of three parts: a large DC electro-magnet generates the applied magnetic field; a smaller AC electro-

[18] Measurements performed on either QD-MPMS system will be referred to as SQUID measurements and any description of a SQUID magnetometer refers equally to both systems.

magnet and asymmetric pole-heads creates the small superimposed alternating gradient field; and a piezoelectric cantilever detects the physical displacement a sample. The magnetic sample affixes to the free end of the cantilever and hangs in the center of the applied field. The alternating polarity of the gradient field drives the sample into vibration and the measured vibration of the sample is translated into a magnetic moment through the relationship between the sample's mass, applied-force (from its dipole moment within the applied field), and vibrational frequency. As a mechanically vibrating system, optimal performance, i.e. highest signal gain, occurs at the resonant frequency of the sample. The sensitivity of an AGFM is determined by the sample's moment-to-mass ratio due to the mass dependence of the mechanical gain and the moment dependence of the applied force. Tuning to resonance before taking a measurement is necessary to determine the unique frequency of each sample. All AGFM measurements were performed at room temperature.

The system used in this study employs a water cooled electro-magnet capable of generating a maximum applied field of 13.5 kOe. Before each measurement the sample-holder of the AGFM probe (the detachable cantilever plus piezoelectric) was cleaned gently by sonication in an alcohol reagent to remove potential magnetic contaminants. Separate probes were used for measurements with the field oriented perpendicular and parallel to the film plane. Samples were mounted on the flat end of the cantilever using a minimal amount of Si grease to ensure sufficient temporary adhesion. The moment of the AGFM was calibrated with a 405 μemu Ni foil and the piezoelectric probe was tuned to determine each sample's unique resonant frequency before every scan. A typical ~10 nm thick FePt sample, on a 4 mm by 4 mm, ~525 μm thick substrate generates a moment of about 100 μemu with an operating sensitivity of about 3 μemu using a field-gradient of 4 Oe per millimeter.

Measuring the M(*H*) of samples whose saturation field is higher than the 13.5 kOe maximum field of the AGFM results in minor hysteresis loops. Coercivities determined from minor loops will always be smaller than the sample's true coercivity and it is not possible to determine the saturation magnetization. The software used to run the Model 2900 allows for the option to correct the measured data for diamagnetic contributions by assuming saturation of the ferromagnetic signal above a certain percent of the maximum applied field. A minor loop corrected in this manner might appear saturated and care must be taken when interpreting the results. When a sample's moment is too small to tune the probe even under the maximum applied field, the resulting data will not be reliable. This can occur when measuring along the hard axis of a highly anisotropic thin film.

3.3.2 Superconducting Quantum Interference Device Magnetometer

SQUID magnetometers equipped with superconducting field coils and the namesake SQUID-based sensing circuitry are popular measurement tools for accurately characterizing magnetic samples with high saturation fields and/or small moments. SQUID magnetometers have numerous advantages over typical AGFMs, such as higher maximum applied fields, higher sensitivity (theoretically 1 nemu, yet typically ~100 nemu in practice), and a wide range of operating temperatures without requiring additional hardware. The relatively slow field-set time for superconducting magnets and the need to wait for a tolerable level of field stability before taking a measurement makes SQUID systems significantly slower than electro-magnet based AGFMs. However, such a trade-off is necessary when studying nanometer scale films of hard magnetic material.

The SQUID magnetometers used in this work employ superconducting coils to generate applied fields up to 70 kOe. The field magnitude is determined from the voltage reading across a shunt resister in parallel to the field coils and a predetermined calibration factor. One concern

with that method is the effect of magnetic flux trapped within the superconducting coils on the net field; field offset of a few tens of Oe can be expected depending on the history of the magnet. An additional effect from superconducting magnets is the lack of field homogeneity immediately following a large change in current. An inhomogeneous field applied to a sample can yield unpredictably spurious results. A few to tens of seconds are required to allow the field to relax before performing a measurement, depending on the field jump and approach mode.

Applied fields can be set using three different modes, hysteresis, no-overshoot, and oscillate, each with trade-offs in set-rate, field accuracy, and liquid-He consumption. In the so-called hysteresis approach mode, the power supply constantly drives a current into the superconducting coils to approximately set the field to within 3% of the desired value. The field is ramped directly from the previous state. The resistive persistent switch connecting the power supply to the magnet remains closed during hysteresis mode, even during measurement, and the heat generated in maintain that state boils more a relatively large amount of liquid-He. The constant coupling with the power supply also reduces the signal-to-noise ratio. No-overshoot mode turns off the persistent switch only while driving the current unidirectionally to achieve consecutive field steps of 70% of the difference between the current and target field values. Once the field is close enough to the set point the switch is turned on and the magnet coils runs in a superconducting state again for the measurement. Helium consumption is significantly less in this mode and the field values are set with high accuracy, albeit slowly. Oscillate mode drives current into the magnet past the set point by about 30% of the field change and then proceeds to oscillate around the set point with an amplitude decaying by 30% each cycle. When the field is within 80 Oe of the target the field is directly set and the magnet is returned to a superconducting state. Oscillating the field relaxes the superconducting magnet to allow faster measurements after large field jumps; however, it is undesirable when precise control over a

samples field exposure is required. No-overshoot and hysteresis mode were predominantly used for measurements in this research, depending on the available measurement time and required sensitivity.

The high sensitivity of these magnetometers stem from the SQUID circuit coupled to the pickup coils around the sample chamber. The pickup coils are wound in a second-order gradiometer configuration to reject constant flux, meaning that the only signal detected is due to flux changes as the sample is moved through the pickup assembly. The reciprocating sample option of the Quantum Design MPMS moves the sample through the pickup coils on a sinusoidal path of vertical position versus measurement time. Before each measurement the sample is centered in the middle of the pickup coils and the fit of the signal versus position with an expected response from an ideal dipole determines the magnetic moment. The amplitude and frequency of the sample oscillations are variable parameters, as are the number of repetitions to be averaged in generating the data. Typical measurement parameters used in this work repeated a 4 cm, 1.0 Hz scan four times for averaging in the digital signal processor, and then averaged 4 of those data points within the Multiview software to determine measurement statistics.

Sample coupons of about 4.5 mm by 4.5 mm were cut for SQUID measurements due to the limited diameter of the sample chamber. The thin film samples could be mounted with the film surface parallel or perpendicular to the applied field. Samples were friction mounted into clear plastic straws[19] such that the corners or edges just touched the straw's inner surface, for perpendicular or parallel orientations, respectively. In cases where the sample was larger than the ideal size the corners would puncture the straw and generate an additional, albeit relatively small, signal. When a sample was cut too small, additional straws were cut vertically, rolled

[19] The straws were ordered from Quantum Design and were guaranteed to contain minimal magnetic contaminants.

slightly, and inserted into the main straw to reduce its inner diameter. This process was repeated until the sample could be affixed firmly within the holder. The use of additional straws seemed to partially mask the sample's signal and any uneven cuts along the inner-straws could generate a signal. Except for a few series of measurements in Chap. 6, all measurements were performed at room temperature.

3.3.3 Magnetometry Data Reduction

Even though the diamagnetic responses of Si, SiO_2 and MgO are relatively small, on the order of 1 $\times 10^{-6}$ cm^3/g, the miniscule sample-to-substrate ratios of the thin films investigated in this work lead to significant diamagnetic signals in the raw magnetometry data. Therefore, it was imperative to isolate the film signal from that of any addendum. To that end, the mass of each sample was measured with a precision of 0.00001 g to calculate a substrate and orientation specific correction. Mass-normalized corrections were subtracted from the raw data as a diamagnetic susceptibility.

Appropriate correction factors were experimentally determined from the diamagnetic signals of blank MgO and thermally oxidized Si substrates measured individually in the SQUID along both in- and out-of-plane directions. A 0.02632 g MgO substrate yielded signals of -3.8698 $\times 10^{-7}$ and 3.6918 $\times 10^{-7}$ cm^3/g perpendicular and parallel to the sample plane, respectively. A 0.02148 g Si substrate gave susceptibilities of -1.3321 $\times 10^{-7}$ and -1.2272 $\times 10^{-7}$ cm^3/g from perpendicular and parallel measurements, respectively. Anisotropic susceptibilities from thin slabs are expected due to the difference in spatial extent of the sample within the gradiometer pick-up coils for the two orientations [3.19]. The 8% difference for the Si substrate is about twice as large as the 3-5% predicted anisotropy from numerical calculations, whereas the 4.6% difference for MgO falls within the expected range. Even with geometric considerations, the measured susceptibilities differ significantly than quoted values for Si (-1.1181 $\times 10^{-7}$ cm^3/g) and

MgO (-2.5308 $\times 10^{-7}$ cm^3/g), where the 1000 Å layer of SiO_2 is accounted for as a 0.1% contribution to the former. Discrepancies between measured and reported values could be due to sample mounting, i.e. deformations of the straw or poor centering, errors in mass measurement, or contaminants. Additionally, unexpectedly large amounts of different oxide species could be present on the rough, etched substrate backs and lead to stronger diamagnetism.

The experimentally determined diamagnetic corrections were applied consistently to magnetic data throughout this research. Errors arising from experimental uncertainty and the correction method would propagate to anisotropy, coercivity, and magnetization estimations.

3.3.4 ΔM Measurements

Remanence curves measured from a system of completely non-interacting single-domain magnetic particles obey the Wohlfarth relation, [3.20]

$$M_{\mathrm{DCD}}(H) = M_{\mathrm{IRM}}(\infty) - 2 * M_{\mathrm{IRM}}(H), \tag{3.22}$$

where M_{DCD} and M_{IRM} are the isothermal remanence magnetization (IRM) and dc-demagnetization (DCD) curves described in Chap. 2.1 (subscripts on the field variables have been removed for convenience). Deviations from this relationship result from interparticle interactions [3.21] and the so-called ΔM curve defines these deviations,

$$\Delta M(H) = M_{\mathrm{DCD}}(H) + 2 * M_{\mathrm{IRM}}(H) - 1. \tag{3.23}$$

Note that the remanence curves in the above expression have been normalized to $M_{\mathrm{IRM}}(\infty)$. Physically, ΔM is twice the difference between the fractions of a magnet irreversibly magnetized by the field H in the M_{IRM} and M_{DCD} measurement modes [3.21]. An example of a ΔM curve is shown in Fig. 3.3. By definition ΔM equals zero for a granular magnet consisting of isolated S-W particles. Typical interpretations of deviations from zero are that positive values indicate interactions which seek to stabilize the current magnetization state whereas negative values

arise from dominant demagnetizing interactions. Mean-field modeling supports this understanding [3.22]. A simplified interpretation is that positive values indicate exchange coupling and negative values demonstrate dominant dipole interactions [3.23,3.24], however dipole interactions can exhibit positive and negative ΔM depending on relative internal spin states.

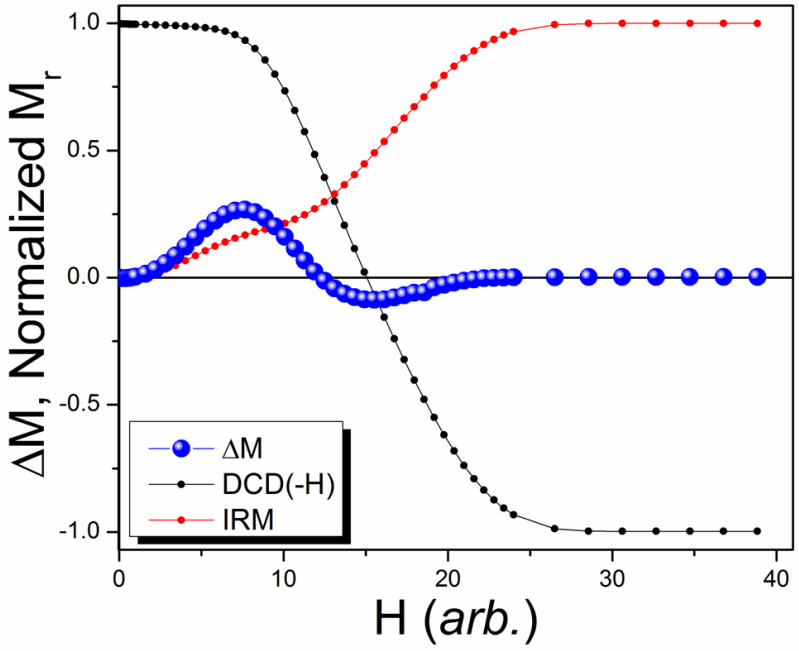

FIG. 3.3. Example of ΔM plot including constituent M_{IRM} and M_{DCD} curves.

Delta-M plots are used in Chapter 6 of this dissertation to examine changes in magnetic behavior in an ECC system with varying soft-phase volume fraction.

3.3.5 ΔH Measurements

Estimating the intrinsic switching field distribution (Δ_{SFD}^{i}) of a particulate magnet requires circumventing the effects of interparticle interactions. Two methods of doing this are the ΔH_c [3.25] and the ΔH [3.26-3.29] methods. Both methods work in the mean-field approximation by assuming weak enough interparticle exchange to be considered on the same level as dipolar interactions. Only the ΔH method is used in this research; however, since it essentially extends the premise of the ΔH_c method both will be described in the following.

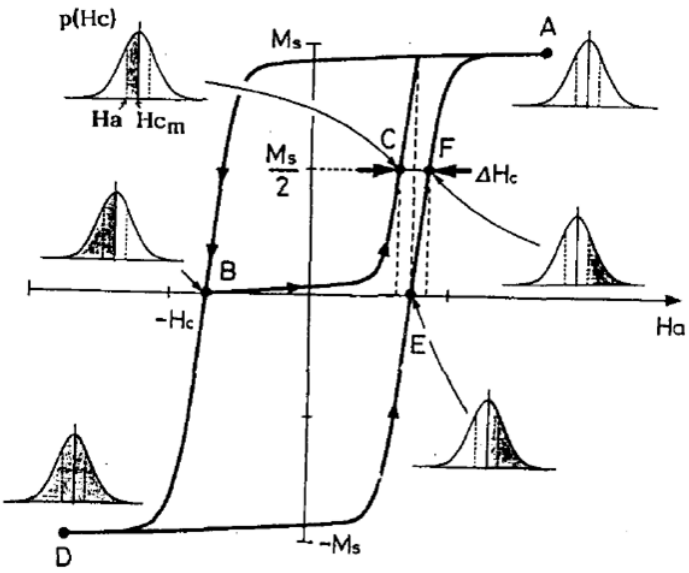

FIG. 3.4. Schematic for measuring ΔH_c and conceptualized switching-field distributions with spin-up (light) and spin-down (dark) populations indicated for six points of interest. See text for details. Figure from Ref. 3.25.

The ΔH_c method estimates $\Delta^{i}_{\mathrm{SFD}}$ by examining the difference between the fields required to achieve $0.5M_s$ on the final branch of a major hysteresis loop and on a recoil curve beginning at H_c. Within in the mean-field approximation, interparticle interactions occurring at those two fields are equal owing to the presumed proportionality between M and the magnitude of the interactions. Figure 3.4 demonstrates the involved magnetization curves and illustrates how the FWHM of the switching field distribution is accessed. The sequence A-B-D-E-F-A tracks the major hysteresis loop and the sequence A-B-C-A follows the recoil of interest. In the schematics of the switching field distribution function (*P*), white and dark regions represent positively and negatively aligned moments, respectively. The key concept of the method is seen by examining the magnetization states at points C and F. The magnetization state at point F is nearly saturated in the positive direction, i.e. three-quarters of the total number of particles have switched and only those particles with high switching field remain un-switched. Assuming a Gaussian form for *P* with a standard deviation of σ_{SF} means that the field at point F is approximately $H_c + 0.675\sigma_{SF}$. On the other hand, the magnetization state at point C has

returned half of the previously reversed population back to positive magnetization. The field at which this occurs is approximately $H_c - 0.675\sigma_{SF}$. Therefore, from the difference in applied field at points C and F, ΔH_c,

$$\Delta^{i}_{\mathrm{SFD}} = 2\sigma_{SF} \cong 1.5\Delta H_c. \tag{3.24}$$

The ΔH method uses the same concept of calculating differences between the fields required to reach identical magnetization values from different initial states. It extends the ΔH_c method by including all values for *M* along multiple recoil curves starting from a range of fields. In doing so, the ΔH method is not limited to providing merely a single value for $\Delta^{i}_{\mathrm{SFD}}$ but allows for an estimation of the entire switching field distribution function.

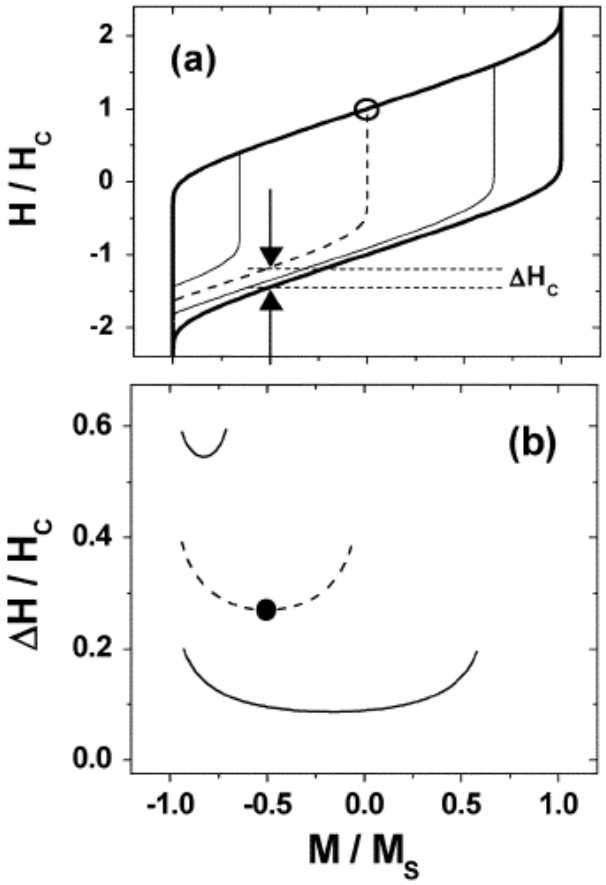

FIG. 3.5. (a) Normalized H-M loop with three example recoil curves used to calculate ΔH(M,δM). (b) Three ΔH curves corresponding to data in (a). See text for further details. Figures from Ref. 3.26.

Formally, ΔH is a function of both the magnetization at which field differences between the major and recoil curves are determined (M) and the deviation in magnetization from saturation at which each recoil curve begins (δM), $\Delta H = \Delta H(M,\delta M)$. Figure 3.5 demonstrates the use of this procedure. The dashed recoil curve in part (a) is the same curve used in the ΔH_c method and the information gained from that method is indicated by the point in 3.5(b) for comparison. The additional field-difference values between recoil curves and the major loop yield the u-shaped curves in part (b), where dashed curve corresponds to $\Delta H(M, 0.5)$. The solid ΔH curves in 3.5(b) correspond to the solid recoils in 3.5(a).

Within mean-field approximation, magnetization values can be determined by Eq. (2.13). Including average interparticle interactions of the form λM, the magnetization is given by,

$$M = 1 - 2\int_{-\infty}^{-[H_M+\lambda M]} P(H_c)dH_c\,, \tag{3.25}$$

after normalization to M_s. The field, H_M in the upper limit is the value required to achieve the magnetization M on the major hysteresis loop. Defining a distribution function I, as,

$$I(-[H_M + \lambda M]) = \int_{-\infty}^{-[H_M+\lambda M]} P(H_c)dH_c = \frac{1-M}{2}, \tag{3.26}$$

allows the determination of the field H_M through the inverse-integration function, I^{-1}, such that,

$$H_M(M) = -I^{-1}\left(\frac{1-M}{2}\right) - \lambda M\,. \tag{3.27}$$

A similar derivation for the field (H_m) on the recoil curve yielding magnetization M is,

$$H_m(M) = -I^{-1}\left(\frac{1-(M+\delta M)}{2}\right) - \lambda M\,. \tag{3.28}$$

The calculation for the desired field difference looks like,

$$\Delta H(M, \delta M) = H_m(M) - H_M(M) \tag{3.29}$$

$$= I^{-1}\left(\frac{1-M}{2}\right) - I^{-1}\left(\frac{1-(M+\delta M)}{2}\right).$$

Recovering the desired distribution function, $P(H_c)$, requires defining a general function $I^{-1}(x)$, ideally from a very large number of ΔH curves. A simpler method assumes a known parameterized distribution function; from that function the corresponding form of ΔH can be calculated and the desired parameters extracted from a data fit. For example, assuming a Gaussian switching-field distribution function of the form,

$$P_G(H_c) = \frac{1}{\sqrt{2\pi} * \sigma} \mathrm{e}^{-2\left(\frac{H_c - <H_c>}{2\sigma}\right)^2}, \tag{3.30}$$

leads to,

$$\Delta H_G(M, \delta M) = \sqrt{2} * \sigma[erf^{-1}(M + \delta M) - erf^{-1}(M)], \tag{3.31}$$

where $erf^{-1}(x)$ is the inverse of the error function.

The ΔH method is used in Chap. 6 of this dissertation to extract the intrinsic switching field distribution from a particulate magnetic film.

3.3.6 Low Temperature Measurements

Measuring magnetic hysteresis behavior at different temperatures can reveal thermally dependent properties of a magnet thin material. For example, the Sharrock equation, Eq. (2.34), derived in Chap. 2 allows the estimation of thermal stability factors and energy barriers by fitting switching field values measured at different temperatures. Measurements made away from room-temperature were performed in the SQUID magnetometer in the range of up to 350 K and down to 50 K. Figure 3.6 demonstrates a particular difficulty with low temperature measurements of thin film samples on the MgO substrates used in this research. Resulting moment versus temperature data exhibits a trend atypical of a pure diamagnet. Additionally, the inset demonstrates a superparamagnetic signal at 10 K not present at 50 K. The large magnetic signal developing at low temperatures is likely due to impurities in the MgO substrate.

The substrates, purchased from the MTI Corporation, are listed at >99.95 % purity with typical impurities of Ca, Al, Si, Fe, Cr, B, and C. The unanticipated large low-temperature signal precluded measurements less than 50 K in this work, and somewhat decreased the reliability of the results from the low-temperature measurements.

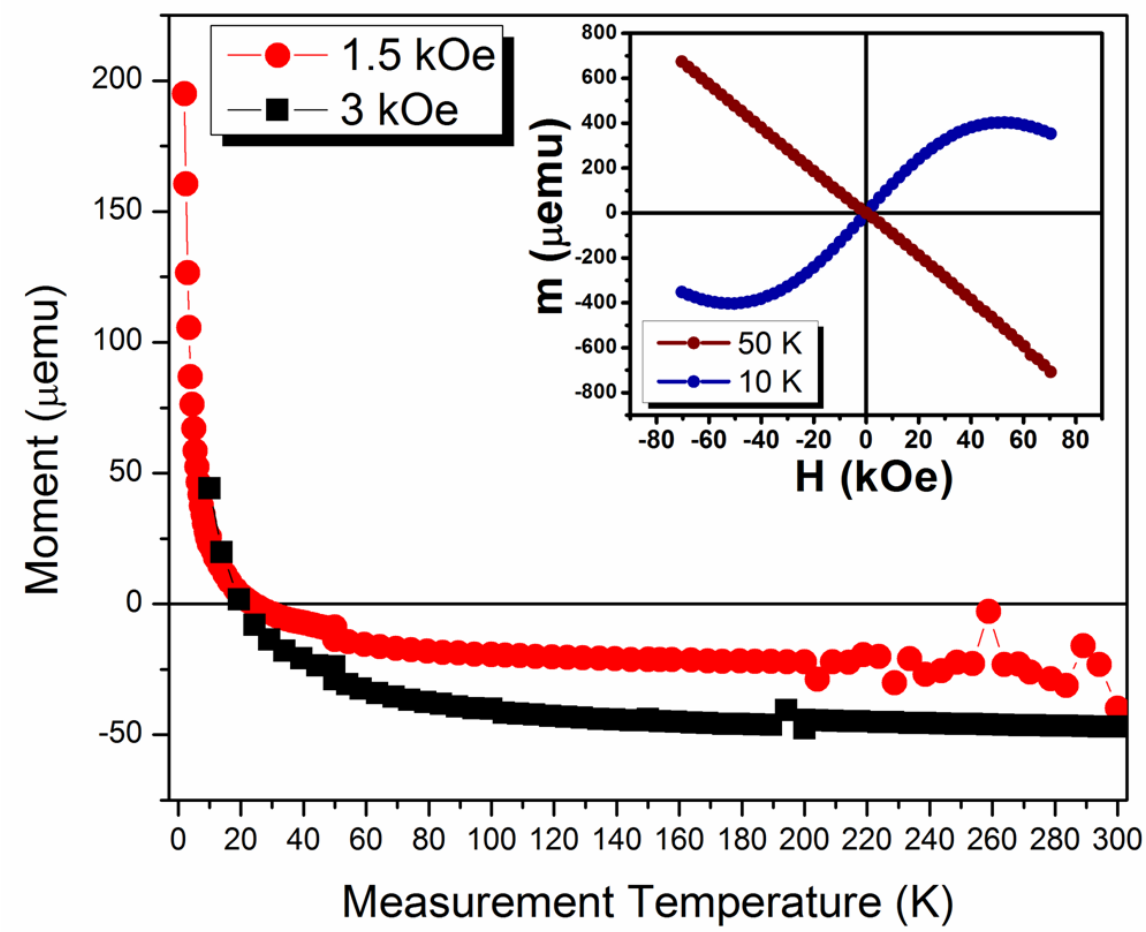

FIG. 3.6. Moment versus temperature of an MgO substrate similar to those used in Chap. 6. Inset is the *M*(*H*) measured at 50 and 10 K.

3.4 Scanning Probe Microscopy

Surface morphology and magnetic domain structure was imaged by scanning probe microscopy (SPM) using a Digital Instruments Nanoscope IIIa Dimension 3100 SPM system. Atomic force microscopy (AFM) in tapping mode probed surface roughness and topological features with a lateral resolution of about ~10 nm. Magnetic force microscopy (MFM) using a

Co/Pt coated tungsten tip coated and interleave mode with a 20 nm lift height permitted an estimated lateral resolution of 20 nm for imaging magnetic domain structures. Raw images were flattened to offset overall sample tilt. Root-mean-square (RMS) roughness values were estimated using the system's software package. Lateral feature sizes were estimated by manually tracing over 100 representative ellipses.

Magnetic correlation lengths were estimated by the average in-plane diameter features of the MFM data using the grain size feature of the software package. Raw MFM images were flattened and filtered for features greater than 50% of the maximum signal to extract meaningful domain patterns. The square of the mean area of the features was taken as the measured magnetic correlation length (L_{exp}). A correction function of the form $L_m^2 + L_{min}^2 = L_{exp}^2$ (where L_{min} is the smallest resolvable feature size due to tip quality and lift height and was taken to be 30 nm), was applied to deconvolute the raw data and access the correlation length (L_m).

3.5 Electron Microscopy

Electron microscopy provides a number of very useful tools for the analysis of composite thin films. Electrons thermionically emitted from a cathode and accelerated to energies between 10 and 20 keV are ideal for probing surface features in scanning electron microscopy (SEM). Transmission electron microscopy (TEM) reveals internal structure using higher energies of >100 keV to allow electrons to pass through ultra-thin samples. Detection of secondary electrons in SEM or transmitted electrons in TEM construct real-structure images of a sample down to nanometer resolution.[20] In TEM, electrons diffracted from a sample's crystalline phases produce patterns useful for structural characterization. Ionization of interior electrons by impinging electrons triggers x-ray excitations whose wavelength is determined by the energy emitted by the electron decaying from an outer orbital. Energy dispersive x-ray spectroscopy

[20] High-resolution transmission electron microscopy offers Angstrom-scale resolution and would be useful in future studies.

(EDXS) examines these x-ray spectra to determine a sample's elemental composition. The small beam spot in electron microscopy allows for electron diffraction and EDXS analysis of select regions of a sample. Such selectivity reveals structural, morphological, and compositional information on a highly local scale. EDXS is also possible in SEM systems.

This research utilized a JEOL JSM840A SEM and a JEOL JEM 2010 TEM for structural, morphological, and compositional analysis of nanocomposite thin films. The TEM uses accelerating voltages of 200 kV to image samples and generate EDX spectra. Sample preparation to create an electron-transparent portion of film involved hand-polishing by increasingly finer-grained sand papers on the backs of the substrates, followed by ion dimpling to expose the back surface of the film itself. Alternatively, small carbon films held together by copper or nickel grids were used when only EDXS measurements were required. The so-called TEM grids were mounted alongside sample substrates in the sputtering chamber to capture material during a deposition process and could be loaded directly into the microscope.

The JEOL SEM accelerates electrons to 15-20 KeV to image samples and capture EDX spectra. No sample preparation was required for performing SEM measurements; samples were mounted to the SEM holder using carbon tape. In some cases a metal foil was gently pressed against the thin-film's surface to discharge electrical buildup detrimental to SEM performance. For some films with especially large static buildup a bridge of carbon tape grounded the surface of the sample to the sample holder.

Accurate knowledge of sample composition is important when investigating alloys. EDXS in the SEM system provides a relatively straightforward method for compositional analysis. Count rates were maintained between 1000 and 1300 c/s to maximize signal while limiting detector dead time. At least four 600 second spectra were collected for each sample from different regions. Each spectrum was corrected for bremsstrahlung background radiation and fit

by the system's software. Specifically, relative Fe-Pt compositions were determined from fitting the Fe K-series and Pt M-series peaks. Resulting precision was found to be affected by film thickness and standard deviations around 1 at.% were typical for ~10 nm films. A higher degree of precision and accuracy could be obtained by calibrating the EDXS software to a composite FePt thin film of known composition or by using more advanced analysis software.

3.6 References

3.1 B. D. Cullity, *Elements of X-Ray Diffraction*, Second ed. (Addison-Wesley Publishing Company, Inc., London, 1959).

3.2 B. E. Warren, *X-ray Diffraction*. (Dover, New York, 1990).

3.3 F. K. Lotgering, Journal of Inorganic and Nuclear Chemistry **9** (1959).

3.4 ICDD Powder Diffraction File, Card No. 03-065-9121 (2006).

3.5 Y. Ding, S. A. Majetich, J. Kim, K. Barmak, H. Rollins and P. Sides, Journal of Magnetism and Magnetic Materials **284**, 336-341 (2004).

3.6 ICDD Powder Diffraction File, Card No. 01-071-5031 (2006).

3.7 ICDD Powder Diffraction File, Card No. 04-001-3171 (2009).

3.8 ICDD Powder Diffraction File, Card No. 00-004-0829 (2012).

3.9 ICDD Powder Diffraction File, Card No. 00-005-0565 (2007).

3.10 R. Young and D. Wiles, Journal of Applied Chrystallography **15** (1982).

3.11 R. C. Reynolds, Clays and Clay Minerals **34** (4) (1986).

3.12 V. Holy, Y. Pietsch and T. Baumbach, *High-Resolution X-ray Scattering from Thin Films and Multilayers*. (Springer-Verlag, Berlin, 1999).

3.13 B. W. Roberts, Acta Metallurgica **2** (4), 597-603 (1954).

3.14 M. F. Toney, W.-Y. Lee, J. A. Hedstrom and A. Kellock, Journal of Applied Physics **93** (12), 9902-9907 (2003).

3.15 A. J. C. Wilson, *International Tables for Crystallography Volume C*. (Kluwer Academic Publishing, Dordrecht, 1995).

3.16 A. Cebollada, D. Weller, J. Sticht, G. R. Harp, R. F. C. Farrow, R. F. Marks, R. Savoy and J. C. Scott, Physical Review B **50** (5), 3419 (1994).

3.17 J. A. Christodoulides, P. Farber, M. Dannil, H. Okumura, G. C. Hadjipanaysi, V. Skumryev, A. Simopoulos and D. Weller, IEEE Transactions on Magnetics **37** (4), 1292-1294 (2001).

3.18 S. C. Chen, C. D. Chen, T. H. Sun, S. L. Ou, C. L. Shen and W. H. Su, Vacuum **87** (0), 205-208 (2013).

3.19 M. Sawicki and et al., Semiconductor Science and Technology **26** (6), 064006 (2011).

3.20 E. P. Wohlfarth, Journal of Applied Physics **29** (1958).

3.21 P. E. Kelly, K. O'Grady, P. I. Mayo and R. Chantrell, IEEE Transactions on Magnetics **25** (5) (1989).

3.22 J. G. Zhu, in *Noise in Digital Magnetic Recording*, edited by T. C. Arnoldussen (World Scientific, Singapore, 1992).

3.23 G. B. Ferguson, K. O'Grady, J. Popplewell and R. W. Chantrell, IEEE Transactions on Magnetics **25** (1989).

3.24 K. O'Grady, M. El-Hilo and R. W. Chantrell, IEEE Transactions on Magnetics **29** (1993).

3.25 I. Tagawa and Y. Nakamura, IEEE Transactions on Magnetics **27** (6), 4975-4977 (1991).

3.26 A. Berger, Y. Xu, B. Lengsfield, Y. Ikeda and E. E. Fullerton, IEEE Transactions on Magnetics **41** (10), 3178-3180 (2005).

3.27 A. Berger, E. Marinero, M. Doerner, X. Bian, K. Tang and A. Polcyn, Journal of Applied Physics **97** (10), 10N115 (2005).

3.28 A. Berger, B. Lengsfield and Y. Ikeda, Journal of Applied Physics **99** (8), 08E705 (2006).

3.29 Y. Liu, K. A. Dahmen and A. Berger, Physical Review B **77** (5), 054422 (2008).

CHAPTER 4 NONEPITAXIAL Fe/Pt MULTILAYER THIN FILMS

4.1 Introduction

Perpendicular magnetic recording requires the easy-axis of the media to align out of plane. Uniaxial magnetocrystalline anisotropy (MCA), the strongest type of magnetic anisotropy and consequently the most useful for achieving high areal densities, follows a specific crystal lattice direction of a magnetic material. Therefore, realizing a media with perpendicular magnetic anisotropy (PMA) requires achieving uniform crystalline texture. Co-Cr-Pt-SiO_2 alloys provided the first generation of perpendicular recording media; however, a larger magnetocrystalline anisotropy is required in the approach to 10 Tb/in^2 [4.1-4.4]. The MCA of $L1_0$-phase FePt, ~70 Merg/cm^3 (7 MJ/m^3), will provide sufficient thermal stability in ~3 nm grains. In the ordered phase, the *c*-axis defines the easy magnetization axis, therefore realizing (001) texture is essential for the application of FePt as a perpendicular recording media.

Crystallographic texture in thin films typically results from preferential *in-situ* grain growth or during thermal processing after deposition. Epitaxial film growth readily achieves crystalline texture through designed lattice registration with preceding layers but requires deposition at elevated temperatures onto seed-layers or single crystal substrates. Non-epitaxial texturing methods avoid the need for expensive single-crystal substrates or additional deposition steps to fabricate seed layers. Rapidly post-deposition-annealed alternating thin layers of Fe and Pt sputtered on amorphous substrates yield highly (001) textured $L1_0$ ordered films via strain energy driven selective grain growth (SEDSGG) [4.5]. The mechanism behind SEDSGG is discussed in Chap. 2.3.3. Successful texturing of FePt films in this manner requires a rapid ordering process to take advantage of the strain state induced by grain growth and defect healing. Studies have examined the effects of various deposition and processing parameters on

the ordering process of FePt thin-films. However, few have paid particular attention to the effect of film thickness[4.5-4.12], deposition scheme [4.6,4.13-4.15], or processing conditions [4.8,4.13,4.16-4.19] on the resulting degree of (001) texture in pure FePt films. In particular, there are no reports on the effect of composition on non-epitaxial texturing of pure FePt thin films.

This chapter reports multiple experimental studies investigating the effects of varying the deposition scheme on the non-epitaxial formation of (001) texture and $L1_0$ order in Fe/Pt multilayer (ML) thin films. The remainder of the chapter is structured as follows: Sec. 4.2 presents general experimental conditions common to all experiments described in Chapter 4; Sec. 4.3 discusses studies of compositional variations; Sec. 4.4 describes the results of varying the Fe/Pt bilayer thickness; Sec. 4.5 examines the effect of total film thickness; and Sec. 4.6 investigates an additional degree of control over (001) texture and film morphology by increasing the thickness of the Pt terminating layer.

4.2 General Experimental Details

All samples presented in this chapter were magnetron sputtered with the 3M or AJA system on thermally oxidized Si substrates. The 100 nm-thick oxide layers provided an amorphous surface on which to non-epitaxially grow the films. The ML samples consist of alternating layers of Fe and Pt sputtered from elemental targets. Individual layer thicknesses within the as-deposited structure and the number of ML repetitions served as control parameter for total film thickness and Fe-to-Pt layer-thickness ratios dictated the Fe:Pt stoichiometry. Specific details such as ranges of investigated parameters used for each experiment are given in the corresponding subsection. The RTP-600 rapid thermal annealing oven (RTA) processed coupons of approximately 4.5 mm by 4.5 mm cut from each as-deposited

sample. A temperature ramp-rate of 100 °C/second and a 25 sccm flow of 5% H_2-in-Ar were used throughout this chapter.

A Bruker-AXS D8 Discover and a Rigaku D/Max-B collected the X-ray diffraction (XRD) patterns using Cu-Kα radiation (λ ≈ 1.542 Å). Resulting XRD spectra were fit with pseudo-Voigt peak profiles to extract structural information and quantify the degree of chemical order (S) and (001) texture, the latter via the Lotgering orientation factor (LOF). Magnetic measurements were performed with an alternating gradient field magnetometer (AGFM) and a superconducting quantum interference device (SQUID) magnetometer. Film topology and magnetic correlation lengths were characterized by atomic force microscopy (AFM) and magnetic force microscopy (MFM), respectively. Real-structure analysis was performed by scanning electron microscope (SEM) and transmission electron microscope (TEM). Energy dispersive x-ray spectroscopy (EDXS) attached to the TEM and SEM determined film compositions. Details regarding the above systems and analysis techniques can be found in their respective sections of Chap. 3.

4.3 Effect of Fe:Pt Composition

The correlation between ordering kinetics in post-deposition annealed FePt thin films and Fe:Pt stoichiometry is reviewed in Sec. 2.3. The need for rapid ordering to achieve a high degree of non-epitaxial texturing by SEDSGG indicates a possible connection between (001) texture and stoichiometry. Non-epitaxially textured thin-films have been reported with equiatomic [4.15] and Fe-rich [4.5,4.7-4.9,4.13,4.14,4.16,4.20,4.21] stoichiometries. However, there has not been an explicit study on the degree of (001) texture achievable when the film composition is varied around 1:1. Since a FePt film's magnetic properties, namely MCA, depend strongly on stoichiometry [4.22,4.23], optimizing the degree of (001) texture and magnetic

hardness via composition is an important step in developing a non-epitaxial means for fabricating $L1_0$ FePt as a perpendicular recording media.

This subsection describes experiments investigating the effects of varying the Fe:Pt stoichiometry on chemical order, (001) texture, and magnetic properties of post-deposition annealed ML thin films. Two series of nominally 11 nm thin-films with different bilayer thicknesses were investigated, denoted S1 and S2. Both series were deposited using the 3M sputtering system. Series S1 stoichiometries range from 43.1 to 56.9 at.% Fe with ~6 Å bilayers and series S2 ranges from 41.8 to 54.5 at.% Fe with a ~3 Å bilayer thickness. Sample compositions were controlled by varying the Fe-layer thickness while maintaining a constant Pt-layer thickness. Coupons cut from each sample were annealed at 600 °C for 5 minutes in the RTA furnace as described in section 4.2. Further details of the sample preparation can be found in Chap. 3.

4.3.1 Sample Series S1 Results and Discussion

Sample series S1 consists of 18 samples with Fe composition ranging from 43.1 to 57.1 at.%. The Pt layer thickness was fixed at 3 Å within the ML structure. $L1_0$ (001) superlattice peak visible in each sample's x-ray spectra in Figure 4.1 indicates the presence of the $L1_0$ ordered phase after annealing. Practically no ordered-phase (110) or (200) peaks are visible. All spectra indicate the presence of predominantly (111)- and/or (001)-oriented grains. The shrinking relative size of the (111) peak with respect to the other peaks for increasing Fe at.% demonstrates a trend of increasing (001) texture. Shifts in peak positions with varying stoichiometry indicate changes in chemical order, via c/a-lattice ratio, or the presence of macro-strains.

Trends in chemical order and degree of (001)-texturing for different Fe:Pt stoichiometries are of primary interest in this study. Figure 4.2(a) shows the trend of S with Fe

at.%, indicating a maximum order parameter of 0.94(1) at 49.2 at.% Fe, slightly on the Pt-rich side of even-stoichiometry. S drops for stoichiometries differing significantly from about a +/- 1at.% window around that composition. Large error bars in S in lower Fe compositions are due to relatively weak (002) diffraction peaks from the corresponding xrd spectra. At the other end of the investigated stoichiometry range, Fe-rich samples exhibit significant variance in order parameter. Considering the maximum possible values for S for the extreme compositions, $S_{max} \approx 0.86$ at 43 and 57 at.% Fe, these samples appear relatively well ordered for their compositions.

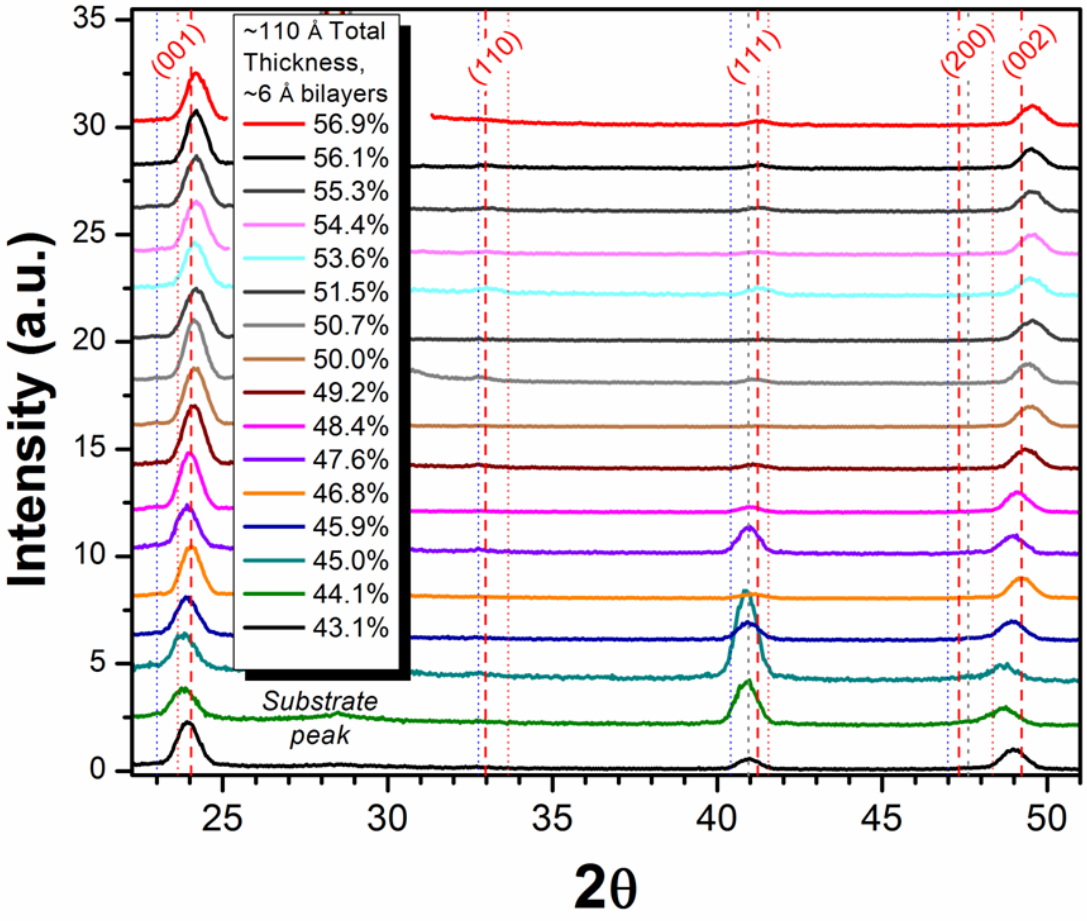

FIG. 4.1. X-ray diffraction spectra of selected S1 series samples. All spectra are normalized to their (002) diffraction peak intensity. Vertical lines denote as-labeled peak positions from anticipated phases: red and grey dashed lines for $L1_0$ and fcc FePt phases, respectively; red and blue dotted lines for ordered Fe_3Pt and $FePt_3$, respectively.

The trend of LOF for (001) textured grains shown in Figure 4.2(b) indicates that the highest degree of texture, LOF = 0.98(1), is found at 51.5 at.% Fe, followed closely by 0.96(2) at 50.0 at.% Fe. The reason for the large drop in LOF for the intermediate sample is unclear. Similar variance is seen in LOF for the Pt-rich films; LOF increases from a low value of 0.16(2) at 45 at.% Fe to 0.68(2) at 43.1 at.% Fe. Aside from a drop at 53.6 at.% Fe, texture in the high-Fe content films decreases gradually and all values of LOF remain relatively high, >0.83 for those compositions.

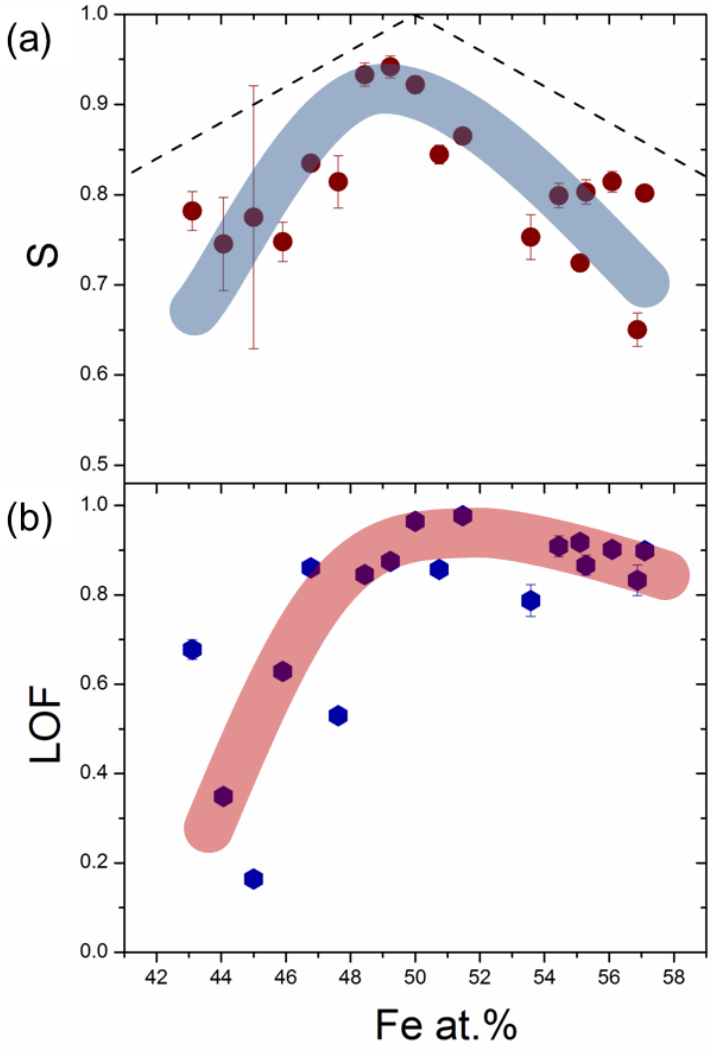

FIG. 4.2. Variation of order parameter, S (a), and degree of (001) texture, LOF (b), with stoichiometry. Dashed line in (a) represents maximum possible S for given stoichiometries and broad lines serve to guide the eye.

The mechanism behind non-epitaxial texturing in these films is assumed to result from SEDSGG during post-deposition processing. To examine structural trends in the S1 series films, c-lattice and $d_{(111)}$ spacings estimated from peak positions extracted from XRD spectra fittings are compared with values reported in the literature. Figure 4.3(a) plots the c-lattice values for series S1, along with c-lattice parameters from bulk $L1_0$ ordered, equiatomic FePt (dashed red line at 3.702 Å), [4.24] a series of powder samples [4.25] and a series of 1 μm films [4.26], the latter two for varying compositions. The *c*-lattice parameters of Pt-rich S1 samples are larger than bulk and decrease gradually with increasing Fe at.%. The value matches that of equiatomic bulk FePt at around 48 at.% Fe and then becomes constant at ~3.676 Å for Fe concentrations greater than ~50 at.%. The two reference datasets follow a similar trend, yet are consistently larger than S1 values. Figure 4.3(b) shows the variation of d-spacing as determined by the (111) diffraction peak. Also shown in that figure are the corresponding reference data, including the $d_{(111)}$ for bulk equiatomic fcc FePt [4.27]. All data follow a decreasing trend with Fe at.% over the given range. Similar to the c-lattice parameters, S1 values are consistently smaller than the reference data. Unlike the c-lattice parameter, $d_{(111)}$ values from the S1 thin-films coincide with that of bulk equiatomic ordered value at a 1:1 stoichiometry.

A decreasing trend in lattice-parameter size can be predicted by Vegard's law for solid-solutions of atomic species of unequal size. However, a simple application of Vegard's law interpolating linearly between fcc Pt and ϒ-Fe anticipates larger *c*-lattice parameters and significantly smaller $d_{(111)}$ values than those found in any of the measured data sets, including the powder samples. The discrepancy is probably due to the tetragonal structure of the ordered phase, which is not considered in Vegard's law and is found in these samples. In ordering, the fcc-FePt c-lattice parameter contracts by ~3%. A simple expression for the c-lattice parameter as a function of stoichiometry and degree of chemical order could be written as $c = [\alpha_{\mathrm{Fe\ at.\%}} +$

$\beta_S + \gamma_{\text{strain}}]c_0$, where c_0 is a reference value for the lattice parameter and the coefficients $\alpha_{\text{Fe at.\%}}$, β_S, and γ_{strain}represent the effects of stoichiometry, chemical order, and strain on the *c*-lattice, respectively. The linear relationships assumed here are merely first-pass approximations for demonstration. The stoichiometry and chemical order based terms would both decrease *c* with increasing Fe concentration and S, respectively. That the *c*-lattice parameters stop decreasing after ~50 at.% Fe is likely related to a balance between the effects of an increasing Fe content, decreasing chemical order, and strain in the Fe-rich samples. To extract a quantitative value for strain from a measured *c*-lattice parameter requires knowledge of the stoichiometry and order coefficients, as well as a reference value. Without that explicit information only qualitative trends can be estimated. For example, comparing S1 lattice parameters with the reference data, assuming similar chemical order, indicates a possible compressive strain out-of-the-plane of the thin-films. This trend and its implications to SEDSGG will be discussed further after introducing data from sample series S2. A similar expression exists for changes in $d_{(111)}$. Ordering leads to a slight decrease in $d_{(111)}$. The S1 data decrease roughly monotonically throughout the investigated range of stoichiometries.

The M-H loops in Figure 4.4 illustrate the effect of varying the Fe content near even-stoichiometry on the magnetic hysteresis of (001)-textured $L1_0$ FePt thin-films. Values of S and LOF for each sample are included. The highest out-of-plane squareness, M_r/M_s = 0.92, occurs in the sample with 50.0 at.% Fe corresponding to the highest LOF among in the series. All samples exhibit relatively high degrees of texture and order; however, a clear trend is not apparent between loop shape and those values. The in-plane loops all display appreciable hysteresis, likely due to (111)-textured grains and/or in-plane c-variants [4.23,4.28,4.29]. A soft-magnetic shoulder appears in the Fe-rich films indicating the presence of a soft magnetic phase of α-Fe, Fe_3Pt or Fe-rich disordered FePt.

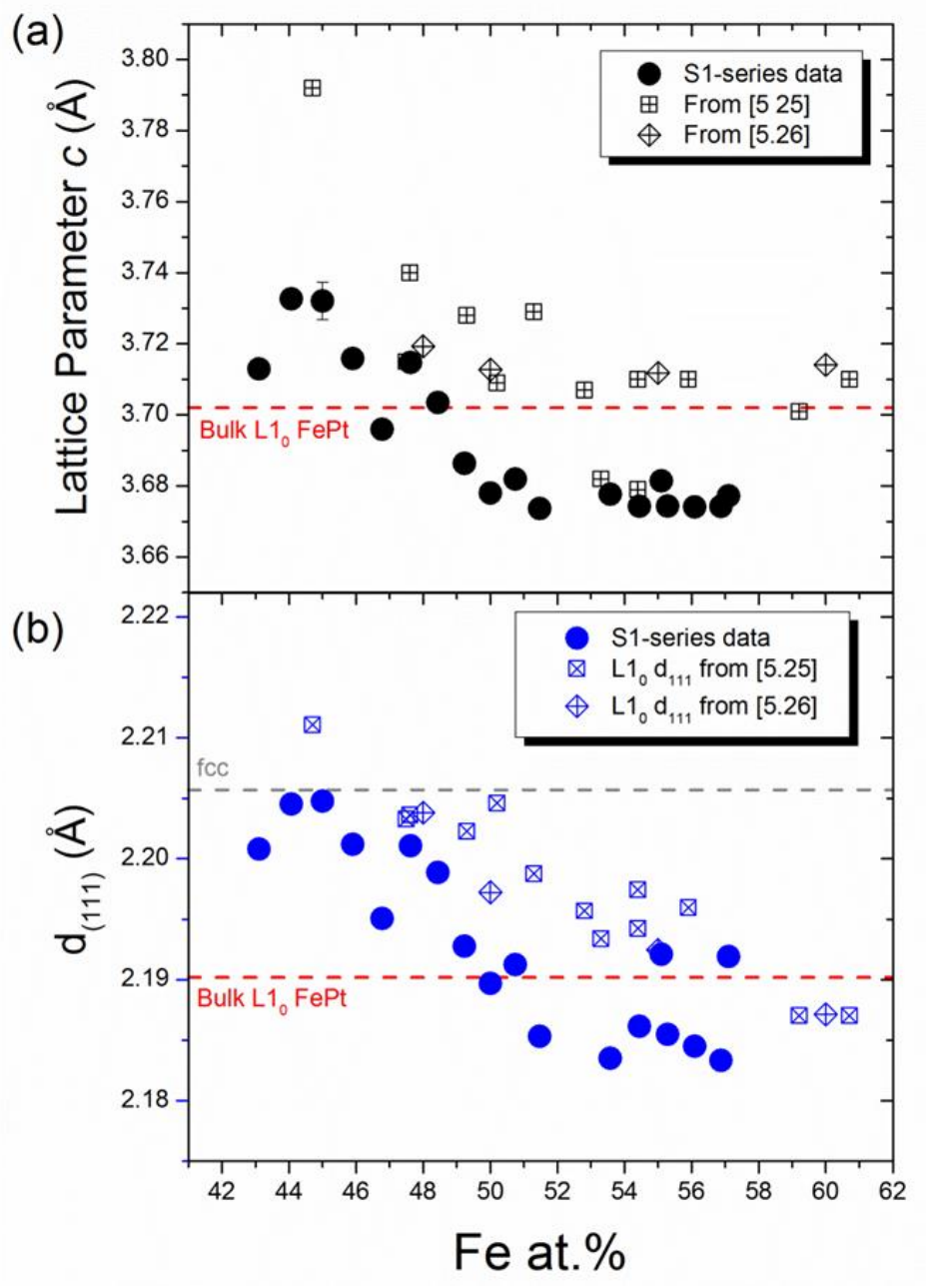

FIG. 4.3. (a) Lattice parameter *c* variations with stoichiometry. Red dashed line denotes the c-lattice parameter for bulk equiatomic $L1_0$ FePt. (b) Variations in lattice spacing determined from (111) XRD peak with stoichiometry. Grey dashed and red dashed lines denote the (111) d-space for equiatomic fcc and $L1_0$ bulk FePt, respectively.

Figure 4.5 plots the out-of-plane coercivities for S1 series samples along with estimated second-order anisotropy constants (K_1) for select samples. Out-of-plane H_c values show a double-peak above and below 50:50 stoichiometry, while K_1 is a maximum for that composition

at 21 Merg/cm^3. Studies have reported maximum coercive forces in Fe-rich samples [4.30-4.35], and considering the error-bar on the 49.2 at.% Fe sample, the S1 series could agree. The consistently larger coercivities for Fe-rich samples seen here is similar to the behavior of 50 nm FePt co-deposited films [4.35]. In those films, magnetic hardness was correlated to the degree of chemical order, which is a known trend for FePt [4.35,4.36]. Only a rough correlation between S and H_c can be drawn for the S1 series samples. Discrepancies could be due to changes in microstructure not directly evidenced by XRD. For example, the samples at 50 and 51.5 at.% Fe exhibit the highest degree of texture in the series, and both of those samples yield relatively low out-of-plane coercivities considering their respective chemical order. The type of SEDSGG suspected here typically yields a microstructure of relatively large flat grains. Larger grains can exhibit smaller switching fields despite possessing a high degree of chemical order and MCA due to increased nucleation sites [4.37] and fewer intergranular pinning sites [4.36].

The trend in K_1 displays a maximum for the equiatomic film. Reported K_1 values have demonstrated peak values in Fe-rich films [4.23]. The relatively small maximum value of 21 Merg/cc, with respect to anticipated values of ~66 Merg/cc, could be due to imperfect chemical order (S = 0.92(1)) or strain [4.38-4.42]. Interestingly, K_1 drops to 12.1 Merg/cc at 48.4 at.%, where chemical order is nearly identical (S = 0.93(1)). Uncorrelated variations in K_1 and H_c are likely due to microstructural features enhancing the coercivity in the films with 46.7 and 55.1 at.% Fe. All anisotropy measurements are subject to inaccuracies due to the nature of the Sucksmith-Thompson method.

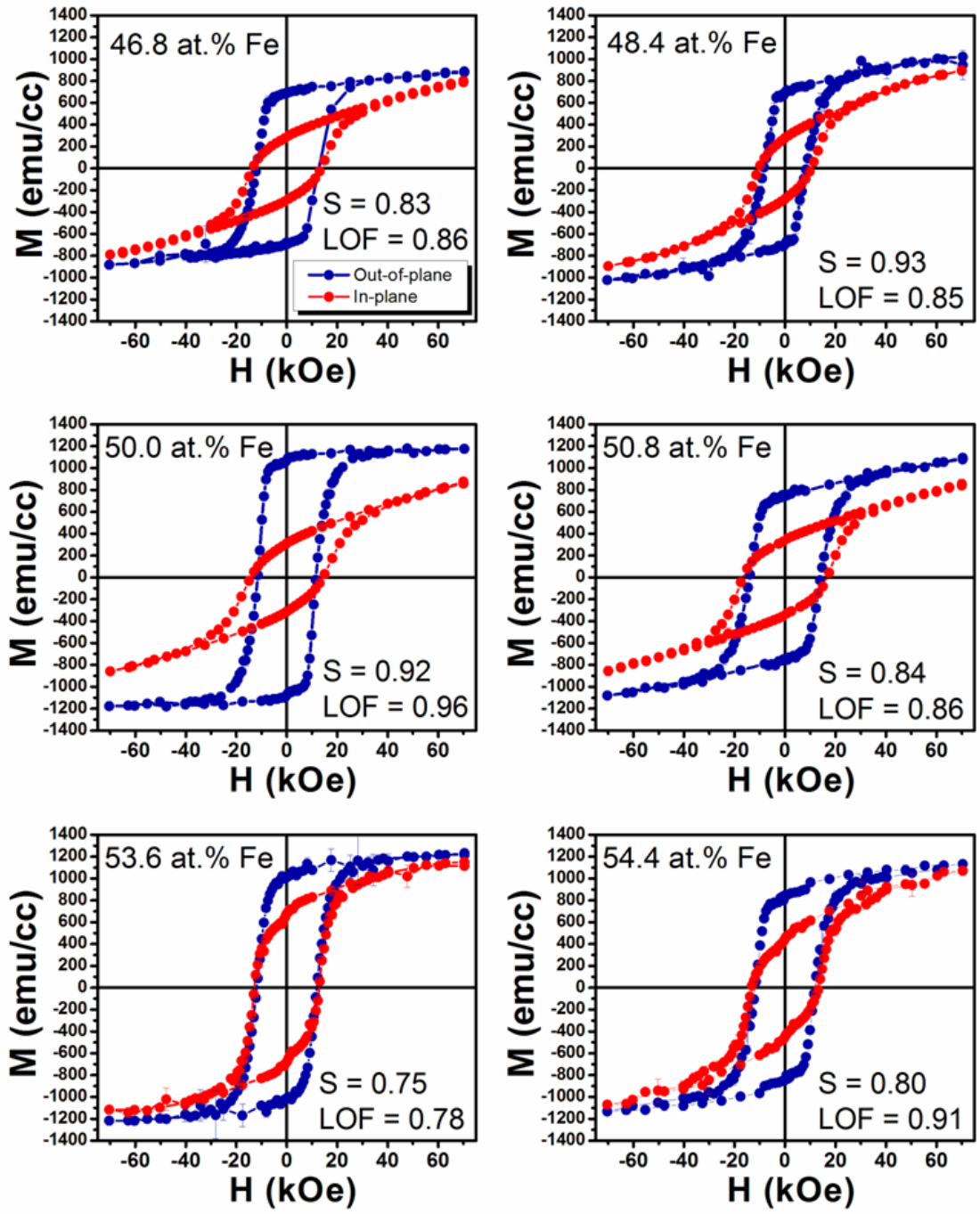

FIG. 4.4. Select in- and out-of-plane hysteresis loops from series S1.

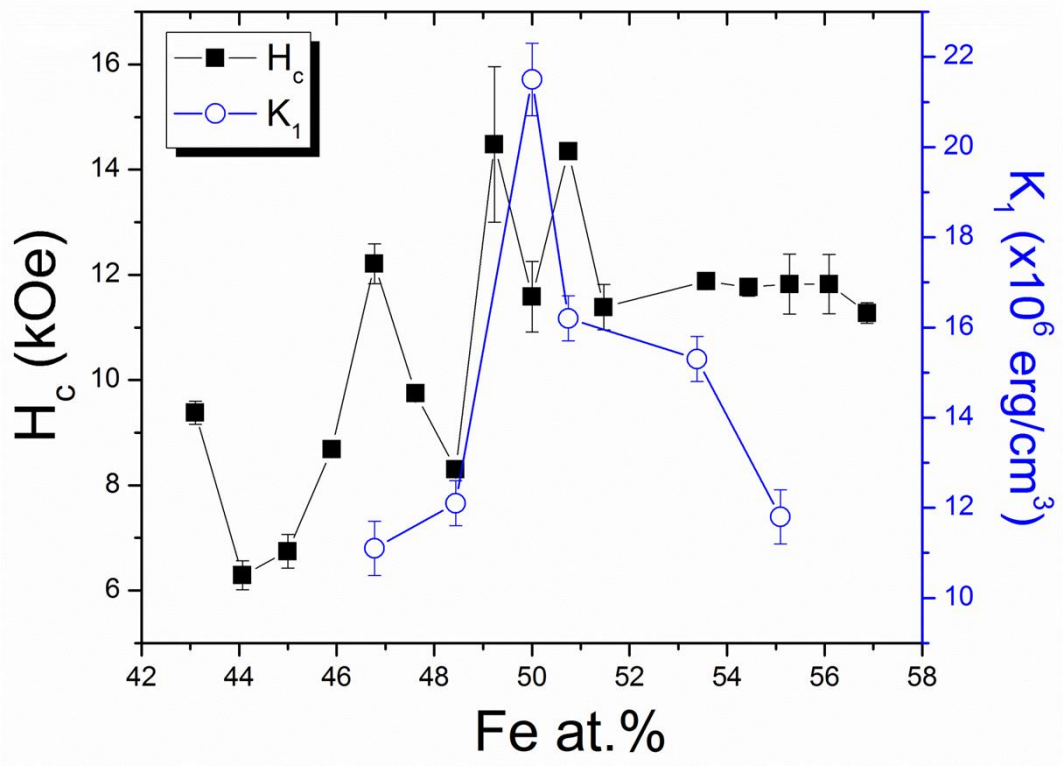

FIG. 4.5. Out-of-plane coercivity and second-order anisotropy constant versus Fe content for sample series S1.

4.3.2 Sample Series S2 Results and Discussion

A second series of ML thin-films with thinner bilayers was also investigated as a function of Fe:Pt composition. Sample series S2 consists of 5 samples with Fe compositions ranging from 41.8 to 54.5 at.%. The Pt-layer thickness is fixed at 1.8 Å and the total bilayer thickness is ~3 Å, about half the thickness used for the S1 series. Thinner bilayers have been shown to enhance (001) texture in non-epitaxially grown FePt thin-films [4.13,4.43]. After annealing under similar conditions as the S1 samples, the XRD patterns in Figure 4.6 reveal a high degree of order and texture in all samples with Fe concentration >41.8 at.%. The (001) and (002) peaks of the 41.8 at.% Fe spectra appear to correspond to those of ordered Fe_3Pt; however, its (111) peak position is shifted toward the $FePt_3$ peak, in the opposite direction. The Pt-rich film probably consists of a Fe-rich-$FePt_3$ solid-solution. Compressive strain caused by excess Fe atoms shifts the peak positions to midway between anticipated $L1_0$ FePt and $L1_2$ $FePt_3$ values. Laue oscillations visible

around the (001)-peaks for $L1_0$-ordered S2 films indicate a high degree of vertical coherence for those diffraction planes among different grains. Morphologically, these interference fringes indicate a film consisting of smooth and flat grains of equal height, coherently diffracting from a large area [4.44]. Fitting the oscillations with the Laue function yields coherent grain heights of 114.8, 114.2, 110.2, and 110 Å, which are close to the respective nominal thicknesses of those samples: 112.0, 112, 111.6, and 114 Å. Application of the Scherrer equation to the same peaks yields an average grain size of 96(2) Å. Differences between the two data-sets are addressed near the end of this subsection.

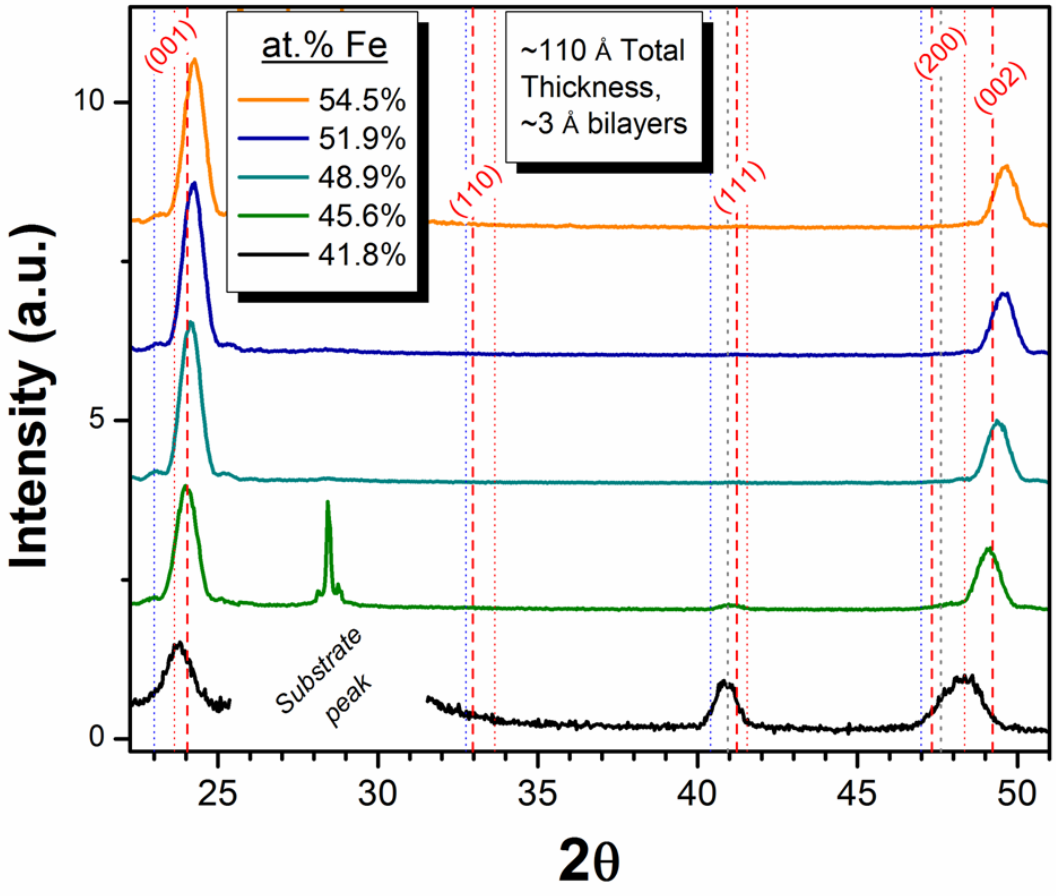

FIG. 4.6. X-ray spectra for samples series S2, varying stoichiometry with a 3 Å bilayer thickness. Data for an extremely large substrate peak was removed for clarity. Vertical lines denote peak positions for possible phases: red and grey dashed lines for $L1_0$ and fcc FePt phases, respectively; red and blue dotted lines for ordered Fe_3Pt and $FePt_3$, respectively.

Figure 4.7 shows the stoichiometry trends of S and LOF from series S2, with S1 data included for comparison. The thinner bilayers of the S2 series result in a higher degree of chemical order in slightly Fe-rich films, with a broader peak in S at 51.9 at.% Fe than that of the S1 trend. However, the value of S = 0.90(1) for that film is less than the maximum from series S1, 0.94(1). Larger LOF values indicate better (001)-texture in the S2 series films for all compositions, most notably at Pt-rich compositions. The breadth of the S2 LOF peak versus Fe at.% somewhat precludes the determination of an optimum composition, although the curve seems skewed toward Fe-rich films. Figure 4.8 shows the similarities in *c*-axis and $d_{(111)}$ lattice parameter trends for the two stoichiometry series. A decreasing trend is apparent for both lattice parameters in the S2 series, similar to those of S1. Estimated c-lattice parameters of S2 films are at least as small as those of corresponding S1 films. The gradual change in curvature for Fe-rich S2 films corresponds with the overall higher degree and slower decline of chemical order for those films, as compared with the sharper drop in S and nearly constant c-lattices of S1 films at similar compositions.

The inverse correlation between LOF and *c*-axis length can be seen in Figure 4.9(a) for both sample series. As mentioned earlier, comparing the measured *c*-lattice parameters with reference data indicates an out-of-plane compressive strain in all S1 and S2 films. Since both fcc and $L1_0$ FePt have positive Poisson ratios, a tensile in-plane strain could be responsible. Similar strains have been reported for non-epitaxially grown FePt thin films, with a comparable correlation to the degree of (001) texture [4.16]. Non-epitaxial texturing by SEDSGG can be understood as the minimization of a grain's total strain energy in an anisotropic stress/strain environment (see 2.3.3). In this way, texturing of a FePt thin film requires an in-plane tensile strain state [4.19,4.45]. Therefore, the negative correlation between LOF and *c*-lattice parameter supports an SEDSGG model of non-epitaxial texturing.

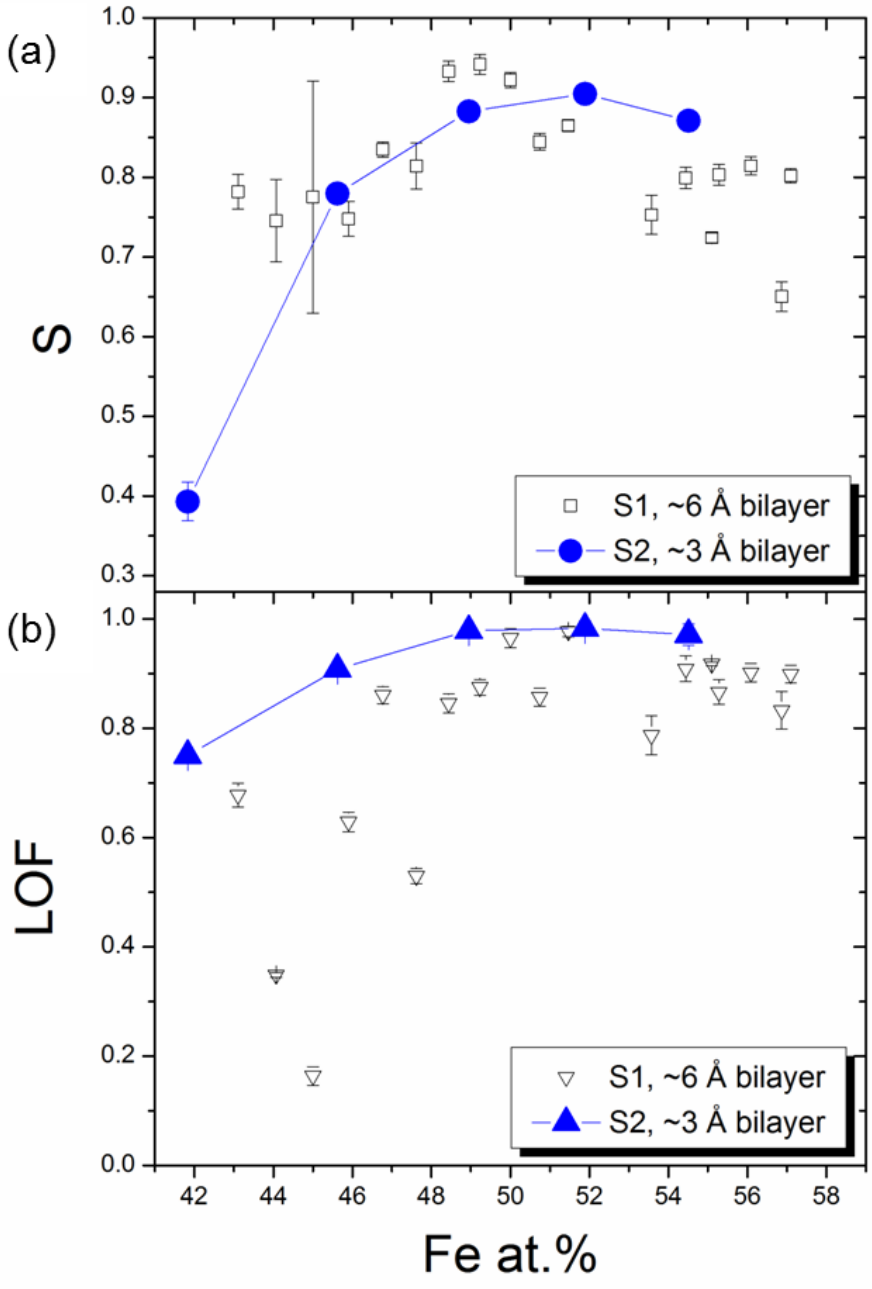

FIG. 4.7. Trend of chemical order (a) and (001) texture (b) for sample series S2. S1 series results included for comparison.

The in-plane tensile strain necessary to drive SEDSGG in FePt thin films can result from two-dimensional grain growth, where out-of-plane growth is limited. Vertical grain growth generally stagnates for grains simultaneously in contact with substrate and the free surface, i.e. when a grain's diameter spans the films thickness. Additionally, those grains would satisfy the

Vook-Witt grain interaction condition, since nothing would be touching them from above. The Vook-Witt condition is considered to enhance (001) texturing in FePt thin films by allowing it to proceed even under slight compressive in-plane strains [4.7]. Therefore, in the extreme case, films texturing in this manner would consist of only a single grain in the vertical direction. Figure 4.9(b) shows the normalized (001)-GS and LOF variations with stoichiometry for both film series. (001)-GS values are determined by application of the Scherrer equation to (001) XRD peaks. GS (Laue) data are from fitting Laue oscillations surrounding the same peaks in the S2 series, where available. Normalization is with respect to nominal as-deposited film thicknesses. Normalized S2 grain sizes estimated from fitting Laue oscillations are clearly much larger than those estimated from peak breadths with the Scherrer equation. The monotonically decreasing trend of those four data points differs from the (001)-GS values for the most Pt-rich film. The overall smaller values determined by the Scherrer equation are likely due to inaccuracies inherent in the form of the Scherrer equation used here or to peak-broadening effects from microstrains. That the normalized Laue-estimated grain heights are close to one can be believed to be accurate due to the morphological implications of those oscillations. Large, flat (001)-textured grains would form by rapid two-dimensional grain growth driven by SEDSGG, and large LOF values from those samples would be expected. Quantitatively correcting all (001)-GS based on four points with different data-trends would be unwise; however, grains sizes determined by the Scherrer method must be qualitatively considered as underestimates.

(001)-grain sizes (from the Scherrer equation) for both series follow a similar trend despite large fluctuations in S1 data. Vertical grain sizes increase with Fe at.% for Pt-rich films and roughly peak just before an equiatomic composition. S2 LOF increases continuously through that composition range. Variations in S1 LOF and (001)-GS track each other well up to 48.4 at.% Fe, where the grain sizes begin to decrease. The peaks in S1 and S2 LOF trends for slightly Fe

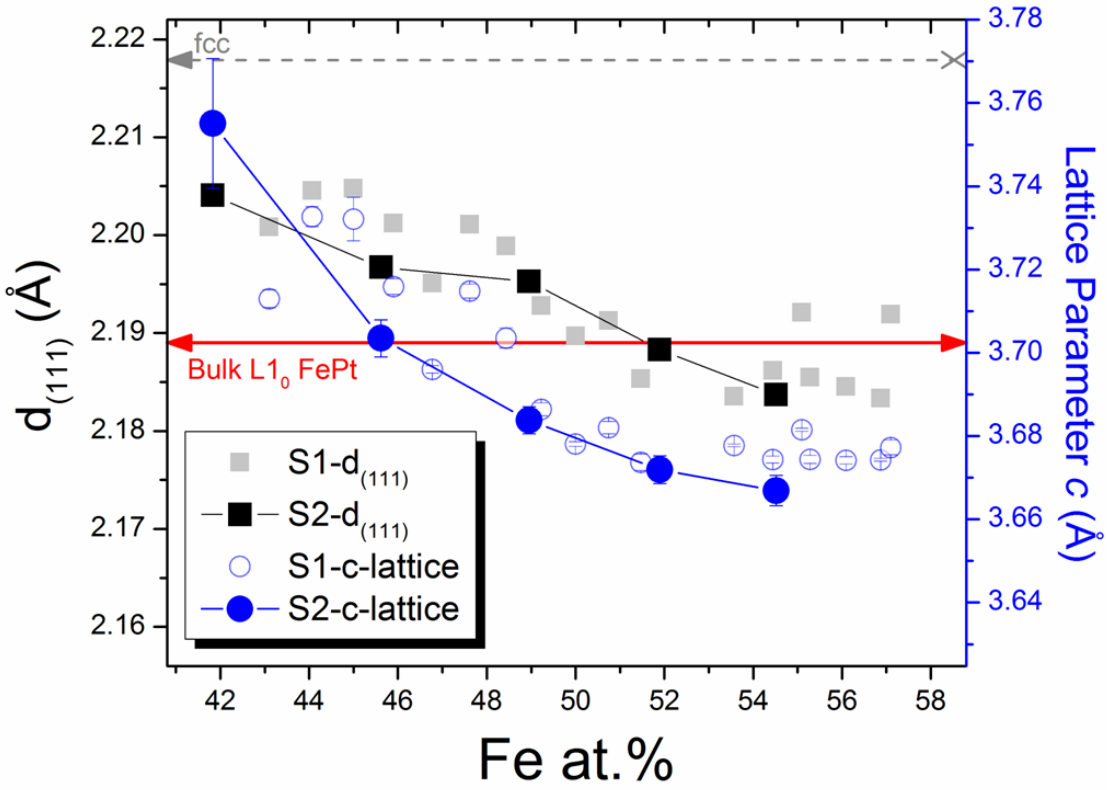

FIG. 4.8. Spacings for the c-lattice and $d_{(111)}$ for sample series S2 as functions of stoichiometry. The respective values from series S2 are included for comparison. Grey dashed line marks the (111) d-space for fcc FePt. Red solid line denotes both the values for $d_{(111)}$ and c-lattice parameter for bulk FePt.

-rich films occur while the respective normalized grain sizes, both Scherrer and Laue determined S2 values, are decreasing. S1 series (001)-grain sizes increase crudely for Fe concentrations ≳54 at.%, while corresponding LOF values remain constant. The highest degree of (001) texture from sample series S1 and S2 were found in films with (001)-GS values ranging from 0.77 and 0.87 and c-lattices smaller than ~3.68 Å. All films with significant texture (LOF > 0.8) possess grains spanning at least 75% of nominal film thickness. Plan-view TEM of the 55.3 at.% Fe S1 film shows lateral grain diameters of at least 50 nm. Therefore, even though the grains may not completely span the film, they are growing anisotropically in the film plane. Additionally, the vertical grain dimensions found here would only permit minimal out-of-plane intergranular interactions for these grains.

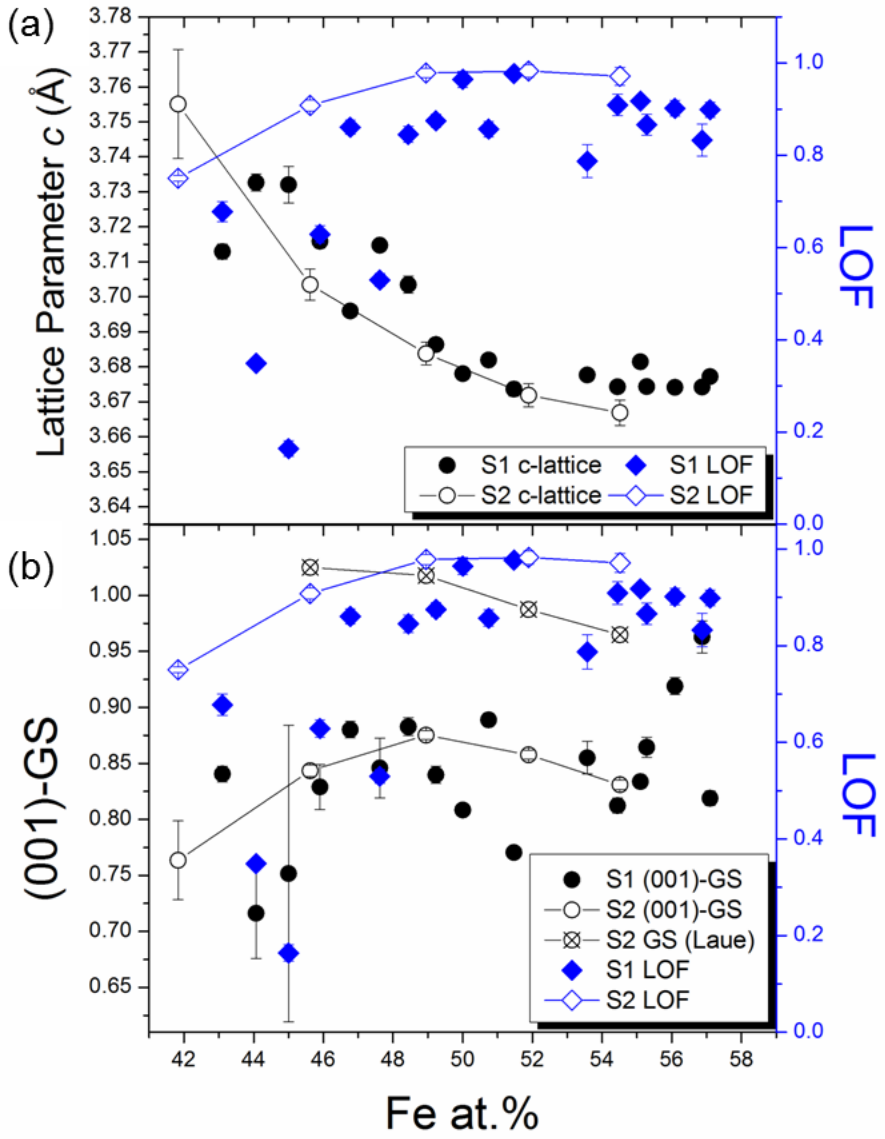

FIG. 4.9. Plot of c-lattice parameter and LOF (a) and normalized (001)-grain size and LOF (b) for varying Fe composition from series S1 and S2.

4.3.3 Sample Series S1 & S2 Conclusions

The degree of chemical order and (001) texture was shown to vary with Fe:Pt stoichiometry in two series of ~11 nm non-epitaxially grown FePt ML thin-films. The highest possible chemical order should be expected for an overall equiatomic composition to match the atomic occupancies in the $L1_0$ phase. However, sample series S1 and S2 exhibit maximum order at slightly Pt-rich and Fe-rich stoichiometries, respectively. Similarly disparate results have been

reported in the literature, where higher degrees of chemical order were measured in post-deposition annealed Fe-rich [4.35] and Pt-rich [4.46] films. The benefits of using off-stoichiometric compositions have been attributed to reduced kinetic ordering temperatures and enhanced atomic diffusion. A lower ordering temperature allows a film to initiate the transformation earlier in an annealing process, possibly during the heating phase, to essentially increase the duration of ordering. Enhanced atomic diffusion can result in a lower ordering temperature, but it also promotes rapid ordering at higher temperatures by accelerating grain growth. Additionally, improved long-range diffusion aids in homogenizing the stoichiometry throughout a film. Both effects have been observed or predicted for Fe-rich and Pt-rich sample compositions. Contradictory compositional trends reported for chemical ordering in FePt samples make it difficult to glean a universal dependence; clearly additional details of each fabrication process must be considered.

Crystallographic texture in thin films results from the minimization of the constituent grains' configurational energy during growth. The degree of (001) texture measured in S1 and S2 series films correspond closely with a contracting c-lattice parameter indicating that the non-epitaxial texturing process can be ascribed to minimizing strain energy. Since the SEDSGG mechanism for (001) texturing relies on the anisotropic strain generated by ordering grains, the trend in LOF for (001) texture could be expected to follow that of S. Accordingly, LOF and S roughly peak near equiatomic composition in both sample series. However, closer examination reveals only a weak correlation, especially in series S1 where the highest degree of order for Pt-rich films is not paralleled by the texturing trend. Therefore, other stoichiometry-dependent factors must contribute to SEDSGG driven texturing as well.

The same effects discussed previously regarding ordering kinetics in off-stoichiometric FePt samples could apply to the texturing process. SEDSGG in thin films requires rapid ordering

and grain growth while avoiding dynamic stress relaxation processes such as yielding or island formation [4.19]. Films ordering at a lower ordering temperature might attain higher ordering-strain energy by transforming earlier in an annealing process. Increased strain-energy would enhance the driving force for abnormal grain growth. Additionally, accelerated grain growth due to enhanced atomic diffusion could propagate a tensile strain state through high-velocity grain boundaries, effectively relaxing a larger fraction of compressively strained grains into the preferred orientation. However, either of those mechanisms would likely affect LOF and S proportionally.

A possible explanation for the observed LOF trends not directly connected to S could be related to changes in intrinsic stress states caused by an asymmetric flux of Pt atoms across grain surfaces during ordering. *In-situ* stress measurements have determined that as-deposited fcc FePt films tend to be compressively stressed due to Pt-enriched grain boundaries [4.47,4.48]. At elevated temperatures, especially once ordering commences, Pt atoms would diffuse into the grains from the boundaries and excess Fe atoms would diffuse out. This type of interdiffusion, along with the relatively high stability of growing $L1_0$-grain surfaces, relaxes the initial compressive stress at a rate proportional to the processing temperature [4.49]. Additionally, the replacement of smaller Fe atoms with larger Pt within the grains could generate further tensile stress/strain. If those grains were arranged in a two-dimensional array, the positive stress/strain changes would occur within the plane and the anisotropic dynamics could encourage parallel relaxation of the $L1_0$ basal plane. Rapid relaxation of any in-plane compressive stress during the growth and ordering of an FePt film, especially in crossing over to a tensile state, would prove advantageous in forming (001) texture. Such a mechanism would explain the relatively high degree of texture observed in most Fe-rich films from both S1 and S2 series. At an overall Fe-rich stoichiometry, the highly Pt-depleted fcc grains would lead to enhanced diffusion of Pt atoms

across the grain surface and amplified changes in stress. While chemical ordering occurs in parallel with the above process, the effect is not necessarily proportional to the degree of order achieved by the interdiffusion across grain surfaces.

Common to both sample series is an inverse relationship between the degree of (001) texture and the measured c-lattice parameter. The trend appears to be valid regardless of the cause of the lattice distortion, whether through increasing chemical order, excess smaller Fe atoms, or a compressive strain.

The dramatic overall differences in chemical order and (001) texture between series S1 and S2 films must be related to the change in bilayer thickness from ~6 Å to ~3 Å. Altering the as-deposited structure by such a seemingly small amount decreases the maximum achievable chemical order in S2 films to 0.90 from 0.94 and shifts the composition at which that maximum occurs from a Pt-rich to a Fe-rich stoichiometry. Trends in (001) texture are in relative agreement, with higher texture found in Fe-heavy samples for both series; however, except for the best textured S1 samples, S2 films maintain much better (001) texture throughout the measured composition range. A closer examination of the as-deposited structure is required to understand the cause of this difference.

Fe and Pt atoms deposited at relatively slow rates of ~0.3 Å/s onto water-cooled substrates, as the S1 and S2 films were, would have limited diffusion lengths during deposition. Such a low-energy process would limit mixing at layer interfaces; however, statistical roughening and self-shadowing could have ruined the idealized structure. Smooth interfaces between ultra-thin Fe-Pt layers are difficult to establish. A periodic structure was confirmed in sputter-deposited Fe-Pt multilayer films only when the individual layer thicknesses were greater than 8 Å [4.50]. A ~5 Å RMS roughness has been observed at the Fe-Pt interfaces of sputter-deposited ML films using 1-3 Å/s deposition rates, ~5 mTorr working pressure and < 240 °C substrate

temperature [4.51]. Even the interface between a 1.4 nm Pt and 4.9 nm Fe layer evaporated at 1.8E-8 Torr showed a roughness of 7.9 Å [4.52]. For repeated ~3 and ~6 Å Fe/Pt bilayers, signature Bragg diffraction peaks near 15° and 29° 2-θ would evidence a well-defined multilayer structure in these thin films, respectively. Figures 4.10(a) and 4.10(b) show XRR and XRD spectra from representative S1 and S2 as-deposited films. Total thickness oscillations are clearly visible at low angles for both films. Superlattice peaks from the 6.1 and 3.4 Å bilayers would manifest at 14.522° and 26.213° 2-θ, respectively, yet only the S1 as-deposited film has any indication of a peak near the anticipated location. Figure 4.10 (a) includes a partial spectrum from a blank substrate (green line) as comparison. The high angle (111) fcc-FePt diffraction peaks indicate interlayer mixing has formed disordered FePt grains of ~5 nm in diameter.

Two possible explanations exist for the observed differences between S1 and S2 series films. Both possibilities relate to the repeated elemental-layer design of the films, despite the lack of a clear as-deposited multilayer structure. The small Bragg peak from the as-deposited S1 film indicates a slight modulation in composition along the direction of film growth. In contrast, S2 films would be compositionally uniform. Any delay in the ordering process caused by diffusion in S1 films could reduce the amount of strain energy generated, resulting in a lower degree of texture. Regarding the trend in ordering with Fe:Pt ratio, ML FePt films demonstrated a higher propensity to order for Pt-rich compositions compared to a single layer film [4.46]. The S1 films, by resembling multilayers, might display a similar tendency. Additionally, the higher maximum chemical order in the S1 series films is similar to what is seen when comparing the resulting order in a homogeneous fcc as-fabricated samples versus a heterogeneous mixture of disordered and elemental Fe-Pt regions [4.53]. The effect would probably not be as pronounced in the thin films investigated here, but any compositional gradient could help homogenize the stoichiometry.

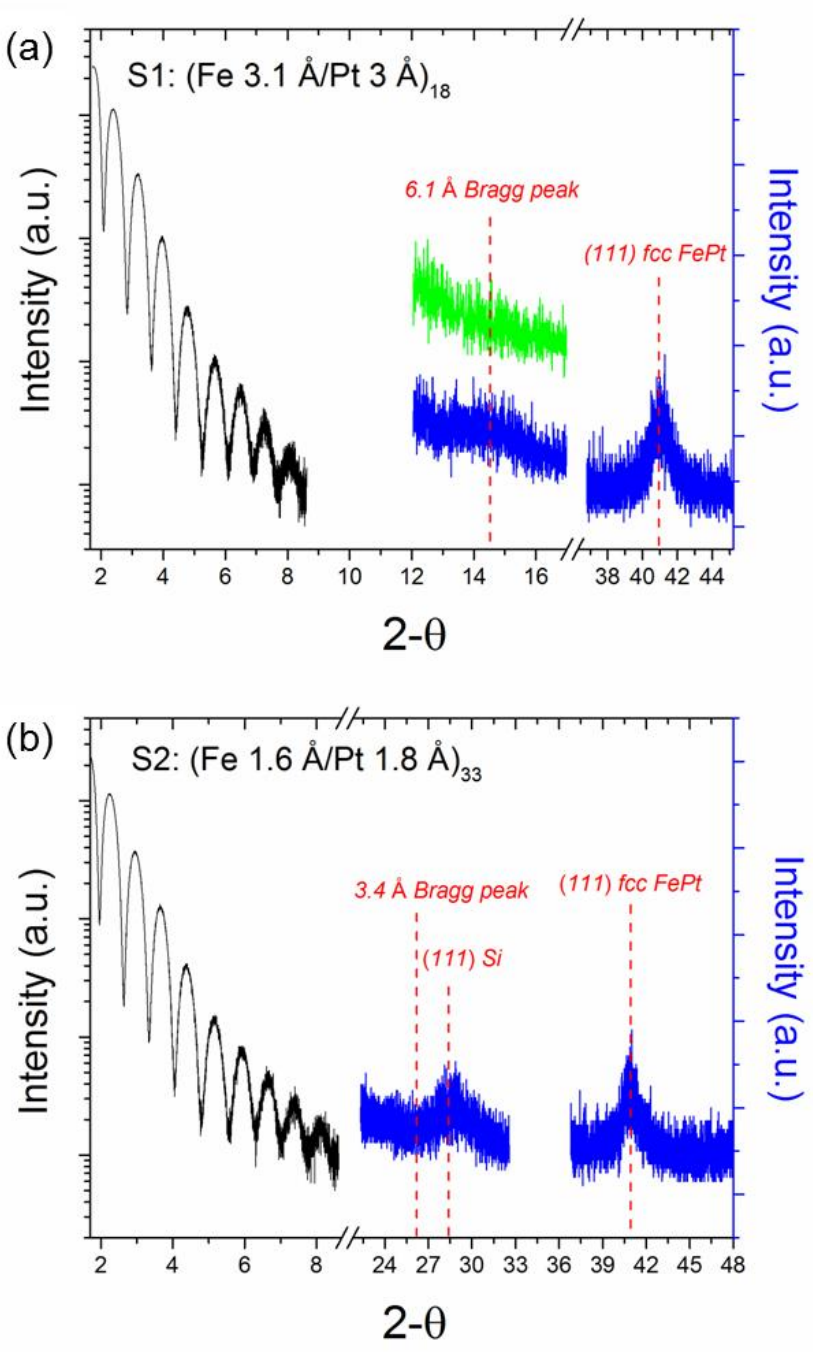

FIG. 4.10. As-deposited XRR and XRD spectra from B-series films with 6.1 Å (a) and 3.4 Å (b) bilayer thicknesses. The green spectrum in (a) was taken from a blank substrate for comparison.

The second explanation is related to a possible consequence of the multilayer deposition mechanism. In the 3M sputtering system, multilayer deposition is accomplished by alternating the substrate's exposure over two different sputtering guns. While the turntable

rotates between each layer, the brief break in deposition would give any remaining gases in the deposition chamber an opportunity to condense on the growing film. Trapped gases buried in subsequent layers would essentially create voids in the deposited film. Similar to other defect structures in thin films, voids typically enhance atomic diffusion during annealing and the $L1_0$ ordering process would benefit from the resulting combined reactions. By maintaining the same ~12 nm total thickness as the S1-series, S2 films require nearly twice as many bilayer repetitions. Therefore, S2 films could have roughly twice the defect density as their S1 counterparts, leading to significantly accelerated kinetics and a higher degree of strain-driven (001)-texture. An analysis of the defect structure in the as-deposited films would be useful to confirm this hypothesis.

4.3.4 Summary of Compositional Dependence Study

The degree of chemical order and (001) texture in ~11 nm non-epitaxially grown FePt ML thin-films clearly depend on Fe:Pt stoichiometry. S and LOF peak near equiatomic compositions for two sample series with different bilayer thicknesses. The degree of (001) texture for all samples corresponds closely with a contracting *c*-lattice parameter and the non-epitaxial texturing process can be ascribed to SEDSGG. The presence of Laue oscillations surrounding (001) XRD peaks of highly textured S2-series films indicates a morphology of flat, grains of large in-plane size and data-fitting yields vertical dimensions close to the nominal film thickness. Correlations between estimated grain size and texture of most films varied considerably and inaccuracies in both film and grain thickness estimates preclude drawing hard conclusions. The measured in-plane grain size indicates predominantly two-dimensional grain growth and all estimated grain sizes point to minimal out-of-plane intergranular interactions, supporting SEDSGG.

Magnetic anisotropy measured for the S1 series samples is maximized for an equiatomic composition and is found to only roughly correlate with the chemical order trend. Series S1 out-of-plane coercivities peak at ~14 kOe for compositions on either side of 50 at.% Fe, with a secondary maximum of ~12 kOe at 46.8 at.% Fe. The drop in coercivity at an equiatomic composition is correlated to a change in the grain morphology of that film. Coercivities in Fe-rich S1 films remain relatively constant at ~12 kOe. All magnetic hysteresis loops demonstrate out-of-plane anisotropy; however, in-plane coercivities are consistently significant. Elimination of in-plane c-axis variants would be required to close those loops. Remanence squareness is highest for the 50 at.% film, corresponding to a high LOF.

Benefits of using an off-stoichiometric composition to attain high degrees of chemical order and/or (001) texture in ML FePt thin films originate from the enhanced ordering kinetics and inherent strain-states afforded by excess Fe or Pt atoms. Consistently better (001) texture was achieved in Fe-rich films; a similar result is seen in CoPt thin films with a higher ratio of smaller Co atoms [4.5]. A universally optimal composition was not determined; trends depend on other film fabrication parameters, in this case the multilayer deposition scheme. Two possible explanations for the observed differences between S1 and S2 series films are given, although confirmation of either requires further evidence. It is hypothesized that decreasing the bilayer thickness and/or increasing the number of layer repetitions accelerates the Fe-Pt ordering kinetics, leading to significantly enhanced (001) texture.

4.4 Effect of Bilayer Thickness

It has been demonstrated that decreasing the Fe/Pt bilayer thickness in non-epitaxially grown thin-films leads to a higher degree of (001) texture [4.13] (see Sec. 4.3). In Ref. 4.13, ten nm films with bilayer thicknesses ranging from 4.3 to 34.4 Å clearly display a greater (001)-to-(111) diffraction peak-ratio with thinner bilayers after annealing for 5 seconds at 550 °C. The

improved texturing is attributed to a structural resemblance of the near-monatomic as-deposited multilayers to an (001)-oriented $L1_0$ crystal. The films with thicker bilayers demonstrated progressively dominant (111)-texture as the increasing required diffusion was presumed to destroy the texture-inducing layered structure. Similarly, a high degree of (001) texture was achieved in 6.1 nm ML films using a bilayer structure of (Fe 1.6 Å/Pt 1.8 Å), and the (001) diffraction peak intensity reduced with increasing bilayer thicknesses [4.43]. The very thin layers used in that study reduced the obligatory diffusion lengths, resulting in a relatively low kinetic ordering temperature. However, a significantly higher annealing temperature was required to achieve chemical order and (001) texture from ML films with monatomic layer thicknesses of ~0.2 Å [4.8].

Compositional heterogeneities can affect the ordering kinetics of FePt samples in many ways depending on, among other things, the size of the different regions and their interfaces. Atomic diffusion is thermally activated and diffusion lengths scale with the square-root of annealing time; therefore, samples with extended regions of differing composition require longer times and/or higher temperatures to complete the ordering process [4.9,4.13,4.43,4.53-4.55]. Conversely, large compositional gradients accelerate diffusion and can enhance the driving force for ordering [4.51,4.56,4.57]. Typical samples used for interdiffusion studies consist of segregated regions with dimensions greater than a few 1 nm. Changes in ordering kinetics between thin films deposited with 3 and 6 Å bilayers, such as those used for sample series S1 and S2, have not been reported. While those particular films do not retain sharp interfaces at the deposited length scales, a slight compositional modulation is seen in the S1 films. Section 4.3 demonstrates that even the small increase in deposited layer thicknesses of ~1.5 Å enhances the chemical order at the expense of (001) texture in slightly Pt-rich films. However, it is unclear

whether the change in properties results from a compositional distribution in series S1 or the increased number of interlayer breaks in deposition in series S2.

This section investigates the effect on chemical order and (001) texture of varying the as-deposited bilayer thickness of FePt multilayer films in the range of 0.3 – 2 nm. Specifically, four films were deposited with bilayer thicknesses of 3.4, 6.1, 12.8 and 19.2 Å, denoted sample Series B. Total film thickness was maintained at ~12 nm by adjusting the number of bilayer repetitions and each film's Fe/Pt layer ratio yielded a composition of ~48 at.% Fe. A fifth, 12 nm film consisting of a single cosputtered layer was included for comparison and is referred to as the co-deposited or "zero" bilayer-thickness film. It represents an analogous film yet without the artificial interfaces or compositional modulations of the ML films. Specific films are referred to by their bilayer thickness, e.g. "3.4 Å bilayer-film" denotes the film fabricated with a bilayer thickness of 3.4 Å.

Low angle XRR and high angle XRD characterize the as-deposited film structures. Coupons cut from each film are processed at 600 °C for five minutes according to the details given in Section 4.2. High-angle XRD is also used to quantify the degree of $L1_0$ order, (001) texture, vertical grain size, and lattice parameters of the processed films.

4.4.1 Series B Results and Discussion

As-deposited structures of the B-series films can be seen from the low-angle XRR and high-angle XRD spectra in Figs. 4.10(a) and 4.10(b), and 4.11(a), 4.11(b) and 4.11(c) for bilayer thickness of 6.1, 3.4, 0, 12.8, and 19.2 Å, respectively. The as-deposited 3.4 and 6.1 Å bilayer-films are discussed in Section 4.3.3, where it is noted that a multilayer-like compositional modulation remains only from the 6.1 Å bilayers. As would be expected, the co-deposited film shows only low-angle Kiessig oscillations from the direct beam. The high angle peak from that sample, near 40.92° 2-θ, represents diffraction from (111) planes of fcc-FePt, and the

corresponding FWHM estimates an average as-deposited vertical grain size of 6.5(2) nm from application of the Scherrer formula. Low-angle Bragg peaks at 7.4° and 5.4° 2-θ visible in Figs. 4.11(c) and 4.11(b), respectively, clearly indicate as-deposited superstructures in those thicker-bilayer films. Similar high-angle diffraction peaks as seen from the other films signify (111)-oriented fcc-FePt grains of 5.9(1) and 6.1(1) nm diameter in the 12.8 and 19.2 Å bilayers-films, respectively. Figure 4.11(d) demonstrates no low-angle superstructure peaks in the XRR data from the processed 19.2 Å bilayer-film.

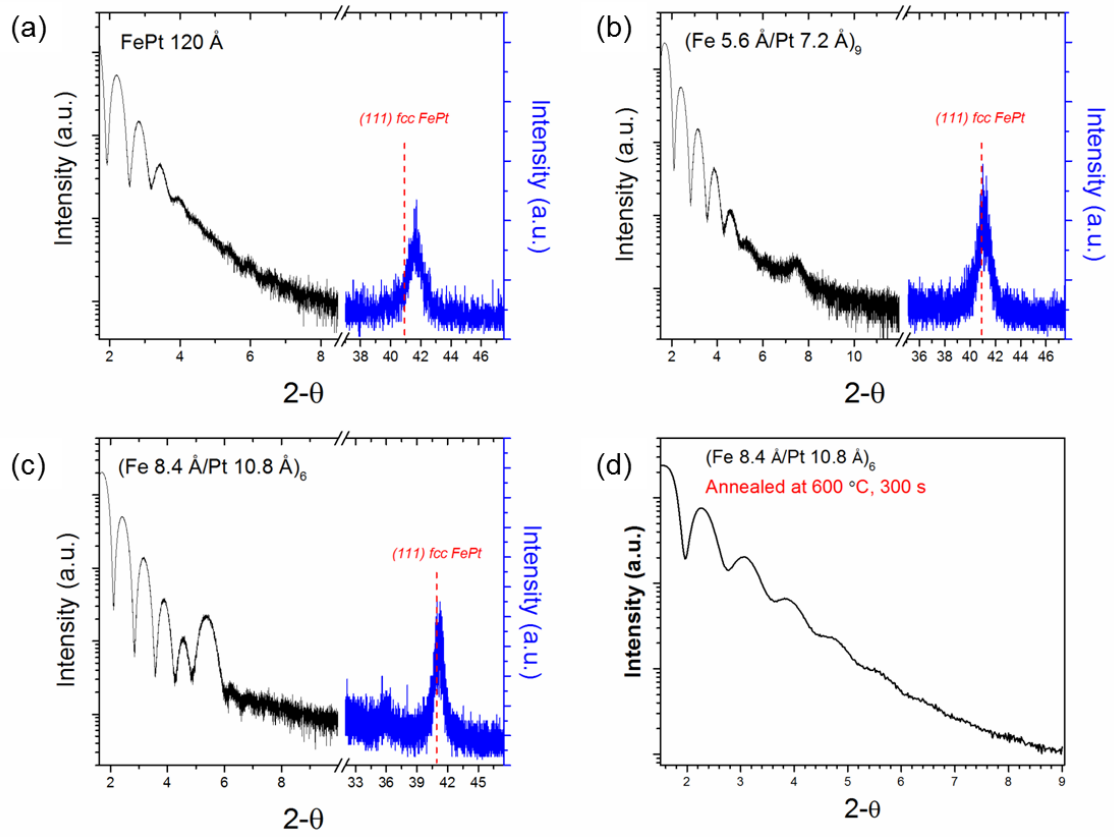

FIG. 4.11. As-deposited XRR and XRD spectra from the B-series co-deposited film (a) and the films with 12.8 Å (b) and 19.2 Å (c) bilayer thicknesses. XRR from the processed 19.2 Å-bilayer film is shown in (d).

Figure 4.12 shows the XRD spectra from processed B-series films. (001) superstructure and (002) peaks shifted to higher angles than the fcc position evidence the ordered phase in all films. The diffracted signal strength decreases with increasing bilayer thickness and is very low in

the co-deposited film's data. A FePt-(111) peak is not visible in the 3.4 Å bilayer-film but is present in all others and even dominant in the co-deposited film. Laue oscillations surrounding the (001) peaks in the 3.4 and 6.1 Å bilayer-films' spectra indicate coherently diffracting (001)-textured crystallites with heights within 2% of their respective as-deposited film thicknesses. Shifting of the (001) and (002) peak positions to lower angles indicates an expanded *c*-lattice parameter for the thicker bilayer-films. The two thickest bilayer-films also have very broad (002) peaks with large low-angle shoulders, possibly from an (002)-textured disordered phase or in-plane c-variants of the ordered phase.

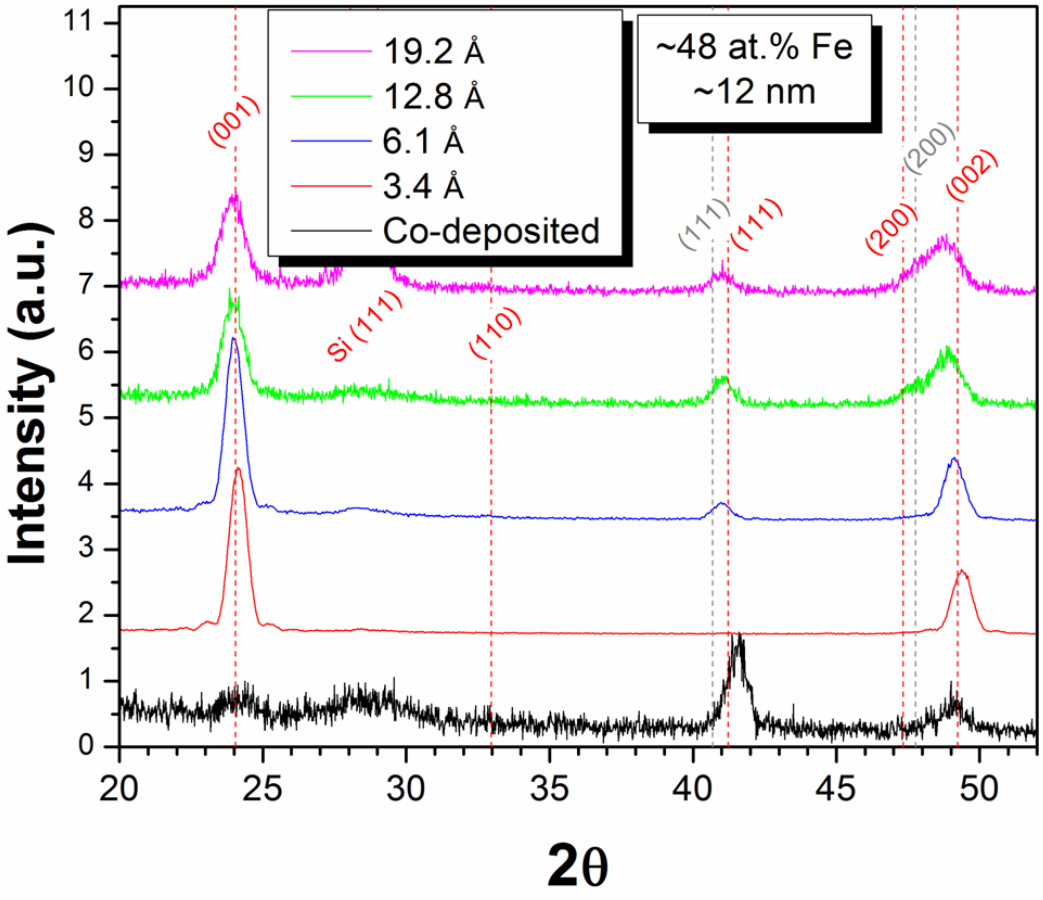

FIG. 4.12. XRD spectra for samples series B1. Red and grey dashed lines represent anticipated peaks for the $L1_0$ and fcc FePt phases, respectively.

Trends in chemical order, (001)-texture, grain size, and c-lattice parameter determined from the x-ray spectra are plotted in Fig. 4.13. The co-deposited single-layer film, denoted by a bilayer thickness of 0, is vastly inferior to the ML films with respect to S and LOF. The best (001) texture is found with the thinnest bilayer thickness, and texture degrades gradually as bilayer thickness increases. As revealed when comparing slightly Pt-rich S1 and S2 series samples, the 6.1 Å bilayer-film exhibits a higher degree of $L1_0$ order than the film with 3.4 Å-bilayers; S then decreases gradually for subsequently thicker bilayers.

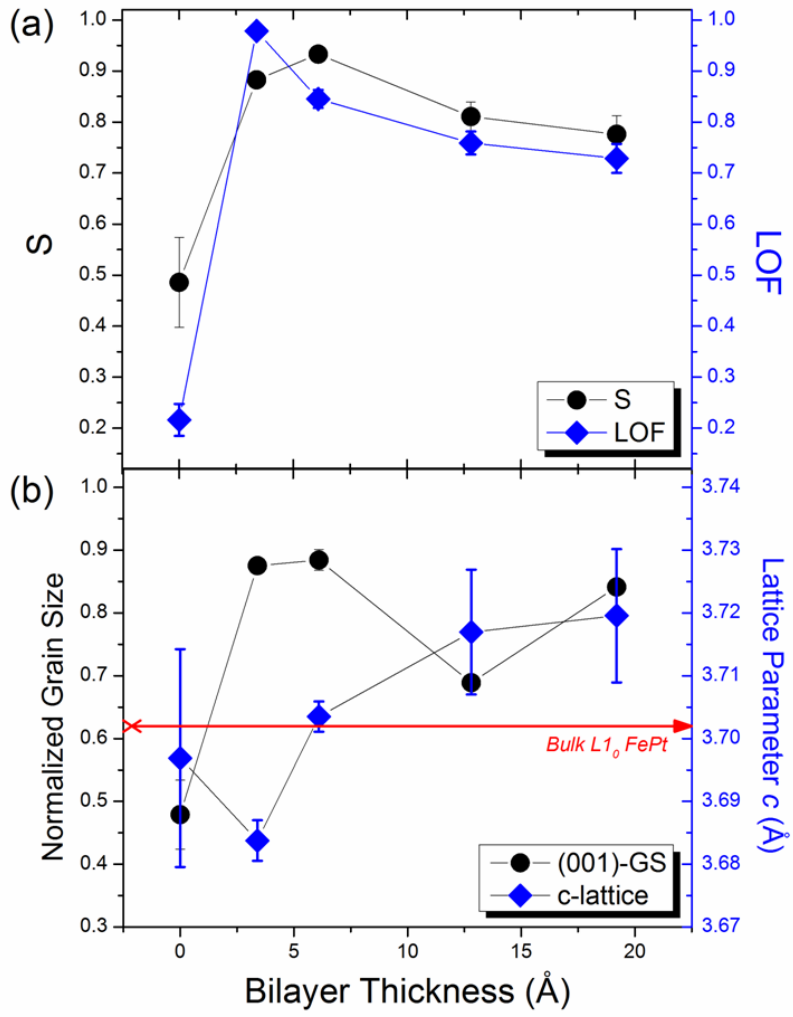

FIG. 4.13. (a) Chemical order, S, and degree of (001) texture, LOF, for series B1 and B2. (b) Normalized (001)-grain sizes and c-lattice parameters for B-series samples. The red line denotes the c-lattice for bulk $L1_0$ phase.

Figure 4.13(b) demonstrates an increasing *c*-lattice parameter in the ML films of larger bilayer thickness. The trend corresponds with a loss of (001)-texture, similar to what was seen in S-series films. The normalized vertical coherence length from the (001)-diffraction planes as estimated by the Scherrer equation, (001)-GS, remains constant at ~0.88 for the first two ML films, drops to 0.69 for 12.8 Å bilayer thickness, then increases to 0.84 for the thickest bilayer. Fitted Laue oscillations from the (001) XRD peaks of the 3.4 and 6.1 Å bilayer-films yield normalized grain sizes close to unity; as was seen in the S-series data, the Scherrer equation likely underestimates the real grain sizes in these films. The co-sputtered film displayed an (001)-GS of < 0.5, significantly smaller than any ML film, and a relatively short *c*-lattice parameter. The latter, however, has a significantly high degree of uncertainty due to the poor SNR of the XRD data.

Low angle XRR of the processed 19.2 Å bilayer-film, the thickest of bilayer investigated, is absent of any superstructure peak [see Fig. 4.11(d)], indicating interdiffusion has destroyed any repeated compositional variations. Estimated diffusion lengths in a Fe/Pt ML film annealed for 300 s at 600 °C are about 5.1 and 1.6 nm for Fe in Pt and Pt in Fe, respectively. Fe tends to diffuse more readily into Pt, however, either route would be sufficient to mix the multilayers used here, supporting the XRR data. Nevertheless, diffusion of Fe in $L1_0$-ordered FePt is significantly more restrictive, with a diffusion length of only 0.3 nm along the c-axis. Ordered nuclei appearing early in a thermal treatment could alter the diffusion process from a simplified Fe/Pt or fcc-Fe_xPt_{1-x}/fcc-$Fe_{1-x}Pt_x$ diffusion couple. The decreasing values of S for bilayers thicker than 6.1 Å could be due to atomic diffusion being hampered in such a way. Longer annealing times could result in improved chemical order. Regarding the similar reduction in (001)-texture, because SEDSGG requires rapid grain growth early in the annealing process, any hindrance would be detrimental to the resulting texture.

The co-deposited film exhibits poor chemical order and (001) texture in general. Films with larger fcc grain sizes tend order less readily than ones with smaller grains due to the increased granular interface density. Additionally, the lack of a strong driving force for diffusion could have resulted in a compositionally inhomogeneous film, despite the likely short required diffusion lengths in the as-deposited structure. An LOF of ~0.2 indicates some preference for (001) textured grains, especially considering the tendency for FePt to develop (111) fiber texture. Non-epitaxial (001) texturing has been achieved using composite targets and co-sputtering techniques with greater success in films much less than 10 nm.

Plotting S and LOF versus the number of interfaces introduced during deposition (not shown) would demonstrate an optimal number of interfaces around 18 for achieving a high degree of chemical order and an increased usefulness of interfaces in generating (001) texture. An experiment investigating the effect either the type or pressure of the chamber gas or introducing pauses during deposition (even without changing targets in a ML scheme) could help clarify the relative importance of individual layer thickness versus interface density.

4.4.2 B-Series Conclusion

Slightly Pt-rich 12 nm FePt films yield better (001) texture with thinner bilayers. Although the 1.6/1.8 Å layers essentially mix during deposition, the trend of increasing LOF does not extend to an analogous co-deposited film. It is possible that the interfaces created by briefs pauses in deposition during ML fabrication enhance the ordering kinetics. A bilayer thickness of 6.1 Å yields the highest chemical order. However, there is no evidence that bilayers thicker than 6.1 Å yield improved diffusion rates as some studies would predict [4.58]. Results suggest that a bilayer of ~6 Å represents the optimal as-deposited structure regarding diffusion lengths and an enhanced driving force for diffusion and ordering. It is possible that the thicker-bilayer films could achieve a similar degree of order with longer annealing times or higher temperatures.

(001) texture might improve in those films with a higher annealing temperature, but probably not with a longer annealing time.

4.5 Effect of Total Film Thickness

Total as-deposited thickness is another factor determining the kinetic ordering temperature, grain-growth behavior, crystalline texture, and resulting magnetic properties of FePt film [4.59,4.60]. Thicker films tend to have a higher number of nucleation sites for ordering and magnetic reversal as well as more magnetic and mechanical intergranular interactions. In contrast, thinner films have fewer such interactions and nucleation sites yet can more readily undergo anisotropic two-dimensional grain growth due to vertical growth stagnation or adopt an island-like morphology. Post-deposition annealed multilayers of [Fe 20.3 Å/Pt 17.3 Å] processed at 300 °C for 15 minutes exhibited significantly larger coercivities for total film thicknesses in the range of 300 and 600 Å, as compared to films as thin as 150 Å or as thick as 900 Å [4.61]. Chemical order has been shown to increase in proportion to total film thickness for various ML films in the range of 5 to 100 nm post-deposition annealed between 400 and 500 °C [4.9,4.60]. On the other hand, monatomic ML films annealed at 700 °C for 30 minutes exhibited a high degree of chemical order at 5 nm with a sharp decline for films thicker than 20 nm [4.8]. Yet another series of thin films displayed no variation in chemical order with film thickness ranging from 22 to 88 nm [4.7].

Crystallographic texture in post-deposition annealed FePt thin films demonstrates a somewhat unusual trend versus total film thickness compared to typical metallic fcc crystals. The closely-packed {111}-planes of FePt and other fcc metals have the lowest surface-energy and therefore tend to orient parallel to the free surface, especially in very thin films where surface-energy dominates the determination of a crystallite's orientation. However, in the presence of an ordering-strain concurrent to annealing, non-epitaxial mechanisms such as

SEDSGG can promote (001)-texture in the thinner films instead. [4.6,4.7,4.9]. This unusual trend is attributed to the ease of the grains in a thinner films to span the film thickness in compliance with the Vook-Witt grain interaction model [4.7].

The exact texture trend with film thickness depends on the deposition and annealing conditions used in fabrication. Codeposited films indicated a sudden loss of (001) texture for total thicknesses greater than 30 nm after annealing at 800 °C for 2 minutes [4.10]. (001) texture in monatomic-ML films annealed at 700 °C for 30 minutes peaked in a 10 nm thick film [4.8]. Drastic changes in film morphology in FePt films less than 6 nm can alter the development and subsequent relaxation of the in-plane tensile strain necessary for (001) texturing by SEDSGG [4.19]. A comprehensive study into the effect of total thickness of ML films with different stoichiometries and bilayer thicknesses would prove useful to understand and optimize the effects of fabrication parameters in achieving highly ordered and (001) textured FePt thin films.

Section 4.5 presents investigations of the effect of total film thickness on chemical order, crystalline texture, film morphology, and magnetic hardness. Three series of ML films are examined, which consist of two different compositions and three different bilayer thicknesses. Series T1 samples have an average Fe-rich composition of 56 at.% Fe[21], average bilayer thickness of 6.2 Å, and range in total thickness from 36 to 126 Å. Series T2 consists of two sub-series near 48 at.% Fe but with bilayer thicknesses of 3.4 and 12.8 Å, with total thicknesses ranging from 40.8 to 200.6 and 51 to 205 Å, respectively. Post-deposition processing was performed as per the description in Section 4.2. Magnetic hysteresis loops were measured by SQUID magnetometer and plan-view TEM images were acquired on the JEOL microscope as described in Chapter 3.

[21] Series T1 actually combines two smaller sets of sample with Fe concentrations of ~55 and ~57 at.%. The apparent noise in the S and LOF data is likely attributed to this compositional variance.

4.5.1 Series T1 Results and Discussion

Studies of non-epitaxial texturing of FePt ML films reported in the literature have predominantly used Fe-rich compositions with total thicknesses between 10 – 20 nm [4.8,4.9,4.13,4.21]. As demonstrated in Section 4.3, a relatively broad range of Fe compositions greater than 50 at.% display consistently high degrees of (001) texture. Two particular studies have investigated the thickness-dependence of texture in the range of 4.3 and 40 nm. As previously mentioned, monatomic MLs exhibited a relatively sharp peak in texture at 10 nm, with degraded texture in films with 5 nm or >10 nm thickness [4.8]. (001) texture in the other study was dominant at 4.3 and 6.5 nm film thicknesses as (111)-oriented grains only appeared in 11.9 nm thicker films or thicker [4.9]. The aforementioned studies utilized monatomic or very thin bilayer for ML deposition, whereas the T1-series films possess thicker ~6.2 Å bilayers.

X-ray diffraction spectra from annealed series T1 samples in Fig. 4.14 all indicate relatively well ordered and textured films. Intensities of (001) superstructure peaks are dominant over both (111) and (002) peaks, the former being very diminutive in the 36 and 50 Å films. Peak positions from the c-axis shift toward higher angles and peak breadths indicate a changing vertical coherent diffraction length, (001)-GS, with increasing film thickness.

Fitting the xrd spectra yields quantitative information regarding the chemical order and (001)-texture in S and LOF, which can be seen in Fig. 4.15 (a). Texture remains relatively high with LOF > 0.9 for all film thicknesses. The large error bars on LOF for the thinnest films are due to very small (111) peaks, and a slight decreasing trend in LOF is likely. As film thickness increases from 36 Å, S initially decreases from 0.77(2) down to 0.69(2) at 75 Å, then recovers back up to its initial value and higher for films > 100 Å. A lower degree of order in thinner films could be related to a dearth of nucleation sites at Fe-rich compositions [4.25], however, this would not explain the upturn in S at 34 Å. Compared to the effects of other deposition

parameters, S and LOF vary only a little with respect to film thickness within the range investigated for these Fe-rich ML films.

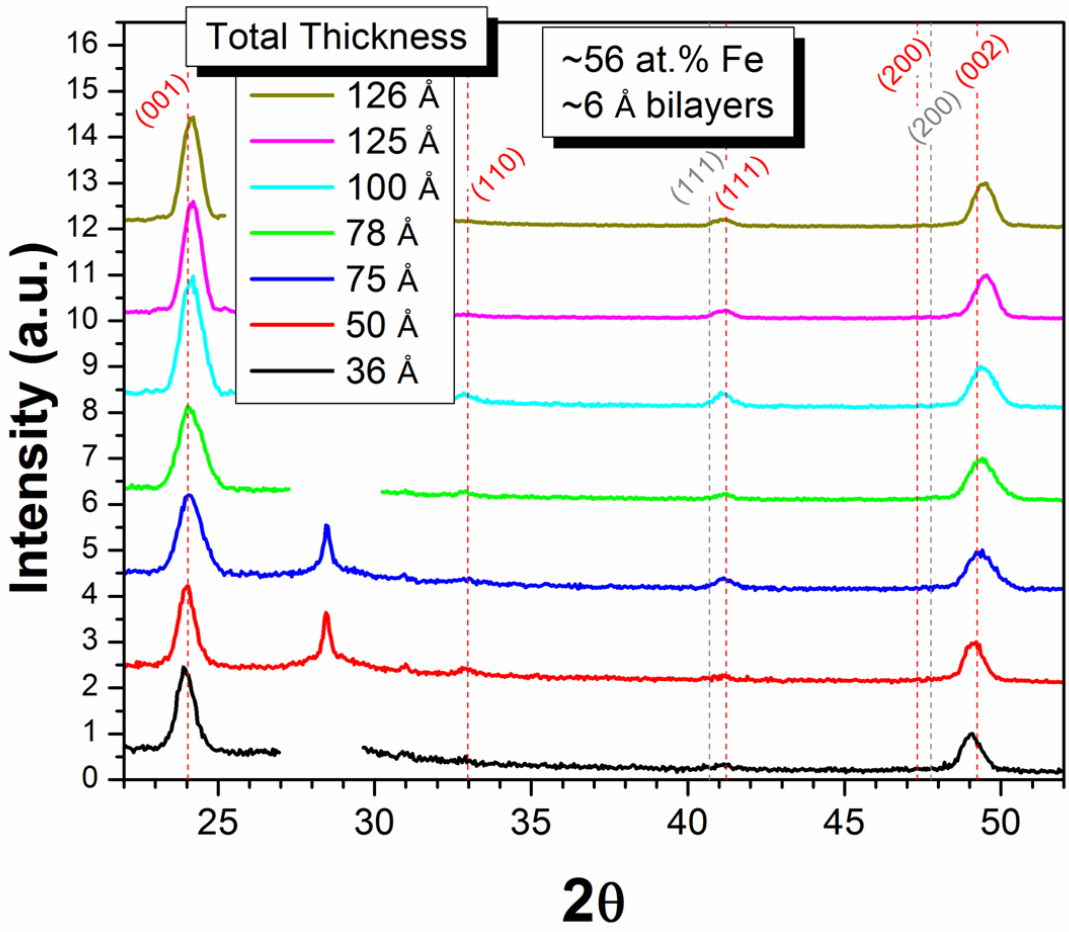

FIG. 4.14. XRD of sample series T1. Red and grey dashed lines represent anticipated peaks for the $L1_0$ and fcc FePt phases, respectively.

Figure 4.15(b) plots both normalized grains size and c-lattice parameter, determined from (001) diffraction peaks FWHM with the Scherrer equation and from the (001) peak positions, respectively. The (001)-grain sizes are normalized to each film's respective nominal thicknesses; therefore, a value greater than one clearly indicates an agglomerated morphology. The phenomenon of nanoscopic islands formation in post-deposition annealed thin metallic films on oxide substrates is well documented [4.9,4.16,4.21,4.62]. Deep vertical grooves developing at grain-boundaries halt lateral growth, and further growth becomes vertical as grain

boundary material agglomerates. Voided regions baring the substrate from the grooves advance rapidly due to the relatively low surface-energy of the substrate versus the FePt grains. Once growth is no longer anisotropically in-plane, compressively strained out-of-plane crystal lattices can relax. The relatively large c-lattice parameters of the thinnest films are likely attributable to

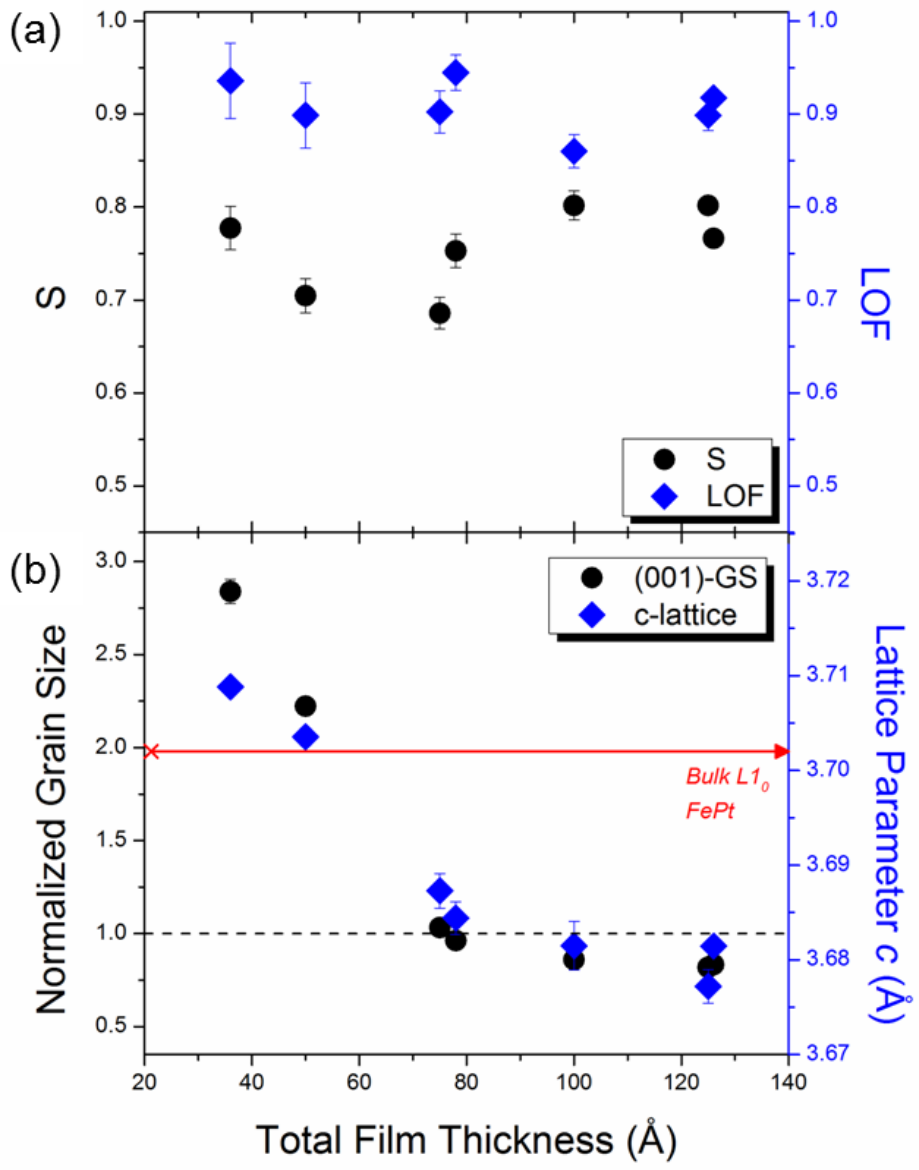

FIG. 4.15. Trends of S and LOF (a), and normalized grain size and *c*-lattice parameter (b), both with respect to total film thickness. The *c*-lattice parameter for bulk $L1_0$ FePt is included as the solid red line in (b). The dashed grey line marks a normalized grain size equal to the nominal film thickness.

this type of relaxation; that those films are highly (001)-textured is due to the rapid onset of in-plane-tensile/out-of-plane-compressive strain early in the annealing process [4.63]. Additionally, grains in these extremely thin films would quickly grow to span the film thickness to satisfy the Vook-Witt interaction conditions. The initially compressed c-axis would relax as growth became primarily vertical, however the (001) texture generated by SEDSGG early in the annealing process would remain. Using the bulk lattice parameter of L10 ordered FePt as a reference, c-axis strain changes from tensile to compressive as the T1 films' normalized grain sizes approach one. The crossover thickness for the change in grain growth behavior is ~75 Å, although this is probably an underestimate due to the inaccuracy of the Scherrer method.

The plan-view TEM image presented in Fig. 4.16(a) shows that a 50 Å film is continuous as deposited. Figure 4.16(b) shows the same film, after processing at 600 °C for 300 seconds, having developed isolated islands with approximately 65% of the film area bare to the substrate. The border between the substrate and film roughly follows the shape of the grain boundary, supporting the notion of thermal grooving. Grain sizes from XRD indicate average grain heights of 112 Å with average lateral diameters of 293(8) Å. The latter was estimated by fitting a lognormal distribution to the areas of 100 grains traced in the *imageJ* program. Figure 4.16(c) and 4.16(d) show the increased coverage with film thickness, with only ~21% bared substrate at 75 Å and full coverage at 125 Å. In-plane grain diameters increased to 455(39) and 571(17) Å for the two thicker films, while vertical grain sizes actually shrank to 77 and 103 Å, respectively. The agglomerative growth visible in the TEM image of the 75 Å film and the 121 and 125 Å vertical grain height given from fitting the two thickest films' (001)-Laue oscillations reinforce the tendency of the Scherrer equation to underestimate vertical grain sizes. For the given annealing conditions, a film of about 125 Å is required to maintain film continuity.

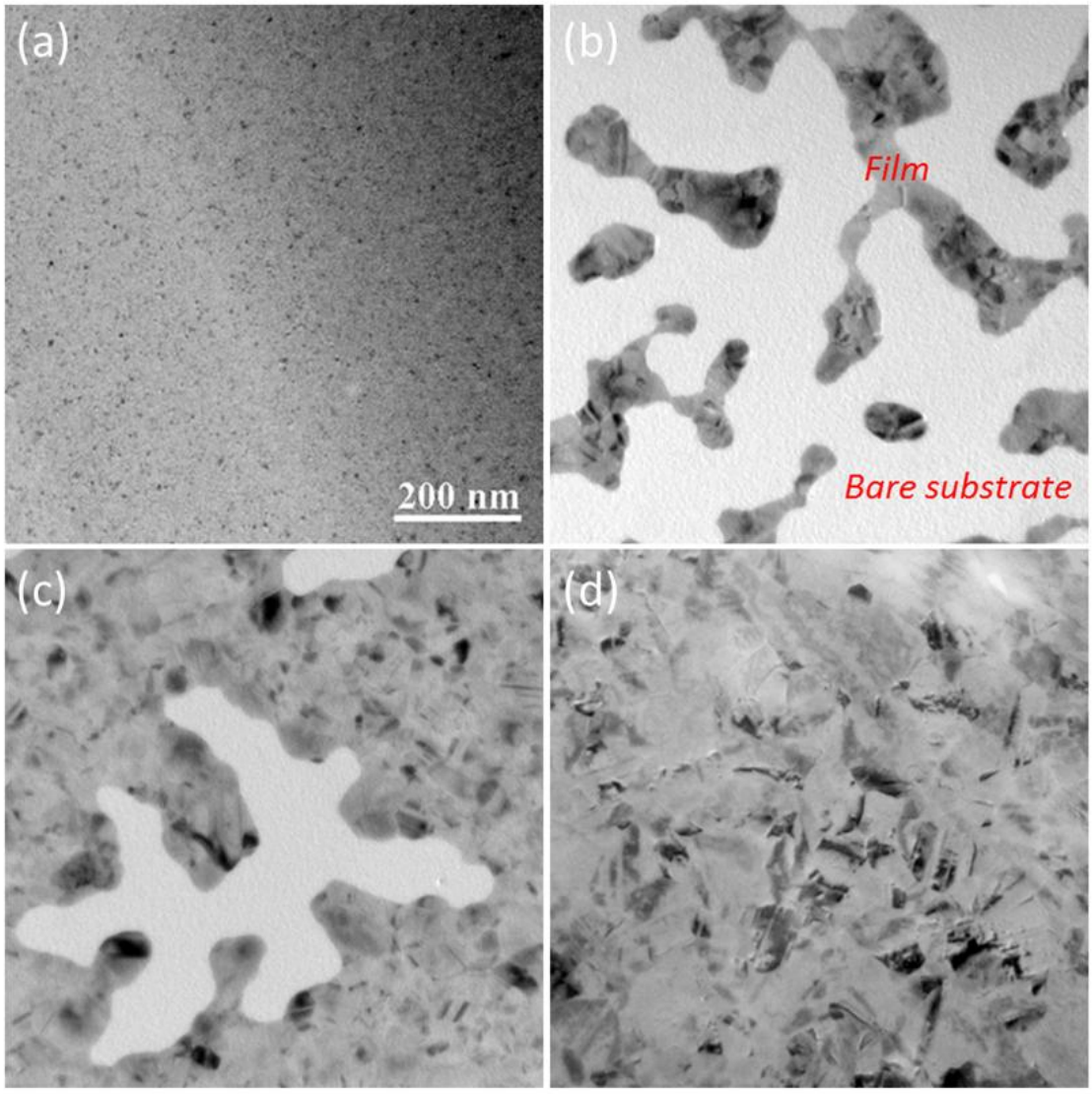

FIG. 4.16. Plan-view TEM of series T1 samples with 55.1 at.% Fe content. (a) and (b) show the 50 Å sample in the as-deposited and post-processed states, respectively. (c) and (d) show processed samples of 75 and 125 Å total thickness, respectively.

4.5.2 Series T2 Results and Discussion

Pt-rich ML FePt thin films have not been extensively investigated in the literature. As previously mentioned, Pt-rich compositions have been predicted to possess a higher density of nucleation sites for the ordered phase which should aid the ordering process of thinner films [4.25]. In a separate study, in-plane coercivities of 60 nm ML films were maximal for Pt-rich compositions, however, (001)-texture was not investigated in that study [4.46]. Section 4.3

revealed greater variation in LOF but the highest overall S for compositions just less than 50 at.% Fe.

The films in samples series T2 average a slightly Pt-rich compositions of 47.8 at.% Fe. Series T2 is subdivided into T2A and T2B for the two bilayer thicknesses investigated, 3.4 and 12.8 Å, over thicknesses ranging from 40.8 to 200.6 Å and 51 to 205 Å, respectively. Two different bilayers thicknesses are investigated to study the effect of utilizing a possible composition modulation versus a well-defined ML deposition scheme in films both thinner and thicker than those in Section 4.4.

Figure 4.17 and 4.18 show the XRD spectra for both T2A and T2B samples. The data is plotted in log-scale to clarify the extremely small (111) peaks in most of the 3.4 Å bilayer-films. Similar to the T1 samples series, all films appear relatively well ordered. In general, T2A films seem extremely well textured, with only a small (111) peak visible in the thinnest and thickest films. (001)/(002) peak positions shift toward a higher angle for 3.4 Å bilayer-films thicker than 51 Å, concurrent with the appearance of Laue oscillations. A minute (111)-peak intensity points to a well-textured T2B film at thickness of 51 Å; however, (001)-texture degrades steadily with increasing film thickness. No peak shifts or Laue oscillations are visible for any of the thicker-bilayer films. The $L1_0$ (200) peak emerges in the 115 Å T2B film and gains prominence in the thicker films.

Chemical order in T2A and T2B series films peak at 150 and 115 Å, respectively, and is higher for the thin-bilayer films at all comparable thicknesses [see Fig. 4.19(a)]. The larger driving force for ordering anticipated for thicker FePt films might explain the initial decrease in S for decreasing total film thickness [4.9,4.64]. This trend agrees with predicted enhanced kinetic barriers to ordering in very small FePt nanoparticles [4.65] along with the effect of the absorption limit of FePt for radiation-based annealing [4.66]. However, this does not explain the

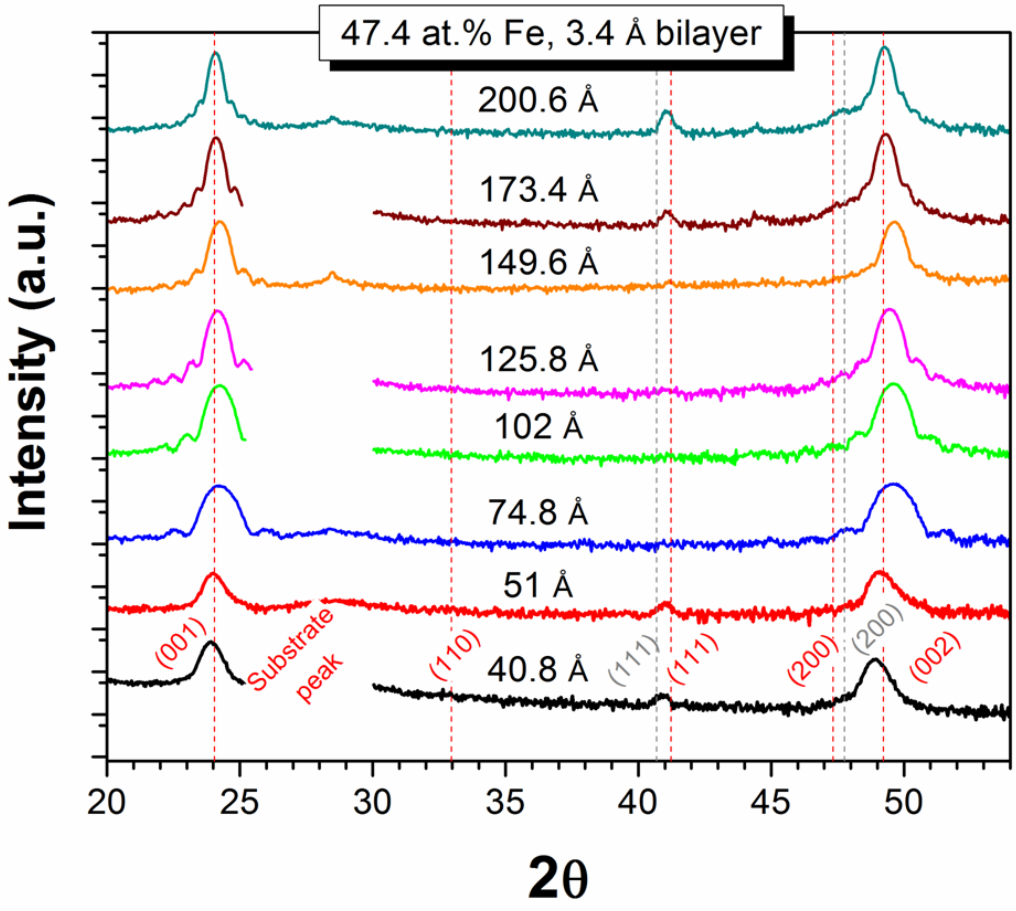

FIG. 4.17. XRD diffraction patterns for sample series T2A. Fe at.% is 47.4 with a bilayer thickness of 3.4 Å. The spectra are plotted on a log-scale to enhance the visibility of the diminutive (111) peak. Large substrate peaks have been removed for clarity. Red and grey dashed lines represent anticipated peaks for the $L1_0$ and fcc FePt phases, respectively.

upturn in the thinnest films nor the decline in S after peaking, although the latter effect was seen in monatomic ML films thicker than 20 nm [4.8]. The higher degrees or chemical order in the T2A films agrees with the results from Section 4.4. Interestingly, the highest chemical order of 0.93(1) for the ~3 Å bilayer-films at a 15 nm total thickness is comparable to that of the S1-series with a similar composition but only 120 Å in thickness.

Figure 4.19(b) shows a high degree of texture in both the thinnest T2A and T2B films. LOF of the T2A films maintains at >0.95 despite the slight dip at 50 Å, yet begins to decline gradually by 200 Å. On the other hand, (001)-texture drops quite rapidly as thickness increases

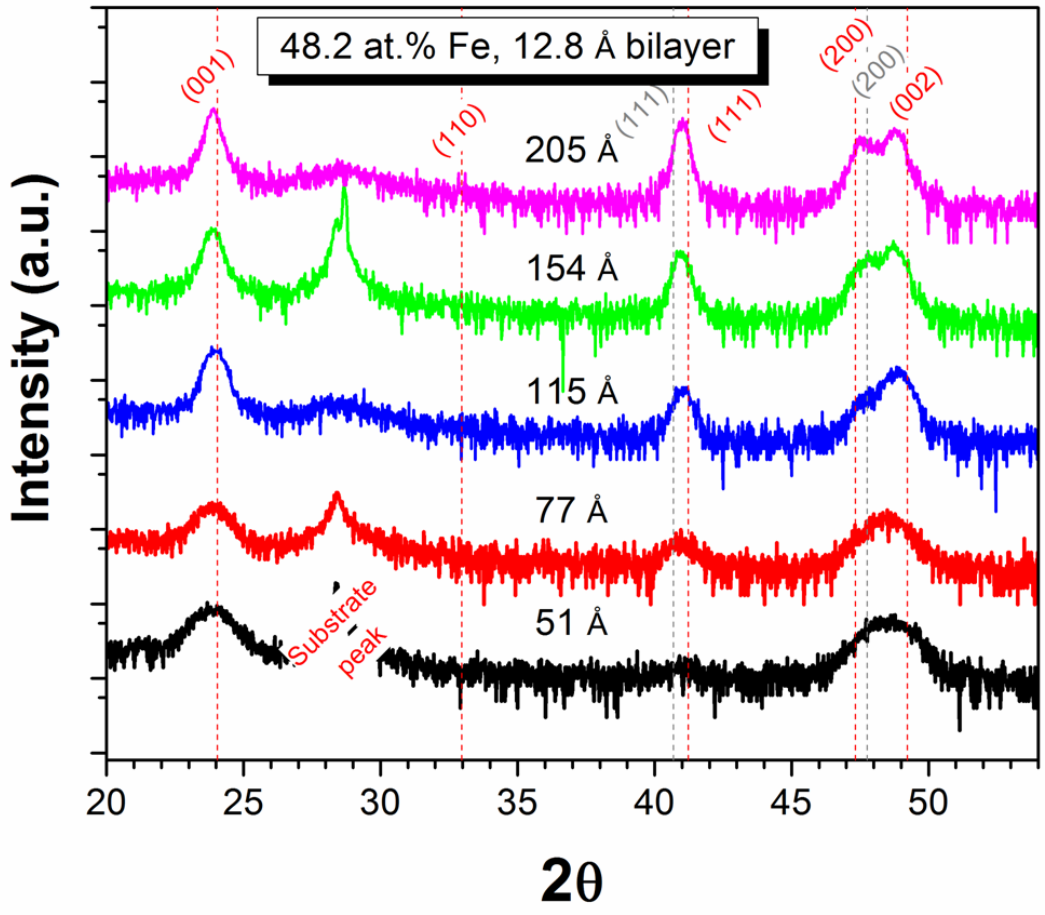

FIG. 4.18. XRD diffraction patterns for sample series T2C. Fe at.% is 48.2 with a bilayer thickness of 12.8 Å. The spectra are plotted on a log-scale for easy comparison with series T2A and T2B.

in the T2B films; a high degree of texture, LOF > 0.9, only occurs in the 51 and 77 Å films. A slight rise in texture is visible in the T2A films at 75 Å as compared to the 41 Å film. It seems that there is an optimal film thickness for non-epitaxial texturing which depends on the deposition, and possibly processing, scheme.

Grain sizes of (001)-oriented grains and c-lattice parameters, plotted in Fig. 4.20, were extracted from the XRD spectra to understand the changes in strain-state and morphology of the T2-series films. Trends in (001)-GS and c-lattice parameter for series T2A are similar to those of series T1 films. The normalized grain size drops below a value of one for the same film where the lattice parameter drops below the bulk value; the description of an evolving strain-state and

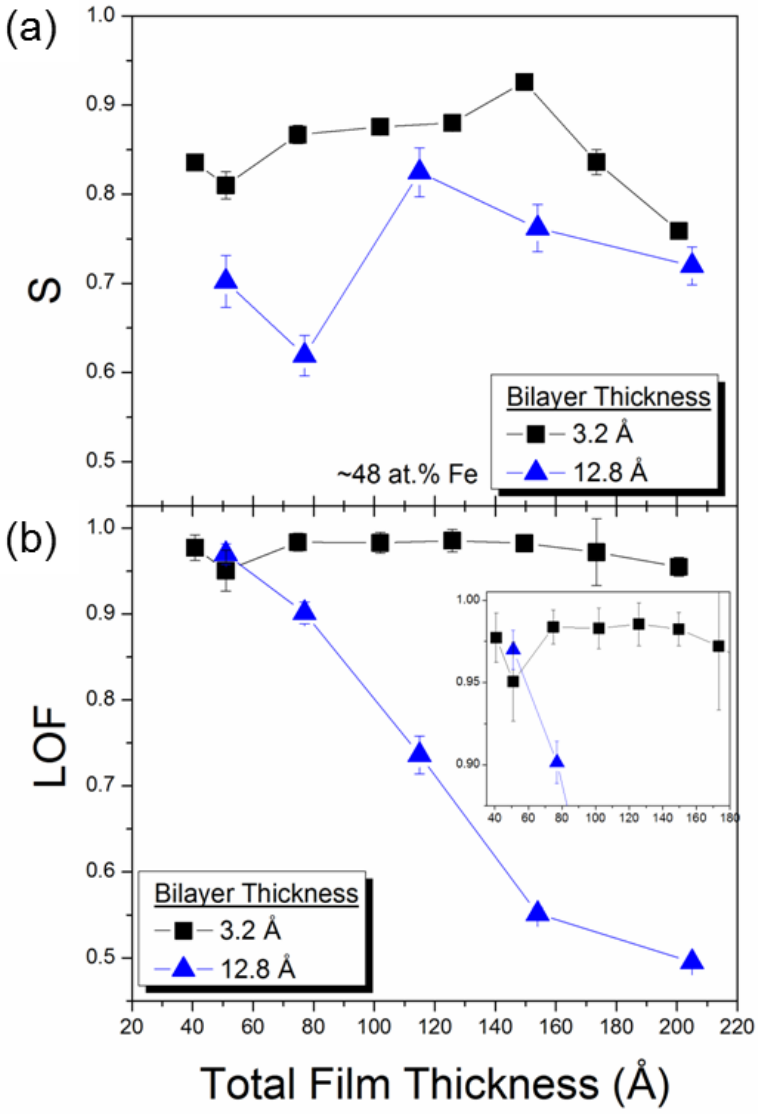

FIG. 4.19. S (a) and LOF (b) for series T2 films. Inset in (b) zooms in the on thinnest region of the LOF data.

grain-growth mode used for the T1-series of films likely applies here, too. On the other hand, c-lattices of the T2B films remain larger than that of bulk $L1_0$ ordered FePt; even the c-lattice in the well textured 51 Å film is relatively large. Only the thinnest of T2B films shows signs of agglomeration, which occurs to a greater extent than in the comparable 50 Å T2B film. A high degree of (001) texture was probably enabled in that T2B film due to the large size of the as-

deposited grains relative to the total film thickness[22]. The large c-lattice parameters and small (001)-grain sizes found in the majority of T2B films are not suggestive of non-epitaxial texturing; the steadily decreasing values of LOF probably stems from a dwindling number of as-deposited grains initially satisfying the Vook-Witt grain interaction condition.

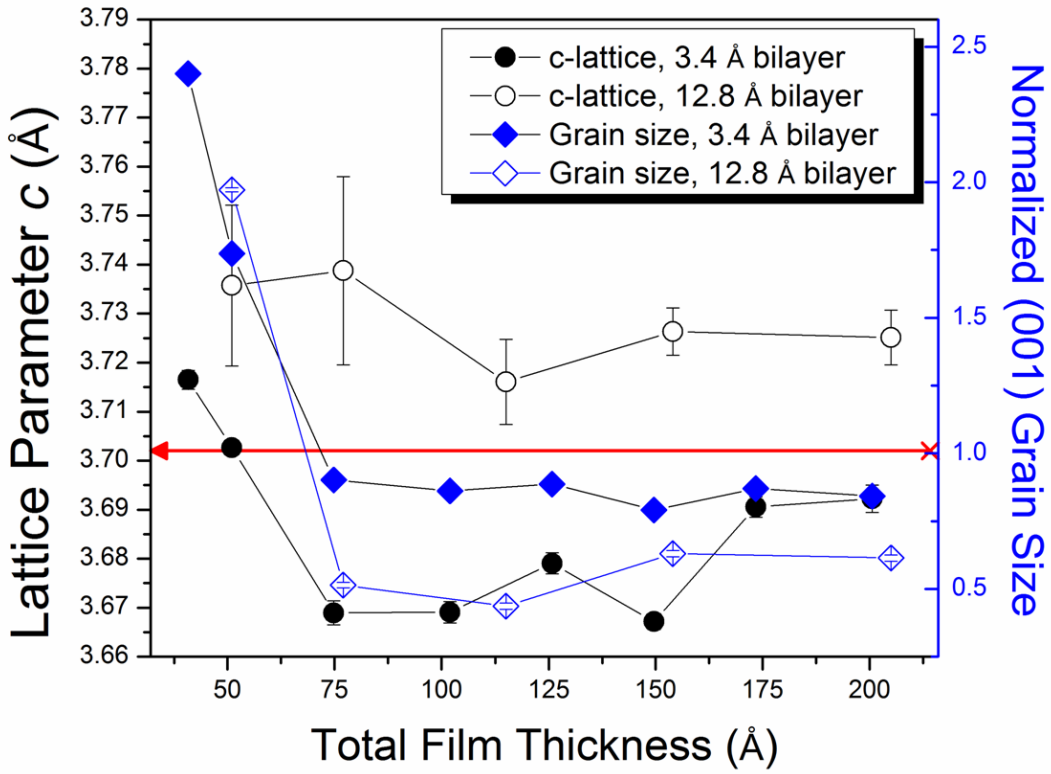

FIG. 4.20. C-lattice parameters and normalized (001) grain sizes for T2A (3.4 Å-bilayers) and T2B (12.8 Å-bilayers) films.

Out-of-plane coercivities plotted versus total thickness in Fig. 4.21 illustrate two very different trends from the T2A and T2B films. The thicker-bilayer films demonstrate a gradually increasing coercivity from 3.6(3) to 6.4(1) kOe over the investigated range of total thicknesses. On the other hand, the T2A series displays a generally decreasing coercivity trend with film thickness. The measured coercivity is relatively high for the 51 Å film, at 21(2) kOe, and drops

[22] ~59 Å *fcc* grains were found in the 12 nm thick, 12.8 Å bilayer-films in series B2. While the as-deposited grains in a 5 nm thick film might not be quite as large, they are still likely spanning the film thickness.

rapidly to 12.4 kOe at 75 Å (note the break on the y-axis). The rate of decline slows as the total thickness increases, with an abrupt spike in coercivity in the 150 Å film.

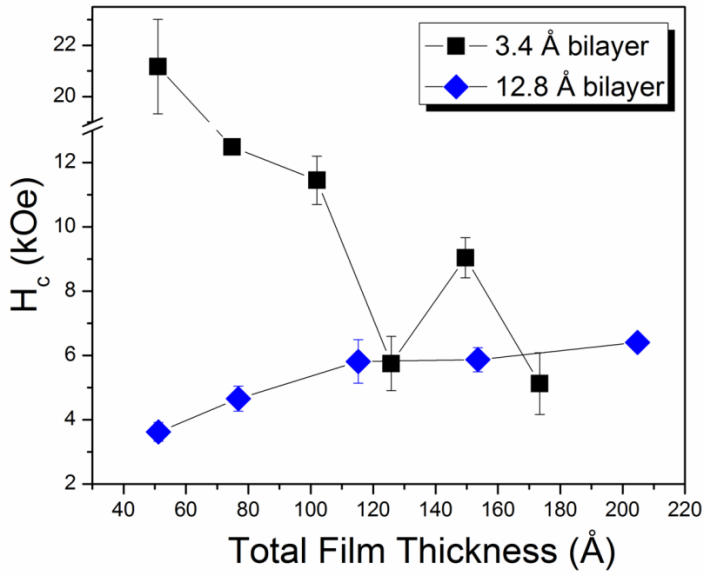

FIG. 4.21. Out-of-plane coercivities for series T2A and T2B films versus total film thickness.

FePt films consisting of small, highly-ordered, non-interacting grains tend to yield the highest coercivities. A reduced overall degree of chemical order or increased exchange interactions, especially with poorly ordered grains, can drastically reduce the switching field. Additionally, grains significantly larger than the limit for coherent rotation switch by domain nucleation and wall motion, which typically occurs at smaller fields. The H_c trends seen here are probably due to a combination of grain size evolution and variations in chemical-order. The large coercivity in the thinner T2A films is likely due to high values of S and a lack of exchange-coupling in the agglomerated morphology. As total thickness increases, films retain their continuous as-deposited structure and the resulting intergranular exchange-coupling decreases the switching field. The spike in H_c at 150 Å in the T2A series is probably related to the maximum degree of chemical order in that film.

The steadily increasing coercivity of the T2B films probably occurs due to the increasing size of single-domain grains. That a similar effect is not seen in the T2A series likely reflects the

non-linearity of the grain-size size effect or its relative magnitude with respect to changes in overall morphology. Lower H_c in the T2B films relative to T2A could be related to the overall smaller S or smaller absolute grain sizes. The former would represent a greater mixture of exchange-coupled magnetically soft fcc and hard ordered grains. Interestingly, the dramatically different in film morphology at 51 Å and fairly wide variation in chemical order are not reflected in H_c.

4.5.3 Conclusions/Summary of Film Thickness Effect

Consistently high degrees of (001) texture are found for Fe-rich and Pt-rich thin films with bilayer thicknesses of ~6 and ~3 Å, respectively, for a range of total film thicknesses. Only a slight decrease in LOF is evident above 150 Å in the latter series. On the other hand, texture drops drastically for Pt-rich films with 12.8 Å bilayers, although LOF is 0.97(1) in the 51 Å film. The thinner-bilayer films likely benefit from a higher density of interfaces induced by the ML design as well as shorter diffusion lengths to achieve chemical order. Thicker bilayers achieve good (001) texture when total thickness is $\leq$ 77 Å, due to large as-deposited grains. These films require only little growth to satisfy the Vook-Witt grain interaction condition, at which point in-plane tensile strain is no longer necessary to achieve texture. Both c-lattice parameters and grain sizes were consistently smaller for thicker bilayers, contrary to a report in the literature [4.57]. Continuous processed films were attained with nominal thicknesses greater than ~75 and 100 Å for Pt-rich and Fe-rich films, respectively. Magnetic switching behavior for the Pt-rich films differed significantly with bilayer thickness. Trends versus total film thickness followed the size of (001)-oriented grains for the thicker bilayers whereas thinner bilayer films seemed more strongly affected by the overall film morphology and degree of chemical order.

4.6 Effect of Pt Terminating Layer

Once ordered, the $L1_0$ phase of FePt is chemically stable and highly resistant to oxidation. Fabricating $L1_0$ ordered FePt films by post-deposition processing, as used in this chapter and the next, inevitably exposes the as-deposited films to atmosphere during transport between the sputtering chamber and the RTA oven. Uncovered Fe at the film's surface is vulnerable to oxidization. Increasing the thickness of the terminating Pt layer of the ML stack serves as a protective coating during transfer to the oven [4.67]. However, as demonstrated in Sections 4.3, 4.4 and 4.5, seemingly minor modifications in the deposition scheme of Fe/Pt ML films can have significant effects on the resulting film properties. The relatively thick Pt overcoat would likely interdiffuse with the underlying multilayers during high temperature annealing. Any degree of mixing might not only change the Fe:Pt stoichiometry, but could also alter grain-growth behavior, ordering kinetics and the strain-state of the film. The aforementioned properties and processes are critical to non-epitaxial texturing of FePt thin films and consequently the use of a thicker Pt-terminating layer could affect the resulting degree of (001) texture.

Only a few somewhat analogous works have been reported in the literature. Overcoat-layers of Ag [4.68], Au [4.69], Cr [4.70], Al_2O3 [4.71], and SiO_2 [4.72] have been employed as protective coverings and to interdiffuse and decouple the underlying FePt grains. The effects of the Pt cover-layer used in the work presented here differ from any of the aforementioned diffusants due to the obviously key role of Pt in the Fe-Pt system. Changes in local stoichiometry could lead to the formation of $FePt_3$ grains, whose antiferromagnetic properties would likely alter the resulting film's magnetic behavior. In a different study, a thin coating of Pt on top of (001)-textured $L1_0$ FePt islands demonstrated spin-polarization at the interface and effectively

reduced the film's anisotropy field [4.73]. This result suggests that small Pt-rich regions could behave as magnetically soft exchange-couples.

This section of Chap. 4 investigates the effect of using an extended Pt terminating layer in FePt ML films, with a focus on chemical order, (001)-texture, magnetic properties and film morphology. Series P1 consists of ~12 nm ML films of varying stoichiometry with ~6 Å bilayers and a 1 nm Pt deposited as an overlayer. P1 films range in composition from 44.3 to 56.6 at.% Fe. Series P2 uses a fixed composition of 46 at.% Fe and ~12 nm total thickness a varying Pt terminating layer thickness from 0 to 10 Å. All films were deposited in the 3M sputtering system as described in Chapter 3 and were processed by RTA as described in Section 4.2. Crystal structure and texture was characterized by analysis of XRD spectra taken on the Rigaku and morphology was determined by TEM, SEM, and AFM. Magnetic hysteresis loops were measured by the MPMS SQUID magnetometer.

4.6.1 Series P1 Results and Discussion

Sample series P1 parallels series S1 in varying the film stoichiometry but also incorporates an additional 10 Å of Pt on the terminating layer. Composition is controlled by changing the Fe/Pt layer thickness ratio while maintaining a ~6 Å bilayer thickness and ~120 Å total film thickness, including the extra Pt. Figure 4.22 shows select XRD spectra from the P1 series. The compositions listed were determined by EDXS and therefore include the additional Pt layer. Note that an (001)-oriented Si substrate was used for the 56.6 at.% Fe film, different from the (111)-oriented Si substrates used in the other films.[23] All spectra demonstrate a strong (001) diffraction peak, either from the $L1_0$ phase or a Fe_3Pt or $FePt_3$ ordered phase. A preference for (001) texture develops for Fe concentrations greater than 45.2 at.%, and the (111) peak disappears for compositions at and above 50.9 at.% Fe. (00*l*) peak positions shift to higher

[23] All substrates had 1000 Å of amorphous thermally oxidized SiO_2 on surface.

angles with increasing Fe content in a similar manner to S1 and S2 series films. Clear Laue oscillations appear around the (00*l*) peaks of the 47.4 at.% Fe film and gain strength with increasing Fe content until they disappear at 56.6 at.% Fe. A low-angle shoulder on the (002) peak is evident for most films with Fe concentrations lower than 50 at.%.

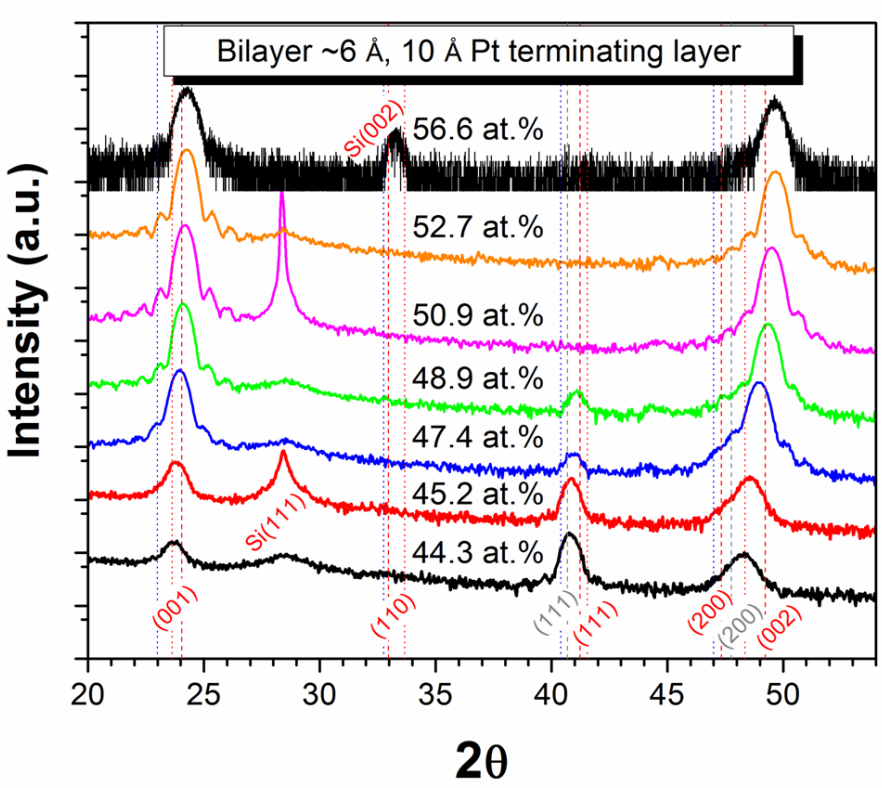

FIG. 4.22. XRD spectra for P1-series films in log scale. Vertical lines denote as-labeled peak positions from anticipated phases: red and grey dashed lines for $L1_0$ and fcc FePt phases, respectively; red and blue dotted lines for ordered Fe_3Pt and $FePt_3$, respectively.

Figure 4.23 illustrates how the degree of chemical order and (001)-texture vary with stoichiometry for series P1 films via the parameters S and LOF in parts (a) and (b), respectively. Data from stoichiometry series S1 is included for comparison. Films with an extended Pt terminating layer achieve a maximum degree of order at slightly Fe-rich compositions, although the gap in data between 52.6 at.% and 56.6 at.% Fe makes it difficult to pinpoint the optimal value. This trend differs from the S1-series films, indicating an effect on the ordering process of the extra Pt layer. The additional 10 Å of Pt effectively decreases the global Fe concentration

measured by EDSX by an average of 1.7 at.%. If the underlying multilayers transformed without disruption from the Pt overlayer, the P1 data would resemble S1 data points shifted to the left by that magnitude. Interestingly, the trend of S in series P1 appears to be shifted in the opposite direction. On the other hand, the trend in (001)-texture for P1 films, seen in part (b) of Fig. 4.23, appears similar to S1 data but shifted to the left, as anticipated. However, the P1 films generally retain a higher degree of (001) texture over a seemingly broader range of Fe:Pt stoichiometries than the S1 films. Both S and LOF trends for the P1 films appear closer to those of series S2, with the thinner bilayers.

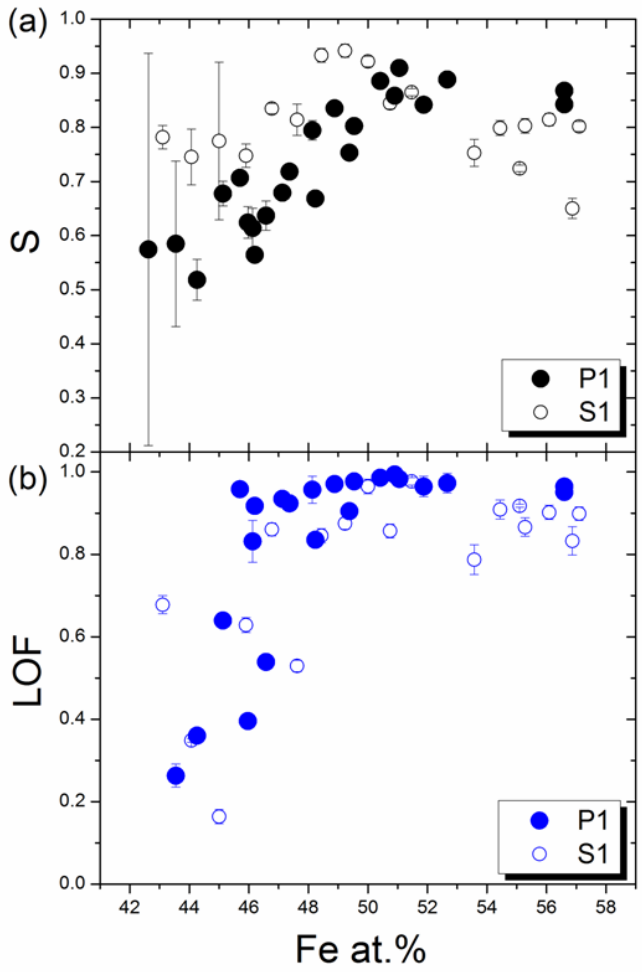

FIG. 4.23. S (a) and LOF (b) estimated for series P1 films versus Fe concentration. Data from series S1 are included for comparison.

The evolution of the c-lattice parameter and normalized (001) grain size with varying Fe content for sample series P1 are shown in Fig. 4.24 along with comparable S1 data. C-lattices for P1 films are higher than those of equivalent S1 films at Fe concentrations ≲ 46 at.%. Between 47 and 48 at.% Fe, the trends of P1 and S1 c-lattice values seem to converge. A similar assessment can be made between normalized (001)-grain sizes of S1 and P1 films; S1 grains are slightly taller for compositions less than 47 at.% Fe and the two series' trends appear converge at higher Fe concentrations after the P1 values sharply increase by nearly 30%.

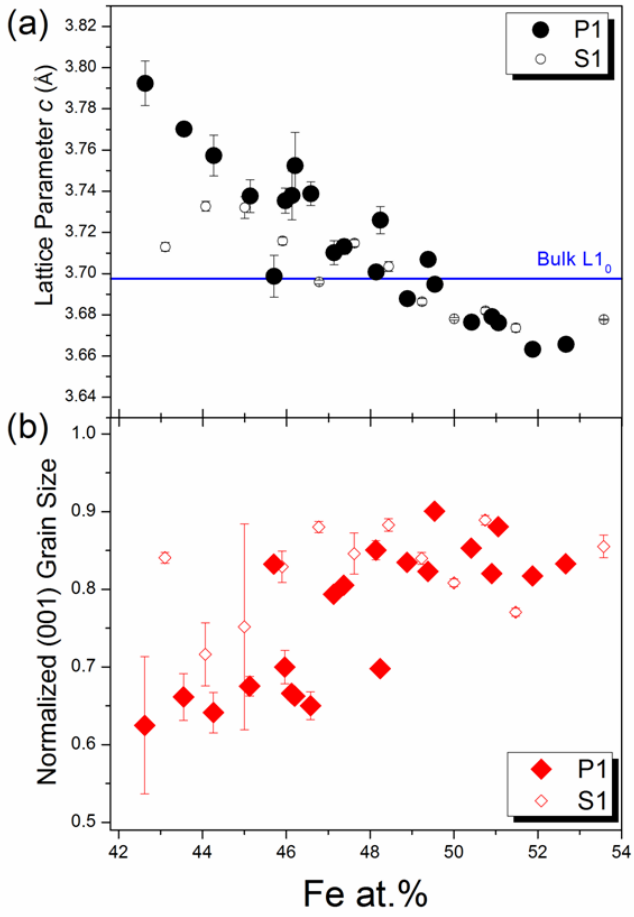

FIG. 4.24. Values for *c*-lattice parameter (a) and normalized (001) grain size (b) estimated for series P1 films versus Fe concentration. Data from series S1 are included for comparison.

Cross-sectional TEM reveals changes in the composition gradient due to annealing a prototypical P1 film. Figure 4.25 shows an as-deposited and post-processing P1 film in (a) and

(b), respectively. The compositions were measured by EDSX with a beam approximately 10 nm in diameter. The beam was moved from outside of the film to a position centered within the film and data was collected approximately at the locations denoted by the red circles. The accuracy of the compositions is compromised by the unusual geometry of the measurement with respect to standard EDSX data collection; however, the values are reliable for comparison. The measurement from region a2 indicates nearly even stoichiometry for the upper portion of the as-deposited film compared to a Fe-rich interior in region a1. The difference is attributed to the Pt overcoat layer. After processing at 600 °C for 5 minutes the compositions measured in regions b1 and b2 are comparable, indicating complete interdiffusion of the extra Pt layer with the underlying MLs. Plan-view TEM in Fig. 4.26 illustrates the effect of a thick Pt overlayer on processed film morphology. Part (a) shows incomplete coverage by a Fe-rich S-series film after processing, whereas (b) shows the effect of maintaining a continuous film by extending the terminating Pt layer by 10 Å. Additionally, the average grain diameter of 62(8) nm increases dramatically to 124(10) nm with the Pt overlayer.

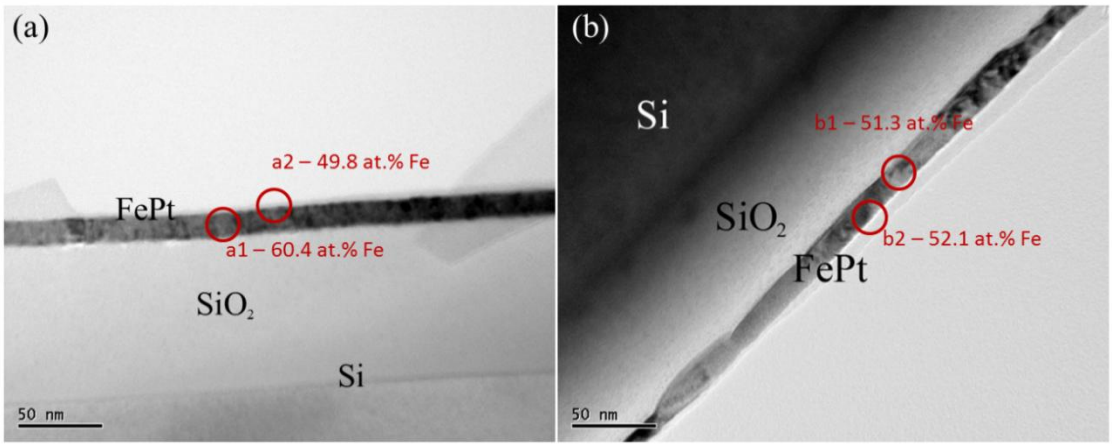

FIG. 4.25. Cross-sectional TEM of P1-series film in as-deposited state (a) and after processing (b).

Magnetic hysteresis loops for select P1 series films in Figure 4.27 show improving out-of-plane anisotropy and loop-squareness with increasing Fe concentration starting at 47.1 at.%. Out-of-plane coercivity roughly increases from 4 to 7.7 kOe, not necessarily following the degree

of chemical order. Coercivities are generally smaller and in-plane loops narrower than comparable S1 films, even for P1 films with a higher degree of chemical order. Out-of-plane loop-slopes at coercivity, α, for the P1 films are also steeper in general than the S1 films, indicating significantly fewer pinning sites in the P1 films.

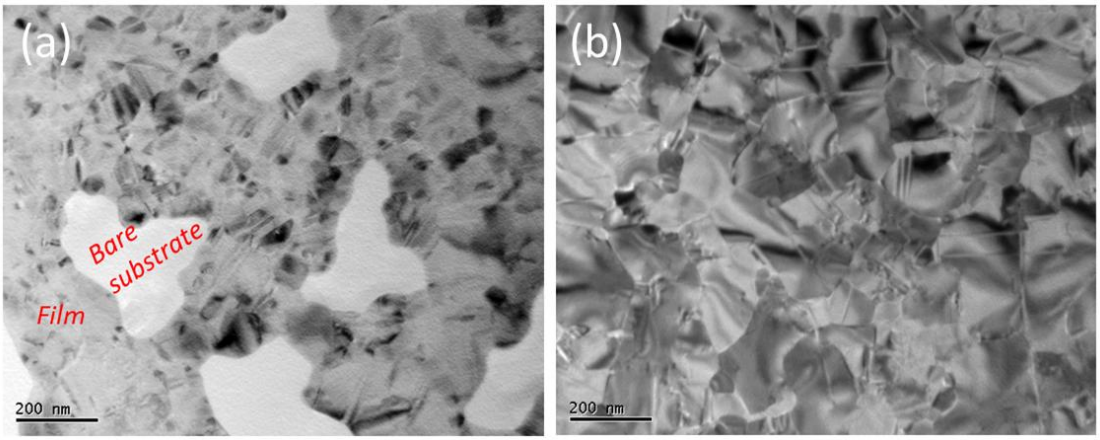

FIG. 4.26. Plan-view TEM comparing grain structure of exemplary Pt-rich S1-series (a) and P1-series (b) films.

The observed differences between S1 and P1 films exceed what a mere shift in composition or change in total film thickness could likely cause. The interaction of the diffusing Pt overlayer with the MLs during annealing greatly affects the development of those grains. Interdiffusion during processing is demonstrated (see Fig. 4.25); using known diffusivity parameters (see Table 2.1) for a 300 second annealing at 600 °C, Pt could be expected to diffuse about 1.5 nm into Fe_xPt_{100-x} (x = 40-60) and Fe would diffuse ~5.1 nm into a Pt. Therefore, Fe from the upper bilayers should easily diffuse throughout the Pt overlayer, yet the Pt atoms might not diffuse completely to the bottom of the film. The latter could yield a slightly Pt-rich composition in the upper portion of the films. Alternatively, significantly faster grain-boundary diffusion could short-circuit the transport of Pt through the depth of the film to form Pt-rich grain boundaries. Since grain-boundaries of as-deposited FePt films have been demonstrated to be inherently Pt-rich [4.47] and the diffusivity of Pt in Fe_xPt_{1-x} varies with x [4.74], the kinetic

behavior of the Pt-overlayer during annealing could be composition-dependent. Such dependence might explain the variability in the differences between S1 and P1 series films. A closer examination of compositional inhomogeneities in the P1 films would be useful in understanding this phenomenon.

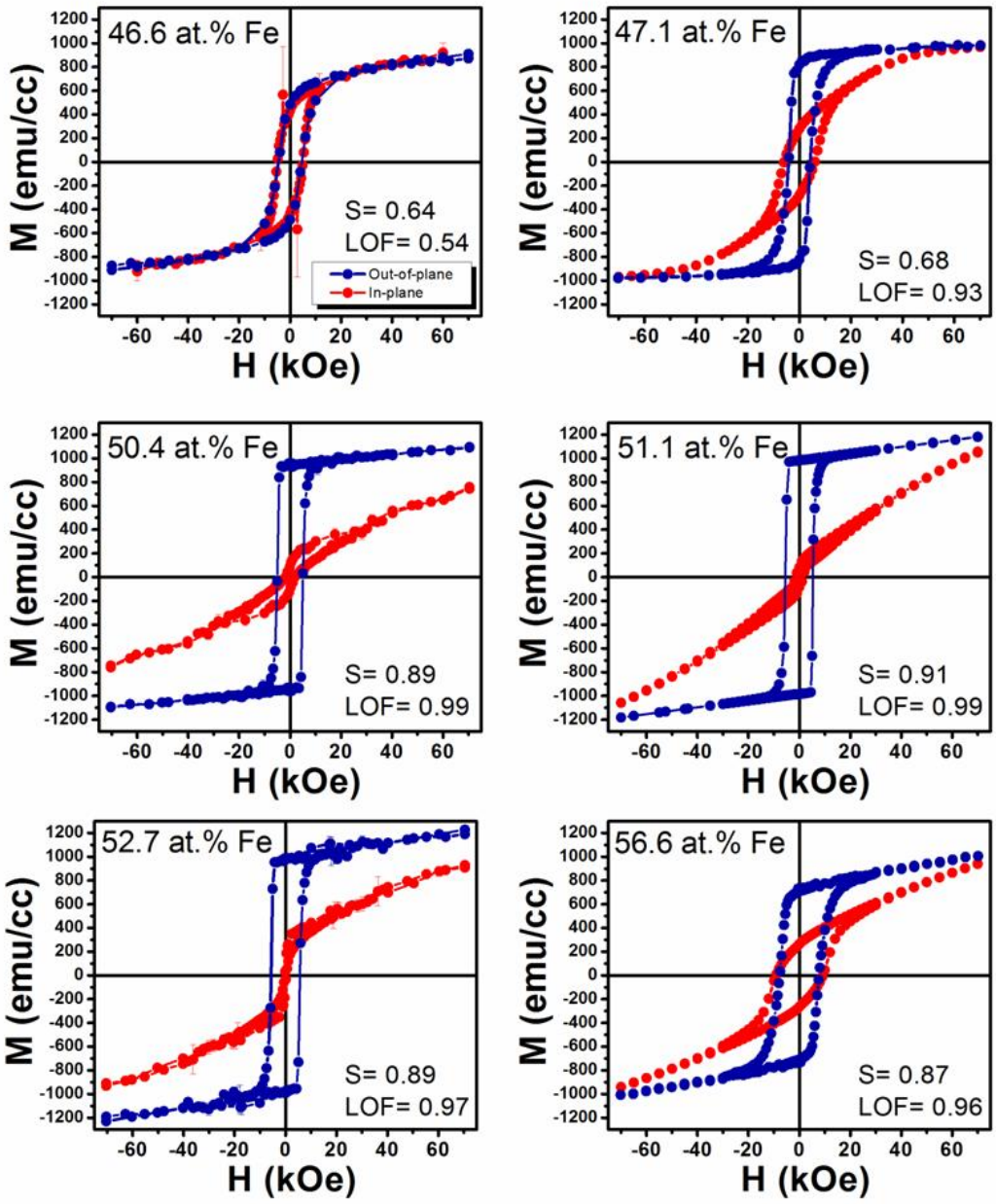

FIG. 4.27. Select in- and out-of-plane hysteresis loops from series P1.

No matter the precise route of diffusion or nature of compositional inhomogeneities, the presence of a Pt layer covering or, at least, enriching the upper portion of an FePt film during annealing will have a protective effect. The Pt would act as a passivation layer for Fe oxidation. Additionally, because Fe evaporation occurs more readily than Pt [4.66], a film with a Pt covering or Pt-enriched grain boundaries would be less likely to develop thermal grooving. Since thermal grooving leads to grain-growth stagnation, Pt-covered films would be expected to consist of larger grains, as is the case here. An improved LOF could be related to enhanced lateral grain-growth and lower coercivities are likely a direct consequence of the resulting grain size and shape.

4.6.2 Series P2 Results and Discussion

Series P2 investigates the effect of varying the Pt terminating layer thickness in a series of FePt thin-films whose composition and total thickness are fixed at 46 at.% Fe and ~12 nm, respectively. Pt terminating layer thicknesses used are 0, 3, 6, 8, 10 Å and the bilayer thickness of the underlying ML film is 6 Å. A composition of 46 at.% Fe was maintained by decreasing the Fe layer thickness in the ML stack to compensate for different Pt cover-layer thickness.

Figure 4.28 shows the XRD spectra for the P2 films. Without a Pt overlayer the film indicates a mixture of (111) and (001) textured grains, and the (00*l*) $L1_0$ peaks are shifted lower than would be expected for a fully ordered film. Adding 3 Å of Pt on the MLs increases the intensity ratio of the (001)/(111) peaks. Thicker Pt additions of 6 and 8 Å shift the (00*l*) diffraction peaks to higher angles and for 8 Å the (111) peak disappears. With 10 Å of extra Pt, the (111) peak resurfaces slightly and the peaks shift back to lower angles. Fitting the XRD spectra reveals the highest value for LOF for the film with the 8 Å Pt overlayer, corresponding to the highest value for S as well. Table 4.1 summarizes the measured properties for the P2 series films.

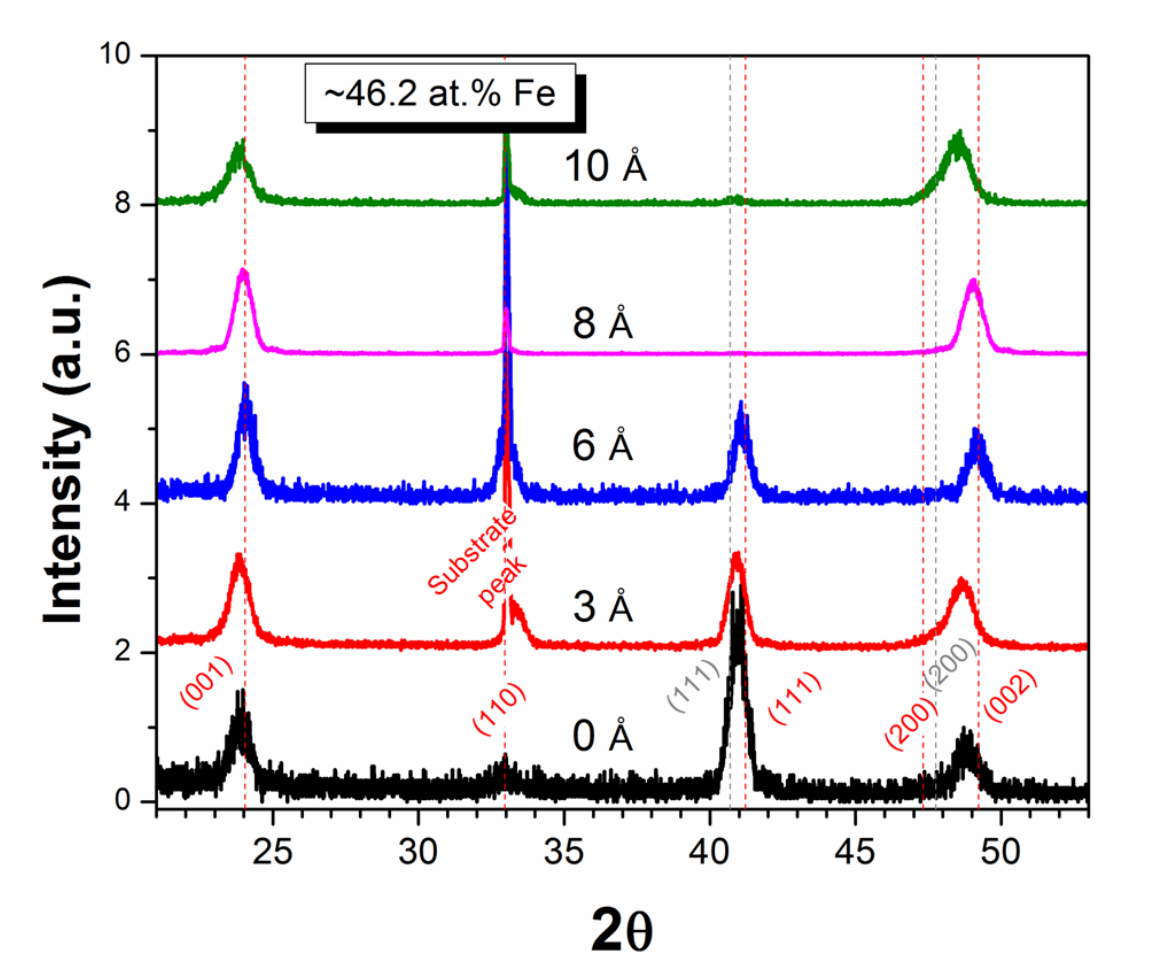

FIG. 4.28. XRD spectra for series P2 films with varying Pt-terminating layer thickness.

Magnetic hysteresis loops in Fig. 4.29 for the film with no additional Pt layer and with 8 Å show improved loop-squareness with the extra Pt, as suggested by the enhanced (001) texture from XRD. Out-of-plane coercivity decreases from 7.3(3) to 4.5(3) kOe for the two loops shown, and drops further to 3.2(2) kOe with a 10 Å Pt-overlayer. In-plane coercivity also decreases from 8 kOe to 5 kOe. A reduced coercivity would be expected from the results of series P1, despite the increase in chemical order for increasing Pt thickness. Also notable is a lower saturation field for the film with a Pt cover layer. This could be due to a reduced MCA, although that would be contrary to the trend in S. Incomplete dissolution of the Pt-overlayer into the FePt grains could

leave a thin Pt coating around each grain, and spin-polarization of that Pt could reduce the anisotropy field as was found for Pt-coated epitaxially grown FePt particles [4.73].

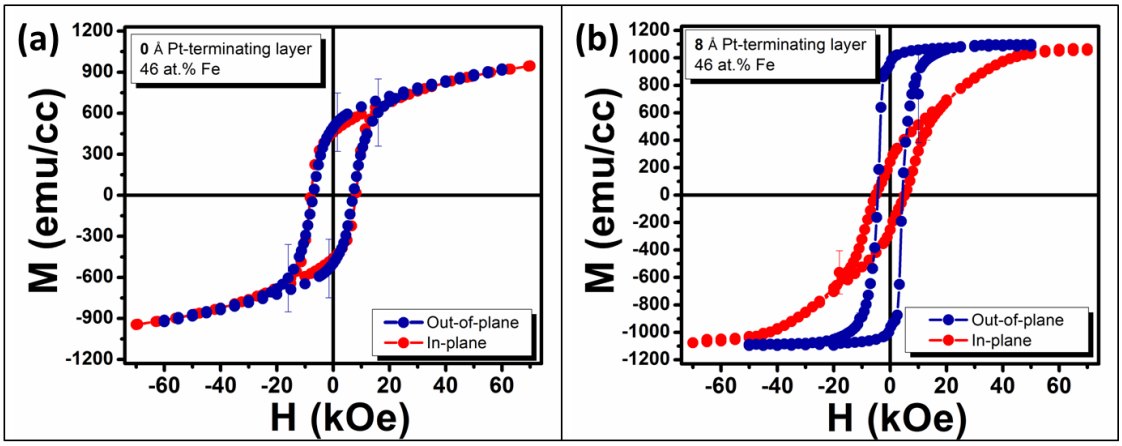

FIG. 4.29. Magnetic hysteresis loops measured in- and out-of-plane for series P2 films without (a) and with (b) an additionally 8 Å Pt terminating layer.

Another striking effect of increasing the thickness of the Pt terminating layer on a ML FePt film is the reduction in surface roughness. Film continuity and low roughness are important considerations for magnetic films intended for bit-patterned media. Figure 4.30 shows AFM images for films with 0, 3, 6 and 8 Å of additional Pt. Roughness values were measured within the denoted regions for each scan. Note the change in depth-scale. RMS roughness decreases dramatically from 2.1 to 0.8 nm for the 6 Å Pt-overlayer, decreases further to 0.6 nm for 8 Å, and then increases again to 0.8 nm at 10 Å (see Table 4.1). Additionally, the additional Pt layer appears to help mitigate the formation of voided regions, in agreement with P1 series results. This effect seems to be optimized for a 6 Å Pt-overlayer, whereas the 8 Å film is the smoothest.

4.6.3 P-Series Summary and Conclusions

Increasing the Pt-terminating layer thickness of post-deposition annealed FePt ML films has beneficial consequences on the development of the $L1_0$ phase, (001)-texture and film morphology. The addition of a 10 Å Pt-layer decreases chemical order in relatively Pt-rich films while increasing S in Fe-rich films. The degree of (001) texture generally improves and lateral

grain sizes increase. The exact reason for these changes could be related to complicated diffusion couple with the underlying film and the effects of grain-boundary diffusion on the strain state. Another reason could be related to the low vapor pressure of Pt relative to Fe and the role of the extended Pt overlayer as a protective coating to prevent oxidization and evaporation of Fe.

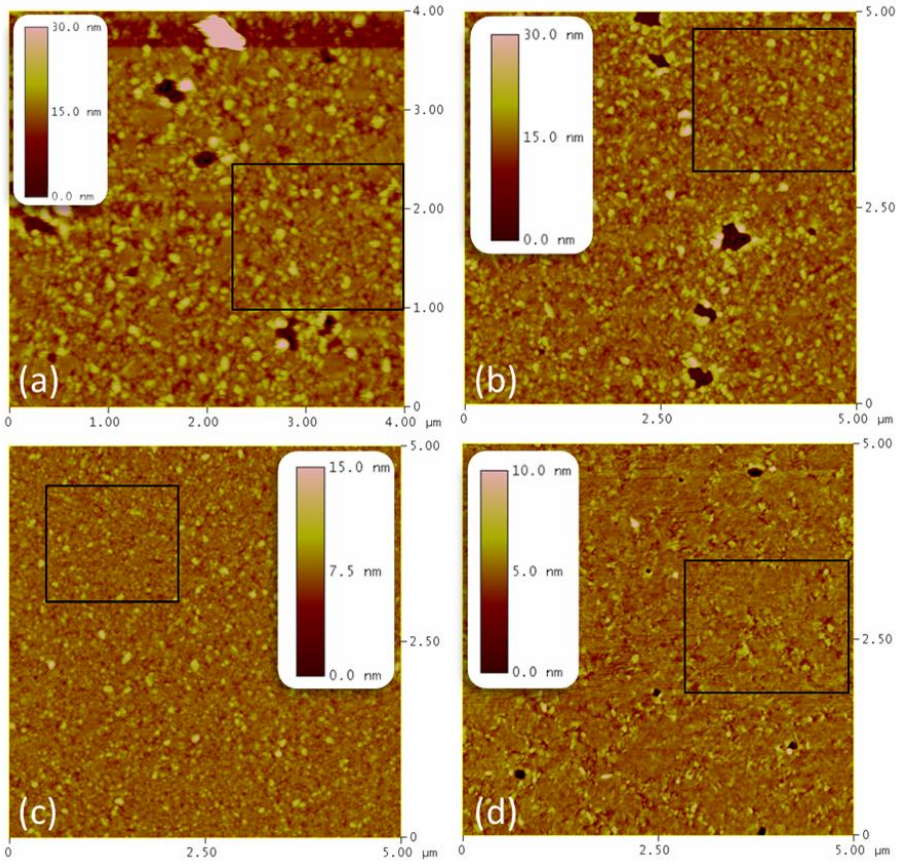

FIG. 4.30. AFM images of series P2 films without additional Pt (a), and with 3 (b), 6 (c), and 8 Å (d). Squares denote region analyzed for surface roughness.

Table 4.1. Compiled results from series P2.

Pt-Overlayer (Å)	S	LOF	Lattice parameter *c* (Å)	(001)-GS	H_c (kOe)	RMS roughness (nm)
0	0.63(3)	0.30(1)	3.724(3)	0.72(3)	7.3(3)	2.1
3	0.65(1)	0.56(1)	3.731(8)	0.71(1)	5.0(1)	1.9
6	0.70(1)	0.60(1)	3.699(5)	0.93(2)	--	0.8
8	0.69(1)	0.97(1)	3.709(4)	0.84(1)	4.5(3)	0.6
10	0.61(4)	0.83(5)	3.738(12)	0.67(1)	3.2(2)	0.8

4.7 References

4.1 D. Weller and T. McDaniel, in *Advanced Magnetic Nanostructures*, edited by D. Sellmyer and R. Skomski (Springer, 2006).

4.2 G. W. Qin, Y. P. Ren, N. Xiao, B. Yang, L. Zuo and K. Oikawa, International Materials Reviews **54**, 157-179 (2009).

4.3 H. J. Richter, G. Choe and B. D. Terris, IEEE Transactions on Magnetics **47** (12), 4769-4774 (2011).

4.4 T. C. Chong, S. N. Piramanayagam and R. Sbiaa, Journal of Nanoscience and Nanotechnology **11** (3), 2704-2709 (2011).

4.5 H. Zeng, M. L. Yan, N. Powers and D. J. Sellmyer, Applied Physics Letters **80** (13), 2350-2352 (2002).

4.6 S. Nakagawa and T. Kamiki, Journal of Magnetism and Magnetic Materials **287**, 204-208 (2005).

4.7 J.-S. Kim and Y.-M. Koo, Thin Solid Films **516** (6), 1147-1154 (2008).

4.8 Y. H. Fang, P. C. Kuo, S. C. Chen, S. L. Hsu and G. P. Lin, Thin Solid Films **517** (17), 5185-5188 (2009).

4.9 Y. S. Yu, T. A. George, W. L. Li, L. P. Yue, W. D. Fei, H. Li, M. Liu and D. J. Sellmyer, Journal of Applied Physics **108** (7), 073906-073904 (2010).

4.10 J. K. Mei, F. T. Yuan, W. M. Liao, A. C. Sun, Y. D. Yao, H. M. Lin, J. H. Hsu and H. Y. Lee, IEEE Transactions on Magnetics **47** (10), 3633-3636 (2011).

4.11 H. J. Kim and S.-R. Lee, Journal of Applied Physics **97** (10), 10H304-303 (2005).

4.12 T. Narisawa, T. Hasegawa, S. Ishio and H. Yamane, Journal of Applied Physics **109** (3), 033918-033917 (2011).

4.13 M. L. Yan, N. Powers and D. J. Sellmyer, Journal of Applied Physics **93** (10), 8292-8294 (2003).

4.14 Y. Itoh, M. Takeuchi, A. Tsukamoto, K. Nakagawa, A. Itoh and T. Katayama, Japanese Journal of Applied Physics **41** (Part 2, No. 10A), L1066 (2002).

4.15 Y. Ogata, Y. Imai and S. Nakagawa, Journal of Applied Physics **107** (9), 09A715-713 (2010).

4.16 C. Brombacher, C. Schubert, K. Neupert, M. Kehr, J. Donges and M. Albrecht, Journal of Physics D: Applied Physics **44** (35), 355001 (2011).

4.17 M. L. Yan, H. Zeng, N. Powers and D. J. Sellmyer, 2002 (unpublished).

4.18 J. K. Mei, F. T. Yuan, W. M. Liao, Y. D. Yao, H. M. Lin, H. Y. Lee and J. H. Hsu, Journal of Applied Physics **109** (7), 07A737-733 (2011).

4.19 S. N. Hsiao, S. H. Liu, S. K. Chen, T. S. Chin and H. Y. Lee, Applied Physics Letters **100** (26), 261909-261904 (2012).

4.20 S. N. Hsiao, S. H. Liu, S. K. Chen, F. T. Yuan and H. Y. Lee, Journal of Applied Physics **111** (7), 07A702-703 (2012).

4.21 Y.-C. Wu, L.-W. Wang, M. T. Rahman and C.-H. Lai, Journal of Applied Physics **103** (7), 07E126-126 (2008).

4.22 H. Sakuma, T. Taniyama, Y. Kitamoto, Y. Yamazaki, H. Nishio and H. Yamamoto, Journal of Applied Physics **95** (11), 7261-7263 (2004).

4.23 K. Barmak, J. Kim, L. H. Lewis, K. R. Coffey, M. F. Toney, A. J. Kellock and J. U. Thiele, Journal of Applied Physics **98** (3), 033904-033910 (2005).

4.24 A. Menshikov, T. Tarnóczi and E. Krén, physica status solidi (a) **28** (1), K85-K87 (1975).

4.25 D. C. Berry and K. Barmak, Journal of Applied Physics **101** (1), 014905-014914 (2007).

4.26 J. Lyubina, I. Opahle, M. Richter, O. Gutfleisch, K.-H. Muller, L. Schultz and O. Isnard, Applied Physics Letters **89** (3), 032506-032503 (2006).
4.27 Y. Ding and S. A. Majetich, Applied Physics Letters **87** (2), 022508-022503 (2005).
4.28 J. S. Chen, B. C. Lim, J. F. Hu, B. Liu, G. M. Chow and G. Ju, Applied Physics Letters **91** (13), 132506-132503 (2007).
4.29 H. H. Li, K. F. Dong, Y. G. Peng, G. Ju, G. M. Chow and J. S. Chen, Journal of Applied Physics **110** (4), 043911-043914 (2011).
4.30 K. Watanabe and H. Masumoto, Transactions of the Japanese Institute of Metals **24**, 627 (1983).
4.31 M. H. Hong, K. Hono and M. Watanabe, Journal of Applied Physics **84** (8) (1998).
4.32 D. Weller, A. Moser, L. Folks, M. E. Best, L. Wen, M. F. Toney, M. Schwickert, J. U. Thiele and M. F. Doerner, IEEE Transactions on Magnetics **36** (1), 10-15 (2000).
4.33 K. W. Wierman, C. L. Platt, J. K. Howard and F. E. Spada, Journal of Applied Physics **93** (10), 7160-7162 (2003).
4.34 K. Kawai, S. Honda, R. Sugiki, M. Komatsu and K. Kawabata, Journal of Magnetism and Magnetic Materials **287** (0), 214-218 (2005).
4.35 B.-H. Li, F. Chun, Y. Tao, T. Jiao, Z. Zhong-Hai, Y. Guang-Hua and Z. Feng-Wu, Journal of Physics D: Applied Physics **39** (6), 1018 (2006).
4.36 R. A. Ristau, K. Barmak, L. H. Lewis, K. R. Coffey and J. K. Howard, Journal of Applied Physics **86** (8), 4527-4533 (1999).
4.37 E. F. Kneller and F. E. Luborsky, Journal of Applied Physics **34** (3), 656-658 (1963).
4.38 A. Sakuma, Journal of the Physical Society of Japan **63** (8) (1994).
4.39 G. Brown, B. Kraczek, A. Janotti, T. C. Schulthess, G. M. Stocks and D. D. Johnson, Physical Review B **68** (5), 052405 (2003).
4.40 S. D. Willoughby, Journal of Applied Physics **95** (11), 6586-6588 (2004).
4.41 R. Skomski, A. Kashyap and J. Zhou, Scripta Materialia **53** (4), 389-394 (2005).
4.42 P. V. Lukashev, N. Horrell and R. F. Sabirianov, Journal of Applied Physics **111** (7), 07A318-313 (2012).
4.43 Y.-C. Wu, L.-W. Wang and C.-H. Lai, Applied Physics Letters **91** (7), 072502-072503 (2007).
4.44 V. Holy, Y. Pietsch and T. Baumbach, *High-Resolution X-ray Scattering from Thin Films and Multilayers*. (Springer-Verlag, Berlin, 1999).
4.45 J.-S. Kim, Y.-M. Koo and N. Shin, Journal of Applied Physics **100** (9), 093909-093906 (2006).
4.46 Y. L. Li, T. F. Feng, Q. Chen, A. P. Huang and Z. Y. Chen, Materials Letters **65** (17â€“18), 2589-2591 (2011).
4.47 K. L. Torres and G. B. Thompson, Ultramicroscopy **109** (5), 606-611 (2009).
4.48 B. Fu and G. B. Thompson, Journal of Applied Physics **108** (4), 043506-043506 (2010).
4.49. B. Fu, W. An, C. H. Turner and G. B. Thompson, Physical Review Letters **105** (9), 096101 (2010).
4.50 T. Sugimoto, T. Katayama, Y. Suzuki and Y. Nishihara, Japanese Journal of Applied Physics **28** (12) (1989).
4.51 N. Zotov, J. Feydt, A. Savan and A. Ludwig, Journal of Applied Physics **100** (7), 073517-073511 (2006).
4.52 J. Ellrich, R. A. Brand and H. Hahn, physica status solidi (b) **247** (9), 2262-2267 (2010).
4.53 J. Lyubina, O. Isnard, O. Gutfleisch, K.-H. Muller and L. Schultz, Journal of Applied Physics **100** (9), 094308-094309 (2006).

4.54 T. Shima, T. Moriguchi, S. Mitani and K. Takanashi, Applied Physics Letters **80** (2), 288-290 (2002).
4.55 M. Verdier, M. Veron, F. Bley, F. Ingwiller, N. M. Dempsey and D. Givord, Philosophical Magazine **85** (26-27), 3157-3172 (2005).
4.56 C. P. Luo, Z. S. Shan and D. J. Sellmyer, Journal of Applied Physics **79** (8) (1996).
4.57 B. Yao and K. R. Coffey, Journal of Applied Physics **103**, 07E107-103 (2008).
4.58 B. Yao and K. R. Coffey, Journal of Magnetism and Magnetic Materials **320**, 559-564 (2008).
4.59 P. T. L. Minh, N. P. Thuy and N. T. N. Chan, Journal of Magnetism and Magnetic Materials **277** (1-2), 187-191 (2004).
4.60 B. Yao and K. R. Coffey, Journal of Applied Physics **105**, 07A726-723 (2009).
4.61 C. P. Luo and D. J. Sellmyer, IEEE Transactions on Magnetics **31** (6), 2764-2766 (1995).
4.62 S. H. Liou, Y. Liu, S. S. Malhotra, M. Yu and D. J. Sellmyer, Journal of Applied Physics **79**, 5060-5062 (1996).
4.63 C. Brombacher, C. Schubert, M. Daniel, A. Liebig, G. Beddies, T. Schumann, W. Skorupa, J. Donges, S. Haberlein and M. Albrecht, Journal of Applied Physics **111** (2), 023902-023904 (2012).
4.64 B. Yao and K. Coffey, R., Journal of Applied Physics **105** (3), 033901 (2009).
4.65 M. Delalande, M. J. F. Guinel, L. F. Allard, A. Delattre, R. Le Bris, Y. Samson, P. Bayle-Guillemaud and P. Reiss, The Journal of Physical Chemistry C **116** (12), 6866-6872 (2012).
4.66 F. Kurth, M. Weisheit, K. Leistner, T. Gemming, B. Holzapfel, L. Schultz and S. Fahler, Physical Review B **82** (18), 184404 (2010).
4.67 L. Han, U. Wiedwald, B. Kuerbanjiang and P. Ziemann, Nanotechnology **20** (28), 285706 (2009).
4.68 Z. L. Zhao, J. Ding, K. Inaba, J. S. Chen and J. P. Wang, Applied Physics Letters **83** (11), 2196-2198 (2003).
4.69 F. T. Yuan, S. K. Chen, W. C. Chang and L. Horng, Applied Physics Letters **85** (15), 3163-3165 (2004).
4.70 W. Y. Zhang, H. Shima, F. Takano, H. Akinaga, X. Z. Yu, T. Hara, W. Z. Zhang, K. Kimoto, Y. Matsui and S. Nimori, Journal of Applied Physics **106** (3), 033907-033904 (2009).
4.71 Y. K. Takahashi and K. Hono, Applied Physics Letters **84** (3), 383-385 (2004).
4.72 Y. Ding, D. H. Wei and Y. D. Yao, Journal of Applied Physics **103**, 07E145 (2008).
4.73 S. Okamoto, O. Kitakami, N. Kikuchi, T. Miyazaki, Y. Shimada and T.-H. Chiang, Journal of Physics: Condensed Matter **16** (12), 2109 (2004).
4.74 T. Kaiser, W. Sigle, D. Goll, N. H. Goo, V. Srot, P. A. van Aken, E. Detemple and W. Jager, Journal of Applied Physics **103** (6), 063913-063916 (2008).

CHAPTER 5 NONEPITAXIAL FePt COMPOSITE THIN FILMS

5.1 Introduction

Sputter deposited Fe/Pt multilayers can form highly $L1_0$-ordered and (001)-textured thin films on amorphous substrates by utilizing a proper deposition scheme followed by rapid thermal annealing. However, the resulting film consists of magnetically coupled grains of relatively uncontrolled size. Achieving recording densities beyond 1 Tb/in^2 using traditional perpendicular recording techniques requires a magnetically decoupled nanostructure with grain diameters of around 6 nm [5.1,5.2]. Magnetic segregation minimizes transition noise and small grains/particle size enhances signal-to-noise. Therefore, in order to implement $L1_0$ phase FePt in a perpendicular magnetic recording (PMR) system it is imperative to control grain size and separation while at the same time maintaining a high degree of perpendicular magnetic anisotropy (PMA).

Varying the fabrication and processing parameters used to achieve strongly anisotropic, pure-FePt thin films affords only limited control over the resulting microstructure. Low processing temperatures limit grain growth yet also yield a low degree of chemical order and texture, and therefore poor PMA. Excessively high processing temperatures can lead to island-like morphologies of magnetically decoupled high-anisotropy particles; however, their size-distribution is typically quite large and difficult to control with this method alone. Increasing the working-gas pressure during sputter deposition or decreasing the individual layer thicknesses in a ML can yield smaller grain sizes [5.3]. Unfortunately, the smaller grains are still exchange-coupled via magnetic grain boundaries. A promising route for controlling and magnetically decoupling a film's grain structure is through doping with a nonmagnetic element or oxide which has a tendency to segregate to the FePt grain boundaries during processing.

A significant amount of work has been devoted to doping FePt thin films with various materials in effort to control the post-processing grain structure, crystallographic texture, ordering temperature and Curie temperature. Attempted materials have included Ag [5.4-5.7], AlN [5.8], Al_2O_3 [5.4,5.9,5.10], Au [5.5,5.11-5.13], BN [5.14], B_2O_3 [5.15], C [5.14,5.16-5.19], Cu [5.5,5.20-5.25], CrMn [5.26], MgO [5.27], Ni [5.28,5.29], SiN [5.30,5.31], SiO_2 [5.32-5.35], ZnO_2 [5.36], and Zr [5.37]. Various studies have determined that Ni and Cu substitute for Fe in forming FePt(Ni,Cu) alloys. The replacement of Fe disrupts interatomic exchange and leads to a reduced Curie temperature [5.29]. Despite evidence of a depressed ordering temperature in FePtCu thin films [5.5,5.20,5.21,5.22], a study of the system's thermodynamics and kinetics indicated no such enhancement versus a similarly prepared pure FePt film [5.24]. The same study demonstrated that the substitution by Ni slows the ordering process. Bi, on the other hand, enters the $L1_0$ lattice interstitially, creating local distortion centers which act as pinning centers for magnetic domain-wall motion [5.38]. Additions of Ag, AlN, Al_2O_3, Au, B, BN, B_2O_3, C, CrMn, MgO, SiN, SiO_2, ZnO_2 and Zr tend to segregate at the FePt grain boundaries, resulting in varying degrees of magnetic decoupling and grain-structure refinement. Relatively low surface energy and immiscibility with FePt characterizes the last group of dopants, giving them preference to diffuse to the FePt grain-boundaries. In doing so, they can alter the fcc to $L1_0$ transformation kinetics either positively or negatively.

Most of the abovementioned doped FePt nanocomposites end up possessing random or (111)-fiber texture. So far, only dopants of Cu, B_2O_3, or SiO_2 have demonstrated a positive effect on the perpendicular alignment of the $L1_0$-FePt easy-axis, and each works by a different mechanism. Substitution of Fe with smaller Cu atoms contracts the c-lattice of an ordered L10 crystal. The resulting increased degree of tetragonality aids the driving force for the preferential growth of (001)-textured grains [5.23]. The insertion of thin SiO_2 layers within a Fe/Pt ML film

enhances grain-boundary diffusion and increases defect density, leading to accelerated ordering and grain growth during rapid thermal annealing; the combined effect allows the grains of the ~6 nm thin films to easily satisfy the Witt-Vook condition for non-epitaxial (001)-texture formation [5.35]. In the case of textured FePt:B_2O_3 films, post-deposition processing above the oxide's melting temperature of ~450 °C permits the ordered grains to minimize the anisotropic strain energy by mechanical rotation, resulting in an out-of-plane c-axis texture [5.39].

Despite tremendous progress in understanding and controlling the underlying mechanisms responsible for the magnetic behavior of granular FePt thin films, fabricating the ideal microstructure with magnetic properties useful for applications in specialized permanent magnets or ultra-high density magnetic recording remains a daunting task. This chapter examines a number of post-deposition annealed ML FePt films with ternary additions of Al_2O_3, Au, and C, with a focus on refining grain-size and controlling intergranular magnetic interactions while maintaining a high degree of chemical order and (001)-crystallographic texture. Section 5.2 presents a study on FePt:Al_2O_3 films, where both as-deposited ML structure and dopant volume percent (vol%) are varied to optimize the resulting properties. Section 5.3 investigates films of FePt:Au and FePt:C and looks closely at the resulting relationships between magnetic correlation length, hysteresis-loop slope and structural disorder.

5.2 FePt:Al_2O_3 Nanocomposite Films

The addition of nonmagnetic Al_2O_3 to non-epitaxially grown FePt thin films forms a segregated nanocomposite upon sufficient annealing due to the low surface energy of alumina (~169 mJ/m^2) relative to FePt (~2.9 J/m^2). As a nonmagnetic segregant, Al_2O_3 could prove useful in forming the desired particulate morphology in a composite thin film with $L1_0$ FePt. FePt-Al_2O_3 films sputtered from a composite Fe-Pt-Al_2O_3 target with thicknesses greater than 100 nm yield ~10 nm (111)-textured grains after conventional vacuum annealing [5.10]. Densification of

amorphous alumina at elevated temperatures and eventual crystallization between 800 and 900 °C makes the oxide a good barrier to the sintering of nanoparticles up to ~730 °C [5.40]. Epitaxially grown films of FePt:Al_2O_3 indicate little degradation of (001) grain orientation when increasing the oxide content up to 40% [5.41-5.43]. However, high vol% additions tend to inhibit the degree of $L1_0$ order in both *in-situ* and post-deposition ordered films [5.9,5.41,5.44]. The effect of adding alumina on $L1_0$ order and (001) texture of nonepitaxial multilayer FePt films processed by RTA is studied in the following subsection. Specifically, variations in matrix volume content, as-deposited structure, and annealing time are investigated.

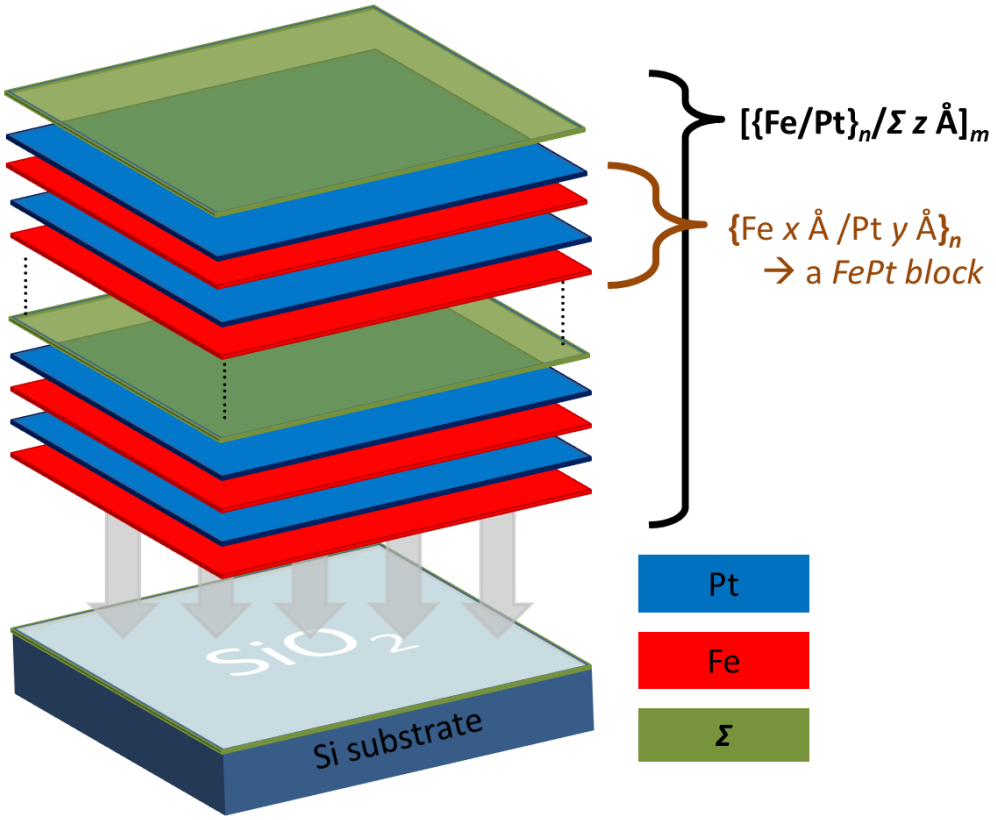

FIG. 5.1. Schematic for deposition of Fe/Pt multilayer film with layer of ternary material inserted between FePt "blocks."

5.2.1 FePt:Al_2O_3 – Experimental Details

Five different series of FePt:Al_2O_3 samples were fabricated in the 3M sputtering system under the deposition conditions described in Chap. 3. All films were deposited on thermally

oxidized Si substrates with 1000 Å-thick buffer layers of SiO_2. The Fe:Pt stoichiometry was estimated at around 51:49 from EDXS measurements. Figure 5.1 shows a schematic of the deposition process ($\Sigma = Al_2O_3$). A ML recipe was employed to promote nonepitaxial (001) texture in the composite film during annealing, in a similar manner to the films presented in Chap. 4. Al_2O_3 layers were introduced from an RF-sputtered oxide target at varying periods within the multilayer stack; the oxide layer subdivides the metallic layers into groups of one, two, three, four, or five bilayers, referred to as blocks. Five of the six film series follow the recipe $[(\text{Fe 3.2 Å /Pt 3 Å})_n/Al_2O_3\ x\ \text{Å}]_m$, with n = 1,..., 5. Table 1 outlines the ranges of Al_2O_3 vol%, deposited film thickness and processing times used for each film-series as well as the series designations used throughout the chapter for clarity. The oxide thickness, x, determined the alumina vol%. The parameter m was varied to maintain total thickness between 11 and 15 nm in series AlO1, AlO2, AlO3 and AlO4, or 21 and 24 nm for series AlO5.

Table 5.1. Various structures of the AlO*n* sample series.

Sample Series	As-Deposited Structure	x (Vol% Al_2O_3)	Total Film Thickness (nm)	Processing Time (s)
AlO1	$[\text{Fe 3.2 Å /Pt 3 Å}/Al_2O_3\ x\ \text{Å}]_m$	0 – 24.4	11 – 12	300
AlO2	$[(\text{Fe 3.2 Å /Pt 3 Å})_2/Al_2O_3\ x\ \text{Å}]_m$	0 – 24.4	11 – 12	300
AlO3	$[(\text{Fe 3.2 Å /Pt 3 Å})_3/Al_2O_3\ x\ \text{Å}]_m$	0 – 24.4	11 – 12	300
AlO4	$[(\text{Fe 3.2 Å /Pt 3 Å})_4/Al_2O_3\ x\ \text{Å}]_m$	0 – 19.5	11 – 12	300
AlO5	$[(\text{Fe 3.2 Å /Pt 3 Å})_5/Al_2O_3\ x\ \text{Å}]_m$	0 – 49.2	20 – 24	300, 1800, 2400

After deposition, coupons of approximately 4.5 × 4.5 mm^2 were cut from each $FePt:Al_2O_3$ sample. The coupons were then processed by RTA at 600 °C for 300s in a 2.5% H_2-Ar base forming gas to induce ordering into the $L1_0$ phase (see Chap. 3 for details). Additional coupons selected from the AlO5 series were processed for 1800 and 2400 seconds to examine the effects of longer processing-times. Theta-2θ X-ray diffraction spectra taken with the Rigaku diffractometer were fit with a series of Pseudo-Voigt functions to characterize the crystal structure and texture as described in Chap. 3. The peak fits were used to determine S, Lotgering

orientation factor (LOF), and grain size for the different FePt:Al_2O_3 films. Magnetic hysteresis loops both parallel and perpendicular to each sample's film planes were measured by AGFM. Select films were measured using the SQUID magnetometer.

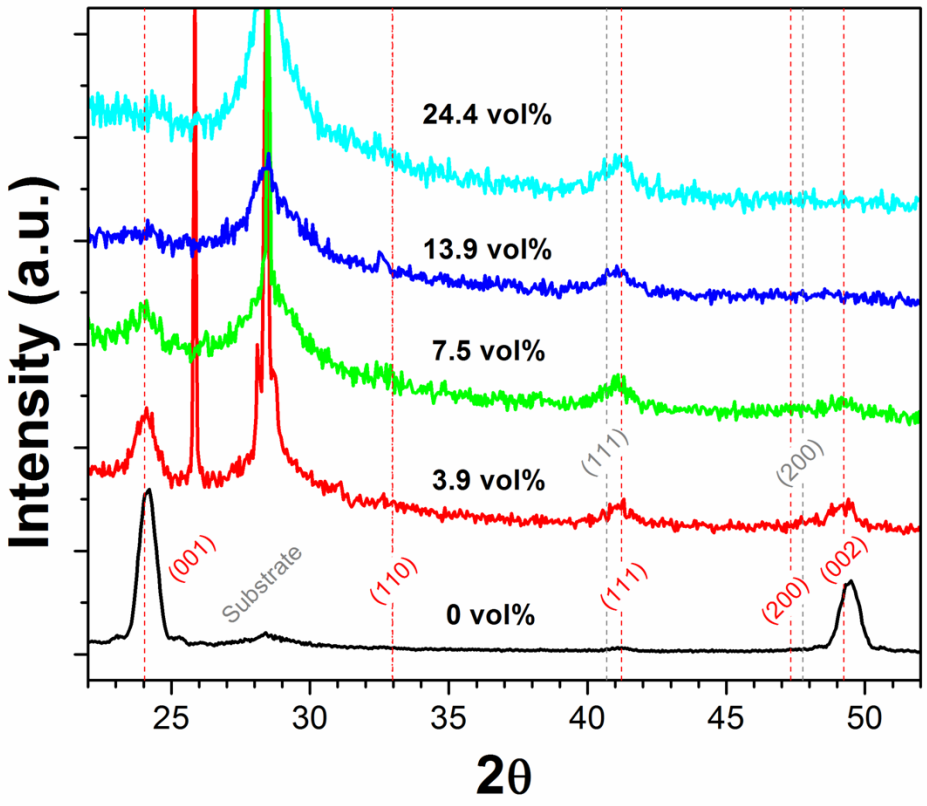

FIG. 5.2. XRD spectra for AlO1 film series.

5.2.2 FePt:Al_2O_3 – Results and Discussion

X-ray spectra for AlO1 series samples are shown in Fig. 5.2. Without the oxide, the pure FePt film shows relatively good crystallinity with (001)-texture and $L1_0$ order quantified by a Lotgering orientation factor (LOF) of 0.96(1) and an order parameter (S) of 0.813(8), respectively. Upon adding 3.9 vol% of Al_2O_3, corresponding to a ~0.3 Å layer between every FePt bilayer, the degree of crystallinity decreases drastically. As compiled in Fig. 5.3 a), LOF decreases by about 25% and S by about 10% for the smallest oxide inclusion. *LOF* continues to drops rapidly as Al_2O_3 content increases to 24.4vol% while S decreases concurrently at a more gradual rate. However, poor crystallinity and noisy data in the samples with higher oxide vol% lead to

large error bars and somewhat unreliable values for the order parameter toward the end of the series.

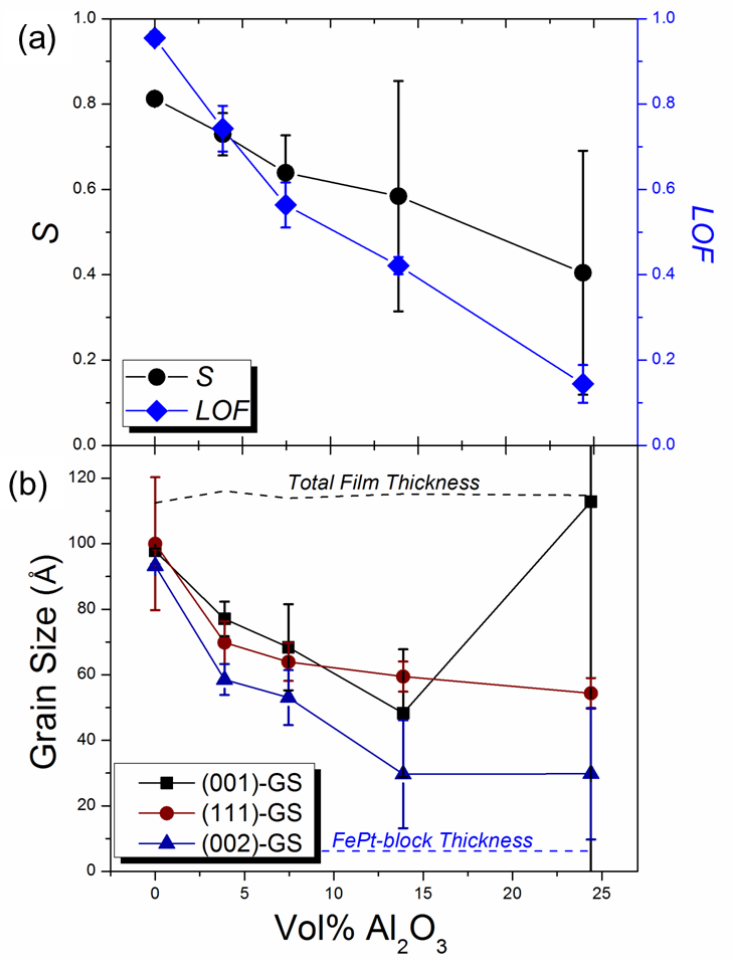

FIG. 5.3. AlO1 film properties: (a) chemical order and (001)-texture and (b) grain-sizes.

Crystallite sizes determined by the Scherrer method for the 11.1 nm pure FePt film show an average vertical grain size (GS) of 9.6 +/- 0.3 nm for grains with (00*l*) texture. That this value is close to the film thickness is not surprising considering the relatively high degree of (001) texture exhibited by this film. Upon adding an increasingly thick alumina layer between every Fe/Pt bilayer, the grain sizes determined from three different lattice reflections decrease rapidly as shown in Fig. 5.3 b). With a 14 vol% or more addition the (111) oriented grains appear to be slightly larger than the other grains. The smaller values determined by the (002) reflections may

be partly related to an artificial broadening of that peak due to an overlap with peaks from lesser ordered $L1_0$-(002) peaks at slightly lower angles. At 24.4 vol% alumina the FePt grains are less than 40% ordered (S ≈ 0.4(3), yet probably lower) with nearly random orientation (LOF ≈ 0.1) and an average *reliable* grain size of ~ 6 nm.

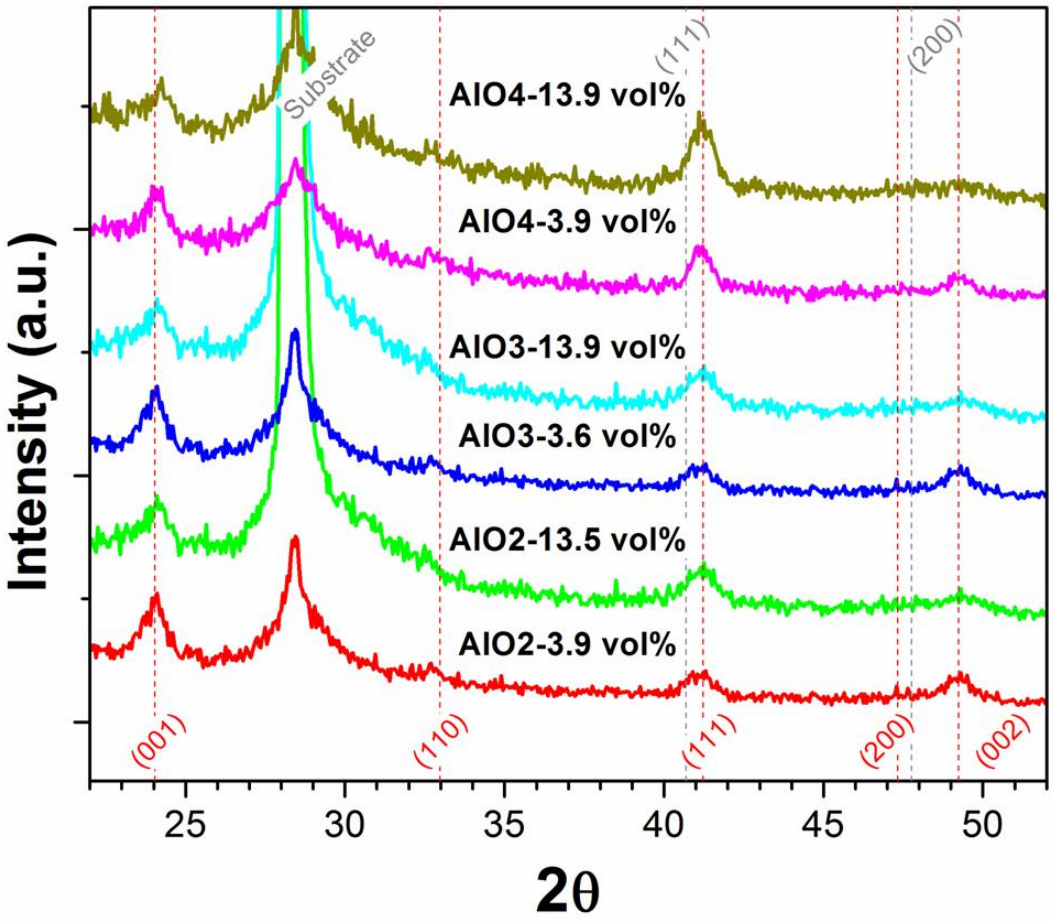

FIG. 5.4. Select XRD spectra from the AlO2, AlO3 and AlO4 film series.

Depositing a layer of Al_2O_3 between every Fe/Pt bilayer certainly affects the subsequent formation of the $L1_0$ phase, grain growth, and non-epitaxial development of (001) texture. Increasing the FePt thickness between interceding oxide layers could reduce any detrimental effects from the metal-oxide interface and decrease the need for the Fe-Pt to interdiffuse with the oxide to nucleate grains. XRD spectra in Fig. 5.4 demonstrate the effect on the crystal structure of decreasing the alumina-layer periodicity within the as-deposited structure. The

corresponding FePt-block thicknesses are 6.2, 12.4, 18.6, and 24.8 Å for the AlO1, AlO2, AlO3, and AlO4 series, respectively. The effects of the oxide in each series can be compared to the pure FePt film shown in Fig.2. Similar to the AlO1 film series, the (00*l*) $L1_0$-FePt diffraction peak intensities decrease upon adding the matrix material; however, the quality of the $L1_0$ diffraction peaks appear to degrade more rapidly with alumina content in the AlO1 film series than the others. Generally, the (111)-peak becomes more prevalent and the (001)- and (002)-peaks both drop in magnitude.

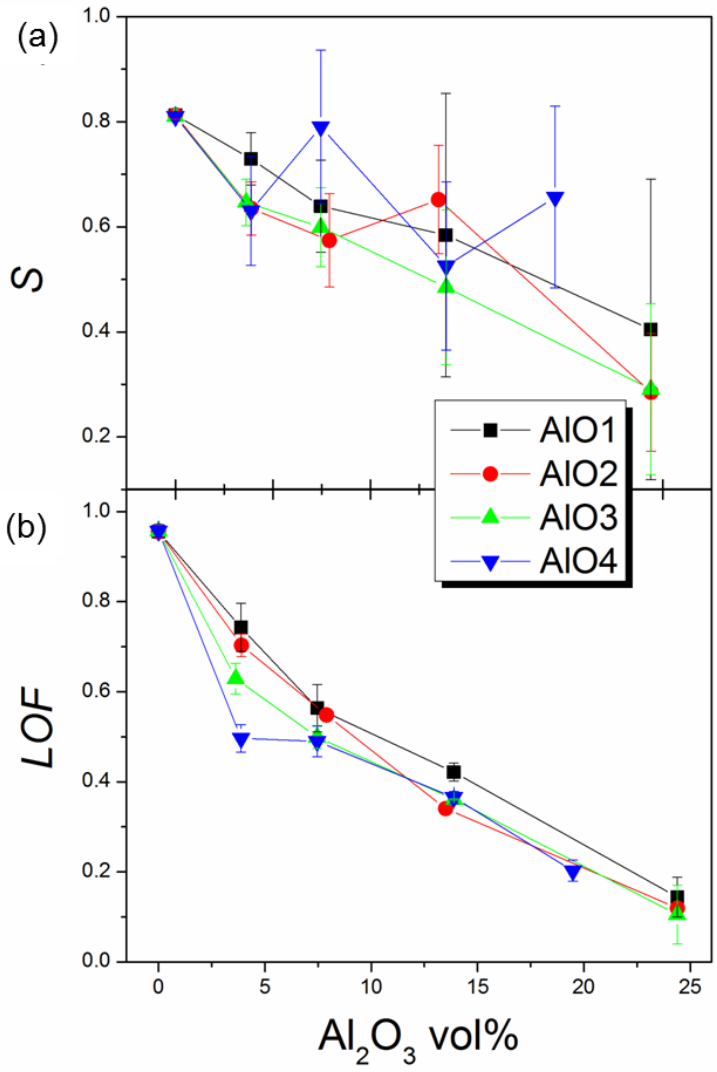

FIG. 5.5. Chemical order and (001)-texture for the first four AlO film series.

Figure 5.5 (a) plots S versus Al_2O_3 vol% to illustrate the effect on chemical order of varying the periodicity and oxide content for the first four AlO*n* sample series. The trend of moderately decreasing chemical order with alumina content holds for all FePt block thicknesses. For the smallest oxide addition, the film with a single Fe/Pt bilayer block appears to maintain better chemical order than those with thicker metal layers. This trend is almost reverse for higher matrix content with an indication of higher ordering in the AlO4 series, however large error might be obscuring any real trend or lack thereof. Figure 5.5 (b) plots the estimated LOF versus alumina vol% for the four sample series, showing a general trend of degrading (001) texture with increasing oxide. Interestingly, the AlO1 films maintain (001) texture to a better degree than the other series films throughout the investigated range of oxide addition. The largest disparity comes at ~3 vol% Al_2O_3 where LOF decreases from 0.75 to 0.5 with increasing as-deposited matrix-layer periodicity.

Vertical grain sizes estimated from the widths of the three main x-ray diffraction peaks for series AlO1 through AlO4 are shown in Figures 6 (a – c), respectively. Part Cc) of Fig. 5.6 includes the individual FePt-block thicknesses for each series for comparison. The grain sizes in all film series follow an identical trend of inhibited growth with increasing oxide content and, in general, larger block thicknesses yield larger vertical grain sizes. Grain sizes from (111) peak widths approach ~ 6 nm for higher alumina volumes, which is larger than any these series' as-deposited block thickness.

Magnetic hysteresis loops of select AlO1 series samples, with 0, 3.9, and 24.4 vol% alumina, are shown in Fig. 5.7 along with a plot of the in- and out-of-plane coercivities versus alumina content. Note that these data were measured by AGFM with a maximum field of 12 kOe. All loops (except for the in-plane loop in a)) were corrected for a diamagnetic background signal assuming high-field saturation. The out-of-plane loop of the 0 vol% Al_2O_3 sample shows a

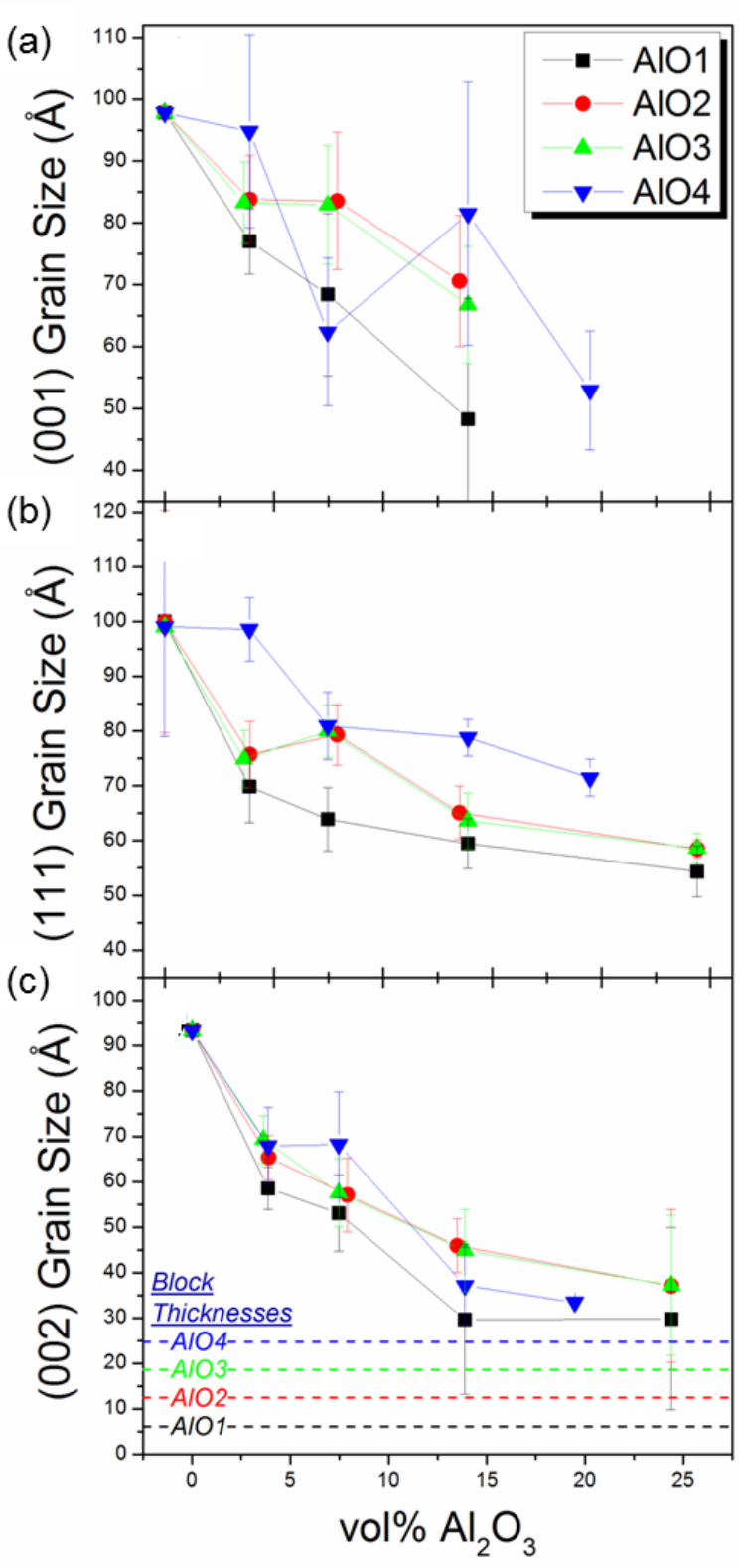

FIG. 5.6. Grain sizes for the first four AlO series of films.

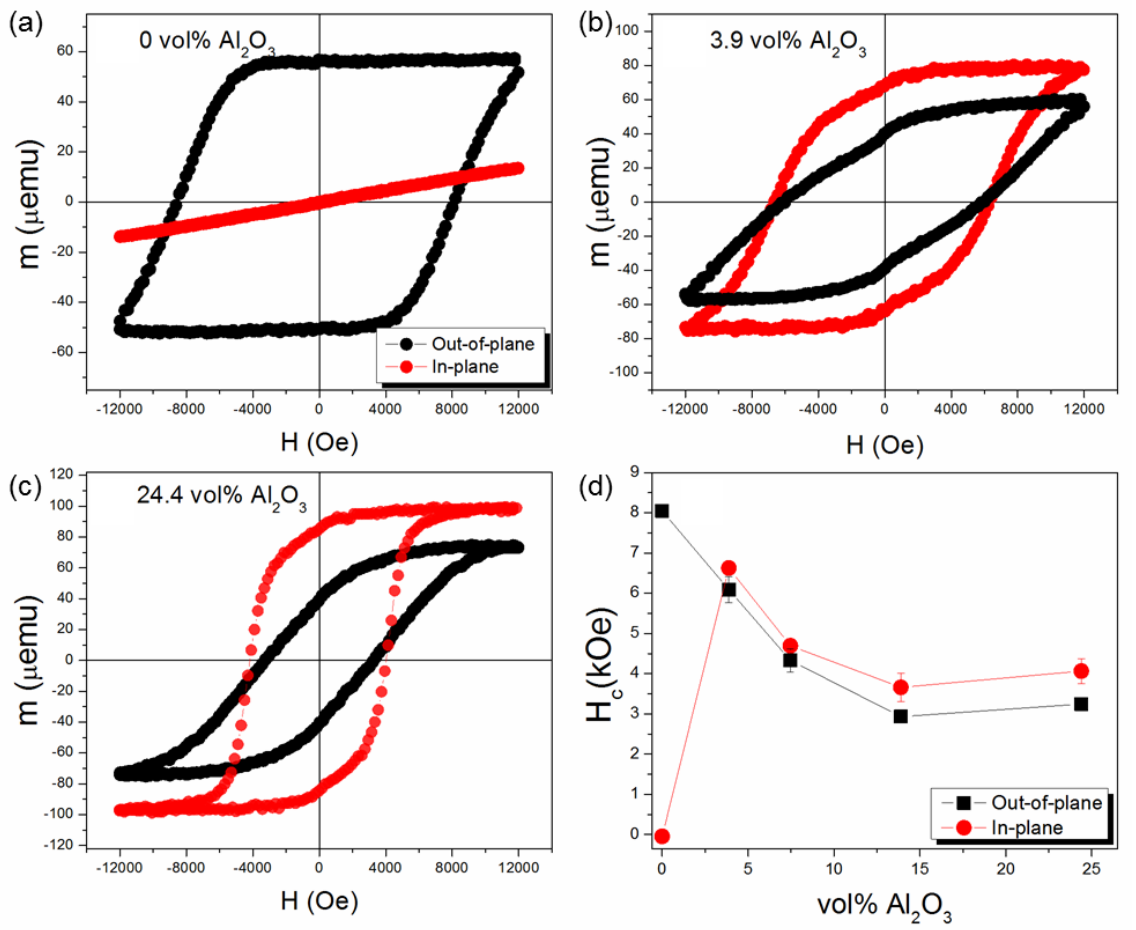

FIG. 5.7. Magnetic hysteresis loops measured by AGFM for (a) 0, (b) 3.9 and (c) 24.4 vol% Al_2O_3. In- and out-of-plane coercivities are summarized in part (d).

magnetic easy-axis and high squareness (albeit unsaturated), and the matching in-plane loop suggests a hard magnetization axis. The in- and out-of-plane hysteresis loops indicate a change in easy-axis direction upon adding 3.9 vol% oxide. The previously easy perpendicular direction becomes more hard-axis-like, a change which is likely accentuated by the strong demagnetization field of the thin-film geometry. The in-plane loop opens up with appreciable remanence and coercivity. The in-plane loop shows irreversible magnetization, with a remanence ratio, M_r/M_s, greater than 0.5, and appreciable coercivity. The low-field kinks in the hysteresis loops indicate the presence of poorly ordered FePt, in agreement with the smaller values of S measured for films with high matrix content. Part (d) of Fig. 5. 7 illustrates AlO1

minor-loop coercivities suddenly changing from anisotropic to isotropic, and then gradually decreasing in magnitude until leveling off for alumina vol% greater than 14. A declining coercivity could be due to shrinking particle size, waning chemical order, or a change in crystalline/easy-axis texture.

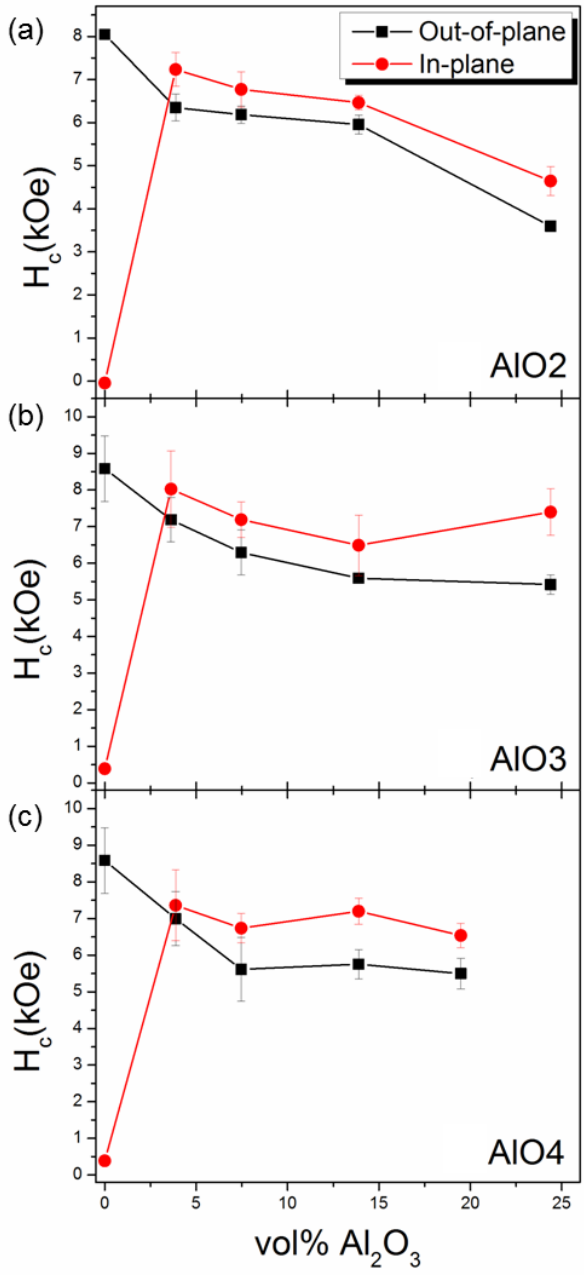

FIG. 5.8. Coercivities measured by AGFM for film series (a) AlO2, (b) AlO3 and (c) AlO4.

Figure 5.8 (a) – (c) show the in- and out-of-plane coercivity trends for the AlO2, AlO3 and AlO4 series, respectively. Similar to the AlO1 series, these sample series exhibit gradually decreasing coercivities with increasing matrix concentration. The corresponding hysteresis loops from series AlO2 through AlO4 also change shape reflecting a rotation of the easy-axis away from the out-of-plane direction. Notably, the decline in coercivity is less severe with a Fe/Pt block thickness larger than in AlO1. However, no clear universal trend in magnetic hardness is evident when reducing the oxide-layer periodicity.

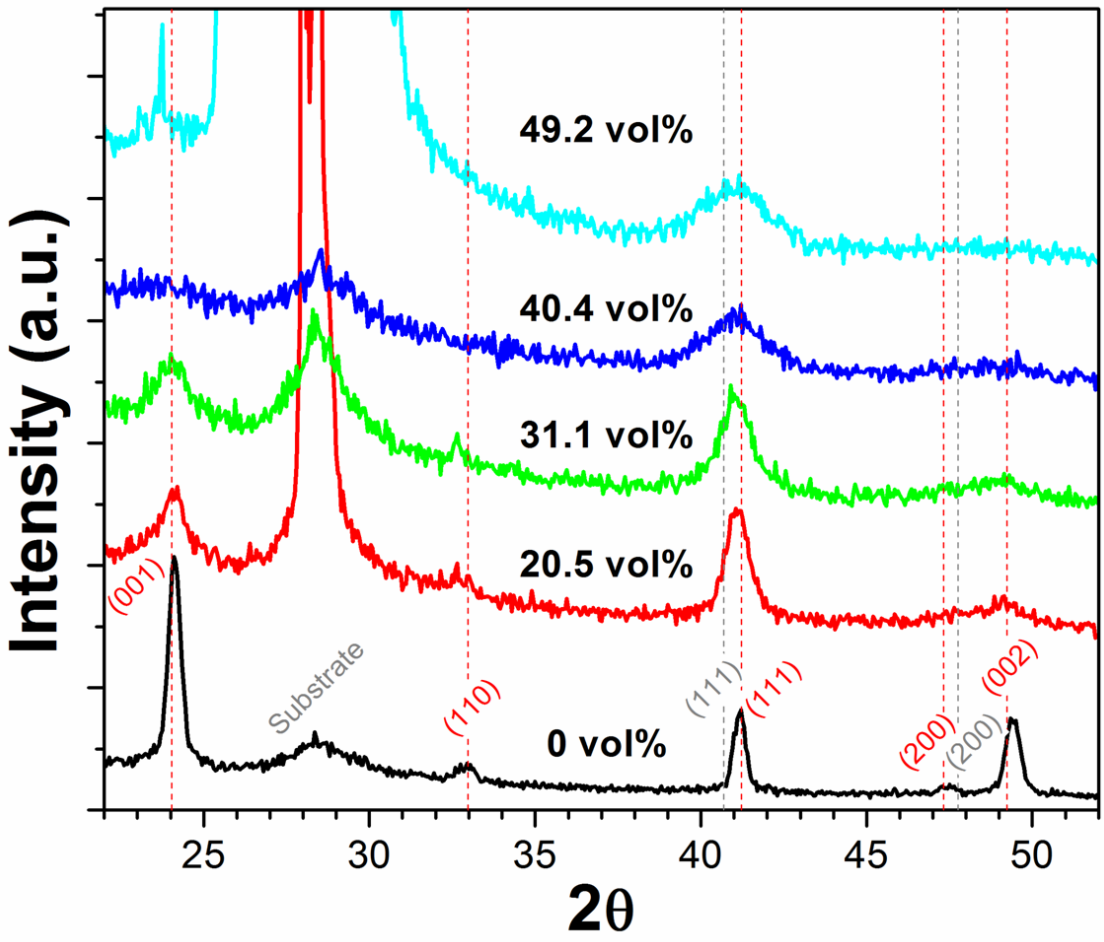

FIG. 5.9. XRD spectra of the AlO5 film series.

The AlO5 film series continues the trend of reducing the alumina-layer periodicity; however, it differs from the previous four series in being ~20 nm thick. The change was made to increase the films' magnetic signal while raising the maximum alumina content to nearly 50

vol%. Figure 5.9 shows the θ-2θ diffraction patterns for this series. The spectra indicate changes in chemical order, crystallinity, grain size, and texture with increasing alumina content similar to the previous series, however the vol% used here is much greater.[24] Figure 5.10 summarizes S, LOF, and vertical grain sizes versus matrix content. The relatively large total thickness of these samples precludes effective nonepitaxial formation of (001) texture in the pure FePt film, as indicated by an LOF of only 0.59(1). Grain sizes for this sample are larger than those in the 0-vol% film from the previous four series due to the relative film thickness. Within the range of 20 – 30 volume percent alumina, overlapping with the previous series, grain sizes here generally remain larger. At ~40 vol% and higher, the estimated grain sizes are reduced to nearly the FePt-block thickness. It is possible that the corresponding Al_2O_3 layer thickness of ~20 Å could be the limit for inhibiting diffusion of FePt between blocks for the given annealing conditions.

Figures 11 and 12 show the compiled chemical order and Lotgering orientation factors for (001) texture from all five sample series as 3-dimensional contour plots, including the data points, to illustrate both the effect of increasing the alumina content and varying its periodicity in the as-deposited structure. The 20 nm pure FePt film has a slightly lower degree of chemical order and a lesser degree of (001) texture as compared with the 11 nm film (0.77 and 0.59 versus 0.813 and 0.96 for S and LOF, respectively), which agree with the trend demonstrated in Chapter 4. The AlO5 film with 31 vol% alumina retains better chemical order and (001)-texture than the previous series at ~24 vol%. It must be noted that the values of S and LOF for the 49 vol% sample are skewed due to the presence of a contamination peak near 24° 2θ.[25]

[24] A sample with ~10 vol% alumina was fabricated for the AlOx5 series. However, the sample fell off the annealing stage during processing and consequently exhibited properties far out of trend with the rest of the series.

[25] The sharp peak probably originates from WLβ_1 radiation (λ = 1.282 Å) diffracting from Si (111) planes of the substrate.

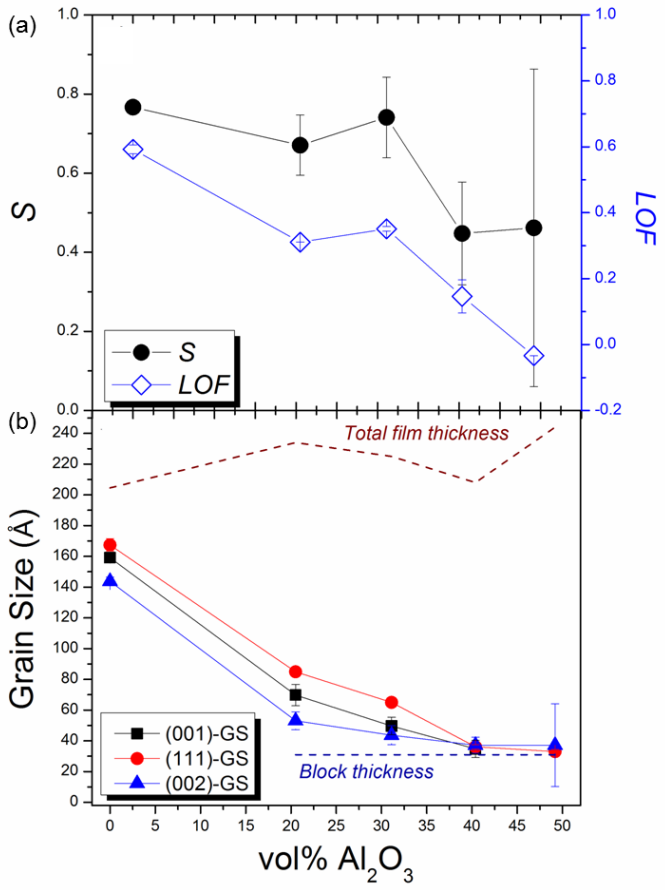

FIG. 5.10. Trends in (a) chemical order, (001)-texture and (b) vertical grain sizes for AlO5 series films.

Hysteresis loops measured on the SQUID magnetometer for films with 0, 25.5, and 31.1 vol% from the AlO5 series are shown in Fig. 5.13 (a) – (c). Despite the nearly-isotropic appearance of the pure FePt film, it must possess some degree of out-of-plane anisotropy to counter the potentially strong and unaccounted for thin-film demagnetization. With 25.5 vol%, the composite film's morphology would resemble dispersed grains and a thin-film demagnetization factor would no longer apply. Interestingly, the 31.1 vol% film appears to develop stronger PMA than the pure-FePt film, despite a smaller value of LOF. Magnetic properties measured by both AGFM and SQUID for the entire AlO5 series are shown in part d) of Fig. 5.13. The approximately equal in- and out-of-plane coercivities both decrease with increasing alumina content.

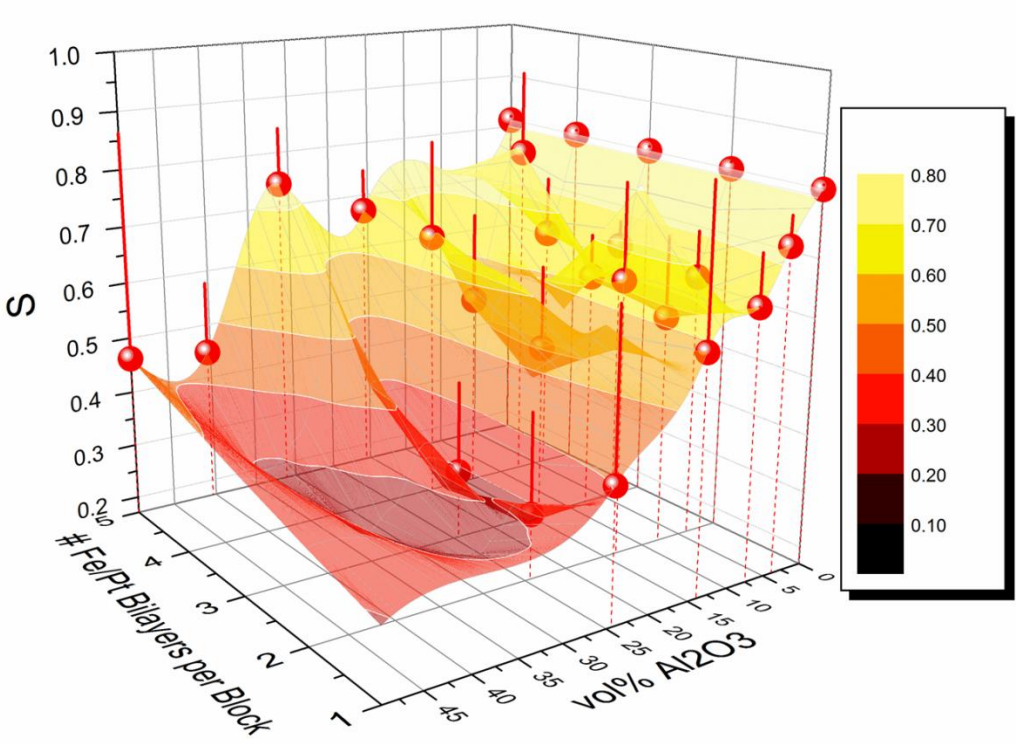

FIG. 5.11. Contour plot of chemical order trends for the AlO*n* films.

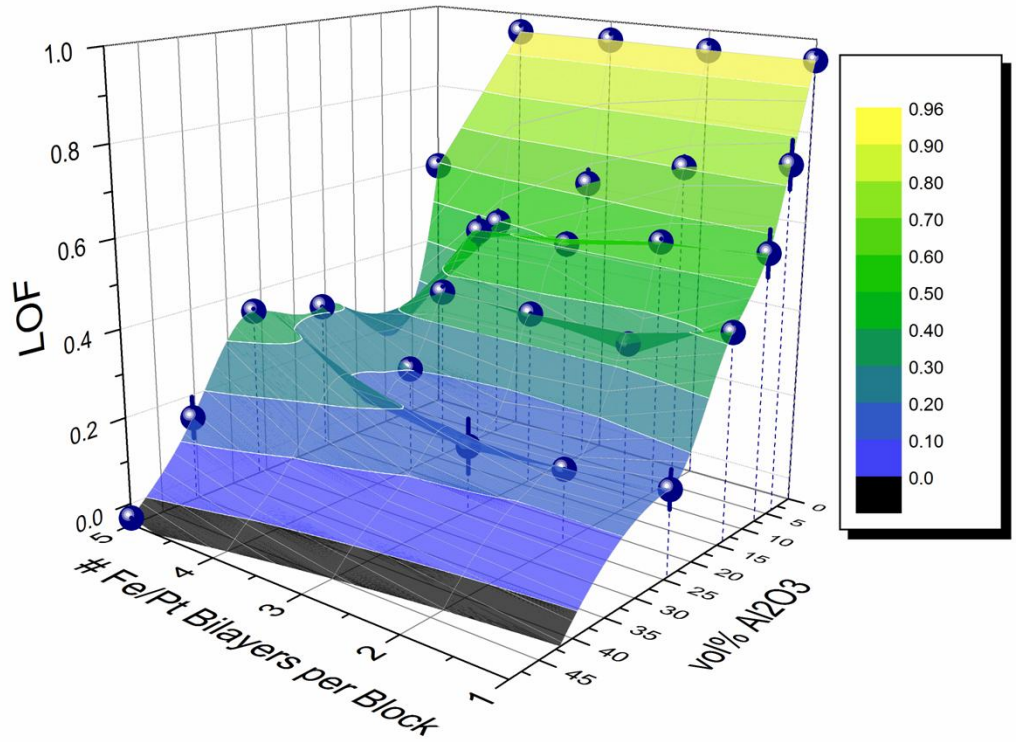

FIG. 5.12. Contour plot of (001)-texture trends in AlO*n* films.

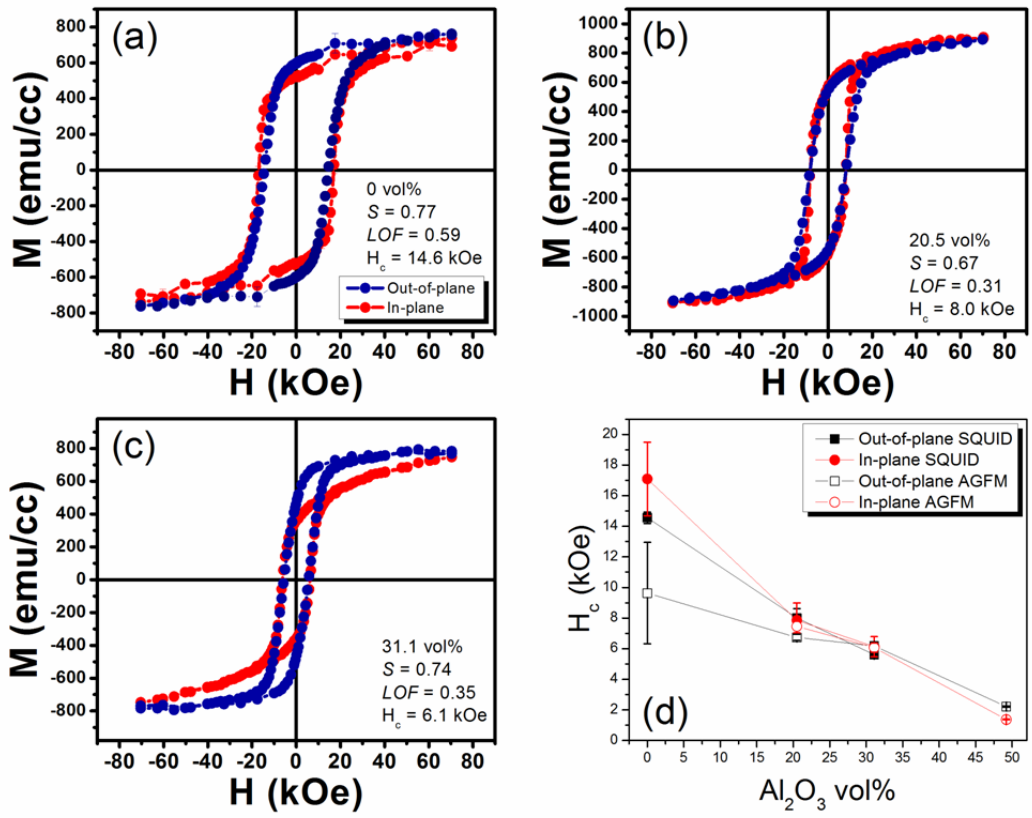

FIG. 5.13. M-H loops measured by SQUID of AlO5 samples with (a) 0, (b) 20.5 and (c) 31.1 vol% alumina. Coercivity trends from SQUID and AGFM are shown in part (d).

The AGFM-measured coercivities are compared with those of the other AlO-film series in Fig.14, where the field values are normalized to their respective un-doped film values. AlO5 film coercivities follow a similar decreasing trend as the other alumina-series, resembling more closely series AlO3 and AlO4, and after a 31 vol% addition the coercivity drops significantly. A similar feature is seen in the AlO2 series' coercivity trend after 13.9 vol%. It is speculated that the AlO3 and AlO4 series might demonstrate a similar drop after a critical matrix concentration exceeding the maximum amount investigated here, but less than the turning point in the AlO5 series. Coercivity variations in a series of nanogranular FePt films can typically be associated with corresponding changes in chemical order, particle size, and/or intergranular magnetic interactions. With the variable insertion of Al_2O_3 layers of different thickness in the ML FePt films, all of the aforementioned film properties are subject to change to some degree in the

annealed film. Pinpointing the exact causes of the coercivity variations in the AlO*n* series of films would require further investigation, for example, into the trends in intergranular interactions and in-plane particle sizes. Such could be the subject of future studies with FePt:Al_2O_3 multilayer films.

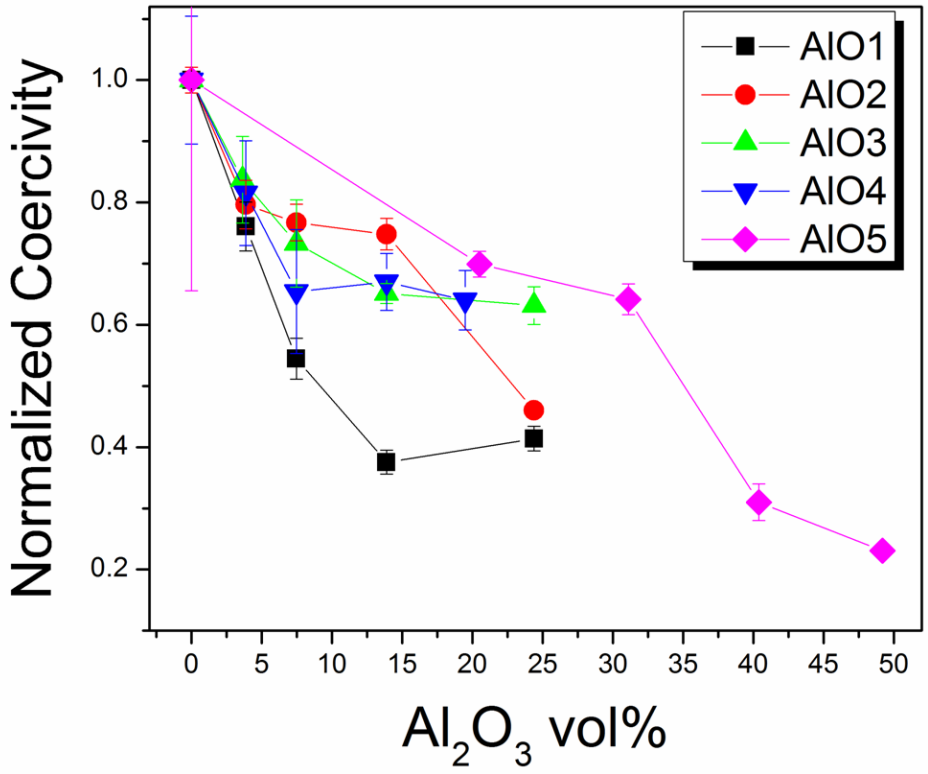

FIG. 5.14. Out-of-plane coercivity trends for all AlO*n* series, normalized to their respective pure-FePt values.

In order to investigate more closely the effects of interdiffusion in multilayer films of Fe, Pt, and Al_2O_3 on chemical order and (001)-texture, additional coupons from select AlO5 series samples were annealed for extended periods of time in the RTA at 600 °C. Figure 5.15 shows the evolution of S and LOF for holding times of 300, 1800 and 2400 seconds for the AlO5 films with 20.5, 40.9, and 49.2 vol% Al_2O_3. For all films the degree of chemical order increases for times up to 1800 s, then appears to decrease afterward. The initial enhancement in ordering is probably due to continued diffusion of Fe and Pt as well as growth of ordered/ordering grains during the

longer annealing time; part (a) of Fig. 5.16 corroborates grain coarsening. The decrease in order after 2400 s could be due to chemical interactions between the FePt and alumina [5.43]. Interestingly, LOF increases for longer annealing durations. Typically, texture formation by SEDSGG occurs early in the annealing process. The unusual trend seen here could be due to a different mechanism leading to enhanced (001) texture. Alternatively, the changes in LOF seen here could be somewhat artificial, being related to an improved XRD signal due to increased crystallinity and the previously mentioned grain coarsening. Figure 5.16 (b) shows how the coercivity changes for the 21 vol% alumina film with increased annealing time. Both in-plane and out-of-plane coercivities loosely follow S, increasing for 2400 s of processing and then dropping slightly after 3600 s.

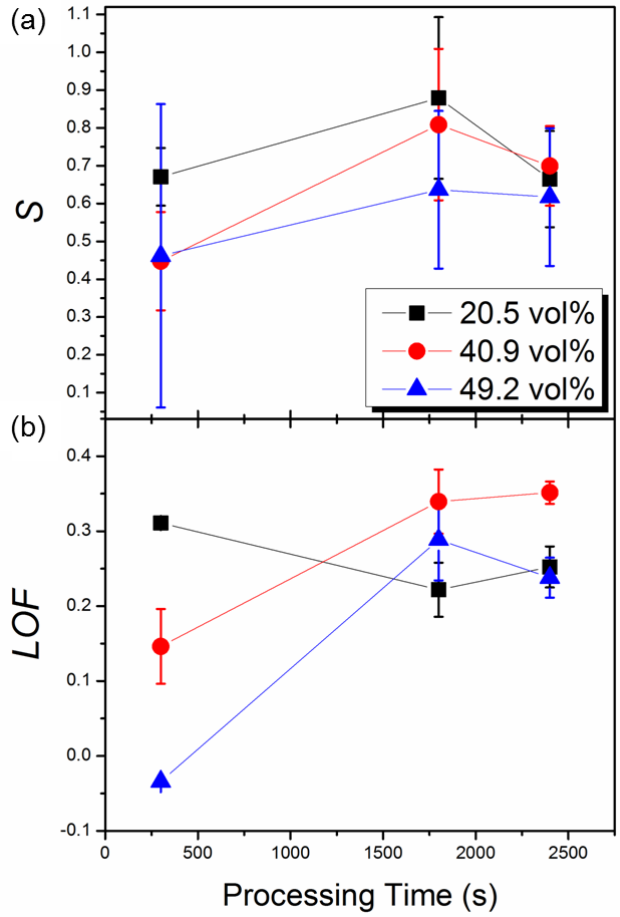

FIG. 5.15. Trends in (a) chemical order and (b) (001)-texture for increased processing time.

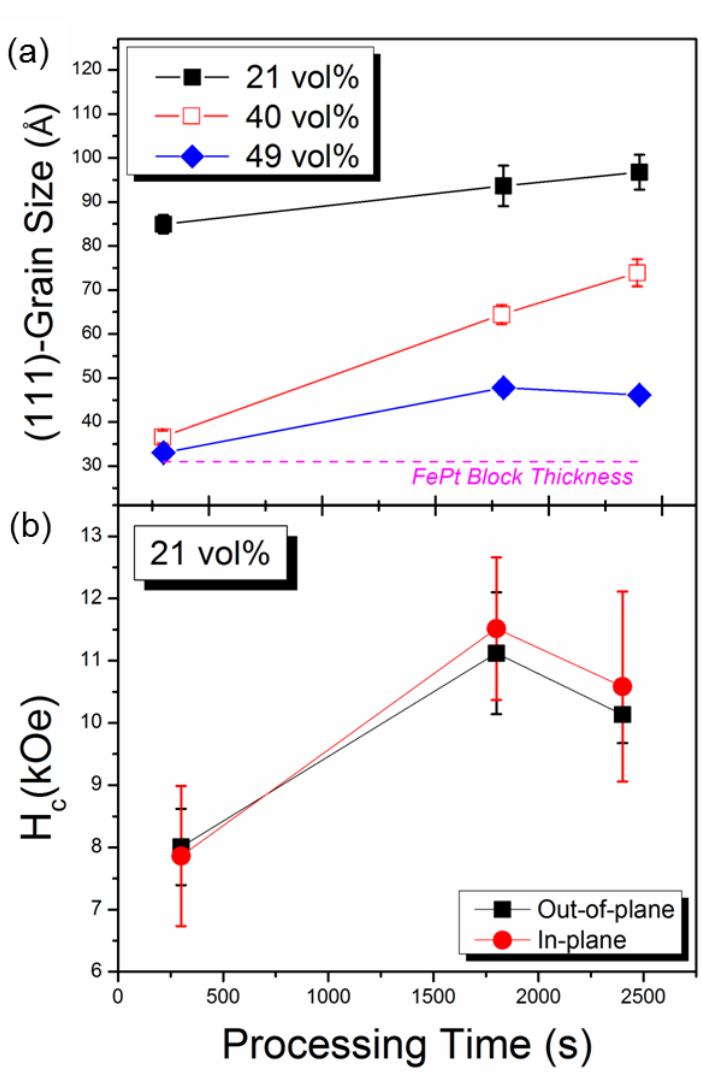

FIG. 5.16. Part (a) shows (111)-grain sizes of select AlO5 samples for longer annealing times. Part (b) shows trend of in- and out-of-plane coercivities of the 21 vol% AlO5 film for increased annealing times.

5.2.3 FePt:Al_2O_3 – Summary and Conclusions

A composite nanostructure is attained in multilayer films of Fe, Pt, and Al_2O_3 after post-deposition processing at 600 °C for 300 s. The oxide acts as a matrix material for magnetically decoupled $L1_0$-FePt nanograins. Vertical grain-sizes of ~4 nm are achieved with the inclusion of >40 vol% oxide. The addition of Al_2O_3 strongly affects the development of chemical order and non-epitaxial (001)-texture; both chemical order and the degree of (001) texture degrade with increasing oxide concentration. Merely inserting a ~0.25 Å alumina layer per ~6.2 Å of Fe/Pt

drastically affects the formation and growth of the ordered phase. The presence of the oxide alters the evolution of strain during annealing, thereby disrupting the SEDSGG of (001)-oriented grains. Increasing the period of insertion of the alumina layer within the FePt-ML stack changes the extent in which the oxide influences ordering process, and chemical order and (001)-texture are improved with thicker blocks of Fe-Pt per alumina layer. The processed nanocomposite films' magnetic properties result from a combination of the granular microstructure, with variable grain-size and intergranular exchange-coupling, and sullied chemical order.

The small grain sizes achieved with an alumina matrix make the FePt:Al_2O_3 system viable for recording media. However, the thermal stability and perpendicular recording performance would suffer due to decreased chemical order and (001)-texture, respectively. As an effective diffusion barrier, alumina may serve in a nanomagnetic system with FePt to control grain size and particle separation where chemical order and texture are strongly controlled by other means, such as with epitaxial growth and *in-situ* ordering.

5.3 FePt:Au and FePt:C Nanocomposite Films

Successful control of post-deposition annealed grain-size and exchange-coupling in a nanocomposite FePt thin film for use as in a PMR system requires a dopant that does not disrupt the formation of (001) texture. Carbon has been demonstrated as a viable addition to FePt in post-deposition annealed ML thin-films, yielding decent order and (001)-texture up to ~32 vol% [5.16]. Numerous effects have been reported on the formation of $L1_0$ order and grain growth when alloying FePt thin films with Au. However, no reports exist on the (001)-texturing of such films on amorphous substrates. The precise effect on the ordering process depends on how the Au is added to the FePt thin film [5.45]. Co-deposited thin films of Au, Fe, and Pt indicated an increased kinetic ordering temperature with respect to a comparable pure FePt film [5.11], whereas the opposite effect was found for multilayer [5.46,5.47] films ordered both *in-situ* and

post-deposition [5.48]. Au has been shown to generally diffuse to the boundaries of FePt grains or particles, refining grain sizes and magnetically decoupling neighboring grains [5.5,5.11,5.12,5.46].

The nanostructure and magnetism of $L1_0$-ordered FePt crystallites in matrices of Au and C is investigated. The effect of dopant content on (001)-texture and degree of $L1_0$ order is examined, with additional emphasis placed on the relation between hysteresis-loop shape, magnetic correlation length (L_m), and structural disorder, as relevant to magnetic recording media. Portions of the following results have been published in Refs. 5.49 and 5.50.

5.3.1 Experimental Details

Multilayer thin films of FePt/Au and Fe/Pt/C were deposited by magnetron sputtering using the 3M system as described in Chap. 3. Unlike other ML films described in this dissertation, the FePt:Au films were fabricated as bilayers of FePt and Au, where each FePt layer was deposited from a composite target as described in Chap. 3.[26] The as-deposited structure of the FePt:Au sample series was therefore [FePt 5 Å/Au x]$_m$. The parameter x took the values 0.6, 1.2, 1.8, and 2.4 Å, for 11, 19, 26, and 32 vol% Au, and m was varied to maintain a ~100 Å total film thickness.

Figure 5.1 depicts the deposition structure for the C-doped films, where in this case Σ = C and n = 4. Individual Fe, Pt and C layer thicknesses of 1.8 Å, 1.4 Å and 0 or 2.5 Å, respectively, were deposited from 2-3 N pure elemental targets in 5.1 mTorr of Ar working gas. The volume percent of carbon matrix was increased by using a progressively thick carbon underlayer, which presumably diffused throughout the composite film's grain boundaries during annealing. Combined with the carbon within the multilayers, films with of 16, 27, 33, and 39 vol% C were achieved. Total film thicknesses ranged from 12 – 19 nm.

[26] The FePt/Au films were fabricated by Minglang Yan.

To achieve $L1_0$ order, (001)-texture, and refined microstructure, coupons of approximately 4.5× 4.5 mm^2 were cut from the as-deposited samples and processed by RTA under 5%-H_2 Ar based forming gas for 300 seconds at 600 °C. Crystalline phase and texture were confirmed by XRD with a Bruker D8 Discover system and magnetic hysteresis loops were obtained by a SQUID magnetometer in fields up to 7 Tesla. Magnetic correlation lengths were estimated by magnetic force microscopy (MFM) after deconvoluting the data as described in Chap. 3.

5.3.2 $L1_0$ Order and (001)-Texture

XRD spectra for the FePt thin films with gold and carbon additives can be seen in Fig. 5.17 a) and b), respectively. In both series the pure FePt films' spectra show only (00*l*) diffraction peaks from the ordered phase of FePt, indicating a high degree of (001) texture.[27] Ordered peak positions of the single-layer co-deposited Au-series film appear shifted slightly to the left of their anticipated position. The peaks shift further left with increasing Au up to 19 vol% Au, and then move slightly back to the higher angles. With increasing Au concentration, an $L1_0$-(200) peak becomes prevalent out of the low-angle shoulder of the (002) peak. In addition, a peak characteristic of (111)-oriented Au grains is visible in the lowest concentration of 11 vol% and rapidly gains prominence with Au content, indicating the presence of distinct and sizable grains of Au. (001)-texture is maintained fairly well throughout the series; only a small fraction of (111)-oriented FePt grains become manifest with even 32 vol% Au. The slight shift of that peak position to a lower angle, along with the slightly higher angle of the Au-(111) peak, indicates the possible close proximity of those grains.

[27] The high degree of texture in a 100 Å FePt film deposited from a composite target is somewhat surprising.

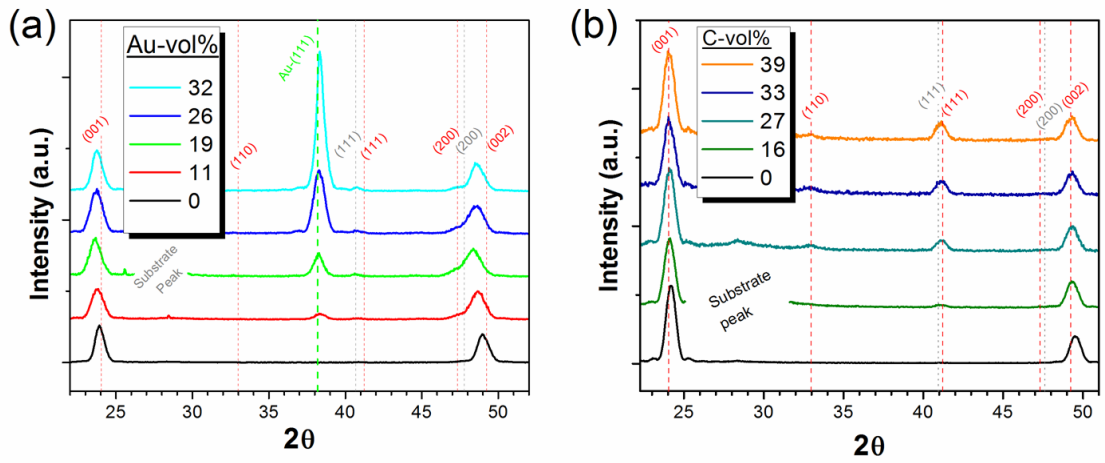

FIG. 5.17. XRD spectra for (a) FePt:Au and (b) FePt:C films with varying matrix concentrations.

Similar to the Au-series, the C-series films are also Pt-rich at about 47 at.% Fe and the right-shifted peaks of the pure-film are somewhat unexpected. Doping up to 39 vol% C yields no additional XRD peaks, however the effect of the carbon matric can be seen in the development of (111)-oriented grains and a slight shift of the $L1_0$ peaks to lower angles.

Figure 5.18 shows the trends in chemical order (S), (001)-texture (LOF), c-lattice parameter, and grain sizes for the both FePt-Au and FePt-C samples as determined from fitting the XRD spectra. The chemical order of the Au-series films, seen in part (a) of that figure, begins relatively low at 0.703(5), possibly due to a limited ordering process afforded by the annealing conditions on a film deposited by a composite target. S fluctuates within +/- 0.08 of this value with the addition of Au. It is plausible that the smallest Au doping hinders the ordering process while an increased amount actually enhances it. The same figure shows the initially high (001)-texture in the pure FePt film, with LOF = 0.983(7), dropping to 0.85(2) at 26 vol% Au, and then increasing to 0.94(3) at 32 vol%. Part (c) shows a c-lattice parameter for the FePt-Au films larger than that of bulk $L1_0$ FePt, which expands when increasing the Au content up to 19 vol% Au, and subsequently contracts. At the same time, the vertical size of the (001)-oriented grains decreases from near the film's nominal thickness of 100 Å to 76.2(4) Å upon adding the Au

dopant, remains relatively constant at that value until increasing again to 89(1) Å at 32 vol%. The addition of Au up to 32 vol% does not appear to detrimentally affect the chemical order or (001)-texture as severely as comparable amounts of Al_2O_3 did, however, neither does the Au matrix seem to restrict grain growth.

Figure 5.18 (b) and (d) illustrate the relatively small effect the carbon doping has on the (001)-textured $L1_0$ FePt films. The pure-FePt film for the C-series begins with relatively high values of S = 0.917(7) and LOF = 0.99(1). Upon inserting C into the ML, S and LOF drop to 0.821(9) and 0.95(1), respectively. Chemical order fluctuates between 0.84(1) and 0.79(1) for increasing carbon vol%. LOF drops to 0.89(2) at 33 vol% C, then jumps back up to 0.95(1) for 38 vol%. Changes in c-lattice parameter and (001)-grain size increase and decrease monotonically, respectively, with the c-lattice parameter remaining below the bulk value for $L1_0$ FePt and the grain size decreasing by only ~11% over the entire range of C dopant. Texture and chemical order of these composite FePt films appear to be even less affected by the C matrix than Au.

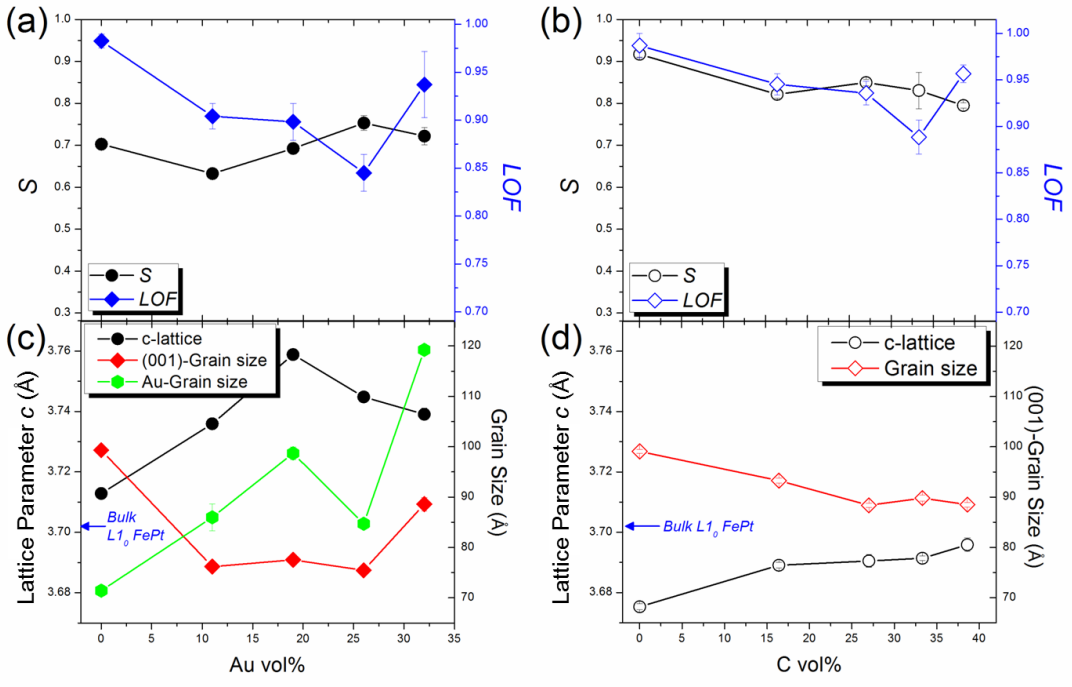

FIG. 5.18. Properties of composite FePt:Au and FePt:C films: S and LOF in (a) and (b) and c-lattice parameter and relevant grain sizes in (c) and (d).

Values for perpendicular coercivity measured from both series are plotted in Fig. 5.19 versus matrix content. With all else remaining static, a decrease in intergranular exchange typically results in higher coercive values [5.4,5.16]. The FePt:Au film series displays this behavior precisely, indicating the disruptive effects of the Au dopant on magnetic exchange between the ordered grains. On the other hand, after only a slight rise in H_c in the FePt:C films with 16 vol% C, the coercivity increases dramatically at 27 vol% and subsequently deceases with further C addition. The decrease in coercivity at the end of the series could be due to a concurrent decrease in chemical order.

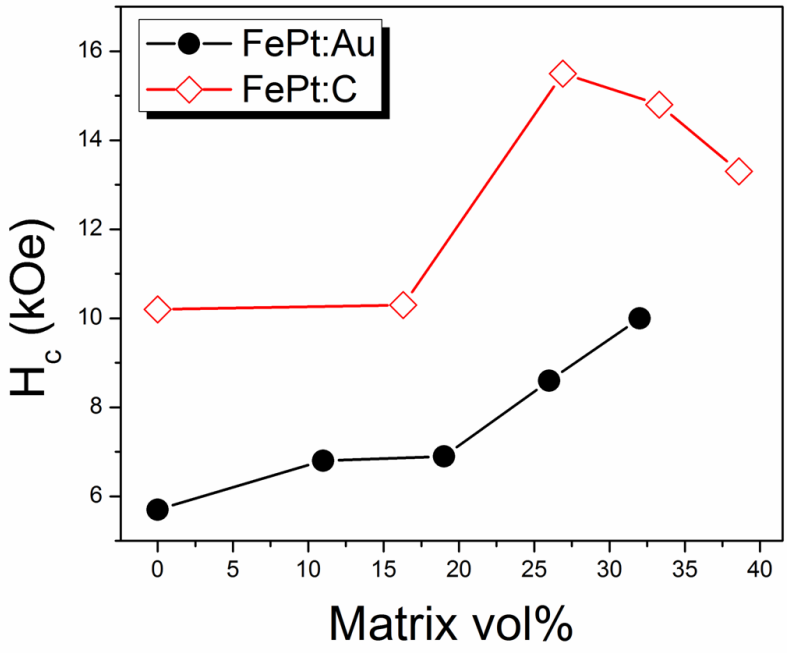

FIG. 5.19. Perpendicular coercivity trends for FePt:Au and FePt:C films with varying matrix concentrations.

5.3.3 Magnetic Correlations

Intergranular magnetic interactions can be analyzed directly by MFM or indirectly through the shape of the hysteresis loop. In particular, the slope at coercivity of a hysteresis curve, $\alpha = (4\pi \mathrm{d}M/\mathrm{d}H)_{H_c}$, may be associated with the performance of a magnetic recording medium [5.51]. Some attention has been paid to the relationship between the parameter α and

the magnetic correlation length, L_{m}, as measured by MFM [5.7,5.52], but little work has been done to connect the two with a model to gain information about the real-structure of a system.

The correlation length L_{m} of a macroscopically homogeneous and isotropic magnet is defined in terms of the correlation function

$$C(R) = \langle \boldsymbol{M}(\boldsymbol{r}) \cdot \boldsymbol{M}(\boldsymbol{r}+\boldsymbol{R}) \rangle - \langle \boldsymbol{M}(\boldsymbol{r}) \rangle \cdot \langle \boldsymbol{M}(\boldsymbol{r}+\boldsymbol{R}) \rangle \,, \tag{5.1}$$

where $C(R) \sim 0$ for $|\boldsymbol{R}| \sim L_{\mathrm{m}}$. Many systems are reasonably well described by $C(R) = C(0)\exp(-R/L_{\mathrm{m}})$, but most image-processing methods estimate $C(R)$ directly from Eq. (5.1) [5.53]. Experimentally, *C*(*R*) is accessible by neutron or x-ray scattering, as exemplified by measurements not only on ferromagnets near the Curie temperature but also on granular magnetic nanostructures [5.54-5.56]. The latter measurements collect information about a variety of micromagnetic features, including flux-closure domains and grain-boundaries [5.57]. However, the emphasis here is on correlations between neighboring grains, that is, on interaction domains.

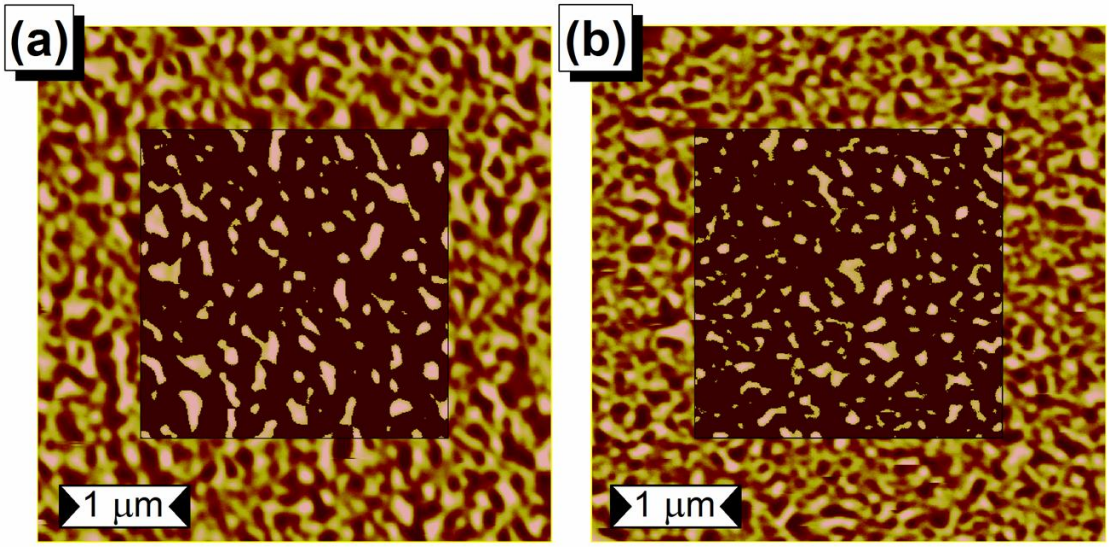

FIG. 5.20. MFM images for FePt:C films with (a) 0 and (b) 33 vol% C. The inner squares have been filtered to show features greater than 50% of the maximum signal.

Figure 5.20 shows MFM scans for the FePt:C system with C volume percents of 0 and 33 in (a) and (b), respectively. These scans illustrate how the magnetic domains decrease in size with increasing matrix content. Without carbon, L_{m} is estimated at 80.4 nm. This decreases to 50.2 nm for 39 vol% carbon. Figure 5.21 shows how L_{m} varies with matrix content for both systems. For the FePt:Au films, L_{m} ranges from 90 nm for gold-free films, to 73.8 nm for 32 vol% Au.

The hysteresis-loop slope at coercivity is also related to intergranular exchange, usually increasing with exchange and decreasing with matrix content. In the FePt:Au system, Fig. 5.21 (a), α decreases from 5.7 for gold-free films to 0.9 for 32 vol% Au. Figure 5.21 (b) shows a similar trend for the FePt:C system; parameter α decreases from 4 to 0.8 as the C vol% is increased. Features such as switching-field distribution, magnetostatic interactions, particle geometry, and the electronic properties of the matrix also affect loop slope. Consequently, exchange strength cannot be derived from a single value of α. However, trends in α reveal trends in exchange, i.e., exchange between grains increases as the slope becomes steeper. In practice, the exchange interactions are often of the contact type, that is, grains are relatively strongly coupled if they touch each other. In addition, there is some exchange mediated by grain boundaries or by the matrix, where the coupling is reduced [5.55] and the magnetization reversal becomes reminiscent of pinning [5.58]. In fact, seemingly minor real-structure changes may translate into very different coupling and reversal mechanisms and yield significantly different parameters in micromagnetic models.

It is clear from Fig. 5.21 that L_{m} and α are closely connected; both reflect intergranular exchange and are controlled by the volume fraction of the matrix phase. It is well-known that the slope α_0 of an ensemble of non-interacting particles is determined by the particles'

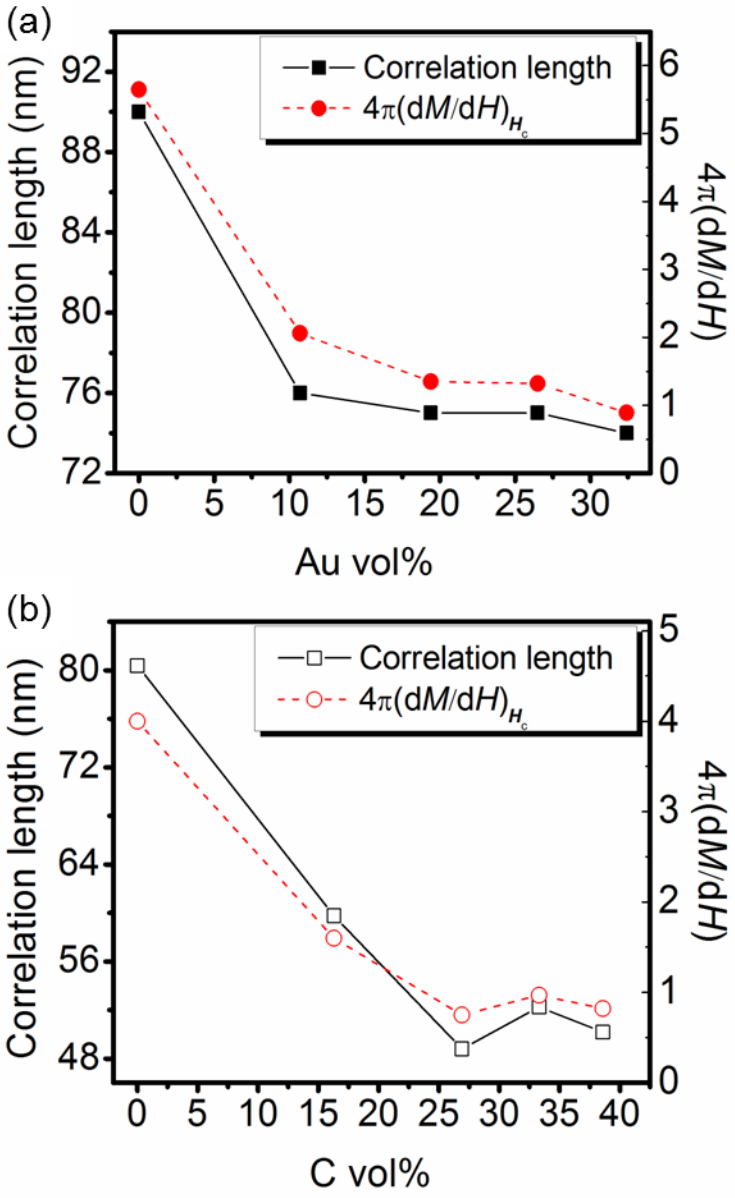

FIG. 5.21. Correlation lengths and parameter $\boldsymbol{\alpha}$ for (a) FePt:Au and (b) FePt:C nanocomposite films.

switching-field distribution, $\alpha_0 \sim M_s/H_{sw}$. Adding an exchange and/or magnetostatic interaction field H_{int} to the external magnetic field yields [5.7],

$$\alpha = \frac{\alpha_0}{1 - \frac{H_{int}}{M_s}}. \tag{5.2}$$

For small interactions this can be rewritten,

$$\frac{\alpha}{\alpha_0} = 1 + \alpha_0 \frac{H_{\mathrm{int}}}{M_{\mathrm{s}}} \tag{5.3}$$

If two non-interacting particles of volume V_0 touch each other with a probability *W*, then the average volume of the cooperative units increases to

$$V = V_0(1 + W) \tag{5.4}$$

In this equation, W can be expressed as $W = \alpha_0 \Delta H_{\mathrm{int}}/M_{\mathrm{s}}$, where ΔH_{int} is a net interaction field. Assuming that each particle is coordinated by z neighbors, it must take into account that Eq. (5.4) describes the clustering of *two* particles only, because the other $z - 1$ neighbors have in general very different switching fields. In other words, the interaction cooperatively couples [5.57] pairs with similar switching fields, and the remaining $z - 1$ neighbors do not interfere in the lowest order. This means that $\Delta H_{\mathrm{int}} = H_{\mathrm{int}}/z$, and for small H_{int}, Eq. (5.4) can be written as

$$\frac{V}{V_0} = \left(1 + \alpha_0 \frac{H_{\mathrm{int}}}{M_{\mathrm{s}}}\right)^{1/z}. \tag{5.5}$$

Comparing Eqs. (5.3) and (5.5) yields, with $V \sim L_{\mathrm{m}}^3$,

$$\frac{L_{\mathrm{m}}}{L_0} = \left(\frac{\alpha}{\alpha_0}\right)^{1/3z}. \tag{5.6}$$

Equation (5.6) makes it possible to extract real-structure information from L_{m} and α.

Figure 5.22 shows a plot of $\log(L_{\mathrm{m}})$ versus $\log(\alpha)$ for both systems. The microstructural parameters $z \approx 0.9$ for FePt:C and z ≈ 8.8 for FePt:Au are very different from each other. The latter is consistent with a picture of a three-dimensional random network of particles. The former is relatively small and may indicate a reversal mechanism different from that assumed in Eqs. (5.2 – 5.4). A more thorough explanation of z requires an explicit calculation of α and L_{m}

from the coupling properties of the matrix and from the structural disorder of the granular system.

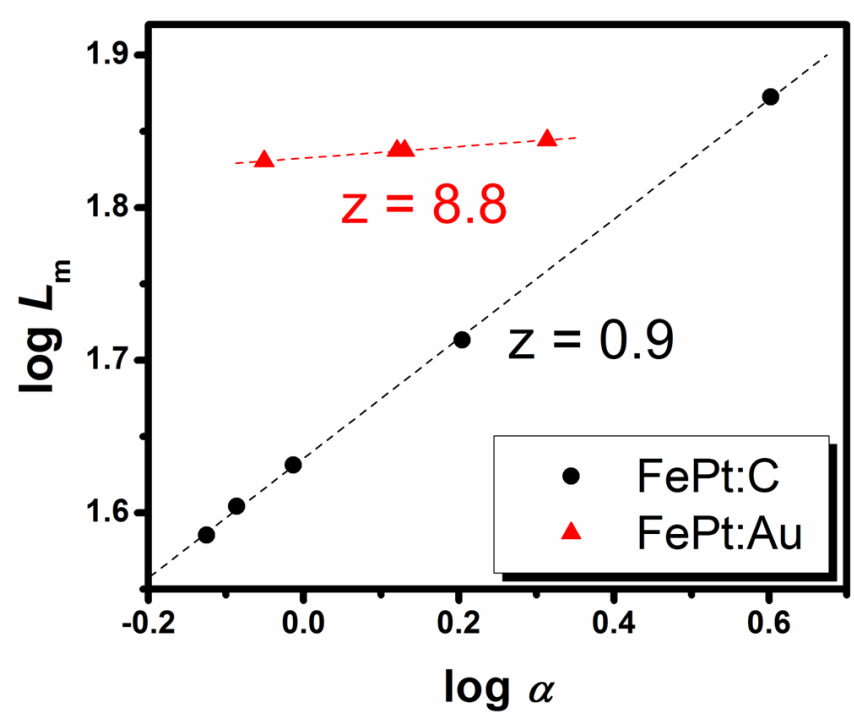

FIG. 5.22. Relationship between correlation length L_{m} and loop slope α. This double-logarithmic plot is used to determine the parameter z.

5.3.4 FePt:Au and FePt:C – Discussion and Conclusions

Non-epitaxial ML thin films of FePt with additives of Au and C have demonstrated relatively little deterioration of chemical order and (001)-texture for dopant-volume percents up to 32 and 39, respectively. A separated phase of Au exists upon adding the smallest investigated amount, 11 vol%, which is consistent with reports in the literature [5.11,5.12]. On the other hand, no additional phases are seen in the FePt:C films ,and C is presumed to occur in an amorphous phase at the ordered-FePt grain boundaries. Both elements serve to decrease magnetic interactions between the $L1_0$-FePt grains. The coercivity and the hysteresis-loop slope at coercivity increase and decrease, respectively, with increasing volume fraction of the matrix. Changes in M-H slope and magnetic interaction length are attributed to reduced intergranular

exchange coupling. A simple model describing how interparticle exchange cooperatively increases both loop slope and correlation length yields different microstructural parameters for the two systems, indicating very different underlying structures or reversal mechanisms.

The presented work assumes that the correlation length, or the size of the interaction domains, is governed by two-particle interactions. This is a rather crude approximation, and it is often more appropriate to start from the opposite limit of a large number of particles with relatively strong interactions. As in the theory of phase transitions [5.59], equations of the type [5.57]

$$A\nabla^2\phi + \left(K_1(\boldsymbol{r}) + \frac{1}{2}\mu_0 M_\mathrm{s} H(\boldsymbol{r})\right)\phi = f(r) \tag{5.7}$$

are micromagnetic analogs to the Ornstein-Zernike equation. Physically, the interactions are not short-range, as described by the local operator ∇, but propagate through the magnet, and the MFM pictures correspond to the result of this propagation. As a rule, the correlation function $C(R)$ exhibits a strong dependence on the applied magnetic field. For infinite fields $\boldsymbol{H} = H_\mathrm{z}\mathbf{e}_\mathrm{z}$, $\boldsymbol{M}(\boldsymbol{r}) = \boldsymbol{M}_\mathrm{s}\boldsymbol{e}_\mathrm{z}$ and $C(R) = 0$. For strong but finite fields there is a small perpendicular magnetization component $m = \boldsymbol{M}/M_\mathrm{s}(-\mathbf{e}_\mathrm{z})$ and $C(\boldsymbol{r}) = M_\mathrm{s}^2\langle\boldsymbol{m}(\boldsymbol{r})\cdot\boldsymbol{m}(\boldsymbol{r}+\boldsymbol{R})\rangle$, where $\boldsymbol{m}(\boldsymbol{r})$ can be determined by methods described in Refs. 5.57 and 5.59. The situation is often more complicated at remanence ($H = 0$) and at the nucleation field ($H = -H_\mathrm{N}$) [5.60,5.61], where the response of the system is of the random-field or random-anisotropy type. Another complication is that fields used in typical laboratory-scale experiments are very homogeneous on the nanoscale, in contrast to actual write fields, which are localized on a length scale *D* given by the head size and the head-to-medium distance. This localization would reduce the measured correlation length to a value that depends on the type of disorder present in the system, but varies between L_m ($D = \infty$) and roughly the Bloch-wall width ($D = 0$).

In conclusion, this section presented investigations of nanocomposite thin films of FePt:C and FePt:Au for potential application in perpendicular magnetic recording. The films are

$L1_0$ ordered with perpendicular *c*-axis orientation up to relatively high matrix concentrations, but varying intergranular exchange affects the performance of the material. The relationship between the hysteresis loop slope α and the magnetic correlation length L_{m} at coercivity is governed by a real-structure dependent parameter$z$. The studies here correlating L_{m} and α, when extended to noise measurements in magnetic media, may enable useful comparisons of competing films structures and compositions for low-noise recording media design.

5.4 Concluding Remarks for Chapter 5

Layers of Au, C, and Al_2O_3 were inserted into FePt ML films in an effort to fabricate a granular nanostructure appropriate for magnetic recording. For each series of films, post-deposition annealing resulted in various degrees of FePt grain segregation and grain-growth constraint. However, the dopants also caused detrimental reductions in chemical order and (001) texture of the $L1_0$ grains. Al_2O_3 exhibited the most influence on the evolution of a textured, granular FePt film. On the other hand, the effects of Au and C on order and texture are less severe, although the vertical grain sizes were not as well controlled. A close examination of the lateral grain sizes in these films would be useful to further understand their behavior as a surfactant for FePt.

Recent progress in realizing a FePt-based thin-film for heat-assisted magnetic recording has brought to light the importance of using an optimized matrix material [5.2]. That work involves *in-situ* growth of the ordered-phase with a high degree of (001)-texture through the use of an MgO-seed layer. A granular microstructure is formed in a similar manner to post-deposition annealed films. It has been demonstrated that at high volume percents, the low C-FePt interface energy yields spherical grains instead of the desired columnar structure, whereas SiO_2 yields a network of interconnected grains in the film plane. Tuning the matrix material has been approached by attempting materials with cohesive energies intermediate to the above

two, or a mixture of two different segregants. Similar considerations could be applied optimizing the matrix for non-epitaxial FePt films, with additional considerations of strain management to support the development of (001) texture.

5.5 References

5.1 R. Wood, Journal of Magnetism and Magnetic Materials **321** (6), 555-561 (2009).

5.2 B. S. D. C. S. Varaprasad, Y. K. Takahashi and K. Hono, Journal of Materials **65** (7) (2013).

5.3 F. Q. Wang, X. H. Li, J. X. Guo, D. F. Guo, L. Xu, J. W. Zhao, B. T. Liu and X. Y. Zhang, Journal of Alloys and Compounds **508** (2), 512-515 (2010).

5.4 D. H. Ping, M. Ohnuma, K. Hono, M. Watanabe, T. Iwasa and T. Masumoto, Journal of Applied Physics **90** (9), 4708-4716 (2001).

5.5 C. L. Platt, K. W. Wierman, E. B. Svedberg, R. van de Veerdonk, J. K. Howard, A. G. Roy and D. E. Laughlin, Journal of Applied Physics **92** (10), 6104-6109 (2002).

5.6 K. Kang, Z. G. Zhang, C. Papusoi and T. Suzuki, Applied Physics Letters **82** (19), 3284-3286 (2003).

5.7 M. L. Yan, R. Skomski, A. Kashyap, L. Gao, S. H. Liou and D. J. Sellmyer, IEEE Transactions on Magnetism **40** (4), 2495-2497 (2004).

5.8 C. Feng, Journal of Applied Physics **110** (6), 063910 (2011).

5.9 M. Watanabe, T. Masumoto, D. H. Ping and K. Hono, Applied Physics Letters **76** (26), 3971-3973 (2000).

5.10 J. Bai, Z. Yang, F. Wei, M. Matsumoto and A. Morisako, Journal of Magnetism and Magnetic Materials **257** (1), 132-137 (2003).

5.11 K. Barmak, J. Kim, D. C. Berry, K. W. Wierman, E. B. Svedberg and J. K. Howard, Journal of Applied Physics **95** (11), 7486-7488 (2004).

5.12 F. T. Yuan, S. K. Chen, W. C. Chang and L. Horng, Applied Physics Letters **85** (15), 3163-3165 (2004).

5.13 Y. S. Yu, H.-B. Li, W. L. Li, M. Liu, Y.-M. Zhang and W. D. Fei, Journal of Magnetism and Magnetic Materials **322** (13), 1770-1774 (2010).

5.14 J. A. Christodoulides, P. Farber, M. Dannl, H. Okumura, G. C. Hadjipanaysi, V. Skumryev, A. Simopoulos and D. Weller, IEEE Transactions on Magnetics **37** (4), 1292-1294 (2001).

5.15 C. P. Luo, S. H. Liou, L. Gao, Y. Liu and D. J. Sellmyer, Applied Physics Letters **77** (14), 2225-2227 (2000).

5.16 M. L. Yan, R. F. Sabirianov, Y. F. Xu, X. Z. Li and D. J. Sellmyer, IEEE Transactions on Magnetism **40** (4), 2470-2472 (2004).

5.17 Y. H. Huang, J. Wan, Y. Zhang, H. L. Wang, G. C. Hadjipanayis, D. Niarchos and D. Weller, Journal of Magnetism and Magnetic Materials **294** (2), 232-238 (2005).

5.18 J. S. Chen, B. C. Lim, J. F. Hu, B. Liu, G. M. Chow and G. Ju, Applied Physics Letters **91** (13), 132506-132503 (2007).

5.19 A. Perumal, Y. K. Takahashi, T. O. Seki and K. Hono, Applied Physics Letters **92** (13), 132508-132503 (2008).

5.20 T. Maeda, T. Kai, A. Kikitsu, T. Nagase and J.-i. Akiyama, Applied Physics Letters **80** (12), 2147-2149 (2002).

5.21 Y. K. Takahashi, M. Ohnuma and K. Hono, Journal of Magnetism and Magnetic Materials **246** (1-2), 259-265 (2002).

5.22 K. W. Wierman, C. L. Platt, J. K. Howard and F. E. Spada, Journal of Applied Physics **93** (10), 7160-7162 (2003).

5.23 M. L. Yan, Y. F. Xu and D. J. Sellmyer, Journal of Applied Physics **99** (8), 08G903-903 (2006).

5.24 D. C. Berry and K. Barmak, Journal of Applied Physics **101** (1), 014905-014914 (2007).

5.25 C. Brombacher, H. Schletter, M. Daniel, P. Matthes, N. Johrmann, M. Maret, D. Makarov, M. Hietschold and M. Albrecht, Journal of Applied Physics **112** (7), 073912-073918 (2012).
5.26 S. Jeong, T. Ohkubo, A. G. Roy, D. E. Laughlin and M. E. McHenry, 2002 (unpublished).
5.27 K. Kang, Z. G. Zhang, C. Papusoi and T. Suzuki, Applied Physics Letters **84** (3), 404-406 (2004).
5.28 M. L. Yan, Y. F. Xu, X. Z. Li and D. J. Sellmyer, Journal of Applied Physics **97**, 10H309-303 (2005).
5.29 D. C. Berry and K. Barmak, Journal of Applied Physics **102** (2), 024912-024919 (2007).
5.30 C.-M. Kuo and P. C. Kuo, Journal of Applied Physics **87** (1), 419-426 (2000).
5.31 Y. H. Fang, P. C. Kuo, A. C. Sun, S. L. Hsu and S. C. Chen, Thin Solid Films **517** (17), 5181-5184 (2009).
5.32 C. P. Luo and D. J. Sellmyer, Applied Physics Letters **75** (20), 3162-3164 (1999).
5.33 D. H. Wei, F. T. Yuan, H. W. Chang, K. L. You, Y. Liou, T. S. Chin, C. C. Yu and Y. D. Yao, Nanotechnology (33), 335603 (2007).
5.34 Y.-C. Wu, L.-W. Wang, C.-H. Lai and C.-R. Chang, Journal of Applied Physics **103** (7), 07E140-143 (2008).
5.35 T. Narisawa, T. Hasegawa, S. Ishio and H. Yamane, Journal of Applied Physics **109** (3), 033918-033917 (2011).
5.36 X.-H. Xu, X.-L. Li and H.-S. Wu, Materials Science and Engineering B **121** (1-2), 183-186 (2005).
5.37 S.-R. Lee, S. Yang, Y. K. Kim and J. G. Na, Applied Physics Letters **78** (25), 4001-4003 (2001).
5.38 C. Feng, E. Zhang, M. Yang, N. Li, B. Li, Y. Jiang and G. Yu, Journal of Applied Physics **107** (12), 123911-123915 (2010).
5.39 T. Ichitsubo, S. Tojo, T. Uchihara, E. Matsubara, A. Fujita, K. Takahashi and K. Watanabe, Physical Review B **77** (9), 094114 (2008).
5.40 A. C. Johnston-Peck, G. Scarel, J. Wang, G. N. Parsons and J. B. Tracy, Nanoscale **3** (10), 4142-4149 (2011).
5.41 T. Suzuki and K. Ouchi, IEEE Transactions on Magnetism **37** (4), 1283-1285 (2001).
5.42 G. Safran, T. Suzuki, K. Ouchi, P. B. Barna and G. RadnÃ³czi, Thin Solid Films **496** (2), 580-584 (2006).
5.43 S. Okamoto and O. Kitakami, Journal of Magnetism and Magnetic Materials **310** (2, Part 3), 2367-2368 (2007).
5.44 M. Matsumoto, A. Morisako and N. Katayama, Journal of Applied Physics **93** (10), 7169-7171 (2003).
5.45 B. Wang, K. Barmak and T. J. Klemmer, IEEE Transactions on Magnetics **46** (6), 1773-1776 (2010).
5.46 C. Feng, Q. Zhan, B. Li, J. Teng, M. Li, Y. Jiang and G. Yu, Applied Physics Letters **93** (15), 152513-152513 (2008).
5.47 S. K. Chen, F. T. Yuan, W. M. Liao, C. W. Hsu and L. Horng, Journal of Magnetism and Magnetic Materials **303**, 5 (2006).
5.48 C. Y. You, Y. K. Takahashi and K. Hono, Journal of Applied Physics **100** (5), 056105-056103 (2006).
5.49 T. A. George, Z. Li, M. Yan, Y. Xu, R. Skomski and D. J. Sellmyer, Journal of Applied Physics **103**, 07D502-503 (2008).
5.50 T. A. George, R. Skomski and D. J. Sellmyer, Journal of Applied Physics **105** (7), 07B736-733 (2009).

5.51 N. Honda, T. Kiya, J. Ariake, K. Ouchi and S. Iwasaki, IEEE Transactions on Magnetics **38** (5), 2030-2032 (2002).
5.52 H. Uwazumi, K. Enomoto, Y. Sakai, S. Takenoiri, T. Oikawa and S. Watanabe, IEEE Transactions on Magnetism **39** (4), 1914-1918 (2003).
5.53 D. Stoyan and J. Mecke, *Stochastische Geometrie*. (Akademieverlag, Berlin, 1983).
5.54 J. Weissmüller, A. Michels, J. G. Barker, A. Wiedenmann, U. Erb and R. D. Shull, Physical Review B **63** (21), 214414 (2001).
5.55 O. Hellwig, D. T. Margulies, B. Lengsfield, E. E. Fullerton and J. B. Kortright, Applied Physics Letters **80** (7), 1234-1236 (2002).
5.56 J. B. Kortright, O. Hellwig, K. Chesnel, S. Sun and E. E. Fullerton, Physical Review B **71** (1), 012402-012404 (2005).
5.57 R. Skomski, J. Phys.: Condens. Matter **15** (20), R841-R896 (2003).
5.58 J. Zhou, A. Kashyap, L. Yi, R. Skomski and D. J. Sellmyer, IEEE Transactions on Magnetism **40** (4), 2940-2942 (2004).
5.59 R. Skomski, *Simple Models of Magnetism*. (University Press, Oxford, 2008).
5.60 Y. Imry and S.-k. Ma, Physical Review Letters **35** (21), 1399 (1975).
5.61 E. M. Chudnovsky, W. M. Saslow and R. A. Serota, Physical Review B **33** (1), 251 (1986).

CHAPTER 6 FePt-BASED EXCHANGE-COUPLED COMPOSITE SYSTEMS

6.1 Introduction and Background

Future magnetic recording systems exceeding areal densities of 1 Tb in^{-2} will challenge the fundamental limits of all three aspect of the well-known trilemma and continued progress will likely require a paradigm shift in the basic technology. For the media material, grains of the CoCrPt-based alloys currently used become superparamagnetic at the proposed dimensions necessary to maintain sufficient signal-to-noise ratio (SNR) at ~750 Gbits in^{-2}. Thermal stability can be assured in smaller grains by using magnetically harder materials such as $L1_0$-phase FePt, whose magnetocrystalline anisotropy (MCA) is an order greater than other viable candidates. However, the requisite write-field would in turn greatly exceed the capabilities of any known purely-magnetic recording head. One proposed solution for reducing the necessary write-field in a high *K*, thermally stable media takes advantage of the exchange interaction between hard and soft magnetic phases. Writing an exchange-coupled (EC) media uses the low switching field of the soft phase to "lever" early reversal of the entire bit.

The fundamental implications of the exchange-coupling mechanism and the numerous proposed applications designed to take advantage of it have motivated experimental and theoretical studies since the 1960's. Chapter 2 lists a few potential uses and describes the general concept behind the resulting coercivity of an exchange-coupled system. The focus here is on EC media in perpendicular recording media (PMR). The importance of incoherent reversal in an optimal EC media has led to the terms domain wall assisted magnetic recording (DWAMR) media [6.1] and exchange spring (ES) media [6.2,6.3].

Various approaches for implementing EC media have spawned numerous architectures and exchange-coupling schemes. For example, the coupled granular continuous (CGC) media

design [6.4] utilizes a continuous soft-phase layer coupled to a granular hard-phase storage layer. In contrast, the exchange-coupled composite (ECC) media design continues the laterally-decoupled granular structure of the hard-phase into the coupled soft-phase layer such that each grain consists of a two-phase stack [6.5]. Antiferromagnetic coupling between magnetic layers has been proposed [6.6] as well as replacing the soft-phase with an antiferromagnet [6.7], in which case a thermally assisted recording process induces an antiferromagnetic-to-ferromagnetic phase transition during writing. In the graded EC media design the soft-phase is replaced by a material with K decreasing in the perpendicular direction from the hard-phase interface [6.8,6.9]. Another investigated feature is an exchange-break layer of a well-tuned thickness interceding between the coupled layers which encourages incoherent reversal for certain combinations of magnetic materials [6.10,6.11]. Significant theoretical work has predicted the thermal stability, switching speed, reversal mechanism, and potential noise characteristics of the different EC media types [6.12-6.16]. Importantly, it has been demonstrated that thermal stability of a properly fabricated EC media is in fact controlled by the hard-phase anisotropy.

Recent experimental work with $L1_0$ FePt-based exchange-coupled systems have utilized soft-phase layers of Fe [6.17-6.20] , fcc-FePt [6.21-6.26], FePt:Cu [6.27], CoPt alloys [6.28], Co/Pt multilayers, and Co/Ni multilayers [6.29]. Laterally decoupled structures are ensured by high-temperature deposition or annealing, or using a matrix material. Soft-phases with moderate anisotropy have been investigated with exchange-coupled layers of Co/Pt, Co/Ni, FePt:Cu and CoPt alloy. It has been demonstrated that moderate anisotropy in the coupled layer will yield the optimize ECC system for magnetic recording [6.8,6.13,6.30,6.31].

In a simple two-layer exchange-coupled system, incoherent reversal is expected for soft-phase dimensions greater than the critical length given by Eq. (2.18), which is ~1.7 nm for a

system using $L1_0$ FePt as a hard phase. Early switching in the exchange-coupled soft phase is reversible as it follows the unswitched hard phase. The system continues to exhibit this exchange-spring behavior until the pinning field is reached and the entire system reverses irreversibly. Coercivity reduces to a minimum value once a charged domain wall can be fully accommodated within the soft-phase (~4 nm for $L1_0$ FePt); additional soft-phase beyond that thickness would reverse independently and not contribute to the switching of the hard phase. The reversal process in an exchange-spring magnet follows two-steps: soft-phase nucleation and interfacial domain-wall (DW) depinning. The shape of a corresponding demagnetization curve depends on the energy barrier of each process, which define the critical fields, as well as the distributions of those barriers. For sufficiently large differences between smaller soft-phase nucleation and larger interfacial pinning fields the demagnetization loop has a two-phase character. If the two fields are close together or the energy barrier distributions are large the loop appears as a single phase. In the latter case, incoherent switching can be identified by examining recoil loops and the resulting differences in H_c and H_{cr}.

Optimizing an ECC system for PMR requires understanding the effects of intrinsic and extrinsic properties of the soft-phase layer on the magnetic behavior. The following sections present a study of an $L1_0$-ordered FePt based ECC system with an EC layer of partially ordered FePt:SiO_2. Three series of samples examine the effect of varying the soft-phase properties while using two different hard-phase layer thicknesses. Series A films have a nominally 2.6 nm thick hard layer coupled to a 3 nm soft layer, the latter deposited at temperatures ranging from 32 to 575 °C. Varying the deposition temperature of the coupled layer changes the morphology and chemical order, and thereby anisotropy, of the soft layer [6.32-6.35]. Series B examines the effect of varying the thickness of a partially ordered soft-phase layer with a 2.6 nm thick hard phase. Series C utilizes a thicker, 7.4 nm thick hard-phase layer and varies the partially ordered

soft-phase thickness. Focus is on switching field reductions, $M(H)$ loop shape, and changes in the morphology of the system. Results from Series A and B were published in Ref. 6.36.

6.2 Experimental Details

The films examined in this chapter were deposited in the AJA magnetron sputtering system using elemental Fe/Pt targets and an oxide SiO_2 target under a working-gas pressure of 5 mTorr Ar after achieving a base pressure of ~2 x 10^{-8} Torr. Details of the AJA system and the sputtering process can be found in Chapter 3. Single crystal (001)-MgO substrates were used for their close lattice match and large surface-energy differential with $L1_0$ FePt. Deposition rates were ~0.3 Å/s for Fe and Pt with a DC power supply and ~0.1 Å/s for SiO_2 using RF sputtering.

Each ECC film consists of two layers: a hard-phase layer, or "base" layer, and a soft-phase exchange-coupled (EC) layer. A two-step process using two deposition temperatures was employed to achieve different MCA in each layer. A schematic of the deposition process is shown in Fig. 6.1. All base layers were deposited at 700 °C after holding the substrate temperature fixed for one hour. Base layers were fabricated as multilayers with the repeated (Fe 1.9 Å/Pt 1.8 Å) bilayer structure for a composition of ~54 at.% Fe. The high deposition temperature on MgO substrates induced $L1_0$ ordering, (001)-texture and an island-like morphology, via means discussed in Chap. 2. Island size is controlled by growth temperature and deposited thickness [6.37].Pure base-layer samples, i.e. without an EC layer, were deposited to establish the properties of the hard phase alone. These samples are referred to throughout this chapter by their relevant sample series, e.g. A-Base or C-Base. Each series' base layer was *in-situ* annealed after deposition at 475 °C for 30 minutes to refine the degree of chemical order and microstructure [6.35,6.38,6.39]. The additional exposure to high temperature also mimicked the high-temperatures used during deposition of the EC layers, enabling a more accurate comparison with the full ECC films. Series A and B base samples consist of seven bilayer

repetitions for a nominal thickness of 2.6 nm, whereas series C and D base-layers have nominal thicknesses of 7.5 nm from 20 bilayer repetitions. Note that A-Base and B-Base are the same sample.

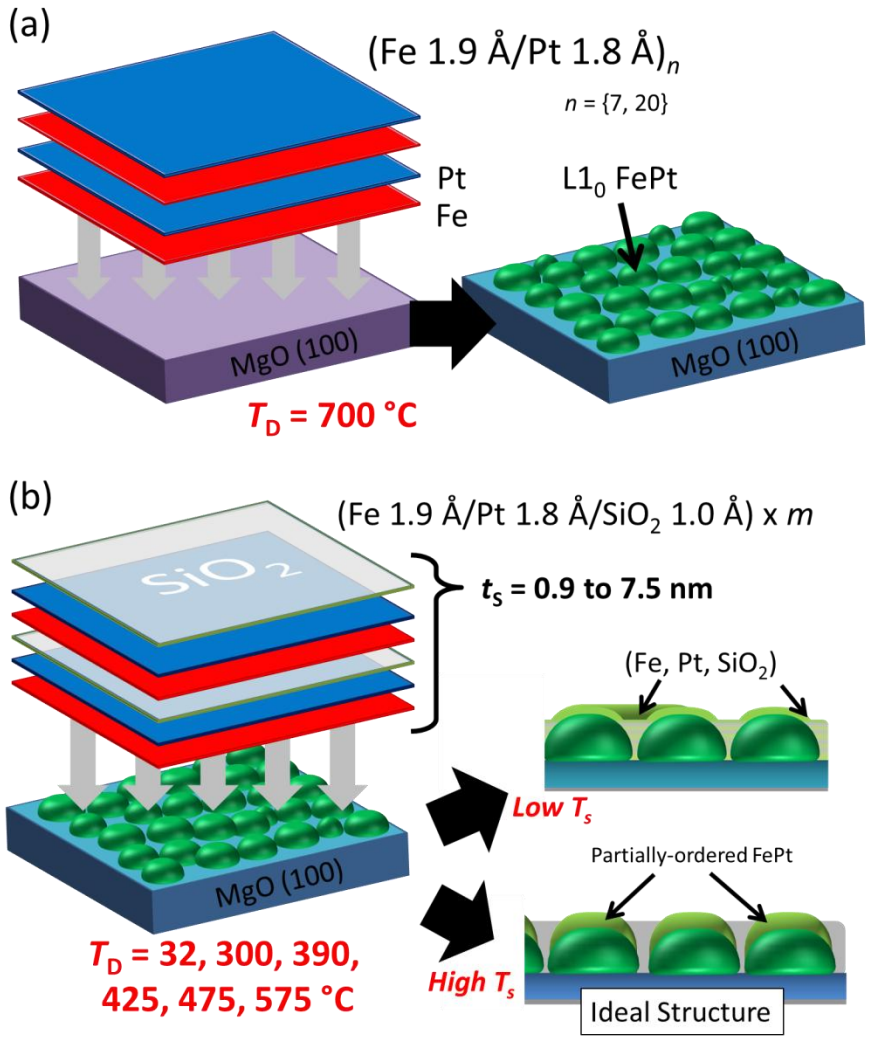

FIG. 6.1. Schematic of two-step deposition used to fabricate FePt-based ECC system: base layer (a) and exchange-coupled composite layer (b). Parameters explained in text.

Following a three hour cool down period to reach ~32 °C, each ECC sample was reheated to a target soft-phase deposition temperature (T_D). Deposition of the composite exchange-coupled layer began after holding that temperature for 30 minutes. Each soft-phase consists of the as-deposited multilayer structure (Fe 1.9 Å/Pt 1.8 Å/SiO_2 1 Å) x n, where n was varied to control the nominal thickness. A silica addition can slightly reduce the degree of

chemical ordering in FePt [6.40] and induce a segregated granular morphology at a relatively low deposition temperature to aid the formation of a columnar structure [6.40-6.44]. Additionally, the off-perpendicular deposition of the AJA sputtering system enables partial shadowing of the islands sides and the trenches between islands during deposition of the upper-most ECC layers, further promoting three-dimensional growth of the ECC structure.

Series A samples are comprised of an EC layer with *n* fixed at 8 (3 nm nominal thickness of magnetic material) while using deposition temperatures of 32 (ambient), 300, 390, 425, 475, and 575 °C. Films in series B were all deposited at T_D = 475 °C for nominal soft-phase thickness of 0.7, 1.5, 2.2, 3.0, 4.4, 5.9 nm, excluding the SiO_2. Series C used a soft-phase T_D of 425 °C for nominal FePt thicknesses of 1.5, 3.0, 4.4, 5.9, 7.4 nm. Samples in series A are referred to by the deposition temperature of their EC layer, e.g. A-300 or A-390. Individual films in B and C are referred to by their soft layer thickness in angstroms, e.g. B-22 or C-74. All samples were covered with a 5 nm protective SiO_2 cover-layer, except for samples A-32, A-300 and A-575 which were covered by a 2.5 nm Pt layer. Additionally, a 7.4 nm single-layer FePt:SiO_2 composite ML was deposited at 475 °C to reveal the properties of the soft phase alone.

Crystal phase characterization was carried out by the Rigaku diffractometer in θ-2θ configuration, as described in Chapter 3. The full 10 x 10 mm^2 samples were used in the diffraction experiments. Quantitative x-ray analysis, as described in Chapter 2 and 3, was limited to the A-Base and C-Base samples due to pronounced background contribution of the MgO (002) peak. In-plane diffraction was performed on sample A-Base by a Rigaku SmartLab system at Rigaku America in The Woodlands, Texas. The SmartLab system used Cu radiation at 40 Kv and 44 mA. Scans ranged from 20 – 90 ° in ϕ (in-plane rotation) with a 0.3 ° ω offset and three different ϕ-couplings, 0, 45, and 90 °. A zero-degree coupling corresponds to alignment of the

beam along the MgO-(200) direction. Data were analyzed by Dr. Aya Takase at Rigaku America using the NIST 660a correction.

In- and out-of-plane hysteresis, delta-H, and delta-M scans used in this chapter were measured by an MPMS SQUID magnetometer. Sample topology was determined by AFM in tapping mode using a NanoScope III SPM controller. Particle sizes were estimated from the AFM images by manually tracing the islands as ellipses and fitting the resulting histogram with a log-normal curve. Film continuity in series B and C was inferred from electrical resistance measurements across 2 mm x 8 mm strips cut from respective samples. Further details of the equipment and measurements can be found in Chapter 3.

6.3 Series A: Varying Soft-Phase Anisotropy

Sample series A investigates the effect on the switching behavior of an FePt/FePt:SiO_2 ECC system with the soft-phase deposited at temperatures of 32 (ambient), 300, 390, 425, 475 and 575 °C. The deposition temperature affects the degree of chemical order of the $L1_0$ FePt and the microstructure the EC layer as it grows on top of the hard-phase base layer. Higher substrate temperatures result in a greater degree of order and therefore MCA in the coupled layer. Additionally, elevated temperatures promote surface diffusion to aid the formation of the ECC structure.

Theoretical studies have demonstrated that the maximum switching-field reduction in an EC system occurs when a charged domain wall can be accommodated by the soft-layer of an ECC system. Equation (2.23) indicates the role of anisotropy in determining domain-wall widths; specifically, larger soft-phase anisotropies reduce the wall width. Additionally, the growth mode of the top layer governs the thickness available to form a Néel DW parallel to the interface. Highly agglomerated growth leads to thicker-than-nominal EC layers. The effect of varying the

soft-layer anisotropy and morphology on the switching behavior of an FePt-based ECC system is explored in the following.

6.3.1 Sample A-Base Properties

In order to establish the properties of the hard-phase alone, sample A-Base was deposited at 700 °C with a nominal thickness of 2.6 nm without a subsequent EC layer. After the Fe/Pt deposition the substrate was cooled and held at 475 °C for 30 minutes to refine the degree of order and an SiO_2 layer covered the film at ambient temperature. Figure 6.2 shows the out-of-plane (a) and in-plane (b) XRD patterns, the latter with φ-couplings of 0, 45 and 90 degrees. The only two FePt peaks visible in the out-of-plane diffraction pattern represent the $L1_0$ (001) and (002) lattice planes, indicating a high degree of (001) texture due to epitaxial growth on the MgO single-crystal substrate. The unlabeled peaks are the extremely large diffracted intensity from the substrate; the enormous peak around 43 ° is the (002) MgO peak and the sharp peak near 21.3 ° is the λ/2 peak diffracting from the same (002) planes.[28] The other smaller sharp peaks are due intense contaminant wavelengths from the x-ray source, e.g. CuKβ, etc. The in-plane spectra in part (b) of the figure show predominantly (200) $L1_0$ FePt peaks when φ is coupled at 0 and 90 °. Small (001) peak are present in each in-plane scan, indicating in-plane c-variants of the $L1_0$ phase. At φ = 45 ° the (110) $L1_0$-FePt peak dominates, as expected for epitaxial growth of the $L1_0$-FePt on (002)-oriented MgO. The shift of the diffraction peaks to smaller angles is due to biaxial tensile strain on the $L1_0$ crystals to accommodate the ~9.6% lattice mismatch match between matching [200] and [020] edges of the $L1_0$-FePt and MgO basal planes.

Quantitative analysis performed on the out-of-plane diffraction data indicates a relatively high degree of chemical order, $S \approx 0.72$, and a coherent diffraction length of ~5 nm.

[28] The λ/2 peak results from ~0.771 Å radiation admitted by the Rigaku's graphite monochrometer.

That the vertical grain size is larger than the nominal film thickness of 2.6 nm indicates significant 3-D Volmer-Webber growth. Analysis of the in-plane spectra reveals an average in-plane grain size of ~10 nm as determined from the (110), (200) and (220) diffraction peaks. These values are highly approximate due to reduced fitting accuracy caused by the large background signal. Further microstructural details of A-Base are discussed in the next subsection.

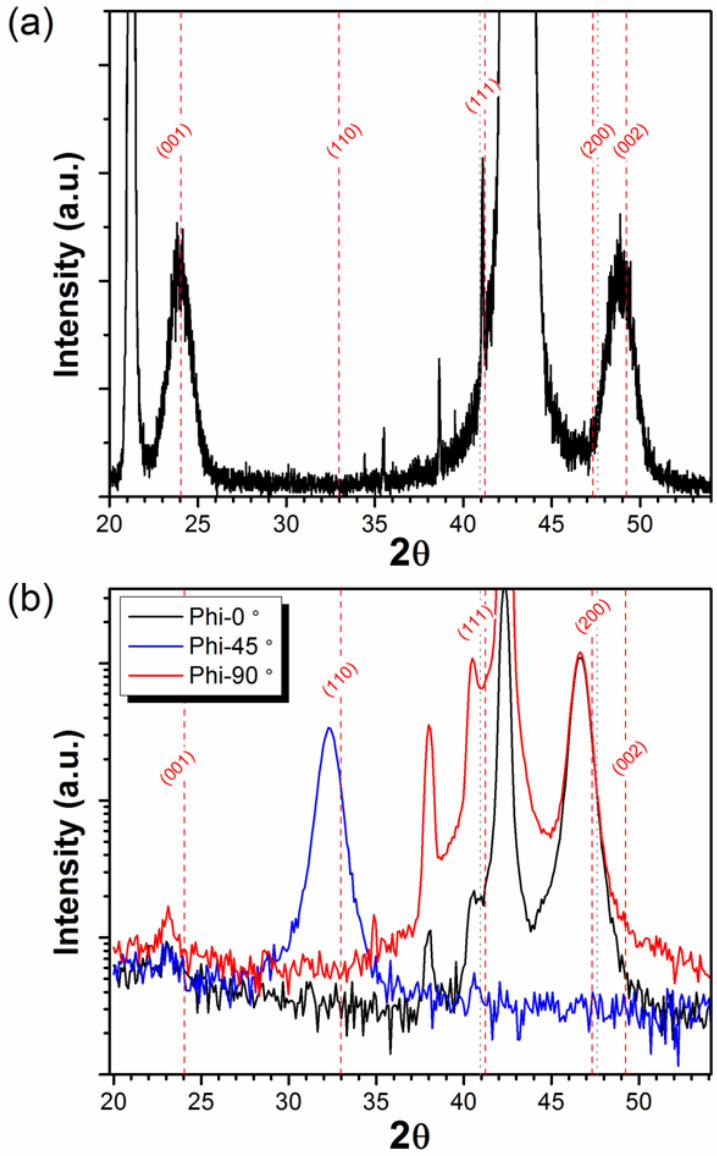

FIG. 6.2. Out-of-plane (a) and in-plane (b) XRD spectra for sample A-Base. Red dashed lines denote L10-FePt peaks and grey dashed lines mark fcc-FePt peak positions.

Magnetic properties of sample A-Base shown in Fig. 6.3 reveal a large out-of-plane coercivity of 26.7 kOe and small in-plane coercivity common to highly (001) textured $L1_0$ FePt phase films. The rapid increase in moment shown by the virgin curve along with the low-field kink in the demagnetization loop signifies the presence of a magnetically isolated soft phase within the base layer. This soft-phase is presumed to exist as a population of small, likely superparamagnetic, particles located within the trenches between the larger islands. It is possible that compositionally-dependent Ostwald ripening [6.45], preferential evaporation of Fe [6.35], or uneven deposition into the trenches due to shadowing has left those regions with poor stoichiometry and thereby a low degree of chemical order and soft/superparamagnetic behavior. Remanence curves (see inset of Fig. 6.3) demonstrate the reversibility of these softer particles. Meanwhile, the single-domain hard-phase islands appear to magnetize and reverse by rotation or curling. The remanent coercivity of H_{cr} = 29.2 kOe is larger than that of the standard $M(H)$ loop and corresponds to peaks in both χ_{IRR}^{DCD} and χ. The difference between H_c and H_{cr} stems from the contributions of the soft-phase trench particles to the $M(H)$ curve. The in-plane data nearly forms a straight line except for a slight "s-curve" around the origin due to the soft-phase particles and probably some small contribution from in-plane c-variants. Extrapolation of the in-plane curve estimates an effective uniaxial anisotropy of 63 Merg/cm^3 (6.3 MJ/m^3).

6.3.2 Series A Results and Discussion

X-ray diffraction spectra shown in Fig. 6.4(a) demonstrate a high degree of (001) texture in all Series-A films resulting from the epitaxial growth directly on the MgO substrate or the $L1_0$ FePt base-layer islands. The addition of a coupled layer deposited at T_D = 32 and 300 °C causes an apparent shift in the (002) peak to significantly lower angles. Figure 6.4(c) enlarges that region of the spectra to illustrate the superposition of the base layer's (002)-$L1_0$ peak with an (002)-fcc peak of the EC layer. Additional asymmetry in that region for those two samples and

sample A-575 is due to the (002)-Pt peak from the Pt cover layer. Figure 6.4(b) focuses on the lower-angle peaks and shows a minimal contribution from the EC layers of samples A-32 and A-300 to the (001) superstructure peak of the base layer, confirming only a very small degree of chemical order in the coupled layer at the two lowest deposition temperatures. Restored symmetry of the $L1_0$ (002) peak and significant increases in the (001) peak for $T_D \geq 390$ °C indicates the onset and increasing degree of $L1_0$ order within the top layer with increasing deposition temperature.

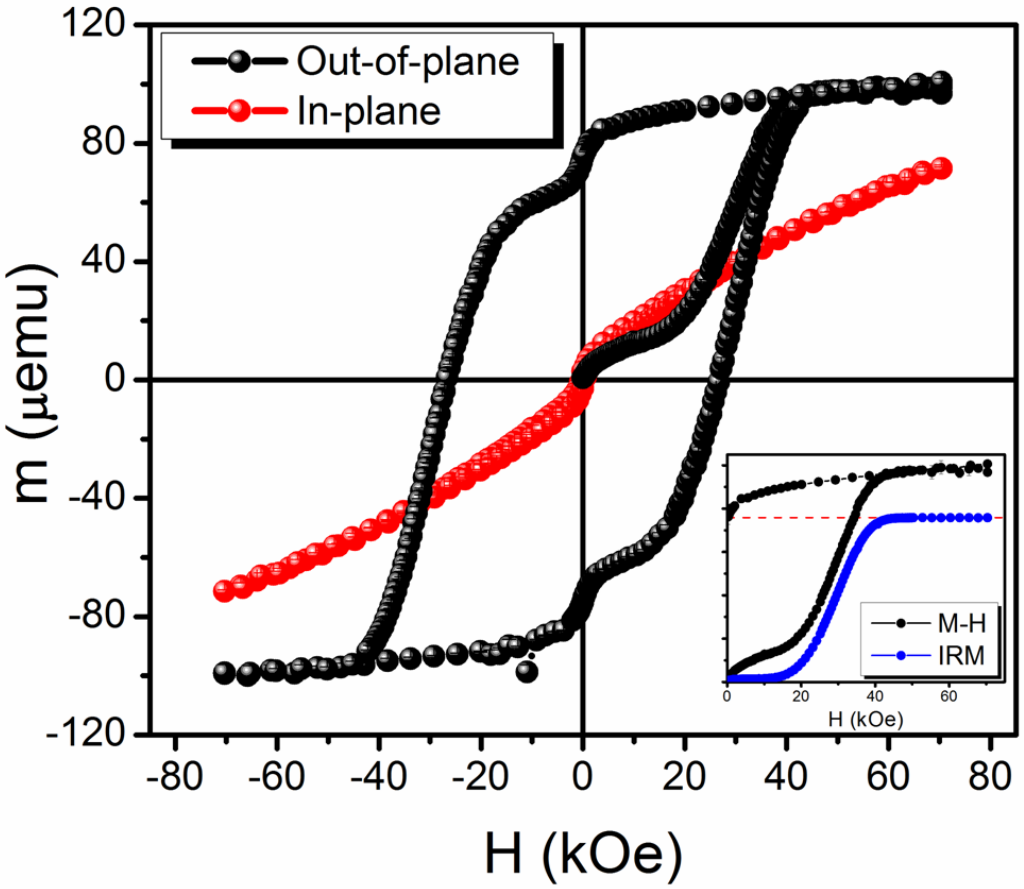

FIG. 6.3. Out-of-plane and in-plane hysteresis loops of sample A-Base, with virgin curve, first-quadrant demagnetization, and IRM (inset).

Changes in sample morphology for Series A films can be seen in the AFM images in Fig. 6.5. Sample A-Base exhibits an isolated nanogranular appearance with island diameters of $d \approx$ 16.8 nm and size distribution (σ/d) of 0.2. In regards to the soft/superparamagnetic particles

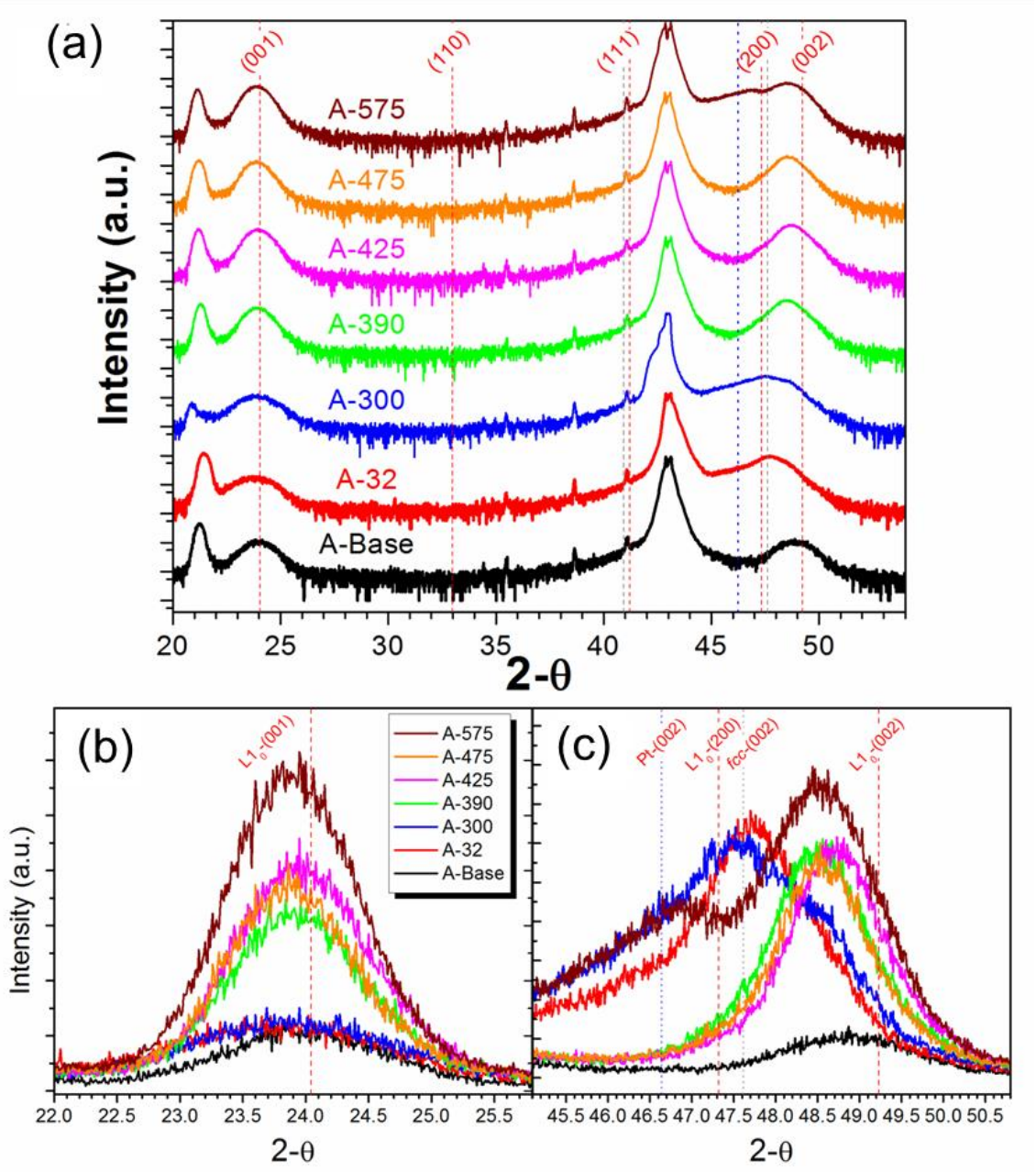

FIG. 6.4. (a) XRD spectra for sample series A, with focus on (001) peak (a) and (002) peak (b). Red dashed lines designate $L1_0$-FePt peaks, grey dashed lines designate fcc-FePt peaks, and blue dotted line marks the Pt (002) peak.

seen in sample A-Base, fully ordered $L1_0$ FePt particles (spheres) become superparamagnetic at a diameter of ~3 nm whereas partially ordered particles with S = 0.1 ($K_1 \approx 7$ Merg/cm^3 = 0.7 MJ/m^3) could become superparamagnetic at ~7 nm. Neither population can be confirmed as these sizes are below the resolution of the AFM. Top layers deposited at T_D = 32 and 300 °C

appear to non-uniformly cover the base-layer particles and join multiple particles together. For $T_D \geq 390$ °C the topology mimics that of the base layer, indicating columnar growth of the top layer on the base layer at sufficiently high deposition temperatures. This can be understood as the increase in adatom mobility with T_D enabling Fe and Pt atoms to grow homoepitaxially on the base-layer FePt rather than on the heteroepitaxially on the substrate. A similar transition to 3-D growth has been observed at that temperature in the literature [6.46]. A deposition temperature of 390 °C coincides with the onset of $L1_0$ order in the coupled layer. This concurrence makes sense as both processes require a relatively high degree of adatom mobility. Estimated particle sizes plotted in Fig. 6.7 show island diameters reduced to close to that of the base-layer for $T_D \geq 390$ °C.

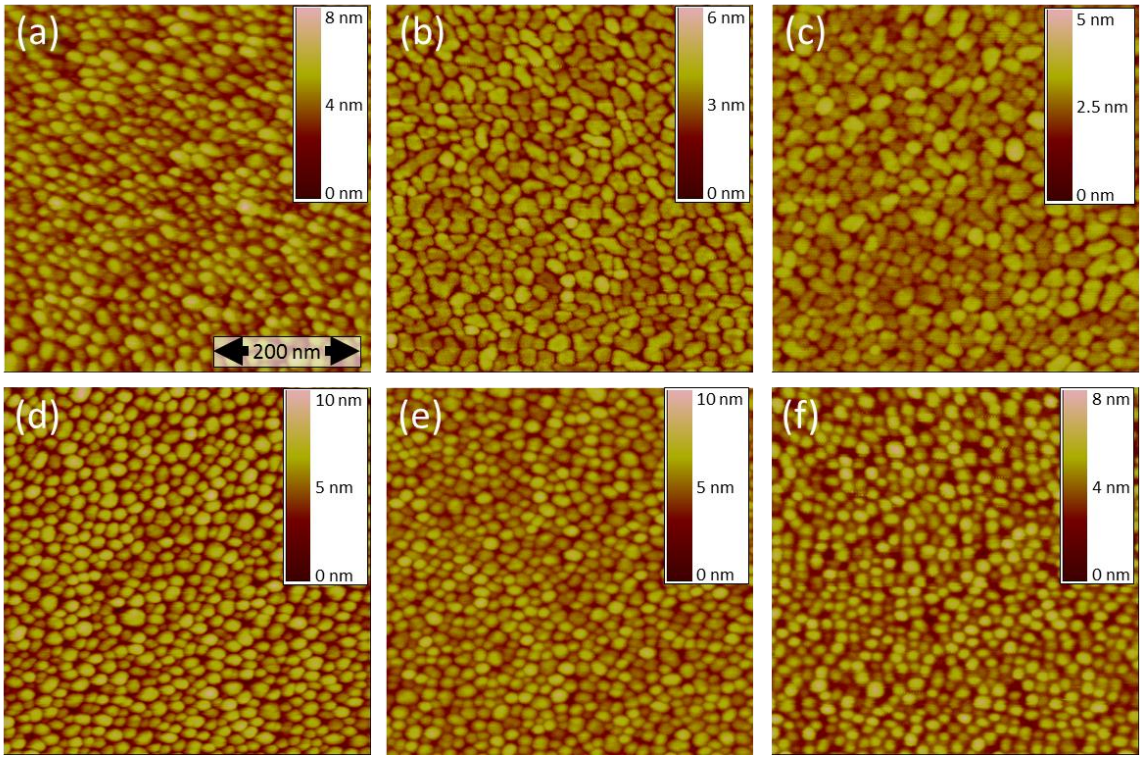

FIG. 6.5. AFM images of samples A-Base (a), A-32 (b), A-300 (c), A-390 (d), A-425 (e), A-475 (f).

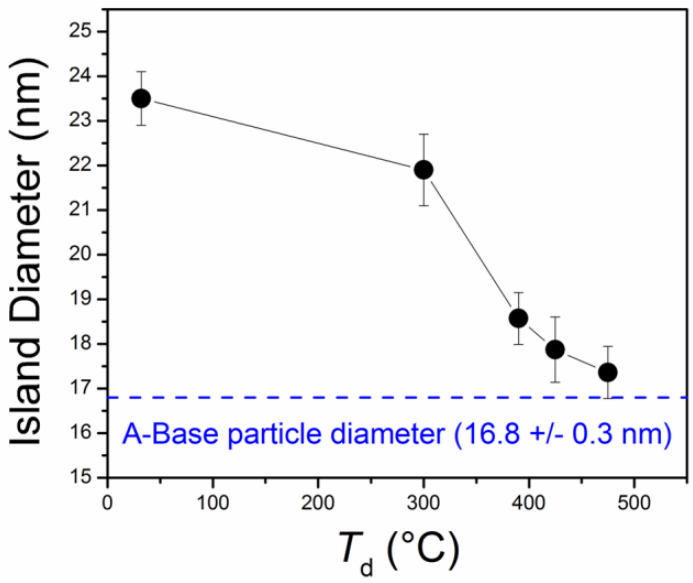

FIG. 6.6. Island diameters of series A ECC samples measured by AFM. Blue dashed line denotes diameter of sample A-Base.

Magnetic hysteresis loops for Series A films measured at room temperature are plotted in Fig. 6.7(a)–6.7(e). Narrow out-of-plane loops with nucleation in the first quadrant are measured when the composite EC layer is soft *fcc* FePt in samples A-32 (a) and A-300 (b). The corresponding in-plane loops demonstrate a soft easy-axis with the influence of the hard phase seen in the large anisotropy field of ~60 kOe. Out-of-plane loops broaden and become squarer as the coupled layer develops $L1_0$ order and a more refined ECC structure for $T_D \geq 390$ °C [see Figs. 6.7(c)–6.7(e)]. Concurrently, in-plane loops progressively resemble those from a hard magnetization direction as T_D increases.

The two-phase behavior seen in sample A-Base's $M(H)$ loop is not evident in any Series-A out-of-plane loop except at $T_D = 425$ (not shown) and 575 °C. Assuming that the soft-phase responsible for that behavior is comprised of small particles located within the trenches between islands (as discussed in Sec. 6.3.1), the development of single-phase behavior probably results from the top layers partially covering those particles or the bare substrate within the trenches. The former situation would increase the size and possibly the degree of chemical order, and thereby magnetic hardness, of the small particles. In the latter case the EC layer

could connect some of the soft particles to the larger islands and enable lateral exchange coupling or material transport to homogenize an uneven stoichiometry. The reemergence of a soft-phase shoulder at higher deposition temperatures could be related to morphological changes induced by enhanced adatom mobility at those temperatures. Interestingly, sample A-475 does not display two-phase demagnetization.

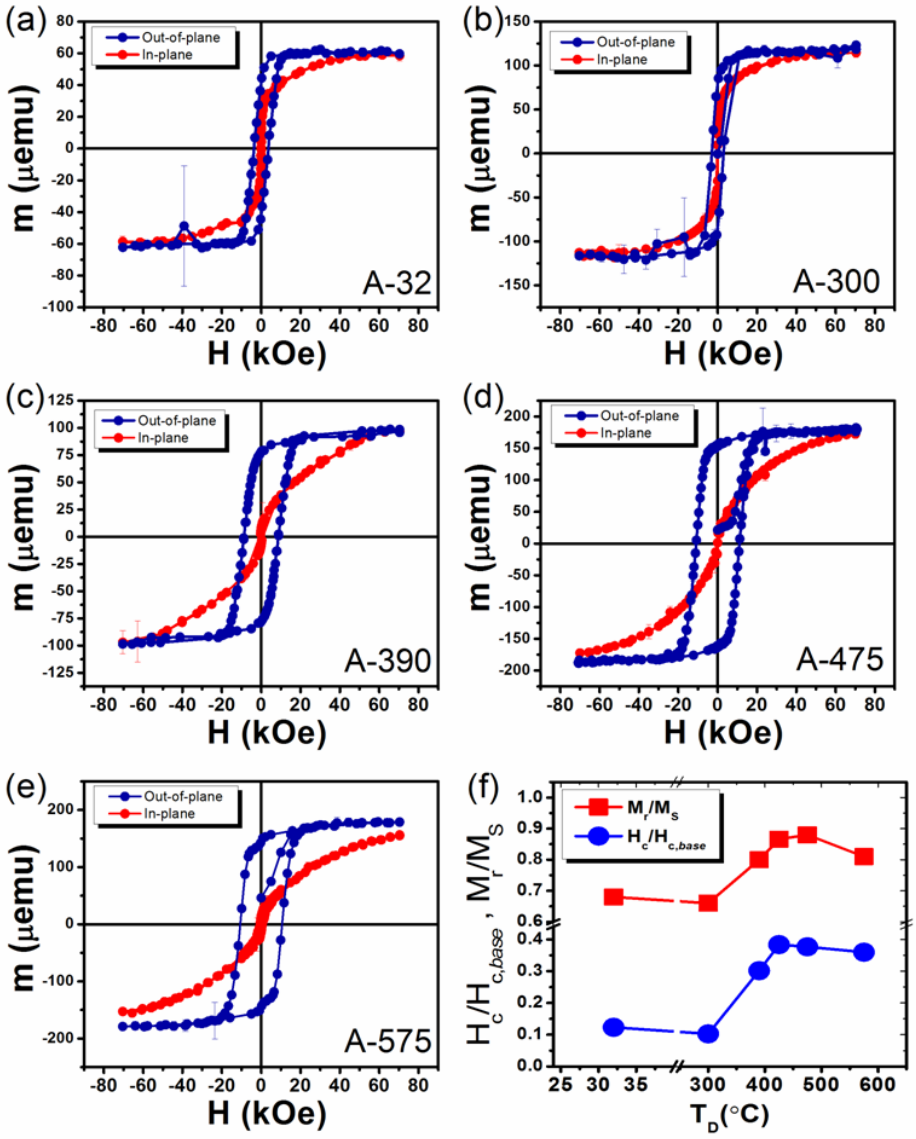

FIG. 6.7. Out-of-plane and in-plane hysteresis loops for series A samples (a) – (e) and normalized coercivity and loop squareness trends versus EC layer deposition temperature for series A samples (f).

Part (f) of Fig. 6.7 summarizes loop-squareness M_r/M_s and coercive field reduction for the different soft-phase deposition temperatures used in Series A. Coercive fields are normalized to the switching field of A-Base. The hard-phase coercivity is quenched by the addition of the fcc FePt composite layer in samples A-32 and A-300. Both coercivity and loop squareness increase in sample A-390 as chemical order develops in the EC layer at T_D = 390 °C. The switching-field reduction is least effective for T_D = 425 °C and the trend decreases gradually for higher deposition temperatures. Remanence ratios becomes quite high as the degree of $L1_0$ order increases in the coupled layer, peaking around 475 °C before appearing to decline; however, the values for T_D = 425 and 575 °C are reduced by the decoupled soft-phase.

The extreme reduction in coercivity in sample A-32 and A-300 is not readily interpretable by a simple model of rigid exchange coupling between vertically stacked hard-soft magnetic layers. However, the increasing and decreasing trends at low and high T_D can be described in a simple way by the proportionality between EC-layer anisotropy and deposition temperature while assuming different coupling regimes within the two temperature ranges. The increasing coercivity of the samples deposited in the range of 300 – 425 °C follows an increasing average anisotropy as a nucleation-driven rigidly coupled system. Conversely, the decrease in switching field exhibited as T_D increases beyond 425 °C follows the reduction in the difference between the hard-soft phase anisotropies for an exchange-spring system reversing by pinning. The decreasing coercivity for high T_D could also be related to the reduction in domain-wall width within the EC-layer [see Eq. (2.19)]; a smaller domain wall width decreases the soft-phase dimension required for the onset of incoherent rotation and should yield a smaller switching field than a rigidly coupled system. This analysis assumes specific microstructures for low and high EC-layer deposition temperatures to produce the different ideal coupling behaviors. As hinted at by the AFM images in Fig. 6.5, the morphologies of these films evolve differently with

EC-layer deposition temperature, but the exact details are not clear. A magnetic system's behavior is always a product of both intrinsic and extrinsic properties, and as such, changes in morphology, chemical order, and possibly other phenomena must be considered to understand the full magnetic behavior of series A.

Explaining the large coercivity reduction in samples A-32 and A-300 requires looking beyond a simple model. Even for an exchange-spring an infinitely thick soft-phase with an anisotropy of zero (one-fifth of the hard phase) would yield a maximum coercivity reduction by only a factor of four (five) [6.47,6.48]. The anomalous behavior is probably due to a combination of three factors: the involvement of the small magnetically soft trench particles, the real geometry of the ECC system, and bombardment damage during deposition of the EC layer. By laterally exchange-coupling the soft trench particles to the hard-phase islands the ECC system would actually consist of a larger soft-phase volume than anticipated. The anisotropy of those unaccounted-for particles would probably harden with increasing substrate temperature; however, they would likely remain softer than the newly deposited EC phase. The resulting ECC system would therefore consist of three different magnetic phases instead of two.

Not only would the inclusion of trench particles change the overall structure of the ECC system, deposition of the EC layer onto the walls of the base-layer islands would yield a "core-shell" geometry instead of vertically stacked two-layer grains [6.19]. The larger interface area created by the soft-phase enveloping the hard-phase enhances the effectiveness of the EC layer [6.49,6.50]. With the third factor, bombardment of the base-layer by EC-layer atoms could induce disorder within the island's surface layers, thereby creating a region of lower anisotropy in the hard-phase. A similar phenomenon is observed in $L1_0$ FePt particles coated by sputter-deposited alumina at room temperature [6.51,6.52] and coated by Fe at elevated temperatures [6.18]. Both systems demonstrate enhanced, and in the case of the alumina coated particles,

unexpected reductions in coercivity. Such an effect could occur here with the deposition of Fe and Pt atoms onto the $L1_0$ ordered islands, leading to an additional low-anisotropy region within the ECC systems. However, an increased substrate temperature ≥390 °C used during the second deposition for some series A samples could serve to "heal," i.e. reorder, the bombarded regions.

In conclusion, the switching behavior of an exchange-coupled $L1_0$-FePt/FePt:SiO_2 system can be controlled by varying the deposition temperature of the composite EC layer. A coercivity reduction to 10.9 kOe, 38% of the hard-phase value, is achieved with a loop-squareness of 0.88 with a 3 nm exchange-coupled layer deposited at 475 °C. The observed trends in magnetic behavior result from changes in chemical order and morphology. The potential complexity of the system precludes description by a simple model of an exchange-coupled two-phase film. The exact microstructural evolution of the system with substrate temperature must be considered as well.

6.4 Series B: Varying EC Layer Thickness on a Thin Base Layer

Sample series B examines the effect of varying the soft layer thickness deposited at 475 °C on top the same 2.6 nm base layer used in series A. That particular soft-phase deposition temperature was chosen because it demonstrated nice properties in series A at 3 nm nominal thickness. Increasing soft phase content in an exchange coupled system should result in a decreasing switching field. As was discussed in Chap. 2.4, analytical and model results have demonstrated that the maximum switching field reduction for an exchange-coupled bilayer occurs when the soft-phase is approximately large enough to support a charged domain wall. This length can be approximated by the domain-wall width of the hard-phase, δ_B, which is ~4 nm for $L1_0$ FePt [K = 63 Merg cm^{-3}, A = 1E-6 erg cm^{-1}, see Eq. (2.11)]. Soft-layer thicknesses ranging from 0.7 to 5.9 nm are investigated in series B to observe the changes in switching behavior and

determine the parameters for optimal coercivity reduction. Note the comparable base-layer sample for Series B is the same as A-Base and was described previously.

6.4.1 Series B Results and Discussion

Figure 6.8 plots the XRD spectra for the Series B samples, including A-Base for comparison. All spectra demonstrate a high degree of (001) texture due to epitaxial growth of the EC layer on top of the $L1_0$ ordered base-layer islands. The centers of both the (001) and (002) peaks shift to lower angles upon adding 7 Å of the coupled layer, with the shift in the (002) peak being more obvious. No subsequent shifts are observed with increasing EC layer thickness. This change is due to the lower degree of chemical order in the soft-phase deposited at 475 °C, as was demonstrated in series A. A lack of further shifting indicates no additional changes in chemical order with increased EC-layer thickness within the range studied.

The effect of increasing the soft-phase layer thickness on the ECC demagnetization curves can be seen in Fig. 6.9(a). The two-phase reversal behavior of sample A-base is less pronounced after adding coupled layers of 7 and 15 Å (see inset). With EC layers of 22 and 30 Å the loops become single phase and squareness M_r/M_s increases; however, further increases in thickness to 44 and 59 Å leads to decreased squareness. Concurrently the switching field steadily decreases, as shown in 6.9 (b), for coercivities normalized to that of base layer. Upon the addition of a 7 Å EC layer the coercivity of the system reduces significantly to ~45% of the base layer value. Coercivity drops again to ~34% for 15 and 22 Å EC layers, and then decreases again at a slowing rate over the final three thicknesses to a maximum reduction of 12%. In comparison, a separate single-layer film of ($Fe/Pt/SiO_2$) deposited on MgO at 475 °C exhibits an out-of-plane coercivity of only 2 kOe (not shown), which confirms the low anisotropy of the soft-phase used in this series.

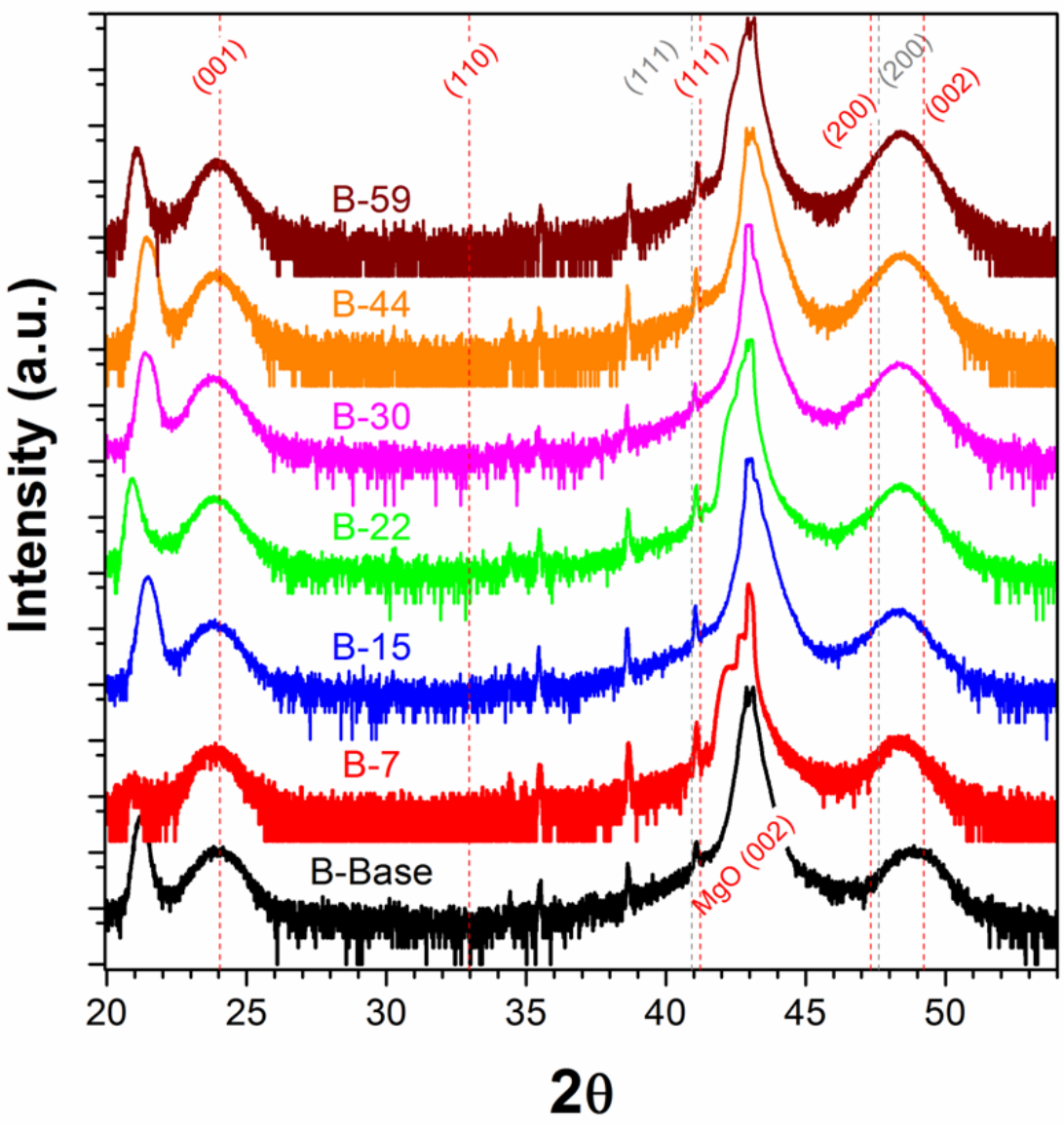

FIG. 6.8. XRD spectra of series B samples. Red dashed line denotes $L1_0$-FePt peaks and grey dashed line marks fcc-FePt peaks.

A decreasing coercivity with increasing soft-phase thickness is anticipated for an exchange-coupled system with the EC-layer thickness less than a few hard-phase Bloch wall widths. To describe the unexpectedly large magnitude of the reduction and the changes in demagnetization behavior of series B films, some of the factors described in Sec. 6.3.2 must be considered in addition to the potential advent of typical exchange-spring-like behavior. First, the gradual elimination of the low-field shoulder in the out-of-plane hysteresis loops evidences that

the regions responsible for that curvature are being affected by even the thinnest EC layer. Assuming again that those soft-regions reside as small, isolated, and poorly ordered particles located within the trenches between hard-phase islands, an accumulation of EC-layer atoms on those particles could increase their stability. Additionally, deposition into the trench regions would eventually couple those particles to the hard-phase islands, leading to an unexpectedly large volume of soft magnetic material in the system. An infinite electrical resistance measured

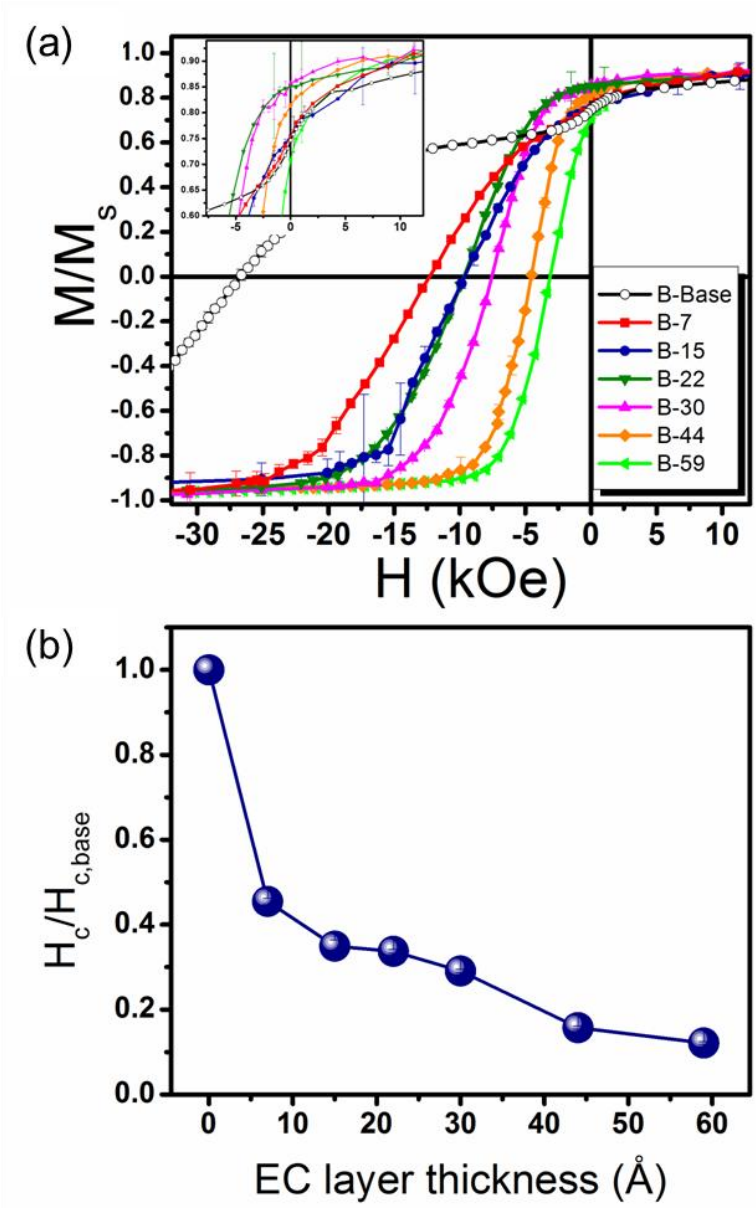

FIG. 6.9. Demagnetization curves for series B samples (a) with close-up of low-field curvature (inset) and normalized coercivity trend versus EC layer thickness (b).

across samples B-7 and B-15 indicates a lack of lateral percolation in those films and therefore only local lateral exchange coupling could be expected. Resistances drop to 70, 1.7, 0.5, and 0.4 kΩ for samples B-22, B30, B-44, and B-59, respectively, indicating percolated structures with increasing lateral connectivity with EC-layer thickness. It should be noted that the apparent increase in loop slope at coercivity with increasing EC layer thickness also indicates an enhancement of inter-island exchange coupling.

Another possible cause for the surprisingly large reduction in coercivity in series B could be the bombardment of base-layer islands during EC-layer deposition. Partial disordering created by this process, as discussed in the previous section, would reduce the hard-to-soft phase ratio as well as alter the interface between the phases from abrupt to graded. The combined effects of disordering and an increasing influence from the trench particles could be responsible for the drastically reduced switching field in sample B-7 and the changes in low-field demagnetization behavior observed in the first few samples in series.

Coercivity reductions after sample B-22 could be related to the onset of incoherent reversal within the coupled soft-phase as the anticipated soft-phase dimension approaches that of the hard-phase DW width. The somewhat complicated nature of these exchange coupled films, which likely involves three different phases (hard islands, soft trench particles, and the EC layer), precludes analysis by a simple model. However, it should be noted that for a system of three exchange-coupled regions of $K^{I} = 0$, $K^{II} = K_{hard}/2$, $K^{III} = K_{hard}$, the coercive field is predicted to be reduced by a factor of 8 versus the hard-phase alone [6.8], which is close to the reduction factor of 0.12 found for sample B-59.

Magnetic hysteresis loops of samples B-Base and B-30 measured at temperatures of 350, 300, 250, 200, 150, 100, and 50 K reveal increasing coercivities trend at lower temperatures. The resulting switching field versus temperature trend was fitted with the

Sharrock equation [Eq. (2.34)] using n = 1.62, t = 100 s, and $f_0 = 10^{11}$ Hz. A value of 1.62 for the energy barrier exponent [Eq. (2.33)] has been determined to be appropriate for slightly misaligned Stoner-Wohlfarth particles [6.53], a measurement time of 100 seconds is appropriate for SQUID measurements at large fields, and an attempt frequency (f_0) of 10^{11} Hz is in the proper range (10^{10} – 10^{11} Hz) for single and multiple-phase thin films [6.54,6.55]. Resulting thermal stability factors ($\xi = \Delta E / k_B T$) of 173 and 137 were estimated for samples B-Base and B-30, respectively. Reductions in ξ have been observed for an EC bilayer of a 3 nm Fe layer on ordered FePt with respect to a pure FePt film [6.56], and a linearly decreasing energy barrier has been estimated for an increasing soft-phase thickness in an ($L1_0$ FePt:TiO_2/fcc FePt:TiO_2) composite system [6.57]. Decreases in energy barrier are explained by a negative anisotropy contribution from large demagnetization fields affecting the exchange-coupled soft phase.

6.5 Series C: Varying EC Layer Thickness on a Thick Base Layer

Sample series C investigates the effect of soft-layer thickness deposited at T_D = 425 °C on hard-magnetic $L1_0$ FePt islands with nominal thickness of 7.4 nm (20 repetitions of Fe 1.9 Å/Pt 1.8 Å). Depositing a nominally thicker base layer results in larger island sizes, both laterally and vertically [6.58]. The taller particles will shadow the trenches to a greater extent than series A and B, thereby limiting the amount of deposition in those areas. Additionally, larger base-layer particles should be more resilient to the disordering effects of surface bombardment by the EC layer deposition due to a higher volume-to-surface ratio.

Films with EC layers of the form Fe/Pt/SiO_2 with thicknesses 15, 30, 44, 59, and 74 Å comprise sample series C. The deposition temperature of 425 °C is less than that used in series B, however series A demonstrated similar results between the two temperatures. The next subsection describes the properties of film C-Base alone, followed by the results of series C.

6.5.1 Sample C-Base Properties

Sample C-base was deposited as multilayers of Fe 1.9 Å/Pt 1.8 Å with 20 repetitions for a nominal thickness of 7.4 nm. Similar to A-base, the substrate temperature was 700 °C during deposition and then was held at 425 °C for 30 minutes afterward for refinement of the chemical order. XRD of sample C-base shown in Fig. 6.10 demonstrates a high degree of (001) textured in the $L1_0$ phase FePt. The inset rocking curve of the (001) peak confirms this crystal alignment with a FWHM of 2.3 °. Quantitative fitting of the wide-angle spectrum yields a chemical order S ≈ 0.69 and average vertical grain sizes of ~9 nm. The large peak around 43 ° 2-θ and the smaller unlabeled peaks are from the single crystal (001) oriented MgO substrate.

Magnetic hysteresis curves for sample C-base plotted in Fig. 6.11 demonstrate a large perpendicular anisotropy in this base-layer film. The broad out-of-plane loop shows a coercivity of 28.1 kOe and the narrow in-plane curve has a shallow linear slope. Extrapolation of the in-plane loop to saturation estimates a uniaxial anisotropy of 64 Merg/cm^3 (6.4 MJ/m^3). DCD remanence yields a remanent coercivity of 29.1 kOe.

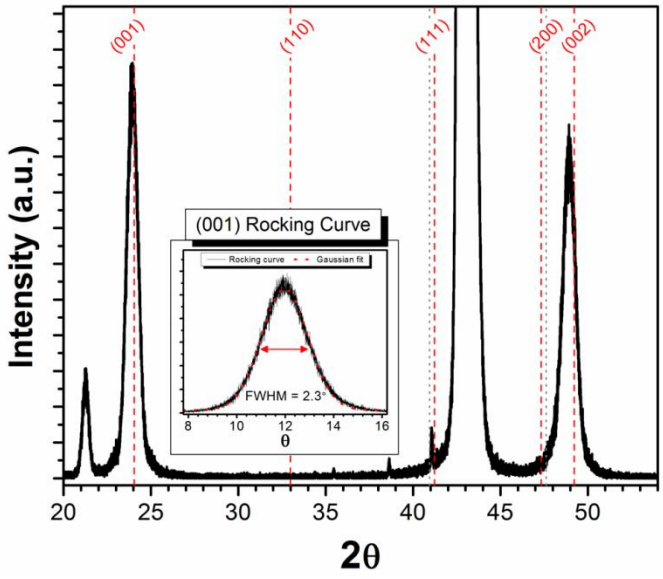

FIG. 6.10. XRD of sample C-Base with (001) rocking curve and Gaussian fit (inset). Red dashed lines mark $L1_0$-FePt peak positions and grey dotted lines mark fcc-FePt peak positions.

The two-step initial-magnetization in the out-of-plane curve direction suggests the presence of two magnetic phases, similar to sample A-Base. However, the IRM curve inset in Fig. 6.11 demonstrates the irreversibility of this population. Additionally, the miniscule low-field dip seen in the demagnetization curve represents only a very small fraction of the film, not the ~25% suggested from the initial curve. Similar magnetization/reversal behavior has been reported for epitaxially grown $L1_0$ FePt islands of varying sizes grown on MgO [6.35,6.58-6.60]. Specifically, a steep initial curve has been correlated to the low-field elimination of mobile domain walls present in the virgin state of multidomain particles, and subsequent reversal from the saturated state occurs only at high fields by domain nucleation. The same phenomenon must be occurring in C-Base; about one-quarter of the film must exist as multidomain particles. The source of the small $M(H)$ shoulder is likely from a highly diminished population of the same type of superparamagnetic trench-particles that exist in A-Base.

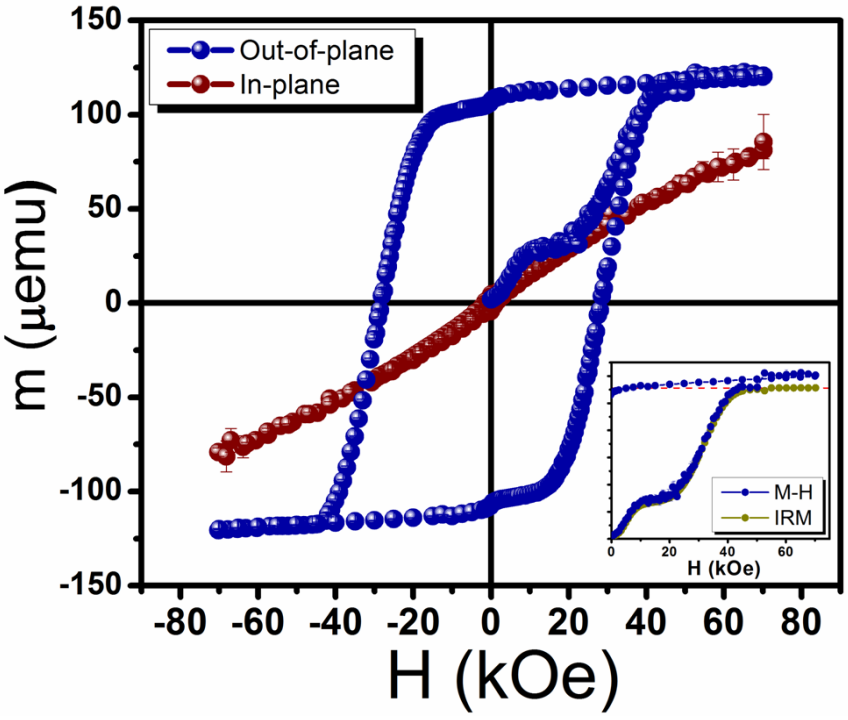

FIG. 6.11. In-plane and out-of-plane hysteresis loops for sample C-Base, with virgin curve, first-quadrant demagnetization, and IRM (inset).

Sample morphology of C-Base as measured by AFM in Fig. 6.12 demonstrates a particulate structure similar to A-Base. An infinitely large measured electrical resistance confirms the discontinuous morphology. The islands are larger than those of the thinner base layer and some appear facetted. Statistical analysis of the particle sizes reveals an average size of d = 38.2 nm with a size distribution of 0.23. By the same argument as in Sec. 6.3.1, any superparamagnetic particles seen in the hysteresis loop exist below the resolution of the AFM. Regarding the multidomain particles, the diameter marking the transition from single-domain to multidomain for well-ordered spherical $L1_0$ FePt particles is ~360 nm [see Eq. (2.12)]. This diameter depends on the exact particle shape and has been estimated be a small as 43 nm for FePt islands grown on MgO at 900 °C at a 7 nm nominal thickness [6.35,6.60].

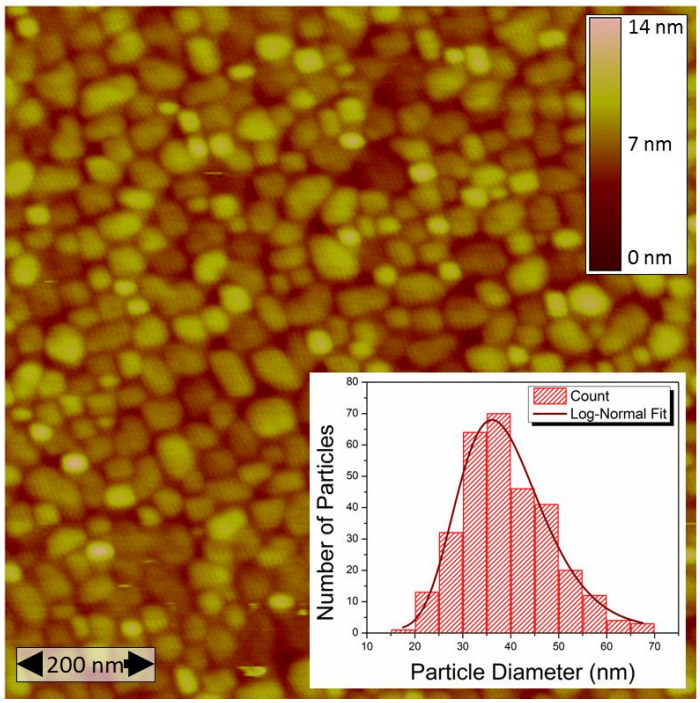

FIG. 6.12. AFM image of sample C-Base and island-size distribution (inset).

In magnetic recording, inhomogeneities between individual grain properties create noise. For example, a broad distribution of switching fields increases transition noise in PMR media [6.2,6.61]. Hysteresis loops measure the ensemble behavior of a system and switching

field distributions are typically inferred from the shape of $\chi(H)$ (see Chap. 2.1.3). However, the distribution of individual switching fields within an array of magnetic particles is influenced by interparticle interactions. The ΔH measurement technique described in Chap. 2.1.5 offers access to the intrinsic switching field distribution $\Delta_{\mathrm{SFD}}^{i}$ by eliminating mean-field-type interactions [6.62]. Figure 6.13 shows the transformed data taken from C-Base using a maximum field of 35 kOe. The resulting intrinsic switching field distribution extracted by fitting with the appropriate curve representing a Gaussian SFD function [see Eq. (2.26)] to the data yields $\Delta_{\mathrm{SFD}}^{i}$ = 0.28. This value is significantly smaller than the 0.50 given by Eq. (2.15), indicating a broadening effect of dipolar interactions between islands in sample C-Base. Note that the intrinsic SFD value of 0.28 is close to the island size distribution, 0.23.

The larger particles in C-Base resulting from a larger nominal thickness should provide a more stable hard phase for studying an exchange-coupled system.

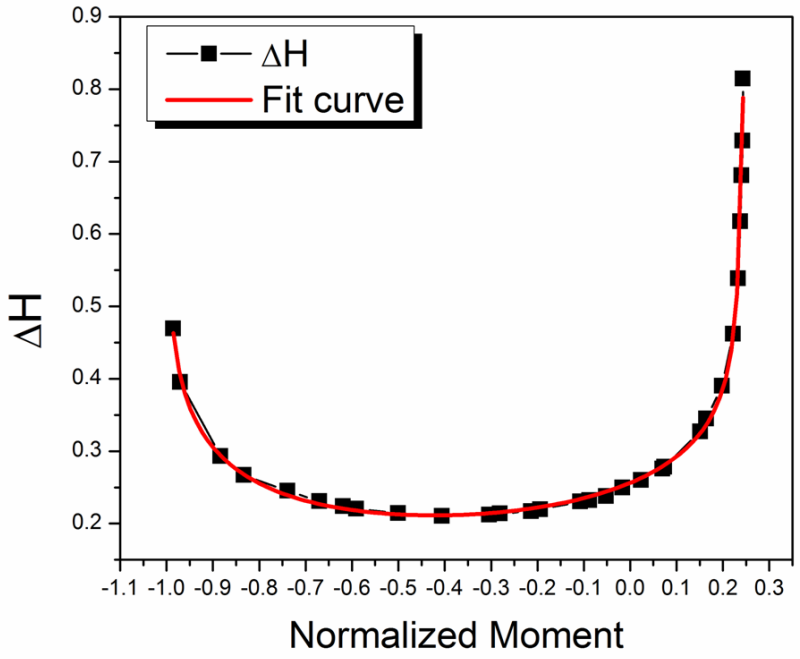

FIG. 6.13. ΔH data for sample C-Base having used a maximum field of 35 kOe. The red curve is the fit by ΔH_G for a Gaussian SFD, as defined in Eq. (3.14).

6.5.2 Series C Results and Discussion

Sample series C utilizes the 74 Å thick base-layer of $L1_0$ FePt islands previously described to investigate an ECC system with exchange-coupled multilayers of Fe/Pt/SiO_2 at thicknesses of 15, 30, 44, and 74 Å deposited at 425 °C. The effect on coercivity and reversal mechanism is examined. Figure 6.14 plots series C XRD patterns, including sample C-Base for comparison. The FePt $L1_0$ (001) and (002) peaks exhibited by all samples suggests the expected epitaxial growth. Small shifts in the (002) peaks toward lower angles in the spectra of the ECC samples indicate a lesser degree of chemical order in the EC layer. The shift in C-15 seems larger than for the subsequent samples. Increased intensity near the fcc-(002) peak of films C-59 and C-74 indicates the increased fraction of partially disordered soft phase in those two samples.

Figure 6.15(a) plots the out-of-plane demagnetization curves and coercivity reductions for series C samples. Remanent coercivity (H_{cr}) values included in part (b) hint at a strong exchange-spring mechanism only for sample C-59. The right-hand ordinate in that figure is normalized to H_{cr} of C-Base. Demag curves in (a) demonstrate a reduction of the low field shoulder visible in C-Base for the thinnest EC layer in a similar manner to series B. Beyond sample C-15 remanence ratios first increase in sample C-30 and then decrease for C-44 and C-59. The drop in remanence could be due to self-demagnetization of the out-of-plane soft-phase moments; the enhanced shape-anisotropy in perpendicular ECC systems can lead to positive nucleation fields and decreased remanence [6.63]. This rotation of the soft-phase can indicate the initial formation of a domain wall within the soft-phase [6.34,6.63,6.64]. The increased remanence ratio in sample C-74 deviates from the perceived trend and could be related to enhanced lateral exchange coupling due to the large thickness of the EC layer.

The initial decrease in coercivity seen in Fig. 6.15(b) for sample series C is significantly less severe than that demonstrated in series-B samples of comparable EC thickness. A 15 Å

coupled layer reduces the system's coercivity to 17.4 kOe, or 62% of the hard-phase value. In comparison, series B coercivity drops to 33% for a similar EC layer thickness despite using a higher deposition temperature. Interestingly, coercivity increases to 19.8 kOe (70%) when the

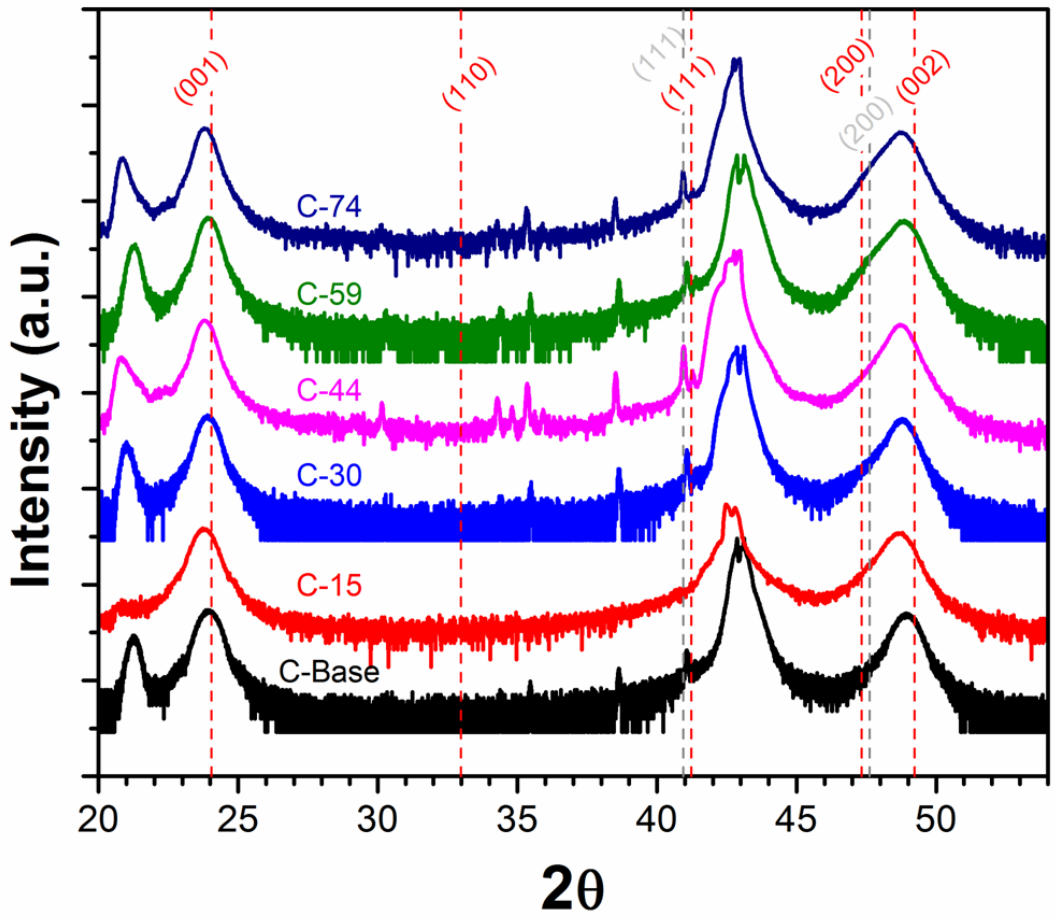

FIG. 6.14. XRD spectra for series C samples. Red dashed lines denote $L1_0$-FePt peak positions and grey dashed line marks fcc-FePt peak positions.

EC layer thickness increases to 30 Å. Further increases in soft-phase thickness yield a steadily decreasing coercivity. Remanent coercivities generally follow the trend of H_c but at slightly larger values. Exceptions occur for samples C-30 and C-59 where the differences are smaller and larger, respectively. The upturn in coercivity and remanence ratio in sample C-30 correlates with a morphological change in the system implied from measured electrical resistance. Resistance values drop from infinite to 4 kΩ for samples C-15 and C-30, respectively, implying a significant

increase in structural interconnectivity in C-30. Measured resistances decrease further to 600, 400, and 180 Ω for samples C-44, C-59, and C-74, respectively.

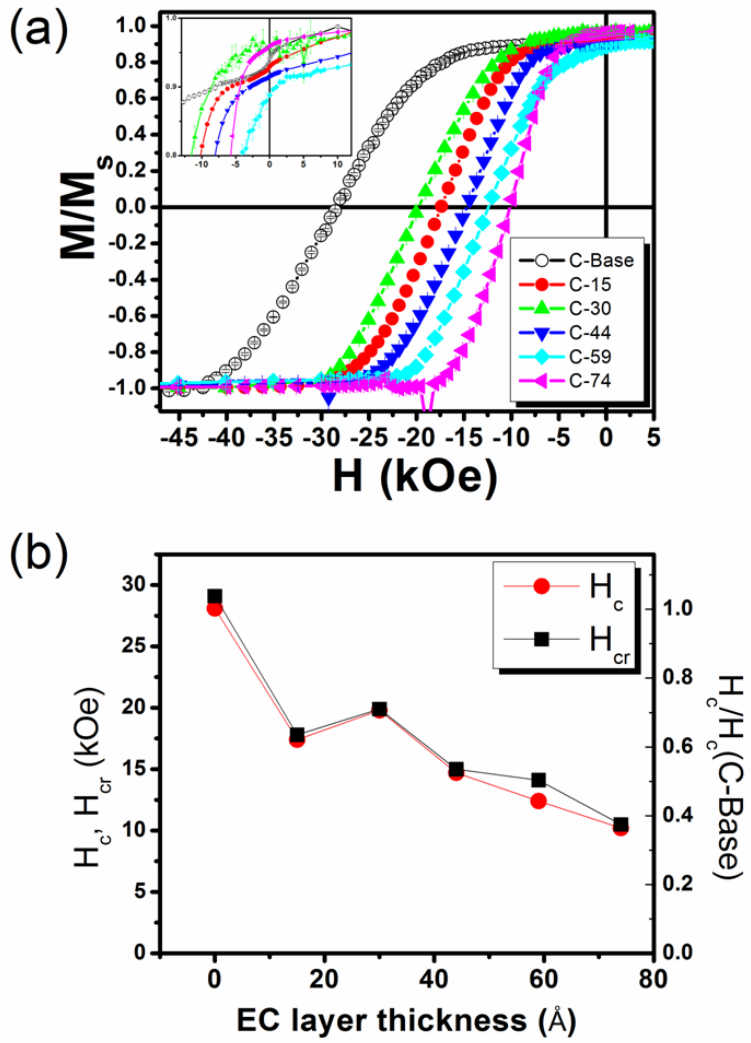

FIG. 6.15. Demagnetization curves for series C (a) with close-up of low-field curvature (inset) and normalized coercivity and remanent coercivity trends versus EC layer thickness (b).

Delta-M (Δ*M*) curves measured for series C samples shown in Fig. 6.16 demonstrate changes in reversal behavior with increasing soft-phase thickness. Both H_c and H_{cr} for each sample are included in the figure for reference. Sample C-base exhibits a large, broad positive hump before crossing to a shallow negative curve near $H_{c/cr}$ before approaching zero. This behavior is vaguely repeated for samples C-30, C-44, and C-74, where the respective positive peaks slightly decrease and become sharper as the negative regions significantly increase and

also become sharper with increasing soft-phase thickness. Additionally, the switching fields no longer correspond to the intercept of Δ*M* but instead occur at a larger value near the negative peak of the curve.

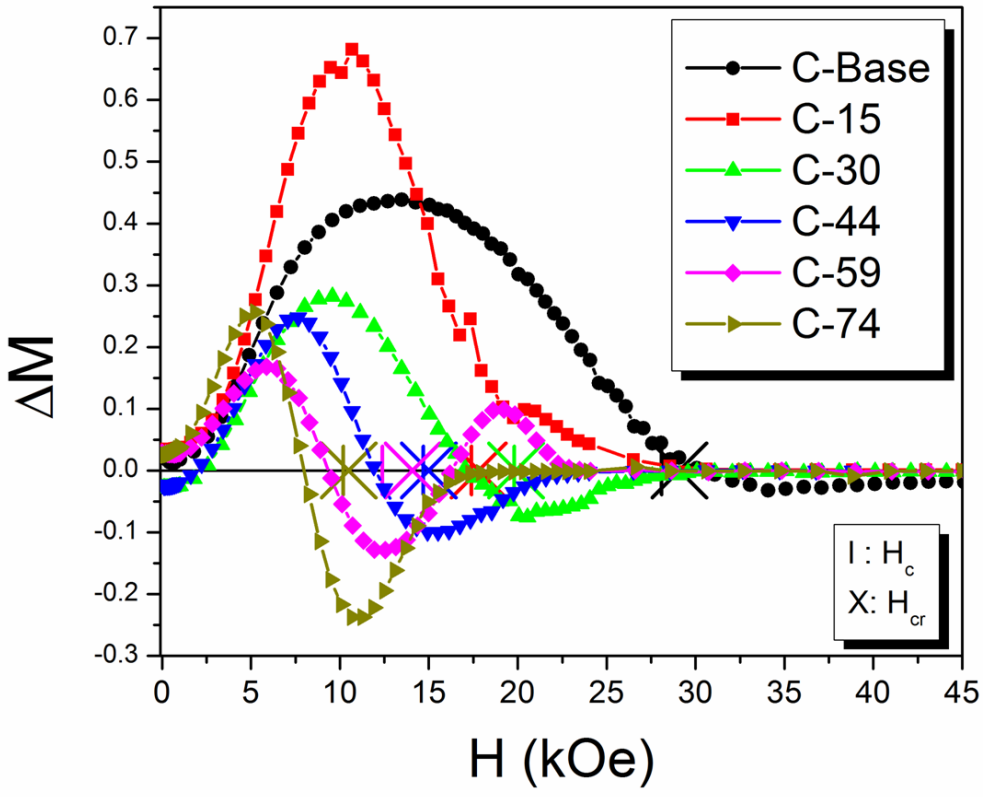

FIG. 6.16. Delta-M curves for sample series C.

Deviations in the behavior described above exist in the Δ*M* curves from C-15 and C-59. Sample C-15 exhibits a second, smaller positive peak and never crosses to become negative. Sample C-59 also has a second positive peak, but that occurs only after a negative one. The switching field of C-15 is close to where the first positive peak might cross the field axis, if extrapolated. On the other hand, the switching field H_{cr} for sample C-59 occurs while the Δ*M* curve is negative and increasing while H_c is close to the negative peak. The latter is similar to the other ECC films.

Typical interpretations of a Δ*M* curve are that positive and negative values indicate interactions which hinder and assist reversal, respectively [6.65,6.66]. In granular films, positive

values are correlated with exchange interactions [6.67] and negative values with dipole interactions [6.68]. Correct interpretation of a Δ*M* curve depends on the dominant reversal mechanism of the considered system and comparison with model simulations breaks down in the presence of strong interactions. A detailed interpretation of the Δ*M* data from series C is not attempted here. However, the somewhat consistent change in behavior supports the notion of an evolving reversal process with the addition of an increasing soft-phase region. The increasingly large negative portion of the curves with thicker soft-phase could signify a change from nucleation dominated reversal to pinning.

Similar to series B, series C exhibits a decreasing trend in switching field with increased soft-phase. The lesser overall coercivity reduction in series C could be due to a number of factors. For one, C-series samples would not incur a large and unexpected increase in soft-phase fraction due to C-base having fewer small soft/superparamagnetic particles in comparison with series A and B. Additionally, the larger volume-to-surface ratio of the C-series base layer islands would mitigate some of the effects of surface bombardment, and the interface geometry would likely approximate more closely that of an ideal exchange-coupled system.

The upturn in coercivity for sample C-30 suggests that sample is abnormal for the series. However, the XRD and Δ*M* data suggest that C-15 could instead be the spurious sample. Aberrations in either sample could be due to errors during sample fabrication or mishandling of the samples. However, data logs from the AJA do not indicate a problem during either film's deposition and all samples were handled with equal care. The coincidence of sample C-30 with the drastic reduction in film resistance could point to a significant effect of the change in film continuity on magnetization reversal. A similar change seemed to occur in series B samples between B-15 and B-22, when the resistance values dropped to within measurable range

coincident with somewhat similar changes in magnetic behavior.[29] Increases in coercivity with increasing soft-phase thickness in exchange-coupled systems have been reported in the literature [6.69,6.70], where one study attributed the phenomenon to lateral exchange coupling [6.69]. It could be interesting to investigate the validity of this potentially unusual trend in the future.

Out of all the exchange-coupled samples in series-C, sample C-59 exhibits the clearest indication of a domain-wall assisted reversal process. The domain wall would form at the positive nucleation field of ~2.5 kOe [see inset of Fig. 6.15(a)]. Subsequent incoherent reversal would lead to the large difference between H_c and H_{cr} measured for that sample. Interestingly, the Δ*M* curve for C-59 exhibits the unusual "double-crossing" of the field-axis; this strange behavior could fingerprint a domain-wall assisted switching process. Further investigation is required to determine whether the behavior is a result of an evolving morphology within the series or if it is coincidental.

Coercivity reduction in series C reaches a maximum of ~36% without indication of saturating. Decreasing remanence and a visible positive nucleation in samples C-44 and C-59 potentially indicate soft-phase domain wall formation; however, coercivities continue to reduce. Furthermore, sample C-74 exhibits an even smaller coercivity yet a much higher remanence ratio, the latter being out-of-trend. Additionally, aside from C-59, the nearly identical H_c and H_{cr} values demonstrate a lack of exchange-spring behavior. The thicker base layers used in series C seem to have provided more resilient hard-phase islands with less soft-phase trench particles than series A and B. However, similar complications remain such as the trench particles and the effects of trench filling, yielding a non-ideal ECC system.

[29] The coercivity of sample B-22 did not increase, yet nor did it decrease.

Switching fields of samples C-Base, C-30, and C-59 measured at temperatures down to 60 K revealed ξ values of 175, 290, and 393, respectively. The similar thermal stabilities estimated for samples B-Base and C-Base, despite the larger grain volumes in the latter, is probably due to incoherent reversal in the C-Base film. The trend of increasing ξ with soft-phase thickness is counter to what was observed between samples B-Base and B-30 and in Refs. 6.56 and 6.57. From a simple expression for the zero-field energy barrier of a hard-soft composite system, $\Delta E = K_{\mathrm{hard}}V_{\mathrm{hard}} + K_{\mathrm{soft}}V_{\mathrm{soft}}$, an increasing ΔE could be expected for a thicker soft-phase regardless of the smaller anisotropy value (K_{soft}), leading to larger values of ξ. On the other hand, if reversal of a composite system occurs by domain-wall motion the energy barrier essentially becomes equivalent to the energy required to form a domain wall in the hard-phase, $4F\sqrt{K_{\mathrm{hard}}A_{\mathrm{hard}}}$, where F is the cross-sectional area of the domain wall [6.55]. Therefore, the exact form of the energy barrier depends on the geometry and dimensions of the ECC system, yet it would seem that the series C films are less deleteriously affected by the soft-phase addition as those of series B.

6.6 Summary and Conclusions

The effects of varying the intrinsic and extrinsic properties of the EC layer in an $L1_0$-FePt based ECC system are presented. Control of coercivity is demonstrated and loops-shape and morphology is examined. Two different (001)-oriented $L1_0$ FePt hard phase base layers are used with nominal thicknesses of 2.6 and 7.4 nm, A-Base and C-Base. Deposition onto an (001)-MgO substrate yields a particulate structure with high chemical order and (001) texture. A-Base films yield islands of approximately 16.8 nm in diameter and 5 nm in height with a σ/d ≈0.2, S = 0.72, and a high out-of-plane remanent coercivity of 29.2 kOe. C-Base consists of 38.2 nm wide and 9 nm tall islands with σ/d ≈ 0.23, S = 0.69, and a 29.1 kOe remanent coercivity. Properties of the

composite FePt:SiO_2 soft-phase layer are controlled by varying the deposition temperature and nominal thickness. Three series of samples are investigated, A, B, and C.

Series A investigates EC-layer deposition temperatures ranging from 32 to 575 °C with 3 nm nominal thickness covering A-Base hard-phase layers. EC-layer morphology changes from non-uniformly coating multiple islands to mimicking that of the hard-phase as deposition temperature increases from 300 to 390 °C. The deposition temperature of 390 °C also coincides with the appearance of $L1_0$ order in the soft-phase. The system's coercivity is quenched to nearly ~10% that of A-Base at deposition temperatures of 32 and 300 °C and increases with T_d to 38% at 425 °C, and then slowly decreases for higher temperatures. The trend in out-of-plane loop squareness follows a similar trend as coercivity with a maximum value of 0.88 at T_d = 475 °C.

Series B examines the effect of varying the EC layer thickness at a T_d of 475 °C on top of A-Base hard-phase islands. The initial addition of a 7 Å soft-phase decreases the coercivity dramatically to 45% of the A-Base value. Increasing the soft-phase thickness from 7 Å to 59 Å reduces the coercivity to 12% that of A-Base at a slowing rate. Series C similarly varies the thickness of the EC layer but uses a T_d of 425 °C and C-Base layers as the hard-phase. An EC layer thickness of 15 Å decreases the coercivity to 62% that of C-Base. After an increase to 70% at 30 Å, coercivity decreases steadily down to 36% that of Base-C. Perpendicular magnetization remanence first increases and then decreases with EC-layer thickness for both series B and C, with the exception of a large increase in C-74.

Select series B and C samples indicate relatively high thermal stability, with $\xi > 137$. Decreasing and increasing values for ξ were determined for increasing soft-phase thicknesses in the measured B and C series films. ECC media performance is quantified by the figure of merit

defined by the ratio of twice the energy barrier to the product of the switching field (H_c), magnetization (M_s), and volume (V) [6.71],

$$\xi' = \frac{2\Delta E}{H_c M_s V}. \tag{6.1}$$

An ideal single-phase perpendicular media, i.e. aligned Stoner-Wohlfarth particles, yields a ξ' of one. Among the B series films, ξ' = 0.39 for sample B-Base. That this value is not one indicates that these base layer islands are not truly ideal Stoner-Wohlfarth particles.[30] Upon adding 30 Å of partially-ordered FePt to B-Base in sample B-30, ξ' increases to 0.66; the decrease in thermal stability is counterbalanced by the decrease in switching field. Select C series films demonstrate significantly smaller values of ξ', at 0.04, 0.07, and 0.11 for samples C-Base, C-30, and C-59, respectively; the small values are due to large grain volumes in the C-series films. The trend of increasing ξ' is encouraging for both series of samples.

Clearly the magnetic behavior of (001)-oriented $L1_0$ FePt nanoparticles can be controlled in an exchange-coupled composite-like system by varying the intrinsic and extrinsic properties of the soft-phase. Large reductions in coercivity and improved magnetic remanence are achieved. However, results indicate varying degrees of lateral exchange coupling and the involvement of superparamagnetic particles inherent in the hard-phase layer. The complicated nature of these films results in a non-ideal ECC system. While the addition of a soft-phase of varying properties is reducing the switching-field of the hard-phase by exchange-coupling, DWAMR applications require an ideal ECC microstructure. Further improvement to the system is required.

Many of the details regarding the real-structure and the nature of the exchange-coupling remain unclarified. Future work on this system would entail TEM, especially cross-sectional studies, to determine the actual geometry of the hard-soft coupling. Additionally, it is

[30] Some works using the ξ' figure of merit normalize their data to the value determined for their single-phase comparison sample [6.56].

possible that thermal activations at room-temperature are precluding the formation of a compressed domain wall within the soft-phase to fingerprint exchange-spring behavior [6.72]. Low-temperature hysteresis and remanence measurements could better illuminate the coupling behavior. Lastly, $H_{c/cr}$ data taken at different temperatures would reveal changes in thermal stability through a Sharrock-type analysis [6.50].

To move this $L1_0$-FePt based system closer to an ideal ECC microstructure would require a new base-layer design. Achieving smaller lateral island sizes with tighter size distribution and no superparamagnetic trench particles is important. Using a higher deposition temperature and/or increasing the post-deposition annealing time and temperature could further improve the chemical order, microstructure while eliminating the smallest particles. Depositing an appropriate segregant material within the base-layer would assist in controlling island sizes and filling the gaps between the islands would prevent lateral exchange coupling from developing along the trench bottoms.

6.7 References

6.1 A. Y. Dobin and H. J. Richter, Applied Physics Letters **89** (6), 062512-062513 (2006).

6.2 D. Suess, T. Schrefl, S. Fahler, M. Kirschner, G. Hrkac, F. Dorfbauer and J. Fidler, Applied Physics Letters **87** (1), 012504-012503 (2005).

6.3 A. Berger, E. Fullerton, H. Do and N. Supper, US Patent No. 0177704A1 (10 August 2006 2006).

6.4 Y. Sonobe, D. Weller, Y. Ikeda, K. Takano, M. E. Schabes, G. Zeltzer, H. Do, B. K. Yen and M. E. Best, Journal of Magnetism and Magnetic Materials **235**, 424-428 (2001).

6.5 R. H. Victora and X. Shen, Magnetic Recording Conference Digest A1 (2004).

6.6 E. Girt and H. J. Richter, IEEE Transactions on Magnetics **39** (5), 2306-2310 (2003).

6.7 J.-U. Thiele, S. Maat and E. E. Fullerton, Applied Physics Letters **82** (17), 2859-2861 (2003).

6.8 D. Suess, Applied Physics Letters **89** (11), 113105-113103 (2006).

6.9 Z. Lu, P. B. Visscher and W. H. Butler, IEEE Transactions on Magnetics **43** (6), 2941-2943 (2007).

6.10 A. Berger, N. Supper, Y. Ikeda, B. Lengsfield, A. Moser and E. E. Fullerton, Applied Physics Letters **93** (12), - (2008).

6.11 J. P. Wang, Proceedings of the IEEE **96** (11), 1847-1863 (2008).

6.12 A. Y. Dobin and H. J. Richter, Journal of Applied Physics **101**, 09K108-106 (2007).

6.13 R. H. Victora and S. Xiao, Proceedings of the IEEE **96** (11), 1799-1809 (2008).

6.14 D. Suess, J. Lee, J. Fidler and T. Schrefl, Journal of Magnetism and Magnetic Materials **321** (6), 545-554 (2009).

6.15 H. Sohn and R. H. Victora, IEEE Transactions on Magnetics **47** (10), 4073-4076 (2011).

6.16 H. J. Richter, G. Choe and B. D. Terris, IEEE Transactions on Magnetics **47** (12), 4769-4774 (2011).

6.17 F. Casoli, L. Nasi, F. Albertini, S. Fabbrici, C. Bocchi, F. Germini, P. Luches, A. Rota and S. Valeri, Journal of Applied Physics **103** (4), 043912-043918 (2008).

6.18 D. Goll, A. Breitling, L. Gu, P. A. van Aken and W. Sigle, Journal of Applied Physics **104** (8), 083903-083904 (2008).

6.19 B. Ma, H. Wang, H. Zhao, C. Sun, R. Acharya and J.-P. Wang, IEEE Transactions on Magnetics **46** (6), 2345-2348 (2010).

6.20 L. Liu, W. Sheng, J. Bai, J. Cao, Y. Lou, Y. Wang, F. Wei and J. Lu, Applied Surface Science **258** (20), 8124-8127 (2012).

6.21 Y. K. Takahashi, K. Hono, S. Okamoto and O. Kitakami, Journal of Applied Physics **100** (2006).

6.22 J. F. Hu, J. S. Chen, Y. F. Ding, B. C. Lim, W. L. Phyoe and B. Liu, Applied Physics Letters **93** (7), 072504-072503 (2008).

6.23 T.-J. Zhou, B. C. Lim and B. Liu, Applied Physics Letters **94** (15), 152505-152503 (2009).

6.24 J. Wan, M. J. Bonder, Y. Huang, G. C. Hadjipanayis and C. Ni, Journal of Magnetism and Magnetic Materials **322** (13), 1811-1815 (2010).

6.25 V. Alexandrakis, T. Speliotis, E. Manios, D. Niarchos, J. Fidler, J. Lee and G. Varvaro, Journal of Applied Physics **109** (2011).

6.26 G. Giannopoulos, T. Speliotis, W. F. Li, G. Hadjipanayis and D. Niarchos, Journal of Magnetism and Magnetic Materials **325** (0), 75-81 (2013).

6.27 D. A. Gilbert, L.-W. Wang, T. J. Klemmer, J.-U. Thiele, C.-H. Lai and K. Liu, Applied Physics Letters **102** (13), 132406-132404 (2013).

6.28 K. K. M. Pandey, J. S. Chen, G. M. Chow and J. F. Hu, Applied Physics Letters **94** (23), 232502-232503 (2009).

6.29 H. H. Guo, J. L. Liao, B. Ma, Z. Z. Zhang, Q. Y. Jin, W. B. Rui, J. Du, H. Wang and J. P. Wang, Journal of Applied Physics **111** (10), 103916-103914 (2012).

6.30 S. Hong, X. Che, Y. Tang and J.-G. Zhu, Journal of Applied Physics **103**, 07F530 (2008).

6.31 R. Skomski, T. A. George and D. J. Sellmyer, Journal of Applied Physics **103**, 07F531-533 (2008).

6.32 Y. K. Takahashi, K. Hono, T. Shima and K. Takanashi, Journal of Magnetism and Magnetic Materials **267** (2), 248-255 (2003).

6.33 A. Martins, M. C. A. Fantini and A. D. Santos, Journal of Magnetism and Magnetic Materials **265** (1), 13-22 (2003).

6.34 F. Casoli, F. Albertini, S. Fabbrici, C. Bocchi, L. Nasi, R. Ciprian and L. Pareti, IEEE Transactions on Magnetics **41** (10) (2005).

6.35 F. Kurth, M. Weisheit, K. Leistner, T. Gemming, B. Holzapfel, L. Schultz and S. Fahler, Physical Review B **82** (18), 184404 (2010).

6.36 T. A. George, Y. Yu, L. Yue, R. Skomski and D. J. Sellmyer, IEEE Transactions on Magnetics **46** (6), 2435-2437 (2010).

6.37 T. Shima, K. Takanashi, Y. K. Takahashi and K. Hono, Applied Physics Letters **81** (6), 1050-1052 (2002).

6.38 F. Casoli, F. Albertini, L. Pareti, S. Fabbrici, L. Nasi, C. Bocchi and R. Ciprian, IEEE Transactions on Magnetics **41** (10), 3223-3225 (2005).

6.39 Y. Yu, T. A. George, H. Li, D. Sun, Z. Ren and D. J. Sellmyer, Journal of Magnetism and Magnetic Materials **328** (0), 7-10 (2013).

6.40 T. O. Seki, Y. K. Takahashi and K. Hono, Journal of Applied Physics **103** (2), 023910-023917 (2008).

6.41 C. P. Luo and D. J. Sellmyer, Applied Physics Letters **75** (20), 3162-3164 (1999).

6.42 S. Okamoto and O. Kitakami, Journal of Magnetism and Magnetic Materials **310**, 2367-2368 (2007).

6.43 E. Yang and D. E. Laughlin, Journal of Applied Physics **104** (2), 023904-023903 (2008).

6.44 D. H. Wei and Y. D. Yao, IEEE Transactions on Magnetics **45** (10), 4092-4095 (2009).

6.45 D. Alloyeau, G. Prévot, Y. Le Bouar, T. Oikawa, C. Langlois, A. Loiseau and C. Ricolleau, Physical Review Letters **105** (25), 255901 (2010).

6.46 F. Casoli, F. Albertini, L. Nasi, S. Fabbrici, R. Cabassi, F. Bolzoni and C. Bocchi, Applied Physics Letters **92** (14), 142506-142503 (2008).

6.47 C. Abraham and A. Aharoni, Physical Review **120** (5), 1576-1579 (1960).

6.48 F. B. Hagedorn, Journal of Applied Physics **41** (6), 2491-2502 (1970).

6.49 C.-K. Goh, Z.-m. Yuan and B. Liu, Journal of Applied Physics **105** (8), - (2009).

6.50 B. Ma, H. Wang, H. Zhao, C. Sun, R. Acharya and J.-P. Wang, Journal of Applied Physics **109** (8), 083907-083907 (2011).

6.51 Y. K. Takahashi and K. Hono, Applied Physics Letters **84** (3), 383-385 (2004).

6.52 G. R. Aranda, O. Chubykalo-Fesenko, R. Yanes, J. Gonzalez, J. J. del Val, R. W. Chantrell, Y. K. Takahashi and K. Hono, Journal of Applied Physics **105**, 07B514 (2009).

6.53 J. W. Harrell, IEEE on Magnetics **37** (1), 533-537 (2001).

6.54 D. Goll and S. Macke, Applied Physics Letters **93** (15) 152512-152513 (2008).

6.55 D. Suess, J. Fidler, G. Zimanyi, T. Schrefl and P. Visscher, Applied Physics Letters **92** (17), 173111-173113 (2008).

6.56 B. Ma, H. Wang, H. Zhao, C. Sun, R. Acharya and J.P Wang, Journal of Applied Physics **109** (8), 083907-083907 (2011).

6.57 T.J. Zhou, K. M. Cher, P. W. Lwin and J. F. Hu, Journal of Magnetism and Magnetic Materials **331** (0), 187-192 (2013).
6.58 T. Shima, K. Takanashi, Y. K. Takahashi and K. Hono, Applied Physics Letters **85** (13), 2571-2573 (2004).
6.59 T. Shima, K. Takanashi, Y. K. Takahashi, K. Hono, G. Q. Li and S. Ishio, Journal of Applied Physics **99** (3), 033516-033515 (2006).
6.60 N. Kikuchi, S. Okamoto and O. Kitakami, Journal of Applied Physics **103**, 07D511-513 (2008).
6.61 H. N. Bertram and M. Williams, IEEE Transactions on Magnetics **36** (1), 4-9 (2000).
6.62 A. Berger, Y. Xu, B. Lengsfield, Y. Ikeda and E. E. Fullerton, IEEE Transactions on Magnetics **41** (10), 3178-3180 (2005).
6.63 G. Asti, M. Ghidini, R. Pellicelli, C. Pernechele, M. Solzi, F. Albertini, F. Casoli, S. Fabbrici and L. Pareti, Physical Review B (Condensed Matter and Materials Physics) **73** (9), 094406-094416 (2006).
6.64 H. Kronmüller and D. Goll, physica status solidi (b) **248** (10), 2361-2367 (2011).
6.65 E. O. Samwel, P. R. Bissell and J. C. Lodder, Journal of Applied Physics **73** (3), 1353-1359 (1993).
6.66 T. Thomson and K. O. Grady, Journal of Physics D: Applied Physics **30** (11), 1566 (1997).
6.67 G. B. Ferguson, K. O'Grady, J. Popplewell and R. W. Chantrell, IEEE Transactions on Magnetics **25** (1989).
6.68 K. O'Grady, M. El-Hilo and R. W. Chantrell, IEEE Transactions on Magnetics **29** (1993).
6.69 H. H. Guo, J. L. Liao, B. Ma, Z. Z. Zhang, Q. Y. Jin, H. Wang and J. P. Wang, Applied Physics Letters **100** (14), 142406-142403 (2012).
6.70 L. S. Huang, J. F. Hu and J. S. Chen, Journal of Magnetism and Magnetic Materials **324** (6), 1242-1247 (2012).
6.71 R. H. Victora and S. Xiao, IEEE Transactions on Magnetics **41** (2), 537-542 (2005).
6.72 E. Girt, A. Y. Dobin, B. Valcu, H. J. Richter, X. Wu and T. P. Nolan, IEEE Transactions on Magnetics **43** (6), 2166-2168 (2007).

CHAPTER 7 OVERALL CONCLUSIONS

The $L1_0$ phase of FePt is an intrinsically promising candidate for future micro- and nanomagnetic technologies such as perpendicular magnetic recording. However, its implementation has proven difficult due to strict requirements on nanostructure and property distributions. For magnetic recording it is important to obtain a structure of magnetically isolated small grains possessing a high degree of (001) texture and chemical order. The research presented in this dissertation addressed these issues at somewhat fundamental levels by examining the structural and magnetic properties of nonepitaxially grown Fe/Pt multilayer and epitaxially grown particulate films.

Chapter 4 presented an investigation of the effects of stoichiometry and as-deposited structure in rapid thermally annealed Fe/Pt multilayer thin films on the resulting magnetic properties, chemical order, and nonepitaxially obtained (001) texture. Variations in as deposited structure included different bilayer thicknesses, total thickness, and using a Pt capping layer. The best film properties were obtained around even Fe:Pt stoichiometry. Consistently higher texture factors occurred at Fe-rich concentrations. Slight variations in the trend existed based on sample fabrication details; chemical order was maximized at Pt-rich compositions for films using 6 Å bilayers whereas order was best in Fe-rich films using thinner bilayers. In general, the multilayer deposition assisted in growth of textured films. In general, higher degrees of (001) texture were obtained in thinner films and a relationship between bilayer thickness and total thickness was determined. Specifically, the thinnest films tended to attain better texture with thicker bilayers. Evidence pointed to strain energy driven selected grain growth in the non-epitaxial formation of (001) texture. Use of a relatively thick Pt terminating layer in the multilayer scheme enhanced the resulting texture and yielded smooth grain surfaces.

Future studies into this system should focus on clarifying the proposed texturing method and reducing the overall film thickness. High resolution x-ray diffraction would allow better examination of the asymmetries of the (002)-$L1_0$ peak and more accurate data fits. Direct measurements of film strain in the as-deposited and annealed states using the $\sin^2 \psi$ method would be enlightening. The role of multilayering in the formation of (001) texture could be further illuminated by intermittently pausing during a codeposition process to mimic the breaks between layers while avoiding the formation of a compositionally modulated structure. Energy dispersive x-ray spectroscopy in a scanning electron or scanning tunneling electron microscope could be used to create elemental mapping of Fe- and Pt-rich regions within the as-deposited and processed films. Finally, a useful direction for nonepitaxially grown FePt films is to fabricate <5 nm thick films with high order, (001) texture and a continuous morphology for bit-patterned media applications. Simple modifications to the as-deposited film structure such as those investigated in this research could provide a method to realize such films.

Chapter 5 presented experimental studies aiming to control the granular structure and intergranular magnetic interactions in three FePt-composite systems with Al_2O_3, Au, and C dopants. A segregated granular microstructure is important for magnetic recording applications, yet high chemical order and (001) texture must be maintained. Variations in dopant content were investigated as well as the as-deposited multilayer structure for the Al_2O_3 films. Films with alumina doping appeared to form a nanogranular microstructure; however, chemical order and (001) texture were severely affected. The effect can be partially mitigated by increasing the FePt thickness between alumina layers in the multilayer stack. While alumina additions do not appear to work in non-epitaxially grown FePt films, it could serve to control grain growth and segregation in a system where chemical order and texture are strongly determined by other means, such as *in-situ* ordering with epitaxial growth. On the other hand, order and texture are

relatively well maintained with Au and C additions up to 32 and 39 volume percent, respectively. A simple model describing how interparticle exchange cooperatively increases both loop slope and correlation length yields different microstructural parameters for the two systems, indicating very different underlying structures or reversal mechanisms. Examination with electron microscopy would reveal the exact microstructure developed in these systems. Similar studies suggested for the nonepitaxial films studied in Chap. 4 would be useful here too; in particular compositional mapping would complement real structure images.

Chapter 6 presented an FePt-based exchange-coupled composite system using epitaxially grown FePt nano-scale islands as the hard magnetic phase. Magnetic properties of the system were tuned with the addition of a composite FePt:SiO_2 layer deposited at various temperatures and thicknesses. The mechanism of coercivity reduction appears to be related to the intrinsic properties of the partially ordered soft magnetic phase as well as an evolving microstructure. Evidence points to a non-ideal exchange-coupled composite system due to lateral exchange coupling and a population of superparamagnetic particles located in the trenches between the hard-phase particles. Cross-sectional transmission electron microscopy would be invaluable to reveal microstructural details. Future improvements to the system would require better control of particle sizes in the hard-phase layer and the use of a nonmagnetic dopant to fill in the trenches.

The research presented here does not provide direct solutions for implementing FePt in perpendicular magnetic recording media; however, it is hoped that the results provide positive directions to that end.

APPENDIX A Publications

1. W. Zhang, S. Valloppilly, X. Li, Y. Liu, S. Michalski, **T. A. George**, R. Skomski, J. Shield, D. J. Sellmyer, "Magnetic Hardening of Zr_2Co_{11}:(Ti, Si) Nanomaterials, Journal of Alloys and Compounds, to be published, Ms. Re. No.: JALCOM –D-13-06029R1.
2. R. Zhang, **T. A. George**, P. Kharel, R. Skomski, D. J. Sellmyer, "Susceptibility of Fe Atoms in Cu Clusters", Journal of Applied Physics, **113**, 17E148 (2013).
3. W. Zhang, S. Valloppilly, X.-Z. Li, S. Michalski, **T. A. George**, R. Skomski, J. Shield, D. J. Sellmyer, "Magnetism of rapidly quenched $Sm_{1-x}Co_5$ nanocrystalline materials", IEEE Transactions on Magnetics **49**, 3353 (2013).
4. Y. Yu, X.-Z. Li, **T. A. George**, W. Fei, H. Li, D. J. Sellmyer, "Low temperature ordering and high (001) orientation of $[Fe/Pt/Cu]_{18}$ multilayer films", Thin Solid Films **531**, 460 (2013).
5. Y. Yu, **T. A. George**, H. Li, D. Sun, Z. Ren, D. J. Sellmyer, "Effects of deposition temperature and in-situ annealing time on structure and magnetic properties of (001) oriented FePt films", Journal of Magnetism and Magnetic Materials **328**, 7 (2013).
6. H. Lu, **T. A. George**, Y. Wang, I. Ketsman, J. D. Burton, C.-W. Bark, S. Ryu, D. J. Kim, J. Wang, C. Binek, P. A. Dowben A. Sokolov, C.-B. Eom, E. Y. Tsymbal, and A. Gruverman, "Electric modulation of magnetization at the $BaTiO_3/La_{0.67}Sr_{0.33}MnO_3$ interfaces", Applied Physics Letters **100**, 232904 (2012).
7. R. Skomski, B. Balamurugan, **T. A. George**, M. Chipara, X.-H. Wei, J. Shield, D. J. Sellmyer, "Hysteresis and relaxation in granular permanent magnets", Journal of Applied Physics **111**, 07B507 (2012).
8. Y. Liu, **T. A. George**, R. Skomski, D. J. Sellmyer, "Aligned and Exchange-Coupled L10 (Fe,Co)Pt-Based Magnetic Films", Journal of Applied Physics **111**, 07B537 (2012).
9. Y. Liu, **T. A. George**, R. Skomski, D. J. Sellmyer, "Aligned and Exchange-Coupled FePt Based-Films", Applied Physics Letters **99**, 172504 (2011).
10. M. Chipara, J. Hamilton, A. C. Chipara, **T. A. George**, D. M. Chipara, E. E. Ibrahim, K. Lazano, D. J. Sellmyer, "FTIR and Wide-Angle X-Ray Scattering Investigations on Polypropylene - Vapor Grown Carbon Nanofibers Composites", Journal of Applied Polymer Science **125**, 353 (2012).
11. Y. S. Yu, **T. A. George**, W. L. Li, L. P. Yue, W. D. Fei, H. Li, M. Liu, D. J. Sellmyer, "Effects of total thickness on (001) texture, surface morphology, and magnetic properties of [Fe/Pt](n) multilayer films by monatomic layer depositions", Journal of Applied Physics **108**, 073906 (2010).
12. Y. S. Yu, **T. A. George**, W. L. Li, L. P. Yue, W. D. Fei, H. Li, D. J. Sellmyer, "Enhanced $L1_0$ ordering and (001) orientation in FePt:Ag nanocomposite films by monatomic layer depositions", IEEE Transactions on Magnetics **46**, 1817 (2010).
13. **T. A. George**, Y. S. Yu, L. P. Yue, R. Skomski, D. J. Sellmyer, "Control of coercivity in exchange-coupled graded (001) $FePt:SiO_2$ nanocomposite films", IEEE Transactions on Magnetics **46**, 2435 (2010).
14. E. Kockrick, F. Schmidt, K. Gedrich, M. Rose, **T. A. George**, T. Freudenberg, R. Kraehnert, R. Skomski, D. J. Sellmyer, S. Kaskel, "Mesoporous ferromagnetic MPT@silica/carbon (M = Fe, Co, Ni) composites as advanced bifunctional catalysts", Chemistry of Materials **22**, 1624 (2010).
15. **T. A. George**, R. Skomski, D. J. Sellmyer, "Magnetic correlations in nanocomposite FePt:Au and FePt:C films", Journal of Applied Physics **105**, 07B736 (2009).
16. **T. A. George**, Z. Li, M. L. Yan, Y. F. Yu, R. Skomski, D. J. Sellmyer, "Nanostructure and magnetic properties of $L1_0$ FePt:X films",Journal of Applied Physics **103**, 07D502 (2008).
17. R. Skomski, **T. A. George**, D. J. Sellmyer, "Nucleation and wall motion in graded media", Journal of Applied Physics **103**, 07F531 (2008).